Blade Passage Flow Structure Effects on Axial Compressor Rotating Stall Inception

by

Donald A. Hoying

GTL Report #224 December 1996

GAS TURBINE LABORATORY
MASSACHUSETTS INSTITUTE OF TECHNOLOGY
CAMBRIDGE, MASSACHUSETTS

Blade Passage Flow Structure Effects on Axial Compressor Rotating Stall Inception

by

Donald A. Hoying

GTL Report #224 December 1996

This research was supported by the United States Air Force through the Palace Knight Program, and by the Pratt & Whitney Division of United Technologies Corporation. Additional computational resources were also provided through NASA Lewis Research Center, at the National Aerodynamic Simulation Facility and at NASA Lewis.

Blade Passage Flow Structure Effects on Axial Compressor Rotating Stall Inception

by

Donald Andrew Hoying

Abstract

A new computational approach has been developed to study the inception of rotating stall in axial compressors. Using this approach the flow structures within the compressor blade passages have been examined in order to determine their influence on the process of rotating stall inception. Both two and three-dimensional numerical simulations were carried out.

The two-dimensional computations showed a long wave-length (or modal) type of stall inception which was found to be well described by existing compressor stability models. The numerical results were used to directly confirm the various assumptions used in the formulation of the stability models.

The three-dimensional computations of rotating stall displayed a short length-scale type of stall inception with the same character as that seen in experiments. The central feature of the flow associated with the development of the short length-scale stall cell was the tip clearance vortex moving forward of the blade row leading edge. Vortex kinematic arguments were used to provide a physical explanation of this motion. The resulting criteria for the the inception of the short length-scale stall depends upon local flow phenomena related to the tip clearance flow. Thus, unlike the modal stall situation, the flow structure within the blade passages must be addressed when describing the stability of an axial compression system to short length-scale disturbances.

Acknowledgments

I would like to take this moment to express my deep gratitude to those who have made it possible for me to achieve this accomplishment. In particular, I would like to express my appreciation to the following individuals and organizations.

First, I would like to thank the members of my committee, especially Prof. Ed Greitzer and Dr. Choon Tan. Their valuable experience and support were key to making the accomplishments of this project possible.

Indeed I am indebted to the United States Air Force for funding my research through the Palace Knight Program. The help and support of individuals like Lu Voronyak is greatly appreciated. In particular, I wish to thank my mentor and friend Dr. Doug Rabe for always supporting and encouraging me with his efforts and enthusiasm.

The faculty, staff, and students of the Gas Turbine Laboratory have been a tremendous support in helping my research along and in making my stay here a positive experience.

Clearly, I could not have performed all of the calculations shown here without some computer support. The majority of the computational work was conducted at the Gas Turbine Laboratory using the computers provided by Prof. Epstein. In addition, computational support was obtained from the NASA Lewis Research Center, NASA Ames Research Center, and the Compressor Research Facility at Wright Patterson Air Force Base. I am extremely appreciative of all the computer time and technical support I have received from all of these sources.

In addition, I would like to thank Roger Davis of the United Technologies Research Center for providing me with the experimental data used for the two-dimensional code

validation, Bob Haimes for use and support of the data visualization software Visual2 and Visual3, Diana Park for producing the video animation of the three-dimensional results, and Dave Car for the software used to generate the computational grids.

On a more personal note, I would like to express my appreciation to all of the people, both at MIT and home, that I am proud to call my friends. Life is far too long a journey not take the time to enjoy the company of those around you.

Also, I wish to express my gratitude and love for my family. Each and every one of them has been a tremendous support to me through my entire life. From my parents, Ivo and Georgianna, I have received the most valuable gifts of their strength and their courage. It is in their memory that this work is dedicated.

Finally, I wish to say thank you to the one person who has given the most to support this accomplishment, my wife Diane. Her expression of love through her own sacrifice is the greatest gift one could hope to receive.

Contents

List of Figures

Nomenclature

Variables

a	Spatial finite difference coefficient
	Eigenvector amplitude
b	Temporal finite difference coefficient
c	Artificial damping coefficient
	Characteristic variables
	Speed of sound
c_l	Turbulence model constant
d	Non-reflecting boundary condition zeros vector
e	Internal energy
	Stress tensor element
h	Generalized curvilinear coordinate metric
i	Generalized curvilinear coordinate direction
k	Axial mode number
	Turbulent kinetic energy
	Coefficient of thermal conductivity
l	Tangential mode number
m	Radial mode number
n	Tangential mode number
p	Static Pressure
q	Heat flux
r	Radial direction coordinate

s	Blade Spacing
	Laplace transform variable
t	Time
u	Velocity
	Axial Velocity
v	Tangential velocity
w	Velocity in rotational frame of reference
	Radial velocity
x	Axial direction coordinate
	Generalized curvilinear coordinate variable
y	Tangential direction coordinate
y^+	Boundary Layer Coordinate $\left(\frac{\sqrt{\tau_{wall}/\rho}}{\nu}y\right)$
z	Third cartesian direction coordinate
C_μ	Turbulence model constant
C_1	Turbulence model constant
C_2	Turbulence model constant
C_p	Specific heat at constant pressure
D	Well posedness coefficient matrix
E	Flux vector
	Total internal energy
	Integrated error function
E^*	Turbulence model constant
F	Flux vector
G	Flux vector
	Turbulent kinetic energy production
H	Source term vector
I	Source term vector
J	Jacobian of transform matrix
M	Mach Number
Q	Source vector

R	Specific gas constant
	Flux Vector
	Transformed source vector
S	Source term vector
	Flux Vector
	Left hand eigenvector matrix
T	Temperature
	Flux Vector
U	Rotor speed
	Vector of conservative variables
V	Velocity vector
W	Turbulence model conserved variable vector
X	Total pressure loss coefficient
NI	Number of axial grid points
Pr	Prandtl number
Re	Reynolds number
α	Fourier wave number
β	Relative flow angle
γ	Ratio of specific heats
δ	Kroniker delta
ϵ	Dissipation rate of turbulent kinetic energy
ϕ	Flow coefficient $(\frac{u_x}{U})$
κ^*	Turbulence model constant
λ	Inertial length of a rotor blade row
	Ratio of tangential wave number to complex frequency
μ	Inertial length of a stator blade row
	Ratio of radial wave number to complex frequency
	Coefficient of viscosity
μ_a	Coefficient of artificial viscosity
ν	Kinematic viscosity

π	Pi
ρ	Density
σ	Weighting parameter
σ_k	Turbulence model constant
σ_ϵ	Turbulence model constant
θ	Circumferential direction coordinate
τ	First order differential time lag
	Turbulence model stress tensor
ω	Complex frequency
	Laplace wave number
ξ	Streamwise body fitted coordinate
η	Normal body fitted coordinate
ζ	Radial body fitted coordinate
Γ	Stress tensor
Λ	Eigenvalue matrix
Π	Viscous stress tensor
Ψ_{T-S}	Total-to-Static pressure rise coefficient $(\frac{p_2-p_{t,1}}{\rho U^2})$
Ψ_{S-S}	Static-to-Static pressure rise coefficient $(\frac{p_2-p_1}{\rho U^2})$
Ω	Rotational speed of rotating frame of reference
$\imath$	$\sqrt{-1}$

Subscripts

1	Quantity upstream of blade row
2	Quantity downstream of blade row
3	Quantity downstream of second blade row
p	At near wall point
u	Derivative with respect to u
v	Derivative with respect to v

r	Radial component
	Derivative with respect to r
t	Total quantity
	Turbulent quantity
x	Axial component
	Derivative with respect to x
y	Tangential component
X	Total pressure loss term
mean	Average quantity
mod	Modified matrix
wall	On solid surface boundary
SS	Steady State
β	Flow turning term
θ	Circumferential component
	Derivative with respect to θ
ξ	Derivative with respect to ξ
η	Derivative with respect to η
ζ	Derivative with respect to ζ
∞	Free stream reference quantity

Superscripts

k	With respect to turbulent kinetic energy
L	Left hand eigenvector
R	Right hand eigenvector
ϵ	With respect to turbulent kinetic energy dissipation
( )	Time step

Operators and Modifiers

δ	Perturbational operator
Δ	Difference operator
$\vec{(\,)}$	Vector quantity
$\overline{(\,)}$	Mean quantity
	Approximation to real quantity
$(\,)'$	Perturbational quantity
	Quantity in rotational frame
	Linearized coefficient matrix
$\tilde{(\,)}$	Fourier-Laplace transformed variable
$\hat{(\,)}$	Unit vector
Im	Imaginary part of complex number
Re	Real part of complex number

Chapter 1

Introduction

1.1 Problem Description

Performance limiting instabilities are inherent in the operation of axial compressors and must be accounted for in the design and operation of a compression system. These instabilities can be divided into two classes; rotating stall and surge. Rotating stall is characterized by fluctuations in compressor performance around the annulus of the compressor which rotate in the same direction as the rotor at approximately half the rotational speed. Surge is a large scale essentially one-dimensional flow oscillation in the compressor. A comprehensive review of the flow instabilities present in compression systems is given by Greitzer [16]. This study will only address the development of rotating stall in axial compressors.

Emmons, Pearson, and Grant [9] were the first to describe the mechanism for rotating stall which is presented in Figure 1.1. In this figure a group of separated airfoils is shown near other airfoils which are operating without separation. The separated blade passages create a blockage which causes the air to divert around them. As a result, the airfoils above the separated region experience an increased angle of attack while the blades below experienced a reduced flow angle. The upper blades are then caused to separate and the lower blades become less separated. The net result is that the region of separated flow and high blockage propagates relative to the blade row in the direction shown.

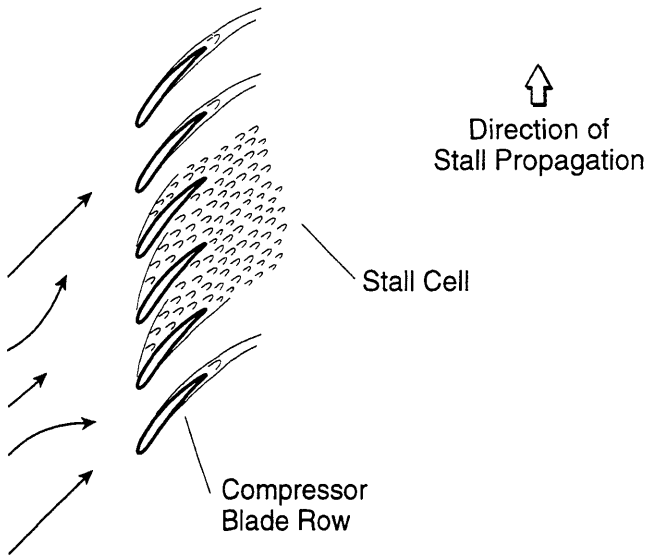

Figure 1.1: Sketch of physical mechanism of rotating stall

Experimental observations have shown that two types of rotating stall inception exist in axial compressors. The first is a long wave-length type which has been found to be well described by simple linear models. The length scale of this type of stall cell is on the order of the annulus of the compressor. This will be referred to as a *modal stall inception.* The second type of stall inception involves the formation of short length-scale stall cells. These stall cells are not much larger than the spacing between the individual compressor blades. Currently, no fluid dynamic description exists to explain the occurrence and development of these stall cells. This second type of stall will be referred to as a *short length-scale stall inception.*

The purpose of this study will be to examine the development of rotating stall in order to provide a mechanistic description of both types of stall inception. The new aspect of the problem which has been included is the direct modeling of the flow fields within the compressor blade passages. Previous studies have ignored these details.

By examining the flow structures of the intra-blade flow fields it will be possible to make direct links between this flow field and the development of rotating stall.

Ultimately, the aim is to link the stalling behavior of a compressor to the design variables.

1.2 Motivation

Rotating stall has been a concern since the first jet engines were produced, but even now, when a new compressor is designed, experiments are relied upon to describe the stalling behavior of the compressor. At times the performance of the engine must be decreased in order to meet operational stability requirements. The ability to relate the stability characteristics of a compressor to the design parameters is crucial to achieving the desired levels of both performance and stability. Even with the use of active control in compressors, which provides the potential for enhanced stability, a better understanding of the fluid dynamics of the stalling process is required.

For the modal type of stall inception well tested models currently exist, but this is not the case for the short length-scale stall inception. In particular, the role that the blade passage flow structures have in the development of rotating stall is currently not well understood.

1.3 Objectives

The objectives of this study can be posed as the following questions.

- How do the flow structures within the blade passage impact the development of rotating stall?
  - For a modal stall inception
  - For a short length-scale stall inception
- When are the assumptions of the current modal stall models valid?

The first question is at the heart of this effort. The goal is to identify the key aspects of the blade passage flow which participate in the stalling process. In addition, the

opportunity exists to directly evaluate the assumptions commonly used in current models of rotating stall.

1.4 Approach

To provide the level of detail necessary to observe the flow features within the blade passage in an unsteady manner, it was determined that a numerical approach was the best suited. Because the problem of rotating stall is a quite large problem to handle numerically, some compromises will be made as a result. The approach used to achieve the objectives of this study is given in the following list.

- Develop a numerical method suitable for computing the development of rotating stall, including the details of the flow within the blade passages.
- Compute the development of rotating stall in geometries of interest.
- Examine the results to establish the sequence of events by which rotating stall develops in compressors.
- Provide a mechanistic description of stall inception for both the modal and short length-scale disturbances.
- Compare the results directly with existing stall models to provide evaluation and validation

Chapter 2

Background

Although axial compressor stall research has been ongoing since the late 1940s, not until the late 1980s were detailed measurements made of the stall inception process. Much of the more recent activity was a result of the renewed interest in compressor stability models and their application to active control of rotating stall [10]. This chapter gives a short review of progress into the understanding rotating stall.

2.1 Stall Inception Experiments

One of the earliest studies of the small scale disturbances which precede rotating stall was conducted by Jackson [26] in 1985. Although the data were limited, Jackson established that the development of rotating stall could be traced to small initial disturbances in the flow field which develop into stall.

McDougall [35] performed a more detailed investigation into the development of rotating stall. Using an array of inlet velocity measurements, McDougall was able to track the magnitude and phase of the Fourier harmonics of the inlet velocity. The stall cell was shown to develop continuously from an initially small amplitude velocity disturbance. During its development, the growth rate of the first Fourier harmonic closely resembled an exponential function in time.

Garnier [12] performed an experimental study focused on the character of these modal waves and compared the experimental results against the predictions of a linear

stall model. The stall model did a reasonably good job of predicting the stalling flow coefficient and rate of rotation of the stall cell. In addition, a system parameter estimation technique was used to compute an estimate of the damping coefficient of the system. It was found that the measured damping (growth/decay rate) decreased in an orderly way towards zero (the stability limit) as rotating stall was approached. This assessment of the stall models was an important step in the development of control methods for rotating stall.

Several other investigations have also been conducted on the inception of rotating stall. A compendium of these results is presented by Tryfonidis et al. [53].

The findings of Day [7] represent a significant departure from the results of McDougall and Garnier. Day presents data which display no noticeable level of modal activity prior to the development of rotating stall. In these cases, stall is preceded by short length-scale disturbances which degenerate into fully developed rotating stall in only a few rotor revolutions.

The short length-scale stall inception perturbations have several characteristics which differentiate them from the modal type of stall inception. The first is their length scale. Modal stall perturbations have a characteristic length of the compressor annulus while the size of the short length-scale disturbances is on the order of the blade spacing. For axial compressors this represents an order of magnitude difference in size. A second characteristic is that short length-scale disturbances initially rotate at higher speeds ($\sim 70\%$) than the fully developed stall cell ($\sim 30 - 50\%$), therefore these disturbances tend to slow down as they grow. The last identifying characteristic of short length-scale disturbances is the fast rate at which they develop from their first detection into full scale rotating stall. This typically occurs over the period of only two or three rotor revolutions.

In the experiments conducted by Day, the short length-scale type of stall inception was not the only type of stall inception seen; in some cases, Day shows data from compressors in which the stall development can be classified as modal. In others, the apparent development of a modal type of stall inception is preempted by the development of a short length-scale disturbance.

In summary the types of stall inception seen experimentally fit into two categories; modal and short length-scale. The computations and analysis presented in this work will seek to provide an understanding of the fundamental mechanics involved in both of these processes.

2.2 Compressor Stability Models

2.2.1 History

Considerable effort has been put into the development of compressor stability models to describe the onset of rotating stall since the initial paper by Emmons, Pearson, and Grant [9]. Although additional physical effects have been added and the form of the model has changed somewhat, the assumptions currently used are not fundamentally different from those applied by Emmons. The compressor is represented by specified functions which describe the pressure rise and turning versus inlet velocity or flow angle. Early models were linearized, but more recently non-linear methods have been employed to examine the development of rotating stall for large amplitude disturbances.

In 1958 Stenning and Kriebel [48] included an unsteady response in the losses in the compressor. The use of an unsteady response modifies the stability criteria so that the modes of the system no longer become unstable at the same operating point. For typical compressors the longest wave length modes become unstable first (at a higher flow coefficient) if this effect is included. Dunham [8] recast the analysis in terms of the overall pressure rise characteristic and presented the now familiar result that a compressor would enter into rotating stall at the peak of the total-to-static pressure rise characteristic.

During the mid-eighties compressor stability models received renewed interest. In a series of papers, Moore [37] [38] [39] presented the linear model in essentially its current form and extended the theory to encompass finite amplitude disturbances using a non-linear model. This concept is further developed by in the papers by

Moore and Greitzer [40] [41] in which the two main instabilities in compressors, surge and rotating stall, are addressed in a unified treatment. The result is a coupled non-linear system of equations which describe the development of compression system instabilities.

2.2.2 Results of Stability Models

Since this study is primarily concerned with the inception of rotating stall, the linear models provide most of the information required for comparison with the computed result; namely the shape of the stalling disturbances and their growth and rotational rates. For the case with infinitely long ducts and uniform background flow, the two-dimensional linear model yields a particularly simple result in that the modes of the system are sine waves in the θ direction. Therefore the modes are the Fourier harmonics.

The results from two-dimensional linear stall models can be summarized as follows:

- The mode shapes are sine waves in the θ direction with wave lengths which are integer fractions of the compressor circumference.

- The flow becomes unstable at the peak of the total-to-static pressure rise characteristic, assuming no lag in the compressor response.

- When an unsteady compressor response is included the first mode is predicted to become unstable first for typical compressor geometries.

Experiments show that these results are correct when the compressor exhibits a modal stall type of inception [12] [18]. For a short length-scale type of stall inception, the assumptions used to formulate this model are no longer valid. Specifically, the assumption that the length scale of the stalling disturbance is long compared to the blade spacing is violated. In addition, the impact that flow structures within the blade passage have on the development of rotating stall is not included.

2.3 Previous Numerical Studies

Several two-dimensional numerical studies of rotating stall have been performed using either vortex tracking methods or conventional CFD. Although not all the results are relevant to this research effort, important features are seen in the results. Two of these previous studies are most relevant to this investigation of stall inception and also contain the relevant conclusions made in the other works.

The first is a vortex tracking method solution by Nishizawa and Takata [43]. Using a single blade row consisting of ten blades, an equilibrium solution is disturbed by reducing the flow a small amount in one of the blade passages. Below a critical inlet flow angle, this disturbance decays after its introduction. Above the critical inlet flow angle, the disturbances grow into rotating stall. Initially several small stall cells are seen to grow, which then evolve into one fully developed stall cell. When the inlet condition was modified to represent the ideal response of a row of inlet guide vanes, the initial stall development was similar, but the final pattern consisted of multiple stall cells. These results serve to demonstrate that the form of the boundary conditions used to compute rotating stall can impact the results. Therefore the effect that the inlet and exit boundary condition modeling assumptions have on the development of rotating stall should be considered.

The other numerical study of rotating stall reviewed here was a Navier-Stokes method performed by He [20]. A single blade row compressor, consisting of twenty blades, was slowly throttled until the appearance of rotating disturbances was observed. When no initial disturbance was applied a stalling pattern with five to seven stall cells was seen. By applying a single sine wave stationary circumferential distortion in total pressure (5%) at the inlet of the computational domain the result changed to a single sine wave stalling pattern. A similar computation with a two sine wave ($sin(2\theta)$) distortion yielded a two sine wave stalling pattern. The stalling flow coefficient was increased by 3% and 6% for the two and one sine wave distortion patterns respectively. These results show that the development of rotating stall can be sensitive to applied disturbances.

He also carried out computations with a rotor-stator compressor geometry. By varying the blade counts between the rotor and the stator it was possible to introduce a one and two sine wave disturbance in the flow field due to the interaction of the blade rows. Like the rotor-only compressor the initial stalling perturbations had the same shape as the applied disturbance. However for the rotor-stator compressor the final stalling pattern was always a single lobed stall cell.

The calculations reviewed here identify several features that must be addressed in the numerical study of rotating stall. First, boundary conditions can change the form of the instability observed. Second, the presence of imposed disturbances can modify the stalling behavior. Finally, the results for a rotor-only compressor geometry appear to have a different stalling character than compressors with multiple blade rows.

Chapter 3

Numerical Modeling

The use of a detailed numerical model provides many benefits, but the increased level of detail does not come without cost. A number of concerns must be addressed in order to arrive at a viable numerical model which incorporates the details of the intra-blade flow fields. These concerns will be discussed in this chapter.

The numerical method used for this study is applicable for computing the development of rotating stall for both two and three-dimensional geometries. Therefore, for the majority of this chapter, no distinction will be made to whether the two or three-dimensional problem is being considered.

3.1 Modeling Requirements

There are many issues that relate to the choice of a computational fluid dynamic model, but only those specifically relevant to this problem will be addressed here. The majority of standard computational issues, such as stability and order of accuracy, are covered in text books such as the one by Anderson, Tannehill, and Pletcher [2] and will not be reviewed. For the problem of rotating stall inception several additional issues are worthy of discussion.

3.1.1 Length Scales

A challenging aspect of this problem is dealing with the large range of length scales involved in the problem of rotating stall. Because this is also an unsteady problem, the large range of length scales gives rise to a large range of time scales as well. The physical length scales vary from compressor circumference down to flow structures with length scales less than the blade spacing. Most turbomachinery computations address only a single blade passage, so the range of length scales is much less. For the study of rotating stall, the number of blades considered will be on the order of ten to twenty. To resolve features of a size as small as one third of the blade passage, the ratio of length scales is thus over fifty. For a steady problem this difficulty can be overcome by stretching the grid where the variations in the flow are small. This economy is lost when considering an unsteady problem where the minimum spacing is dictated by the minimum wave length to be computed. This results in a dense grid for the majority of the flow field.

The accurate propagation of waves through the computational domain can be addressed in two parts, amplitude and speed of propagation. Errors in amplitude are called dissipative errors, and those of propagation speed are referred to as dispersive errors. All known numerical schemes display at least one of these types of error for short enough wave lengths.

The challenge involved in computing a solution which is both accurate and feasible will be to choose a numerical method which remains accurate on as coarse a grid as possible but is not so complex as to out weigh the benefit of using the coarser grid. This criteria favors the more accurate, and more complex, schemes.

3.1.2 Viscous Effects

Another consideration in the study of rotating stall is the inclusion of viscous effects. It is the effects of viscosity which gives rise to the loss mechanisms which give the compressor characteristic its shape. A turbulence model is generally used to approximate the viscous fluid effects near the blades. However, many turbulence models

perform poorly in the presence of separated flow. Since this is expected to occur during the development of rotating stall, a suitable turbulence model must be chosen to handle the separated flow situation.

3.1.3 Relative Blade Motion

Another challenge is the inclusion of relative motion of the rotor and stator blade rows. This will require that the grids used for the different blade rows be allowed to move relative to each other.

3.2 Code Development

The number of existing computational methods which could satisfy the stated modeling requirements was quite limited. All of them required an impractical amount of computational resources to solve the problem of three-dimensional rotating stall inception. To accomplish this task is was necessary to construct a new numerical method which was focused on the satisfying the modeling requirements in the most practical means possible. Several of the key problems, and their solutions, which went into creating this method are described below.

3.2.1 Dispersion Relation Preserving Scheme

The primary dissatisfaction with existing unsteady methods was their accuracy for short wave lengths. To create an optimum method for capturing a large range of wave lengths it is necessary to incorporate a measure of this accuracy in the process for constructing the numerical method. Such an approach has been created by Tam and Webb [50]. The resulting numerical integration method is called a Dispersion Relation Preserving (DRP) scheme. This method was optimized for its dissipative and dispersive character rather than using a standard order of accuracy analysis. The basic concept is to minimize the error involved in taking a numerical approximation to a derivative over as large a range of wave lengths as possible. The resulting method

is a finite difference approach using an explicit time integration scheme. The details of the construction of this method are contained in Appendix C.

The use of the DRP scheme affects the choice of the form of the equations of motion to use. Some computational simplicity and efficiency can be gained by casting the equations of motion into a strong conservation form. When this is done the evaluation of the grid metric terms must be performed in such a way as to satisfy the geometric conservation law; otherwise non-physical sources will be generated in the flow field. Due to the high-order scheme used, it becomes difficult to satisfy the geometric conservation law near the boundaries. To overcome this, the chain rule conservative form of the equations was used as recommended by Thomas and Lombard [52].

For the accurate propagation of waves (within 1% in wave speed), the DRP scheme has the ability to capture nearly twice the range of waves lengths than does the commonly used four-stage Runge-Kutta integration scheme. Therefore, for a given range of wave lengths, half the number of grid points is required. For a three-dimensional problem, this yields a factor of eight fewer grid points and a corresponding doubling of the time step possible. This reduction in the numerical size of the problem was essential in enabling a solution using current computing resources.

3.2.2 Viscous Modeling

In the study of rotating stall flow solutions which include substantial amounts of flow separation will be expected. This places constraints on the type of turbulence models which can be used.

The simplest turbulence models use only local information and describe the effects of viscous boundary layers using analytical equations. However the state of a boundary layer at one location is affected by the state of the upstream flow, therefore it is more appropriate to describe the evolution of the boundary layer using differential equations. The most popular of these methods is the $k - \epsilon$ turbulence model which has been tested in a large variety of flow situations. In addition, no special treatment is needed for the computation of separated or reversed flows.

The biggest drawback to the use of the $k-\epsilon$ turbulence model is that the computational time required to implement it is on the same order as that required to integrate the equations of motion. Also, to calculate the viscous effects with accuracy, the grid resolution must be several orders of magnitude finer than needed to compute an inviscid flow. For these reasons, it was not feasible to include the turbulence model in all parts of the flow field. Thus, only the regions of the flow in and near the boundary layer of the blade surfaces were treated as viscous.

In addition, the inner most region of the boundary layer was treated analytically through the use of wall functions. The use of wall functions modifies the solid wall boundary condition by allowing a slip velocity so that the proper viscous stress can be provided to the flow field without the necessity of computing the boundary layer all the way to the wall. This method is well suited for use with the $k-\epsilon$ turbulence model and was part of the reason for its choice.

Details of the development and application of both the $k-\epsilon$ turbulence model and the use of wall functions are contained in Appendix F.

3.2.3 Boundary Conditions

One of the more challenging aspects of any computational model is the correct representation of the boundary conditions. There are many different types of boundary conditions represented in this problem including periodic, solid boundaries, and inlet/exit planes.

In the computational space, the annulus of the compressor has been unwrapped in the circumferential direction. To represent the periodic nature of the cylindrical geometry, a periodic boundary condition is used where the physical domain has been cut.

At solid boundaries there is no transport of mass, momentum, or energy (adiabatic) normal to the wall. The first two conditions can be satisfied by forcing the surface velocity to be parallel to the surface. The magnitude of the surface velocity will be determined by the wall functions as described in Appendix F. A zero gradient in temperature normal to the surface is also specified. The remaining pressure

boundary condition is derived from the radial equilibrium equation.

The most difficult boundary conditions to specify are the inlet and exit boundary conditions. These boundary conditions must satisfy two types of constraints. The first is that they provide the correct average flow quantities. The second is that they allow the interior flow solution to 'feel' as if the computational domain extends to infinity in order to duplicate the boundary conditions of the linear model. This is also done to remove sensitivity of the solution to the numerically imposed boundary conditions and to reduce the size of the computational domain.

Average inlet and exit boundary conditions can be computed using one-dimensional characteristic theory as presented in Appendix G. However the flow variations involved in rotating stall are not one-dimensional, and the one-dimensional characteristic boundary equations alone are not sufficient to represent the inlet and exit boundaries. One method to deal with this problem is to use very long inlet and exit ducts. Since rotating stall perturbations will die away with distance from the compressor, any interaction of the perturbation with the improper boundary condition will be so small as to not adversely affect the solution, if the ducts are long enough. However, larger domains and longer simulation times are then required.

A better solution is to implement non-reflecting boundary conditions which allow perturbations which are moving out of the computational domain to exit the domain without creating non-physical reflections. When non-reflecting boundary conditions are used, the boundaries can be placed much closer to the flow field of interest. The details of the construction and implementation of the non-reflecting boundary conditions are covered in Appendix H for the two-dimensional case, and in Appendix I for three-dimensional flows.

3.2.4 Relative Motion

An additional concern in the computation of compressor flow fields is the presence of relative motion in the geometry. The most common method is to divide the computational domain along simple boundaries and allow the separate regions to move past each other. The remaining problem is primarily a book-keeping one in transferring

information between the two grids. However, relative motion is not the only reason to consider the use of multiple grids. Since different types of structured grids lend themselves more easily to different flow situations, it is often advantageous to use multiple grids for stationary problems. The details of how the relative motion of the grids is accounted for is contained in Appendix D.

3.2.5 Grid Construction

The duct regions of the compressor flow field are most easily treated using a H-grid topology. Since the ducts are simple geometries, a computational economy can be gained by aligning all of the grid lines with lines of constant axial position, radius, and circumferential angle.

Near the blades, an O-grid topology was found to be the most effective. One of the advantages of the O-grid is the ease with which points can be clustered near the blade, especially near the leading and trailing edges. Another advantage is the ability to create grid lines which are perpendicular to the blade surface. Because the majority of the viscous effects are contained in the normal derivatives, the viscous terms can be computed directly along given grid lines. A representative grid is shown in Figure 3.1 which displays the O-grids surrounding the blades superimposed on the underlying H-grid.

For additional economy, viscous effects were included only in the O-grid region. Outside this region the grid is generally too coarse to accurately represent the details of a viscous flow. The use of the multiple grids also made the separation between viscous flow regions and the outer inviscid region simple. In the O-grid regions the Navier Stokes equations were solved. In the surrounding H-grid region the Euler equations were solved.

As discussed in the previous section, is is sometimes necessary for these grids to move relative to each other. Due to the use of a high-order numerical integration scheme, it is necessary to transfer more than just the edge values. Sufficient overlap is required to give information to the numerical solver for the required number of grid points. Since the two grids cannot be made to line up directly with each other, inter-

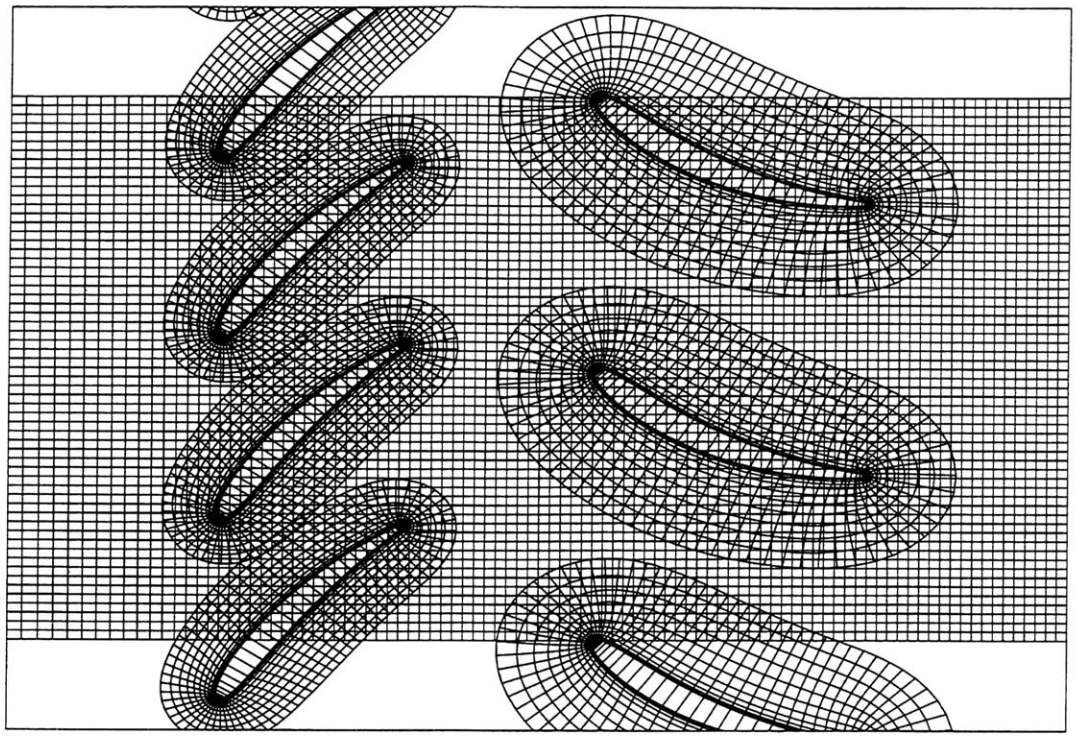

Figure 3.1: Two-dimensional computational grid

polation of the data is required. For a stationary set of grids, all of the interpolation coefficients can be computed before the calculation is begun, but the situation can be more complex when relative motion is required. By exploiting the regularity of the underlying H-grid a method of computing the interpolation coefficients without doing a grid search was developed. The grid construction methods are described in detail in Appendix D.

Tip Clearance Region

For the three-dimensional computation, the effects of the tip clearance flows are of interest. Storer and Cumpsty [49] have shown that the flow in the tip clearance region is primarily two-dimensional and inviscid. Since the two-dimensional Euler equations satisfy these conditions and are straight forward to implement, they were used to compute the flow in the tip gap region. The details of the implementation of this tip clearance model are given in Appendix E.

3.2.6 Equations of Motion

The set of equations used to compute the inception of rotating stall in axial compressors are a combinations of the Thin-Layer Reynolds-Averaged Navier-Stokes equations and the Euler equations as presented in Appendix B. The form of viscous model used was the $k - \epsilon$ turbulence model as described in Appendix F.

3.3 Code Validation

An evaluation of the code was used to determine its applicability to the problem of rotating stall inception. To do so, it was first necessary to describe the criteria by which it is to be judged. Because the primary interest in this investigation is to determine the basic mechanisms of the stalling process, measures of the absolute levels of performance are not required. What is necessary is that the code provide the proper trends in response to changes in operating conditions. More specifically, the results of the compressor stall models demonstrate that it is the derivatives of the compressor performance that determine its stability rather than the absolute levels (see Appendix A). Therefore, the merit of this code will be judged primarily on its ability to capture the proper trends in performance. Additionally, since the influence of the tip gap clearance flow is to be considered in the three-dimensional case, the code will be required to provide the correct trends in the response of this flow structure.

3.3.1 Two-Dimensional Code Validation

To evaluate the use of this code for the computation of rotating stall the computed results were compared with experimental data. Data were obtained for a two-dimensional geometry from Hobbs and Weingold [22]. A numerical study was conducted using this data by Davis, Hobbs, and Weingold [6] using a two-dimensional Navier-Stokes solver. These results are repeated here for an additional comparison.

The grid used for the computation is shown in Figure 3.2. Only the O-grid which envelopes the blade is shown. There is also a background H-grid with a resolution

similar to the coarse portion of the O-grid. Figure 3.3 compares the loss coefficient ($\equiv (p_{t_1} - p_{t_2})/p_{t_1}$) of the cascade for the current method (RS2), the method used by Davis et al. [6] (VISCAS), and the data of Hobbs and Weingold [22]. The comparison was conducted at a wheel speed Mach number of 0.4 and a Reynolds number based on the chord of the airfoil of 300,000.

The results obtained from the two codes compare reasonably well in trend and magnitude. One difference is the minimum loss coefficient found for each method. The VISCAS code agrees well with the data, while RS2 gives a somewhat higher value. This difference is attributable to the lower resolution of the RS2 code in the boundary layer region which was dictated by the use of a time-accurate explicit method. As a result of the lower resolution, artificial damping becomes more significant where the boundary layers are especially thin, such as near the leading edge and on the pressure side of the airfoil. The increased artificial damping contributes to a somewhat higher overall loss prediction.

Both codes predict different trends than the data in the high positive incidence region. The data show an increase in the amount of loss generated at a 5° lower angle of incidence than either of the numerical methods. The reason cited for this difference by Davis et. al. [6] is the use of a fully turbulent viscous model. With this type of method the code is incapable of predicting regions of laminar flow and possible laminar separation. Both codes use a similar turbulence model, and the results from the two codes tend to agree well. The results of Halstead et. al. [17] indicate that a substantial region ($\sim 50\%$) of laminar flow will exist at Reynolds numbers in the range used for this comparison. The presence of high losses at lower incidence angles is consistent with the premise that flow separation over the blade may be laminar in the experiment. As a result, the onset of separation (and high losses) would likely be delayed for a fully turbulent flow case.

The air exit angle for the same cases is shown in Figure 3.4. An exact comparison is more difficult in this case because of changes in the two-dimensional stream tube height in the experiment due to wall boundary layer removal in the experiment. The VISCAS solver incorporated an estimate of this contraction, while RS2 did not. Since

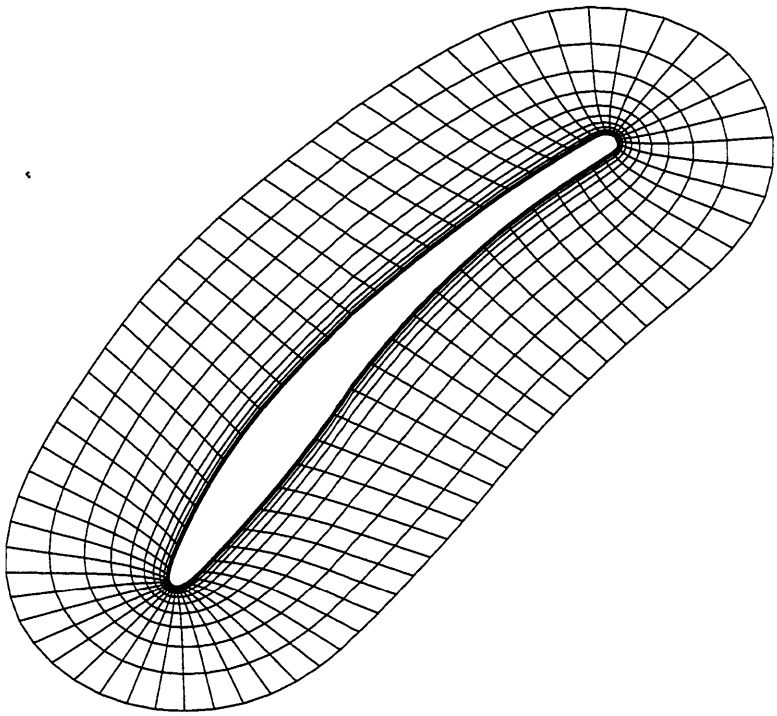

Figure 3.2: Grid used to solve for flow about the Controlled Diffusion airfoil (background grid omitted)

the exit angle can be sensitive to this effect, it is appropriate to verify that the trends compare rather than the absolute values. Both codes capture the trends in exit flow angle.

Overall, the results from the comparison are satisfactory. The difference in the minimum loss level is not seen as a concern for this study since a detailed performance measure is not being sought. However, the differences between the computed results and data in the high positive incidence region is of greater importance. It appears that the experimental result may exhibit a different type of flow separation than that predicted by the two codes. Due to assumptions made in the development of RS2, only turbulent flow solutions can be generated. Therefore, it is important to keep in mind that the results of this study will apply to flows which exhibit loss profiles that are the result of turbulent flows.

In many computational works grid refinement studies are utilized to show that the details of the flow have been resolved adequately. When finer grids were used (two, four, and eight times finer) the absolute level of losses were reduced to a level

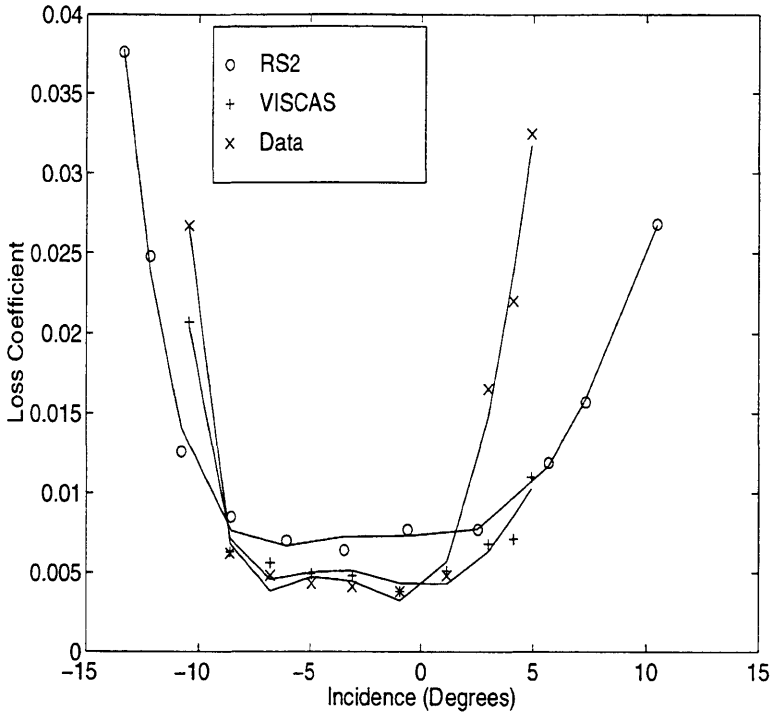

Figure 3.3: Loss profile comparison for the Controlled Diffusion airfoil

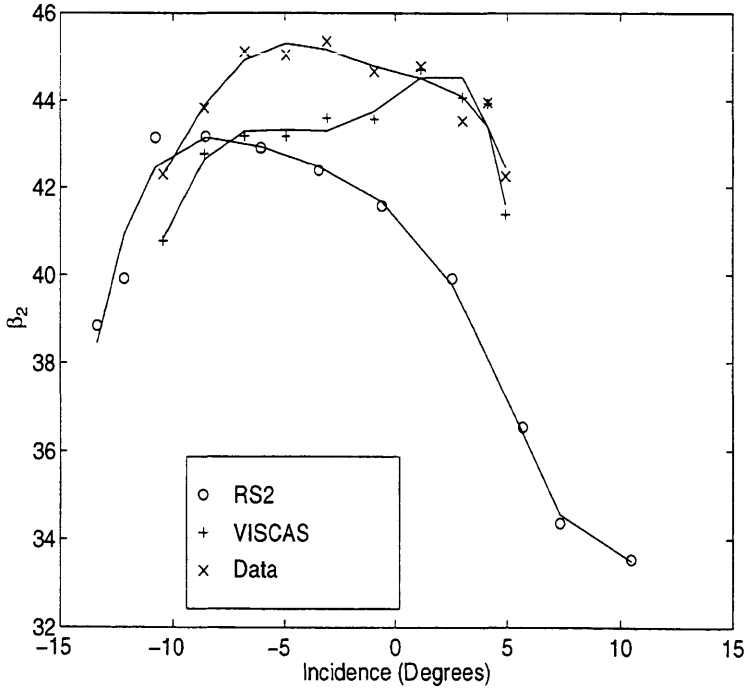

Figure 3.4: Flow turning profile comparison for the Controlled Diffusion airfoil

closer to that given by experiment. However, these finer grids are not practical for use in the study of rotating stall because of the excessive demands they place on the computational resources. Therefore, the fundamental goal of the computation must not be the absolute level of performance, but rather the trends; which the analysis of rotating stall requires and the RS2 code has been shown to capture.

3.3.2 Three-Dimensional Code Validation

To evaluate the performance of the three-dimensional version of this code (RS3), a comparison was performed with the calculations done by Khalid [27] using the code developed by Adamczyk et al. [1]. The blade used for this comparison was the rotor of the E^3 compressor geometry as tested by Wisler [55]. The comparison was conducted at a Mach number of 0.2 and a Reynolds number based on the tip chord of 400,000 for comparison with Khalid's computation. A comparison was made of the pressure rise characteristics for the two different tip clearances studied by Khalid. Khalid's computations were shown to compare well with experimental data [27] [55]. The results are presented in Figure 3.5. There is a noticeable offset between the two results. This was found to be a result of the higher levels of total pressure loss in the RS3 results. When the losses were subtracted out of both sets of calculations the offset disappears. The high level of losses given by the RS3 program was consistent with those experienced during the two-dimensional code validation, and is primarily the result of higher profile loss due to a larger separated flow region on the suction surface of the blade. To reduce the excess loss it would be necessary to use a larger amount of grid points in the computation but this would make the numerical solution to the problem of rotating stall intractable at this time. Again, for this study, absolute levels of performance are less important than trends in performance, and two sets of characteristics have similar pressure rise characteristics.

The effect of an increase in the tip clearance is also well represented in the results. The RS3 code shows a similar decrease in pressure rise due to the change in tip clearance as Khalid's [27] result, which was also shown to compare well with the experimental data.

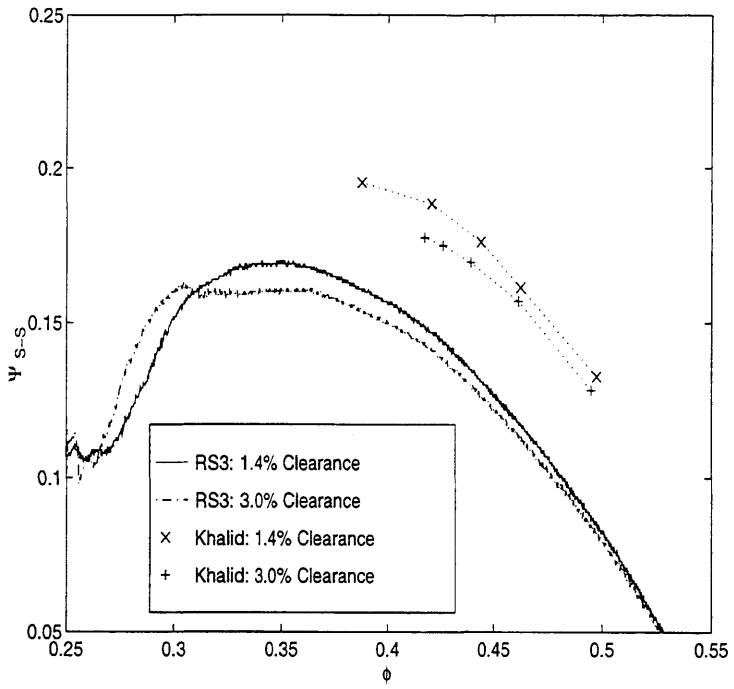

Figure 3.5: Comparison of compressor characteristic between RS3 code and numerical results of Khalid

A further comparison of the flow fields is given in Figures 3.6 and 3.7. These plots show contours of the axial velocity at the exit plane of the rotor for comparable operating points. The two basic flow features evident in these figures are the tip clearance vortex and the suction side boundary layer. As mentioned previously, the RS3 code yields a higher profile loss which is reflected in the results as a notably thicker suction side boundary layer at the exit plane. The tip clearance flow structure is relatively similar in shape, but is located much closer to the suction side of the blade in the RS3 result. This is due to the absence of a casing boundary layer in the RS3 result which has the effect of unloading the tip. This resulted in the Khalid's computation having a higher incidence angle at the tip which yielded higher tip clearance mass flows near the leading edge. This can be seen in the plot of the tip clearance normal velocity (component perpendicular to the blade) shown in Figure 3.8. The net result is that the tip clearance vortex rolled up closer to the leading edge in Khalid's result and therefore migrated farther across the blade passage.

The RS3 code has demonstrated satisfactory performance for use in the compu-

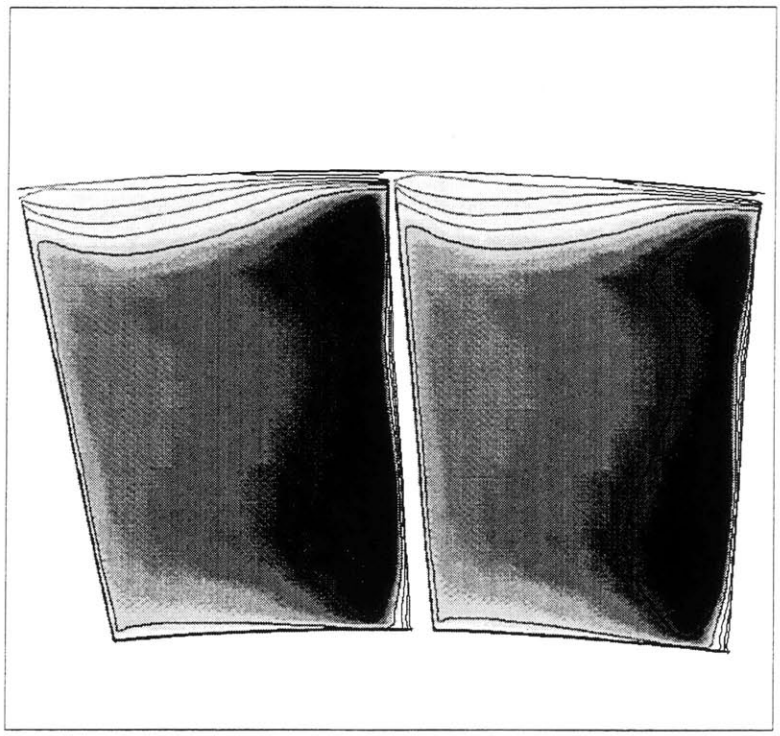

Figure 3.6: Axial velocity contour at the exit plane for the E^3 rotor as computed by Khalid

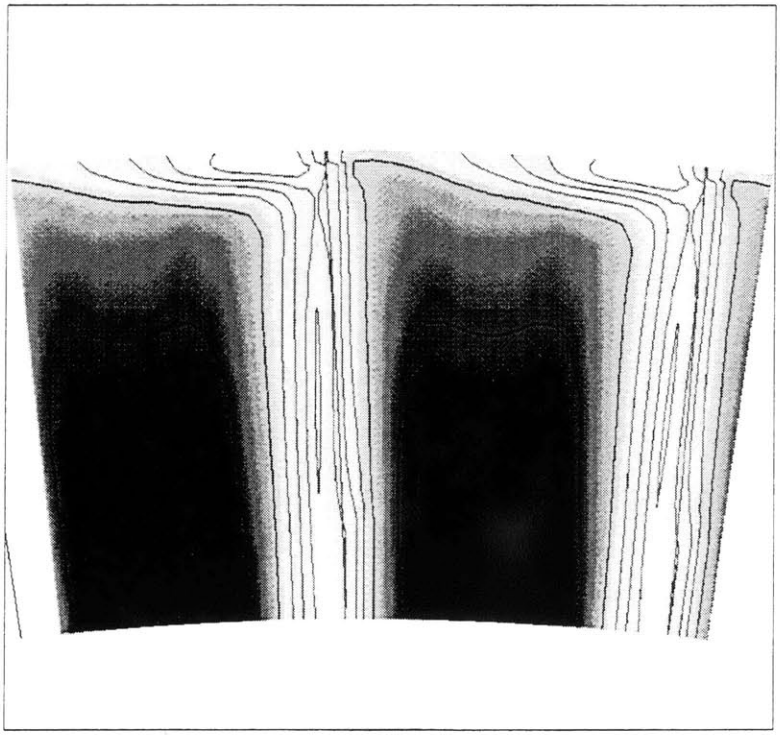

Figure 3.7: Axial velocity contour at the exit plane for the E^3 rotor as computed using RS3

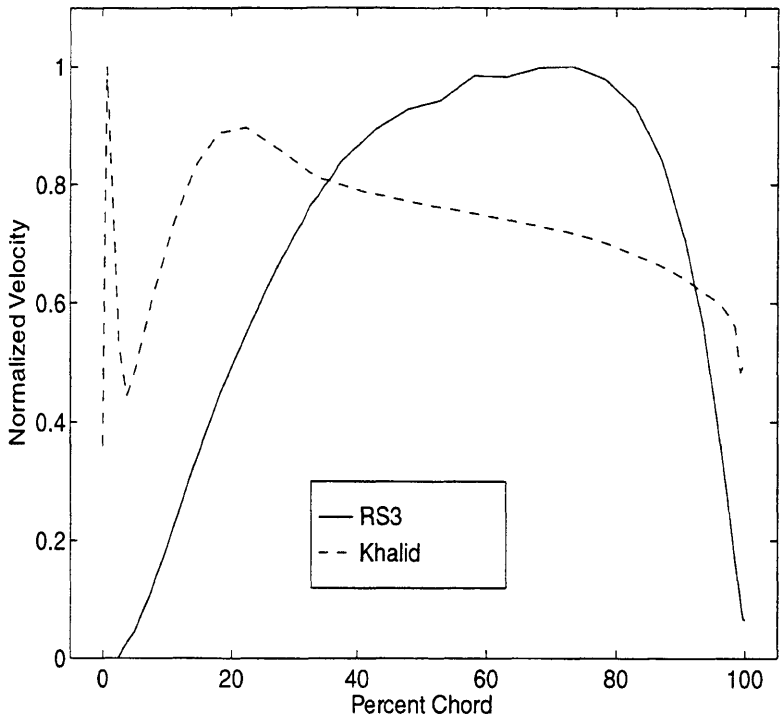

Figure 3.8: Comparison of tip clearance flow normal velocity between RS3 and numerical results of Khalid

tation of rotating stall inception. The evaluation demonstrates that it is capable of producing the correct trends in performance which are required for the study of rotating stall. In addition, the code has been shown to provide the correct qualitative features of the tip clearance flow field.

Chapter 4

Two-Dimensional Results and Analysis

Two dimensional calculations of rotating stall were performed for a rotor-only and a single stage compressor configuration. These computations were performed in order to answer the following questions.

- What is the role of the blade passage flow structures on the development of rotating stall?
- When are the assumptions of the current modal stall models valid?

4.1 Rotor-Only Compressor Stall Inception

The first geometry considered was the mid-span profile of the low-speed version of the E^3 compressor as tested by General Electric in the Low-Speed Research Compressor [55]. This geometry is representative of current compressors. The profile of this blade is shown in Figure 4.1.

4.1.1 Axisymmetric Performance

A basic input into most compressor stability models is the axisymmetric pressure rise versus flow characteristic. The axisymmetric characteristic provides the local

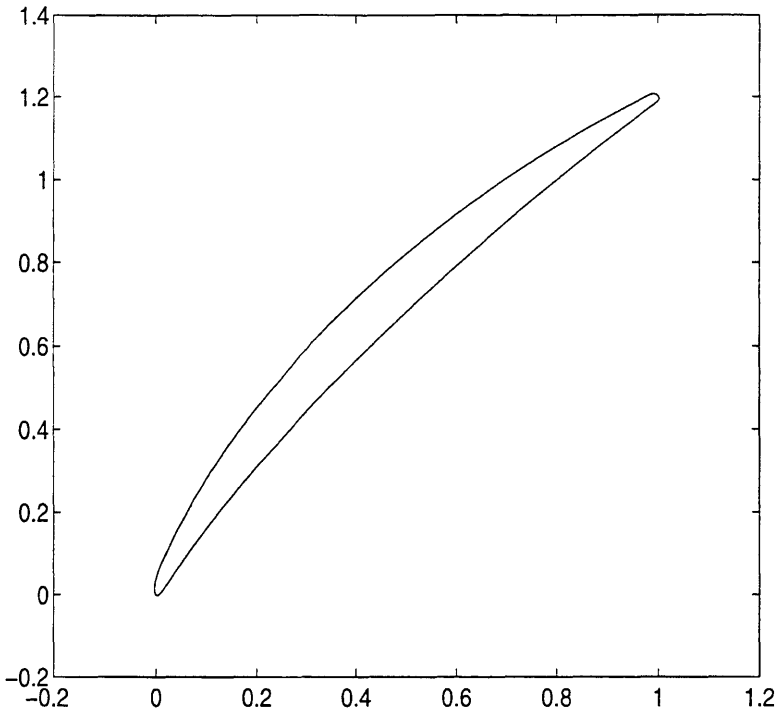

Figure 4.1: E^3 mid-span blade profile

performance relation of the compressor. In a non-axisymmetric flow different parts of the compressor operate at different points on the axisymmetric characteristic, so the overall performance of the compressor will not necessarily follow this curve (see Moore [39]). To compute the axisymmetric characteristic a calculation was done using a single blade passage with periodic blade-to-blade boundary conditions at a blade speed Mach number of 0.2 and a Reynolds number based on chord of 300,000. A low Mach number was used in order to allow a comparison with the incompressible compressor stability model. A throttle transient was carried out to yield a curve of pressure rise versus axial flow as shown in Figure 4.2. The throttle rate was set to be slow enough so that the performance was independent of the closure rate. The general shape of the characteristic is consistent with that described by Moore and Greitzer [41] for use in their stall model.

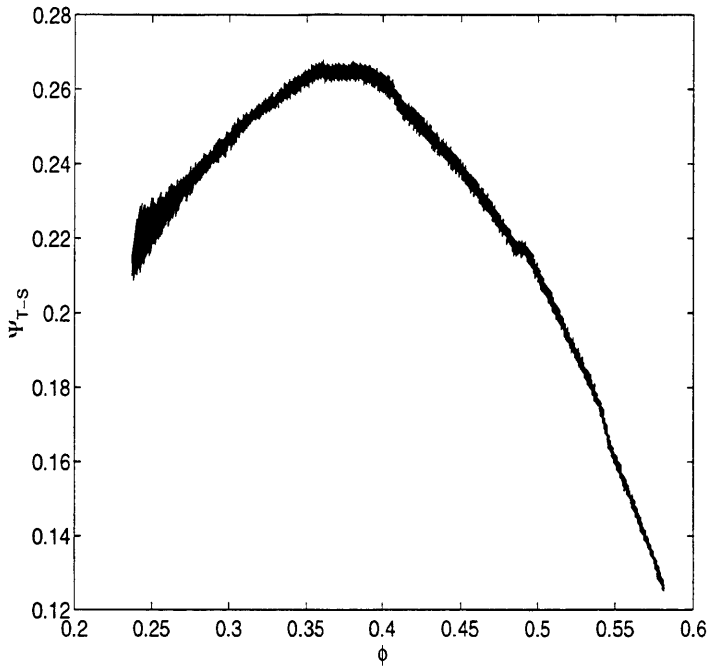

Figure 4.2: Axisymmetric characteristic of two-dimensional E^3 mid-span blade profile

4.1.2 Stall Inception

Using the same geometry, a computation was performed using eight blades (with periodic boundaries). This number of blades was considered adequate to capture at least the first spatial harmonic using the criteria presented by Longley [32]. The stalling mode observed was the first harmonic. Although it would be preferable to analyze a modal stall inception using a larger number of blades, when more blades were used the stalling mode moved to the second harmonic. A discussion of the reasons for this is given in Section 4.4. The net effect of using a smaller number of blades is that all disturbances with wave lengths greater than eight blade spacings will be removed from consideration.

To provide a nearly constant background flow (as assumed by the linear stall models) the throttle was held constant during the development of rotating stall. Typically, the throttle was set to a given value and the results were observed to see if asymmetries grew in the compressor. If no growth was detected, the throttle setting was changed to lower the flow coefficient and held at the new setting. This procedure was

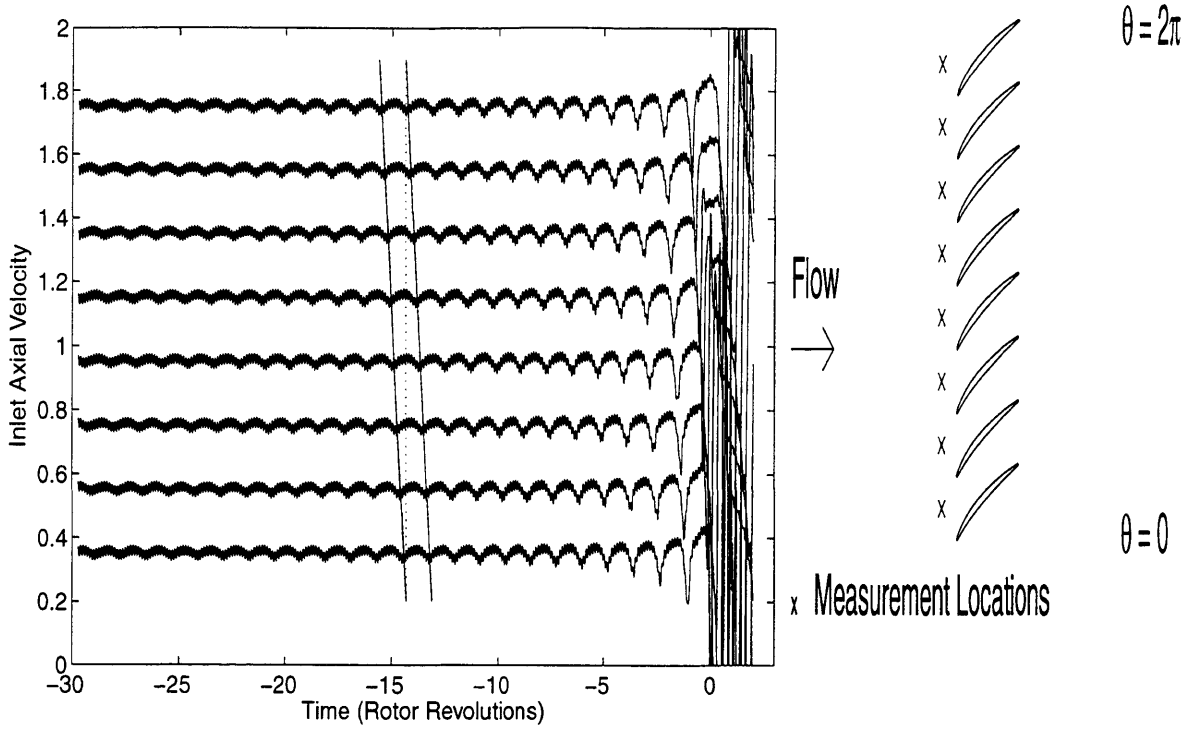

Figure 4.3: Inlet axial velocity traces during a transient to stall for the eight bladed compressor

repeated until asymmetries began to grow. Once this occurred, the throttle setting was held constant while the disturbances grew into a fully developed stall cell. The same process was used for all the rotating stall results presented in this chapter. For the computational method used, small asymmetries were present in the calculation due to finite computational rounding errors. Thus, it was not necessary introduce additional asymmetries in order to trigger the development of rotating stall. The initial asymmetries in the velocity were approximately 0.001% of the mean flow, and were found in comparable magnitudes in all of the harmonics.

To compare qualitatively with experimental results, velocity values at eight evenly spaced circumferential locations 1/4 chord ahead of the rotor blade were recorded during the development of rotating stall. Time histories of these inlet axial velocities can be seen in Figure 4.3 as the compressor entered into rotating stall. An artificial offset has been added to all but one of the traces to allow all of them to be viewed on the same plot. The traces show the evolution of the small amplitude disturbances during the inception of rotating stall. In addition, the higher frequency of the blade passings

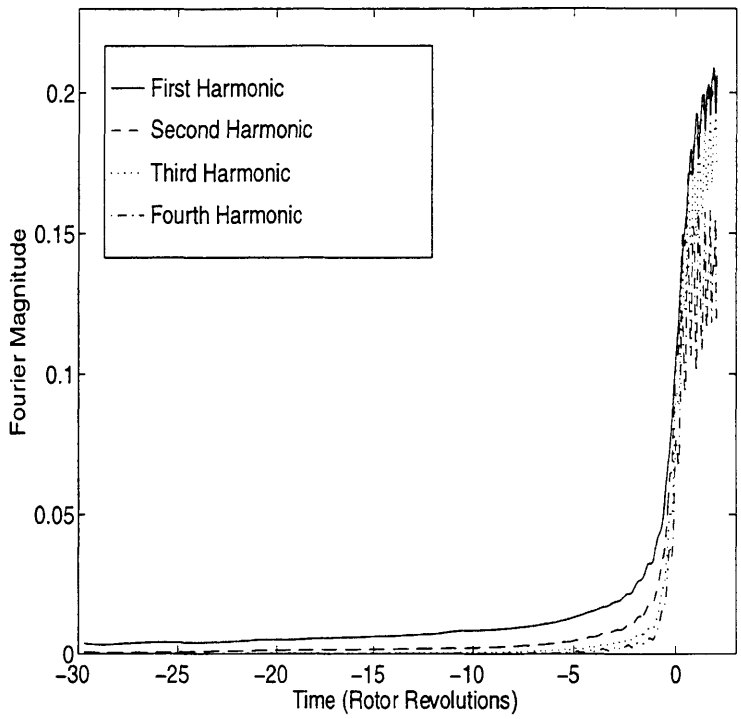

Figure 4.4: Traces of the magnitude of the Fourier harmonics of the inlet axial velocity during a transient to stall for the eight bladed compressor

can be seen. The initial perturbation consists of a single sinusoidal variation. As the stall cell matures, the sinusoidal variation in velocity gives way to a disturbance with steeper variations in velocity. By following the hills and valleys of the perturbations, it can be seen that the wave is moving circumferentially (rotating). This information can be seen in a more quantitative fashion by plotting the magnitude and phase of the spatial Fourier transform of the inlet velocity. For these plots, all of the available information was used instead of just the values from the eight traces shown. The magnitude of the first four Fourier harmonics versus time can be seen in Figure 4.4. During the initial phase of the stall inception process, the disturbance is made up of primarily the first harmonic. As the stall cell grows, the higher harmonics begin to become more significant.

The phase of the Fourier harmonics can be used to gauge the speed of these disturbances. Figure 4.5 shows the unwrapped phase of the first four harmonics. The phase of each harmonic has been normalized by its corresponding harmonic number so that the slope of the line gives the rotational rate. A small change in slope can be

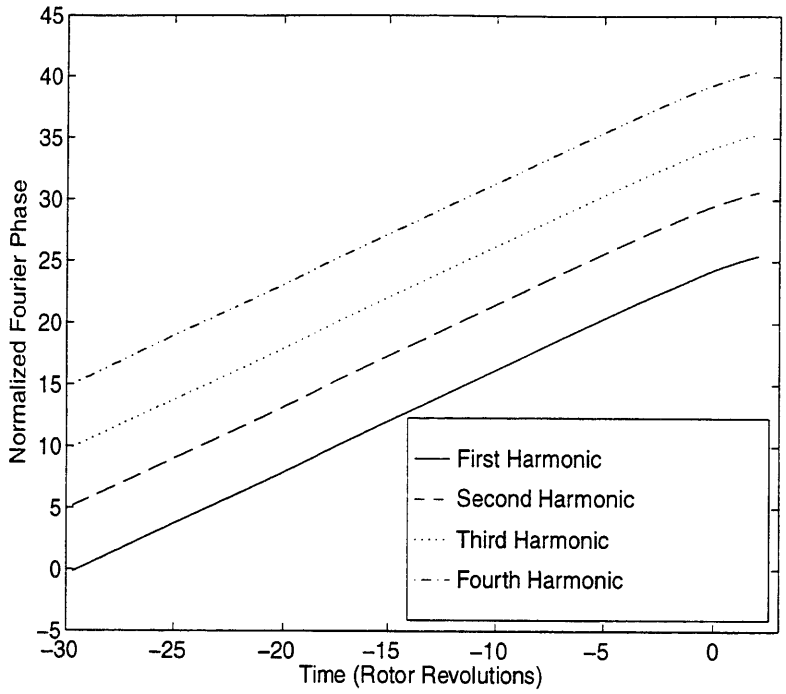

Figure 4.5: Traces of the phase of the Fourier harmonics of the inlet axial velocity during a transient to stall for the eight bladed compressor

seen as the stall cell amplitude becomes large near Time=0. This is consistent with experiments conducted on rotating stall [24].

From the derivative of the phase, the rotational speed of each harmonic can be computed as shown in Figure 4.6. All of the Fourier harmonics are seen to rotate at the same speed of about 83% of the rotor speed. This speed is close to the value predicted by a linear stability model for the first mode of 80%. The linear analysis predicts that each of the harmonics has a distinct rotational frequency, but the predicted frequencies are all within 8% of each other. Since all the harmonics are rotating at the same speed, it appears that the response seen in the higher harmonics is the result of a mode which is not a pure sinusoid, rather than the presence of multiple modes of the system. This is a result of the mode interacting in a non-linear way with the relatively small number of blades.

Snapshots of the flow as the stall cell develops can also be utilized to view the development of the rotating stall cell. Figure 4.7 shows an entropy contour of the flow field prior to the onset of non-axisymmetric flow. In this view the rotor blades

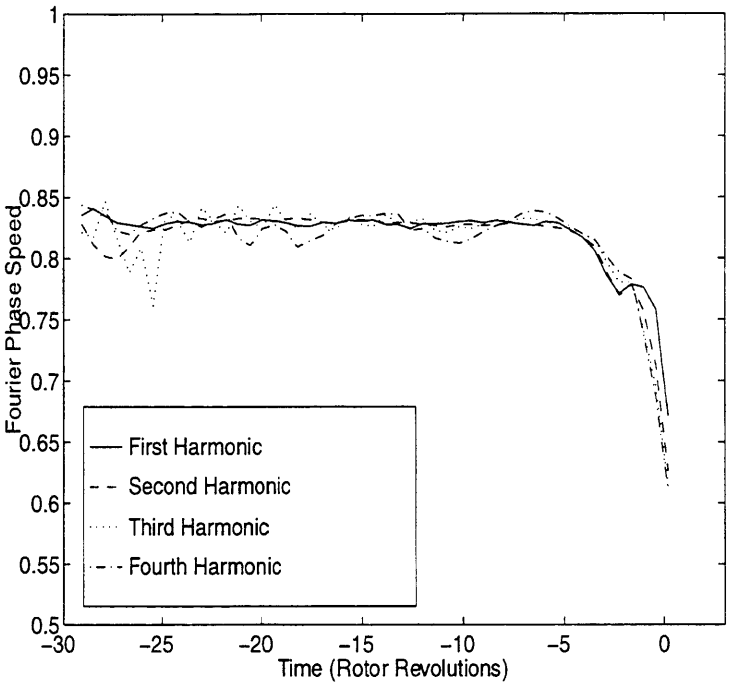

Figure 4.6: Speed of Rotation of the Fourier harmonics of the inlet axial velocity during a transient to stall for the eight bladed compressor

are translating downward. Entropy contours are used to display the regions of high losses. Also, since entropy is convected with the flow, a portion of the time history of the flow can be inferred. Figure 4.8 shows the flow field after the asymmetries have reached a large enough magnitude to become noticeable. The single-lobed shape of the disturbance is evident. By comparing Figures 4.7 and 4.8 it can be seen that the amount of separated flow varies about a mean level of separation approximately equal to the amount seen prior to their development. This linear type of variation is essential to the application of simple linear stability models. This feature is considered more quantitatively in Section 4.4.

As the stall cell continues to grow, the region of highly separated flow becomes more intense and more localized. This development is chronicled in the sequence of views of the flow field presented in Figures 4.9 through 4.12. These views have been taken at even time intervals during the final stages of the development of rotating stall. A central flow feature which participates in the development of rotating stall is the separated flow region near the trailing edge of the blade.

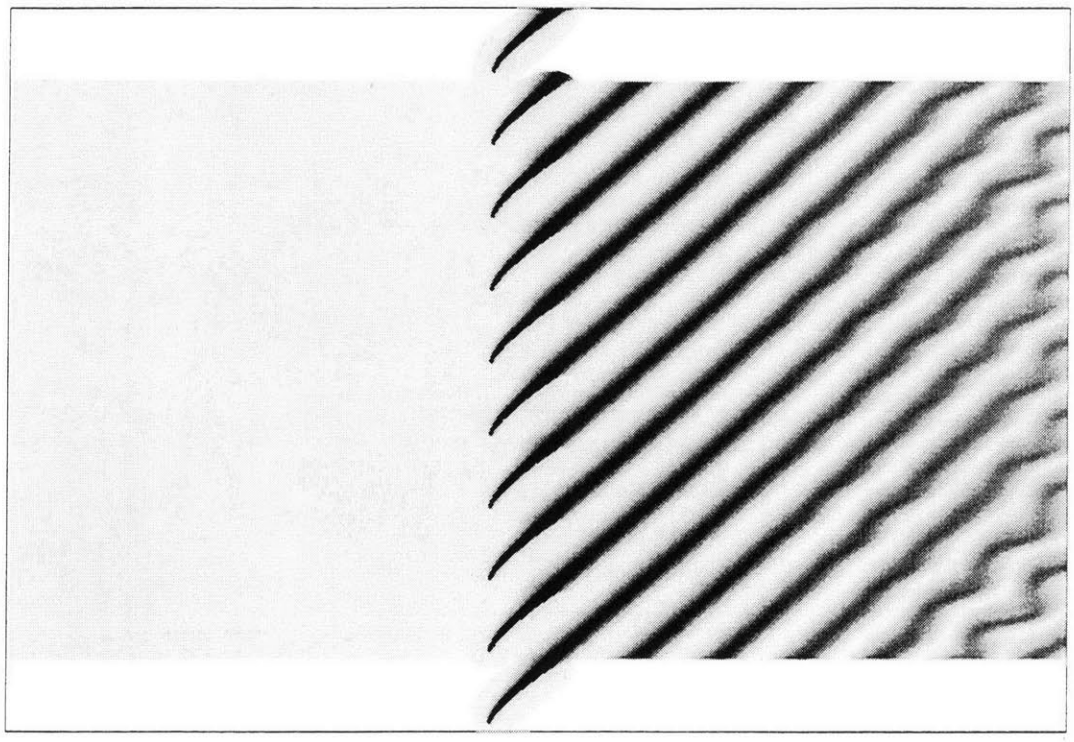

Figure 4.7: Entropy contour of the eight bladed compressor prior to rotating stall onset

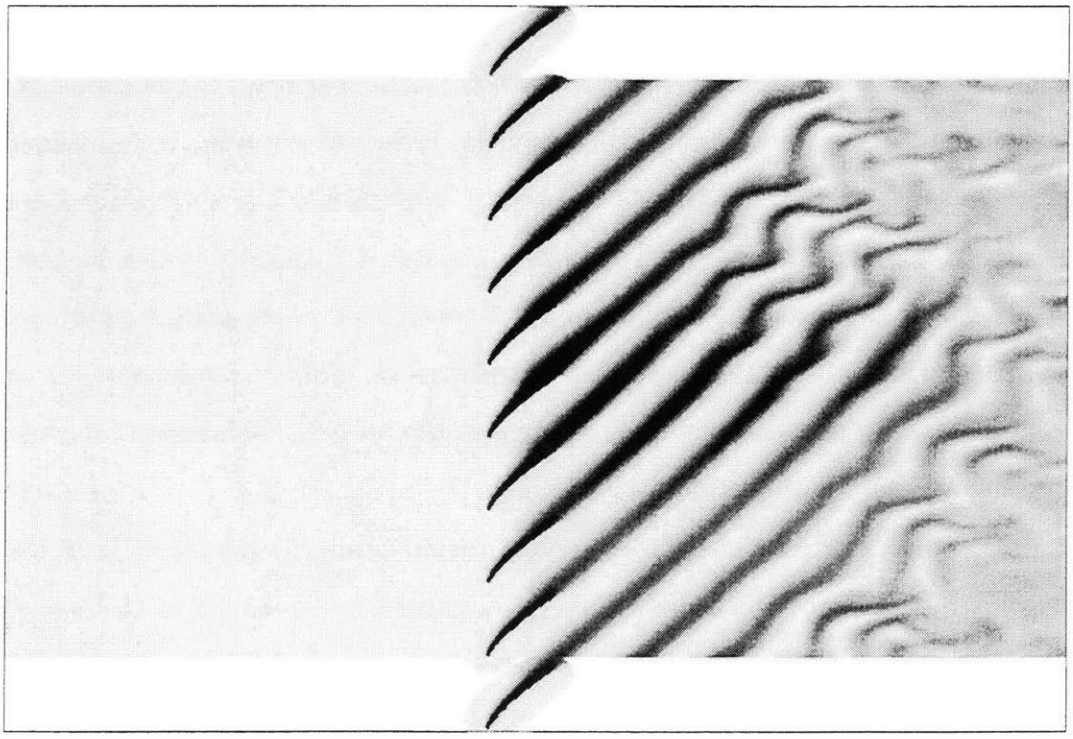

Figure 4.8: Entropy contour of the eight bladed compressor during small scale stall inception at Time = -7.7

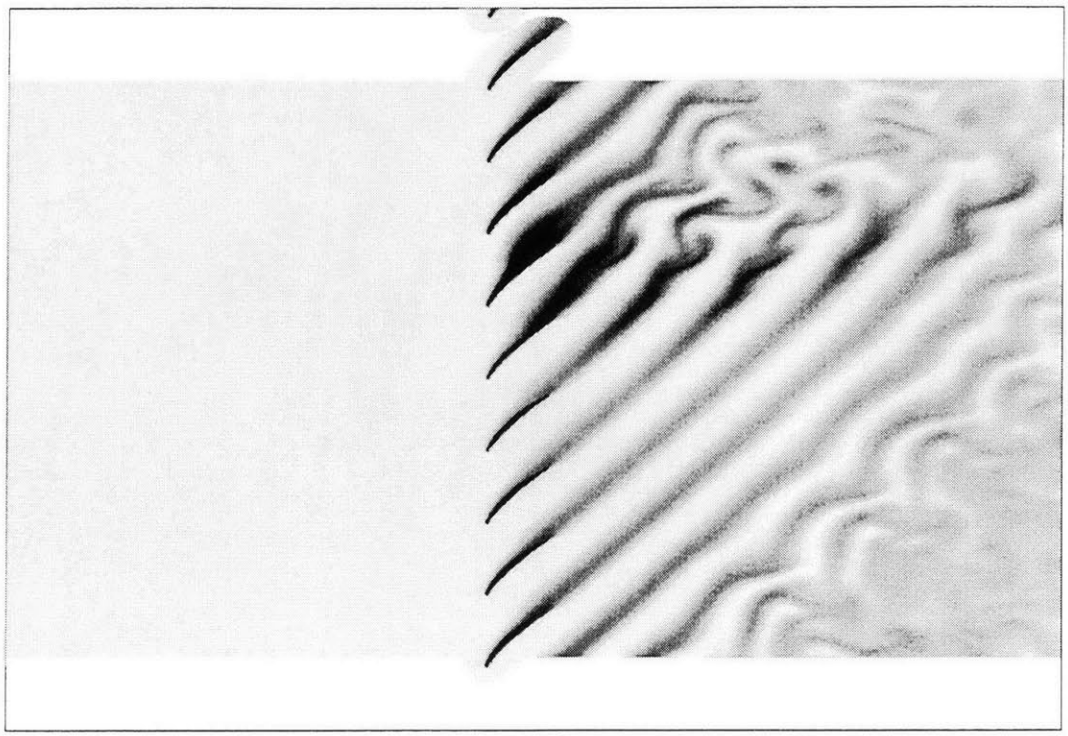

Figure 4.9: Entropy contour of the eight bladed compressor during stall inception at Time = -3.1

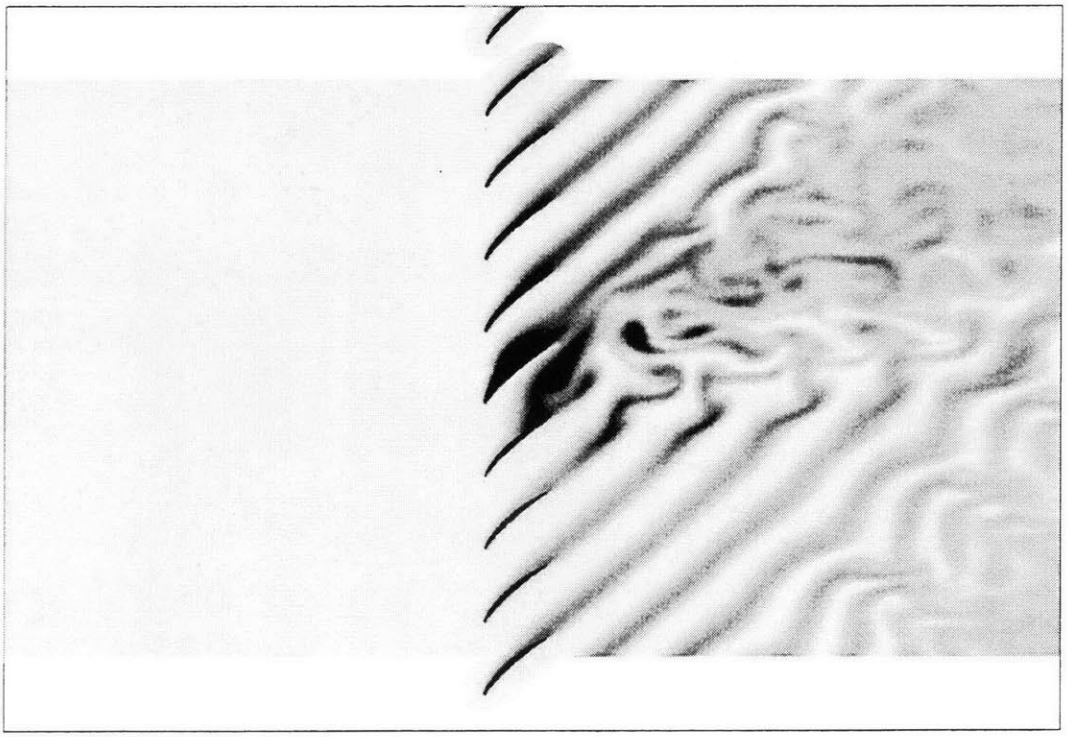

Figure 4.10: Entropy contour of the eight bladed compressor during stall inception at Time = -1.6

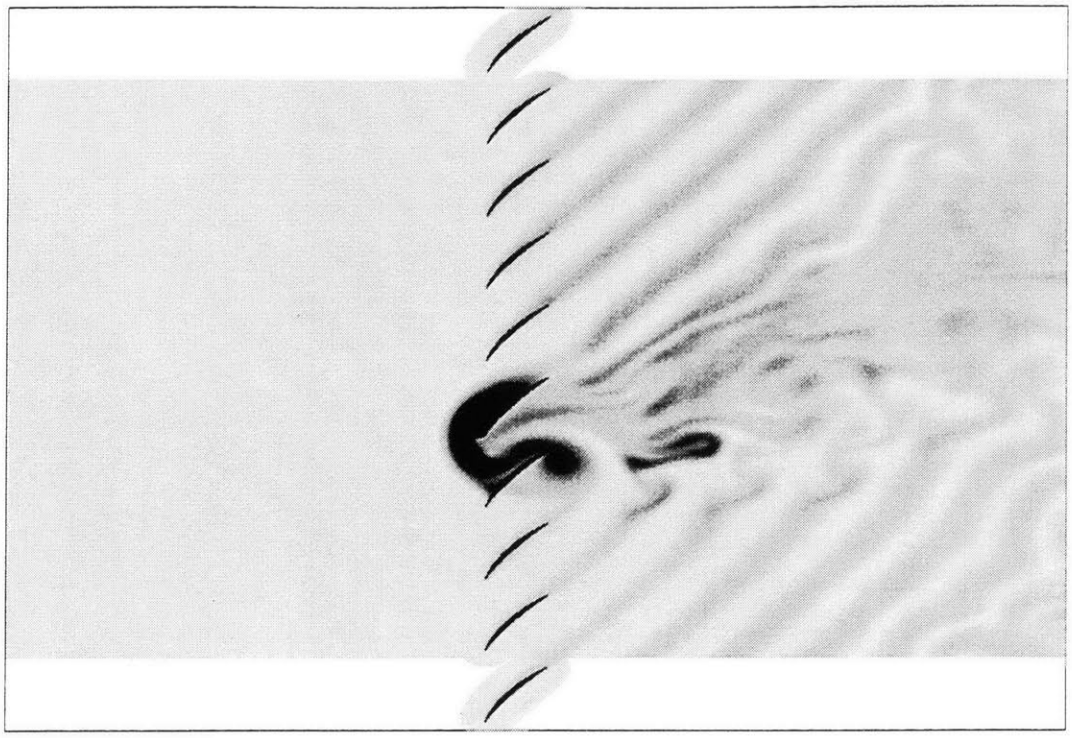

Figure 4.11: Entropy contour of the eight bladed compressor during stall inception at Time = -0.1

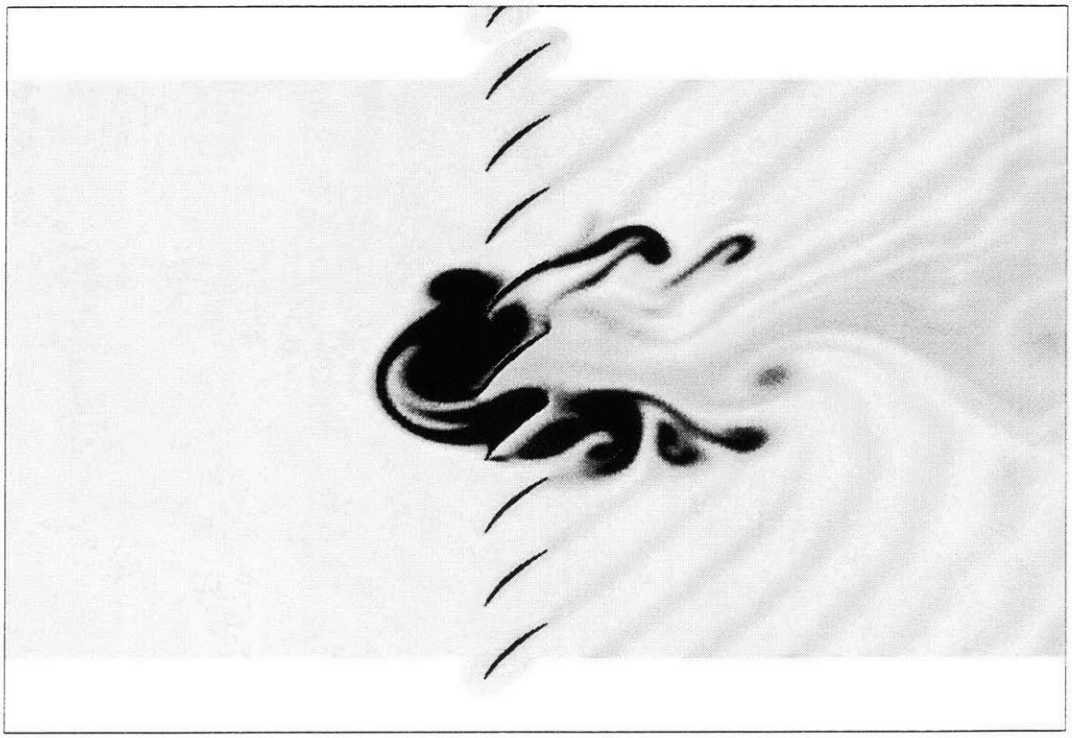

Figure 4.12: Entropy contour of the eight bladed compressor during stall inception at Time = 1.4

As the magnitude of the stall cell increases, the sinusoidal variation in the blockage gives way to more localized deviations as first shown in Figure 4.9. By the next frame in the time sequence (Figure 4.10) one of the passages has been completely filled by the separated flow. As the stall cell continues to develop, reversed flow occurs as shown in Figures 4.11 and 4.12. The presence of substantial reversed flow in the compressor is consistent with the numerical results presented by He [20] and the experiment of Sovran [46].

4.2 Effect of Operating Point on Stall Inception

When a sixteen bladed compressor with the same blade geometry as the eight bladed compressor was stalled, rotating stall occurred at the same flow coefficient but the stalling mode moved to the second harmonic. Therefore, the stalling pattern was identical to the eight bladed case, but was repeated twice in the circumference of the sixteen bladed compressor. By changing the flow coefficient at which rotating stall developed, a different stalling pattern was seen. This was done by throttling from a stable operating point to a flow coefficient 1% lower than the original stalling flow coefficient.

The resulting stalling pattern is best characterized by a plot of the velocity traces ahead of the compressor as shown in Figure 4.13. The disturbance which grows into the fully developed stall cell is relatively small in circumferential extent ($\sim$ 3 blade spacings). Although the stalling pattern resembles the short length-scale stall events shown by Day [7], it was found to be the result of having more than one unstable mode growing at the same time. This is evidenced by the plot of the rotational speeds of the harmonics of the inlet axial velocity shown in Figure 4.14. Even during the initial stall inception, distinct rotational frequencies are observed for the first two harmonics which are each within 3-4% of the speeds predicted by the linear stability model for the respective modes. Thus, the first two modes are both unstable at this flow coefficient while only the second mode was unstable at a 1% higher flow coefficient.

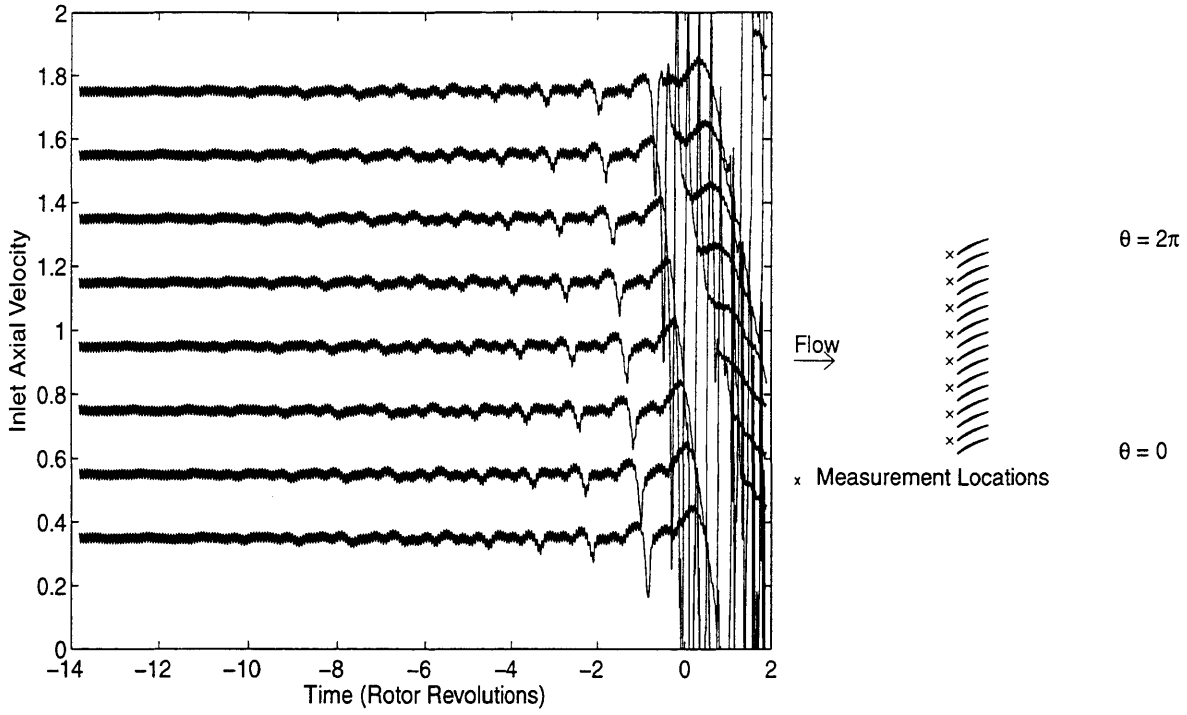

Figure 4.13: Traces of the inlet axial velocity during a transient to stall for the sixteen bladed compressor

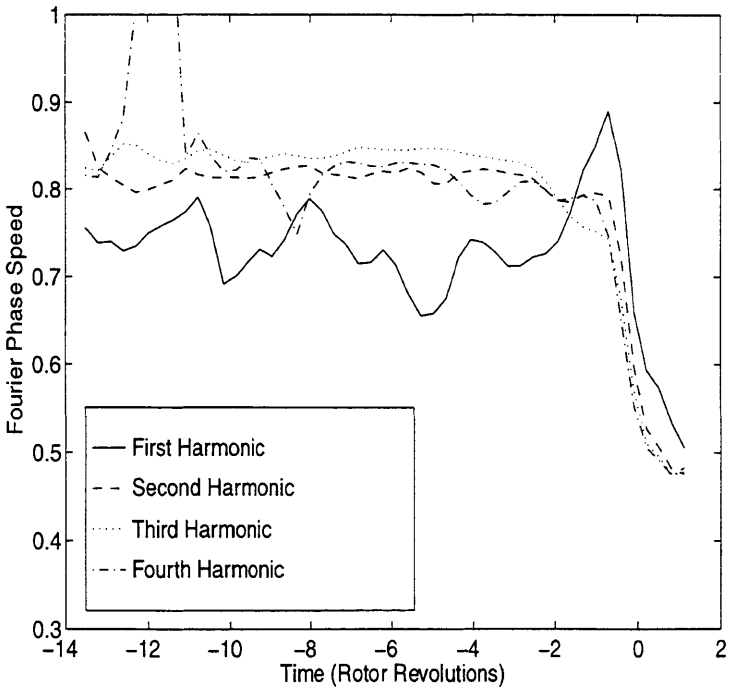

Figure 4.14: Rotational speed of the Fourier harmonics of the inlet axial velocity during a transient to stall for the sixteen bladed compressor

This result was found to be in qualitative agreement with the linearized stability analysis presented in Section 4.4.

4.3 Single Stage Compressor Stall Inception

Because the compressors used in modern gas turbine engines contain more than just a single blade row, it is important to determine if the results from single blade row calculations can be applied to multiple blade row geometries. The compressor geometry used was the one studied experimentally by McDougall [35].

4.3.1 Review of Experimental Results

The compressor used for this study was investigated thoroughly by McDougall in his PhD Thesis [35]. The compressor consisted of a single stage with 51 rotor blades and 36 stators. The blade geometry was constructed using a C4 profile based on a circular arc camber line with a thickness to chord ratio of 10.0%. The flow ducts ahead, aft, and through the compressor were of constant area and radius. The high hub-to-tip radius ratio of 0.80 resulted in a geometry which was relatively similar from hub to tip. This allowed the compressor to be represented reasonably well as a two-dimensional compressor for this study. The tests were conducted at a tip Mach number of about 0.12 which allows the use of an incompressible stability model.

In the experiment the compressor was observed to exhibit a modal type of stall inception of the first harmonic which rotated at 45-50% of the rotor speed.

4.3.2 Computational Results

To compute the two-dimensional axisymmetric speedline for the McDougall compressor the mean-line geometry of the compressor was used. The computation was performed at a low (essentially incompressible) Mach number of 0.2 and a Reynolds number based on chord of 300,000. To approximate the rotor to stator blade count ratio with a minimum number of blades, three rotor and two stator blades were used.

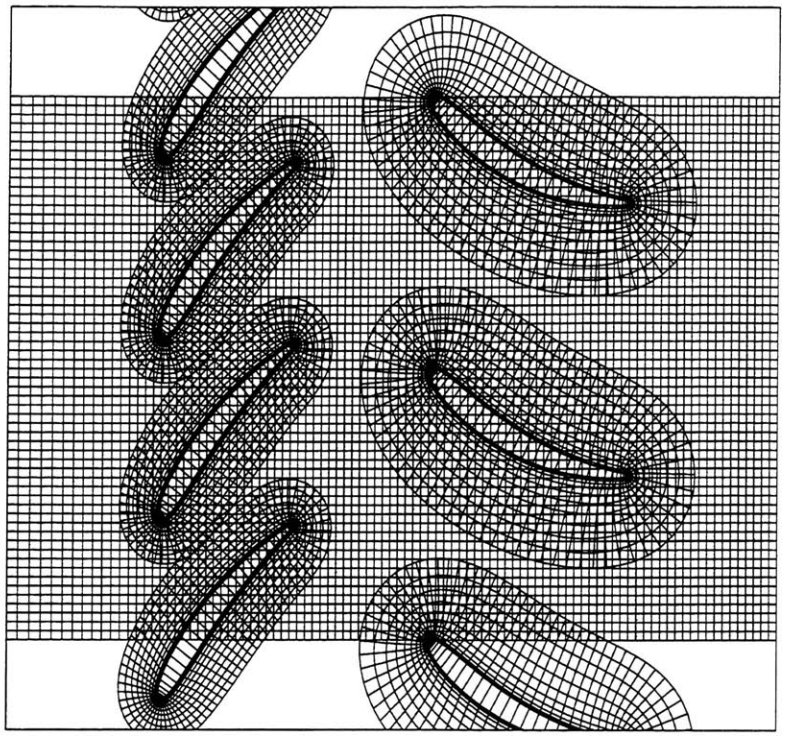

Figure 4.15: Grid used for calculation of axisymmetric speedline the single stage compressor

A view of this geometry can be seen in Figure 4.15 (note that additional blades have been added to show periodicity).

The computed speedline is presented in Figure 4.16. The results from the test performed by McDougall are also shown. A notable discrepancy exists between the experimental and computed speedline. The experimental results showed that there is substantial end wall blockage, especially at the near stall point. This blockage not only causes the remainder of the compressor to experience a higher flow coefficient than that measured, but also leads to a decrease in the deliverable pressure rise when compared to the two-dimensional performance. The end result is that the two-dimensional computation provides a different level of pressure rise than the experiment, but the two characteristics have the same general shape and experience stall at nearly the same flow coefficient. In the linear stall model, the slope of characteristic has the largest effect on the predicted instability point rather than the absolute level of pressure rise. Therefore, this difference is not expected to alter the process of stall inception in the numerical simulation.

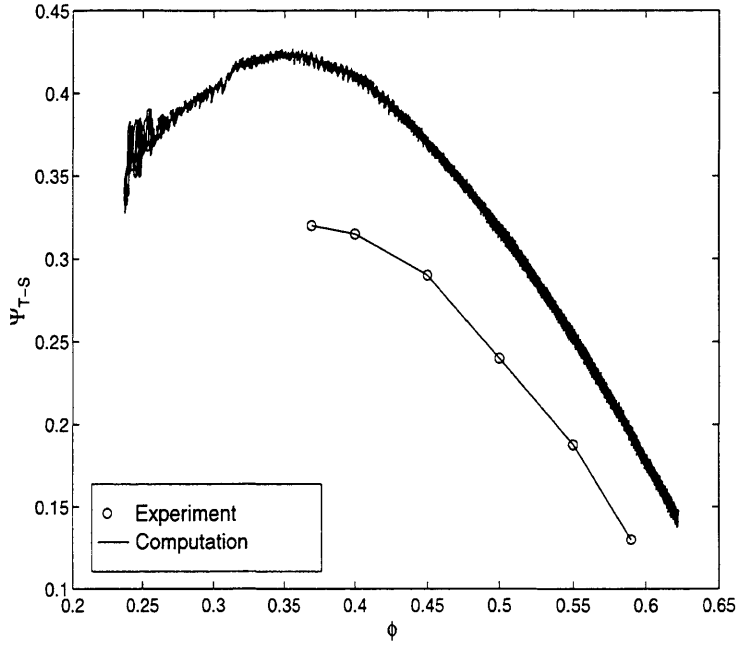

Figure 4.16: Computed and measured speedline for the single stage compressor

To examine the stalling behavior of this compressor, a calculation was run using 17 rotor blades and 12 stators. This number of blades corresponds to one third of the number in the experiment. This means is that the lowest harmonic it was possible to compute corresponds to the third harmonic of the real system.

A plot of the steady state compressor characteristic as it was incrementally throttled into stall is shown in Figure 4.17 along with the axisymmetric speedline. The discrepancy in performance between the axisymmetric speedline (3 rotors, 2 stators) and the full computation (17 rotors, 12 stators) is a result of the inability to keep the same rotor to stator blade count ratio. The in-stall behavior of the compressor is also shown. Dotted lines are used to connect the stalled and un-stalled operating points at the throttle settings at which the compressor entered into and recovered from rotating stall. The hysteresis of the stalling process is evident.

Figure 4.18 displays the axial velocity at the inlet of the compressor during the development of rotating stall. These values were taken from eight equally spaced locations about the annulus, 1/4 chord upstream of the rotor. An artificial offset

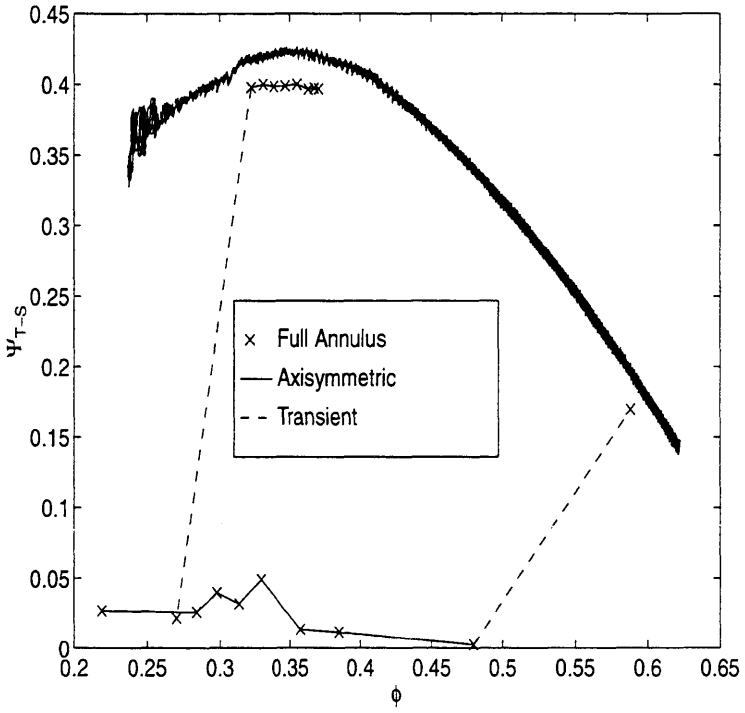

Figure 4.17: Computed total-to-static pressure rise characteristic of unstalled and stalled equilibrium operating points for single stage compressor (Axisymmetric speed-line shown for comparison)

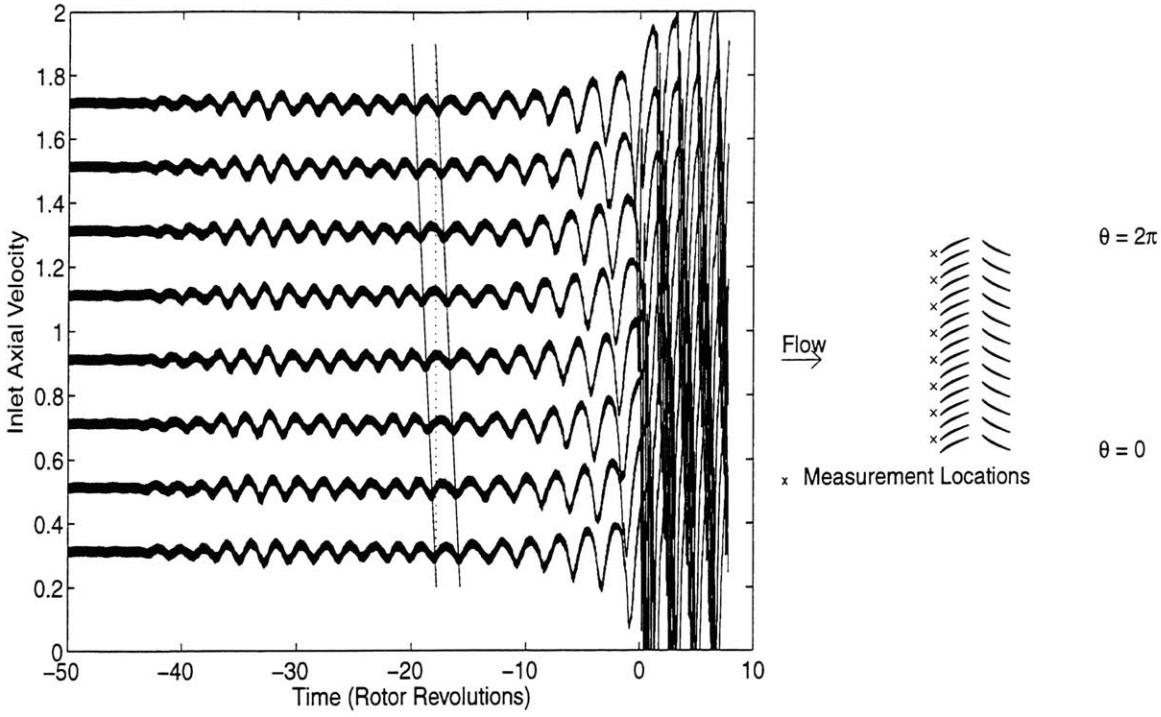

Figure 4.18: Inlet axial velocity traces during a transient to stall for the single stage compressor

has been added to the top seven traces. The plot shows the development of a first harmonic circumferentially traveling wave which grows into rotating stall.

A plot of the magnitude of the first four spatial harmonics of inlet velocity versus time is shown in Figure 4.19 for the computation and in Figure 4.20 for the experiment. In McDougall's experiment, only the first spatial harmonic was computed. The limits on the plot of the numerical results have been chosen to be comparable with the experiment. In both figures the development of the first harmonic can be observed to grow in an exponential manner during the transition from a small amplitude disturbance into fully developed rotating stall. The growth rate of the numerical result was approximately half of the rate observed in the experiment. Because this value is sensitive to the operating point of the compressor, this level of agreement is considered adequate for a qualitative comparison.

The higher harmonics participated minimally in the stall inception process. During the majority of the stall inception process all but the first harmonic remained at their pre-stall levels. It is not until the first harmonic magnitude reached approxi-

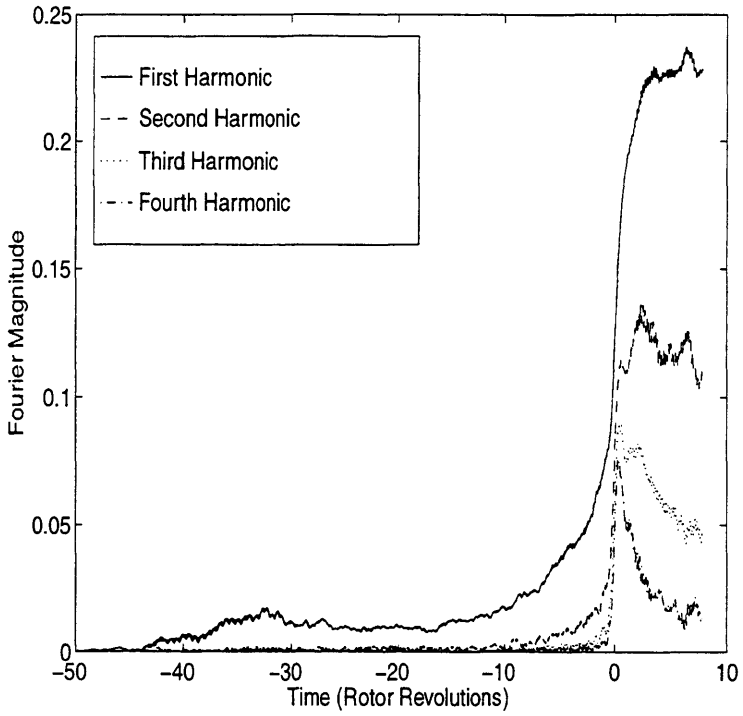

Figure 4.19: Time traces of the Fourier magnitude of the inlet velocity during a stall transient for the single stage compressor

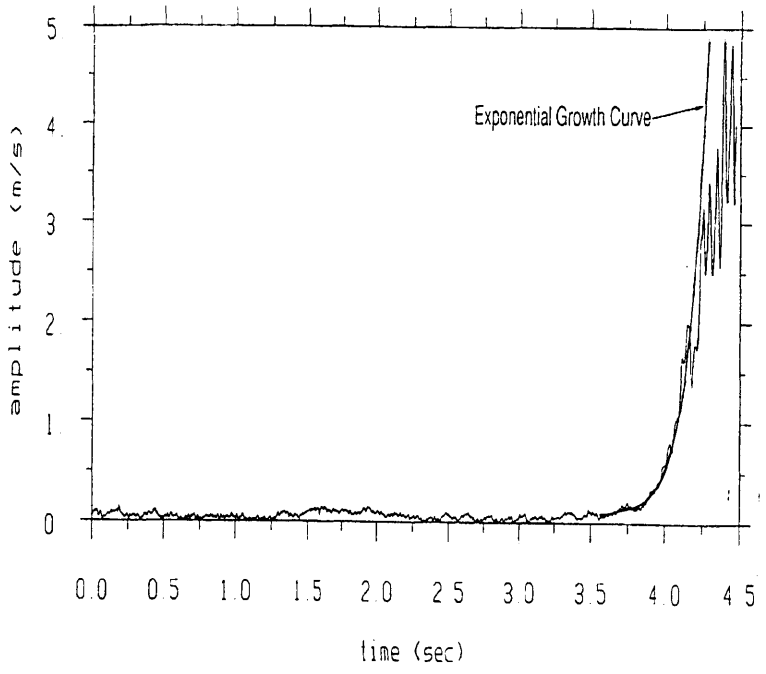

Figure 4.20: Experimental time traces of the Fourier magnitude of the inlet velocity during a stall transient for the single stage compressor

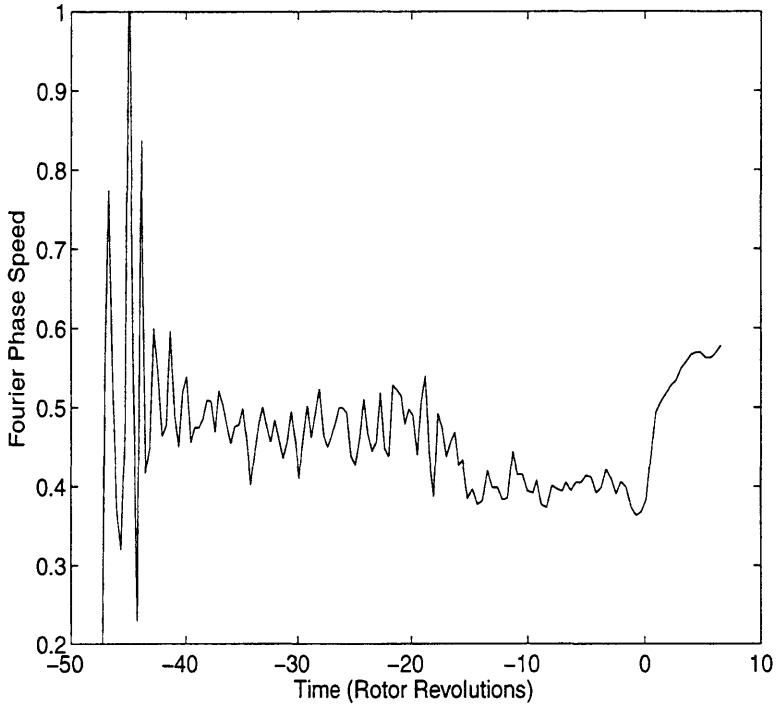

Figure 4.21: Time trace of the slope of the Fourier phase of the inlet velocity during a stall transient for the single stage compressor

mately 10% of its final level that the higher harmonics began to grow.

A plot of the phase speed of the first harmonic is shown in Figure 4.21. The frequency has been normalized by the rotational frequency of the rotor. Since it is difficult to take an accurate numerical derivative, the results are somewhat noisy. A phase speed of between 45% and 50% of the rotor speed can be seen during the initial inception of rotating stall. The experimental value was also found to be between 45% and 50% of the rotor speed. As commonly seen in experiments, there is a change in the rotational speed of the disturbance at the transition between inception and large scale stall [24]. In addition, there was also a small change in the rotational speed of the disturbance prior to the occurrence of full scale rotating stall.

Views of the compressor flow field can be utilized to examine the blade passage flow features which participate in the formation of rotating stall. In this computation, the rotor blades (first row) are translating with a downward velocity.

An entropy contour is presented for the flow at the last stable operating point before rotating stall in Figure 4.22. Although the flow cannot be completely axisym-

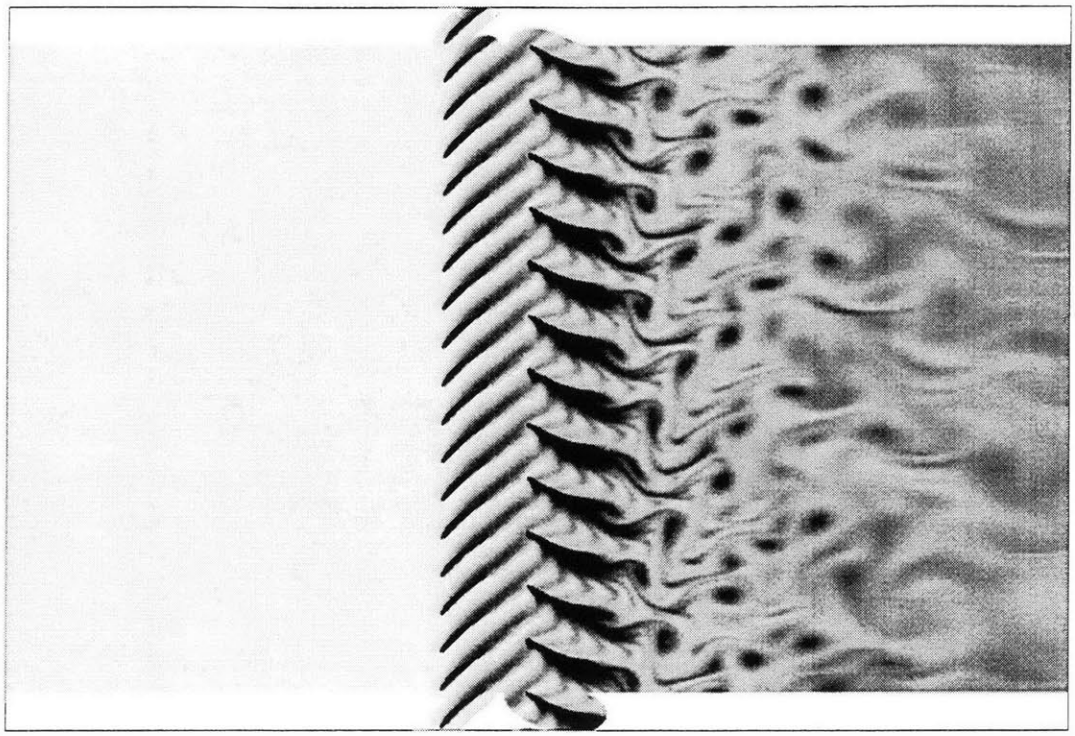

Figure 4.22: Entropy contour of the single stage compressor prior to stall

metric due to the uneven blade count, virtually no asymmetry can be observed in this plot.

Prior to the period of exponential growth (Time=-18.9) the flow has the form shown in Figure 4.23. Large variations of the flow are evident in the stator blade passages. Even though these disturbances do not appear sinusoidal, only a first harmonic disturbance is apparent in the inlet axial velocity.

After the interval where the first harmonic is nearly constant, the first harmonic begins to grow in an exponential manner. The end result is full scale rotating stall. A series of figures are presented which show the transition into rotating stall at equal time increments from Time = -3.7 to 0.6 rotor revolutions, in Figures 4.24 to 4.28. In Figure 4.24 the first harmonic structure of the stall inception has become clear in both the rotors and stators. In the stalled section, the blockages are substantially higher than in the unstalled section. As time advances, the amount of blockage in the stalled section of the compressor continues to increase as shown in Figures 4.25 to 4.27. Viewing these snapshots in series, the rotation of the stall pattern is also

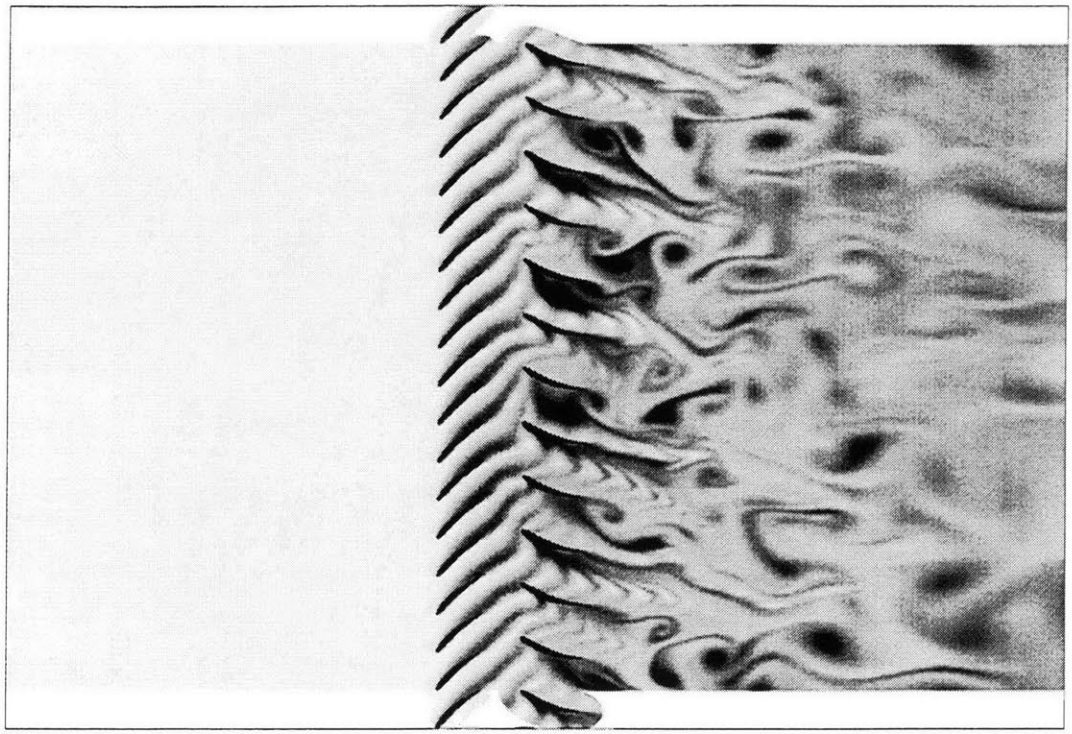

Figure 4.23: Entropy contour of the single stage compressor at Time = -18.9

evident. In Figure 4.27 at least one of the rotor passages becomes so badly blocked that flow spills into the neighboring passage from the front of the blade passage. After this, the flow degenerates rapidly into the flow pattern seen in Figure 4.28. At this point, the stalled section of the compressor is blocked to incoming flow by the jet of fluid with negative axial velocity emanating from the blades near the leading edge of the stall cell.

A view of the final stall cell is presented in Figure 4.29. Although the size of the stall cell has increased, the flow pattern is essentially the same as that shown in Figure 4.28.

Using the linear model developed in Appendix A, the rotational speed of the rotating stall inception was predicted to be 48% of the rotational speed of the compressor. The value is in good agreement with that measured from the computation of between 45% and 50%.

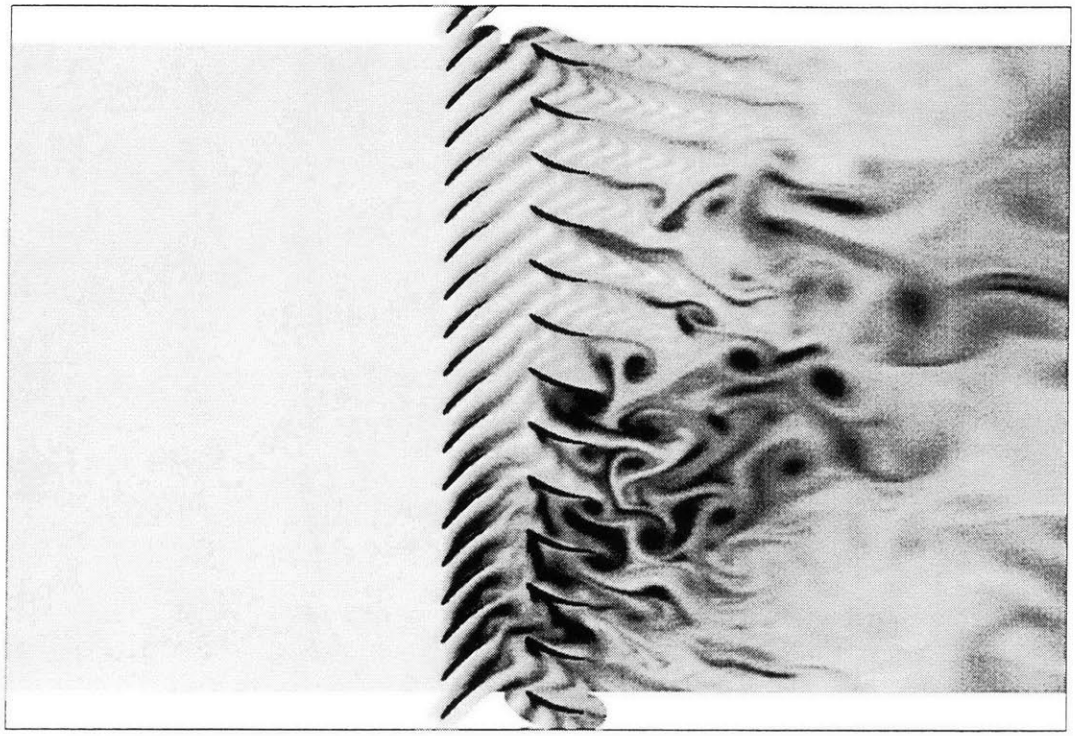

Figure 4.24: Entropy contour of the single stage compressor at Time = -3.7

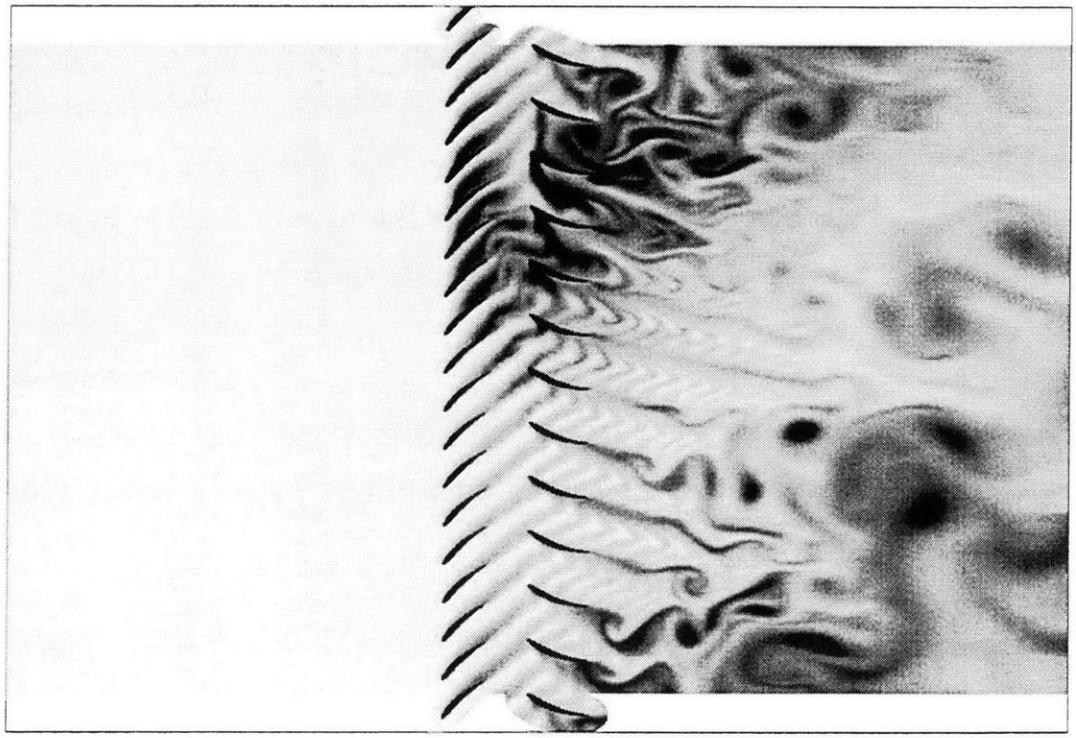

Figure 4.25: Entropy contour of the single stage compressor at Time = -2.6

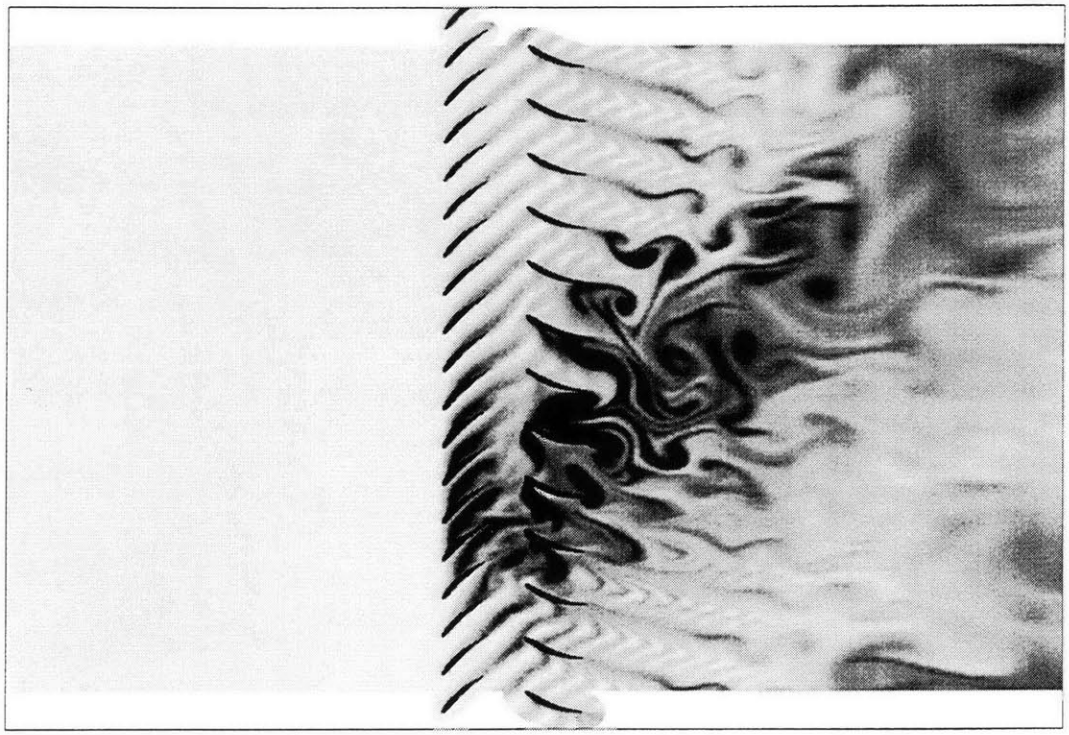

Figure 4.26: Entropy contour of the single stage compressor at Time = -1.6

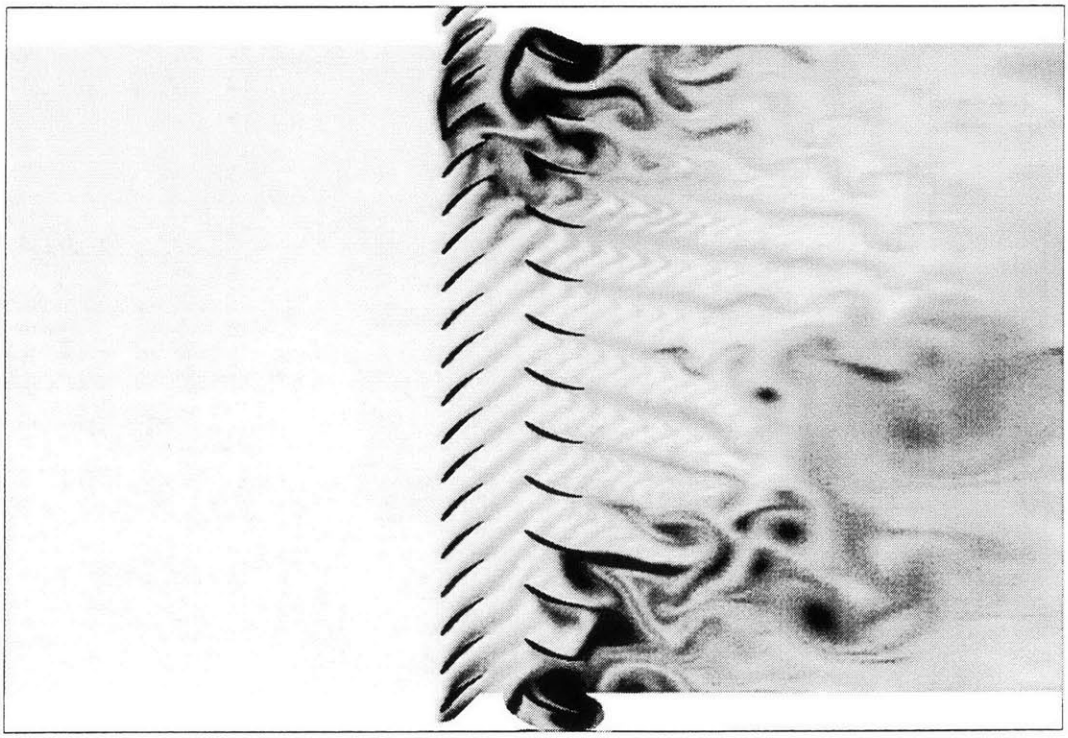

Figure 4.27: Entropy contour of the single stage compressor at Time = -0.5

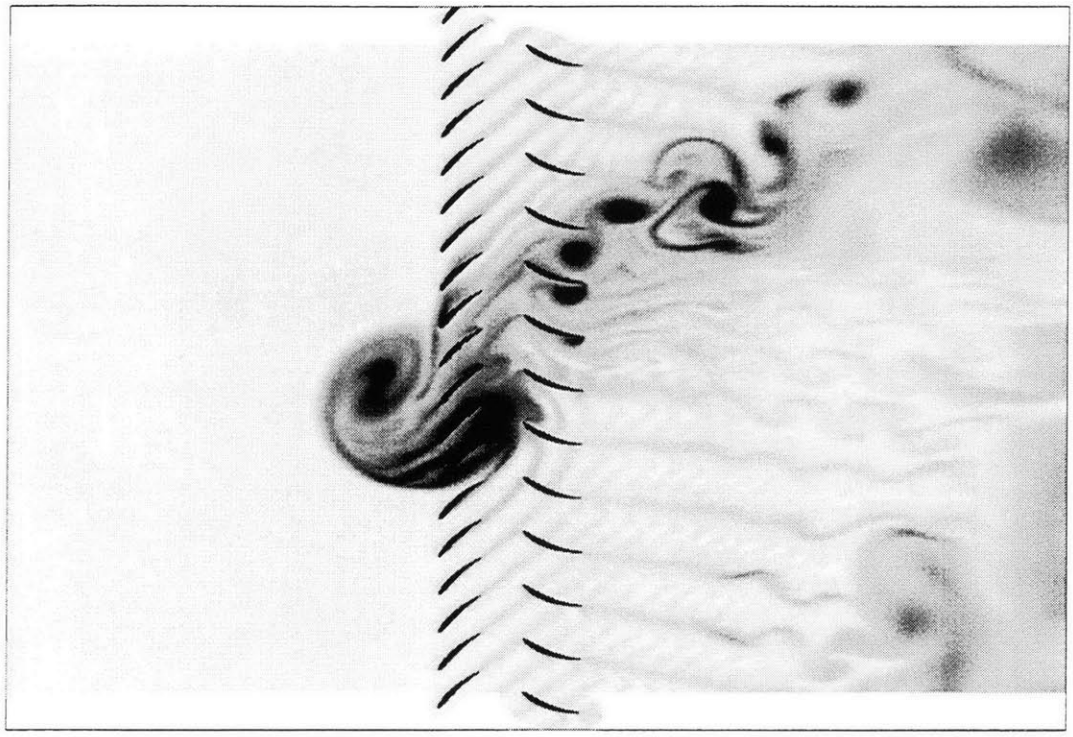

Figure 4.28: Entropy contour of the single stage compressor at Time = 0.6

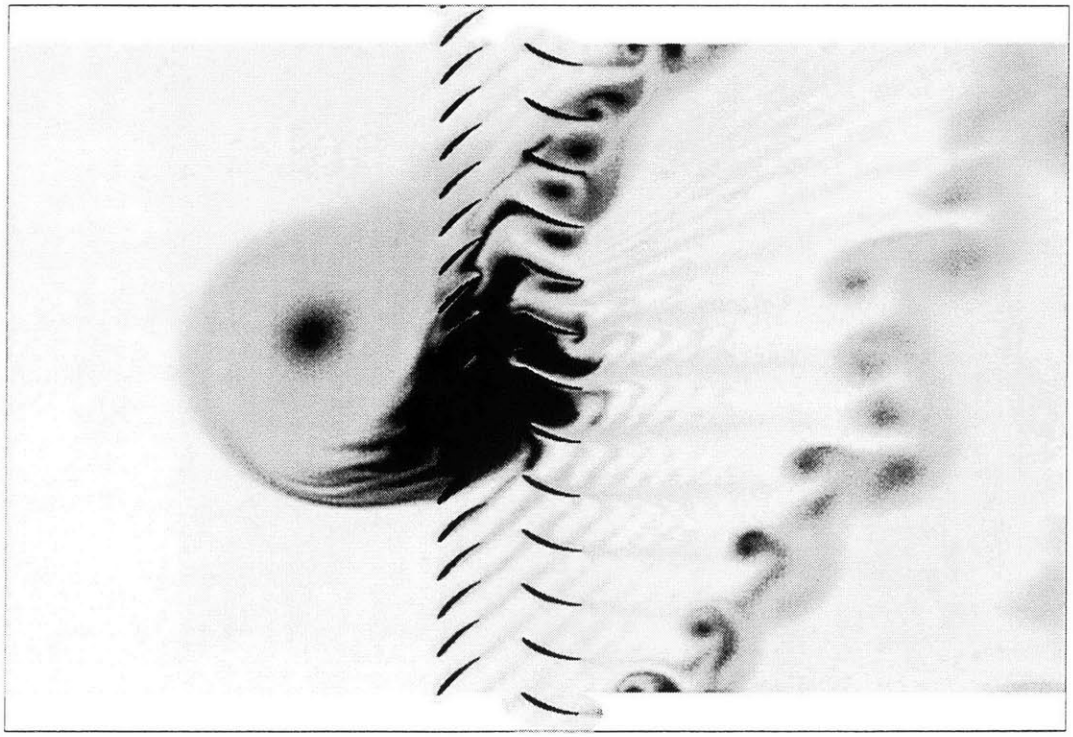

Figure 4.29: Entropy contour of the single stage compressor at Time = 6.0

4.4 Evaluation of Compressor Stall Models

4.4.1 Background

Various forms of stall inception models have been used to characterize the development of rotating stall, beginning with Emmons et al. over forty years ago [9]. These models have been used with an increasing amount of success to predict stall inception points, rotational stall frequencies, stall cell shapes, and the unsteady development of rotating stall. However, these models are almost all based on the same basic set of assumptions regarding the representation of the compressor and the background flow field.

The assumptions used in the formulation of models of rotating stall fall into two categories. The first is the assumptions that are made of the flow outside of the compressor blade rows. Typically this flow is assumed to be inviscid. In addition the variations are often assumed to be small enough to be linearized about a mean background flow. This portion of the model will be referred to as the flow field model. The second set of assumptions are used to describe the response of the compressor. The simplest of these assumptions is that the compressor will respond locally as if it were in a steady flow situation. The most common extension to this assumption is that the unsteady performance of the compressor will act as if there were a lag between the input and the output response. It is generally assumed that the time scale of this lag is on the order of the flow through time of the compressor. This portion will be referred to as the blade row model.

For the most part, these assumptions have not been rigorously tested. The primary 'proof' is that current models do a good job in describing the behavior of axial compressors as they enter into rotating stall as evidenced by data and the use of these models to provide active control of rotating stall. Some efforts have been made to measure the parameters governing the modeling of a compressor undergoing rotating stall. Nagano, Machida, and Takata [42] performed an experimental investigation to match the unsteady performance of an axial compressor to a blade row model. Their study resulted in a description of the blade row in which the loss in total pressure

across a blade row followed a first order differential lag equation with a time constant about equal to 1.1 flow through times of the blade row. A less direct method was used by Haynes [18] to estimate the unsteady performance of the compressor. In his study, the dynamics of the compressor were measured experimentally and compared with predictions given by a linear stability model. An unsteady performance time constant of about 1.5 flow through times was found to yield the best agreement with data.

4.4.2 Flow Field Modeling Assumptions

The flow field models used to construct a compressor stability model are used to describe the behavior of the fluid in the upstream and downstream ducts. They can also be used if substantial space exists between any of the blade rows of the compressor. A basic assumption employed by many of the flow field models is that the flow outside of the compressor can be modeled as a small perturbation about a mean background flow. In addition, it is often assumed that the mean flow is steady and is spatially uniform.

For a constant mean (or background) flow, small perturbations about that flow must take on specific forms as described by the linearized Euler equations. This point is discussed in some detail in Appendix A. The result for a two-dimensional flow with uniform inlet conditions is that in the upstream region the flow perturbations must take on the form of the appropriate eigenvector.

$$\begin{pmatrix} u_1' \\ v_1' \\ p_1' \end{pmatrix} = A \begin{pmatrix} 1 \\ \imath \\ -\frac{\omega}{n} - \overline{u} - \overline{v}\imath \end{pmatrix} e^{n x + \imath n y + \omega t} \tag{4.1}$$

The primed quantities represent perturbations from an equilibrium background flow, and the over-barred quantities represent the mean flow (eg. $u = \overline{u} + u'$). Similarly, for a downstream region with no perturbations coming from the downstream components,

the flow perturbations are of the following form.

$$\begin{pmatrix} u_2' \\ v_2' \\ p_2' \end{pmatrix} = B \begin{pmatrix} 1 \\ -\imath \\ \frac{\omega}{n} - \overline{u} + \overline{v}\imath \end{pmatrix} e^{-nx+\imath ny+\omega t} + C \begin{pmatrix} 1 \\ \frac{\overline{v}}{\overline{u}} - \frac{\omega}{\overline{u}n}\imath \\ 0 \end{pmatrix} e^{-\frac{\omega}{\overline{u}}x - \frac{\overline{v}}{\overline{u}}nx\imath + \imath ny + \omega t} \tag{4.2}$$

To obtain data for this study, the values at the inlet and outlet to a single blade row (rotor) compressor have been taken from the computation at a fixed point on the annulus. These values have been averaged over a blade pitch remove the blade passing frequency. Thus, for this given axial and circumferential position, the form of the perturbations becomes

$$\begin{pmatrix} u_1' \\ v_1' \\ p_1' \end{pmatrix} = A \begin{pmatrix} 1 \\ \imath \\ -\frac{\omega}{n} - \overline{u} - \overline{v}\imath \end{pmatrix} e^{\omega t} \tag{4.3}$$

for the inlet, and

$$\begin{pmatrix} u_2' \\ v_2' \\ p_2' \end{pmatrix} = \left[B \begin{pmatrix} 1 \\ -\imath \\ \frac{\omega}{n} - \overline{u} + \overline{v}\imath \end{pmatrix} + C \begin{pmatrix} 1 \\ \frac{\overline{v}}{\overline{u}} - \frac{\omega}{\overline{u}n}\imath \\ 0 \end{pmatrix} \right] e^{\omega t} \tag{4.4}$$

for the exit.

In this form, the perturbation in each variable takes the following form.

$$f = Ze^{\omega t} \tag{4.5}$$

In this representation Z is the complex magnitude of the flow perturbation and ω is the complex frequency. A least squares curve fit can be used to compute Z and ω for each flow variable. (By neglecting the real part of ω, Z can also be determined using a Fourier transform.) To be consistent, the value of ω for u, v, and p should be the same. Provided this is true, the complex magnitudes can be plotted on a phase

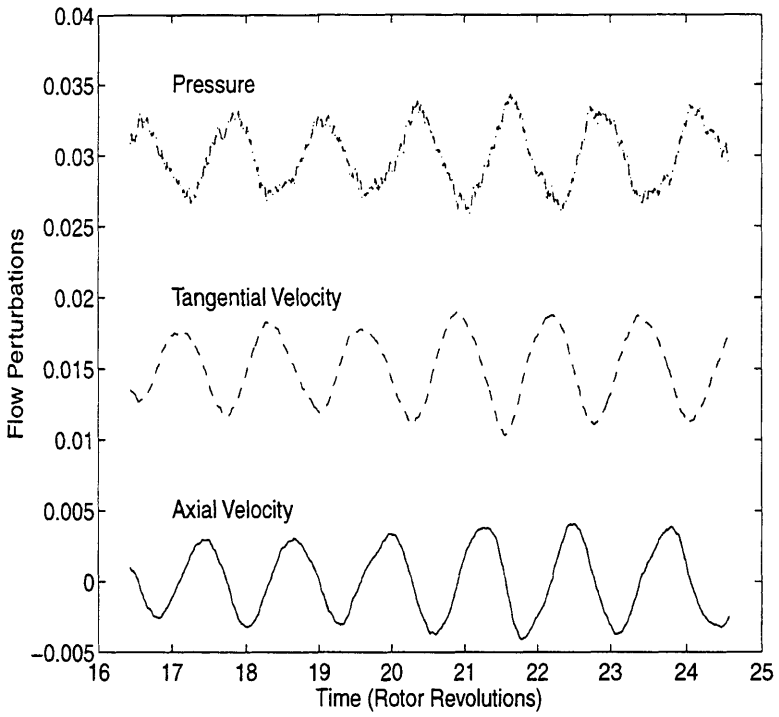

Figure 4.30: Time traces of inlet data during initial stall development from the numerical results

diagram. Using the assumed form of the perturbations (4.3 and 4.4) at least one of the complex magnitudes can be deduced from the others and compared with the measured result to test the flow field modeling assumptions.

The data from the rotor-only compressor computation of rotating stall is presented in Figure 4.30 for the inlet flow field. An artificial offset has been added to two of the traces. A sinusoidal variation can be seen along with a small level of growth. As expected, the value for frequency (ω) agreed for all three variables.

A plot of the phasers (complex magnitude and phase) for the inlet flow variables is given for the values obtained using the data fit of Equation 4.5 and an FFT is given in Figure 4.31. In addition, the values obtained using the axial velocity (u) and the shape of the eigenvector to predict v and p are shown. All of the values for the complex magnitudes are in excellent agreement. Therefore, the approximation that small perturbations of the inlet flow can be modeled as a single upstream decaying potential mode is a good one indeed.

In the downstream region of the flow field a similar analysis was performed. How-

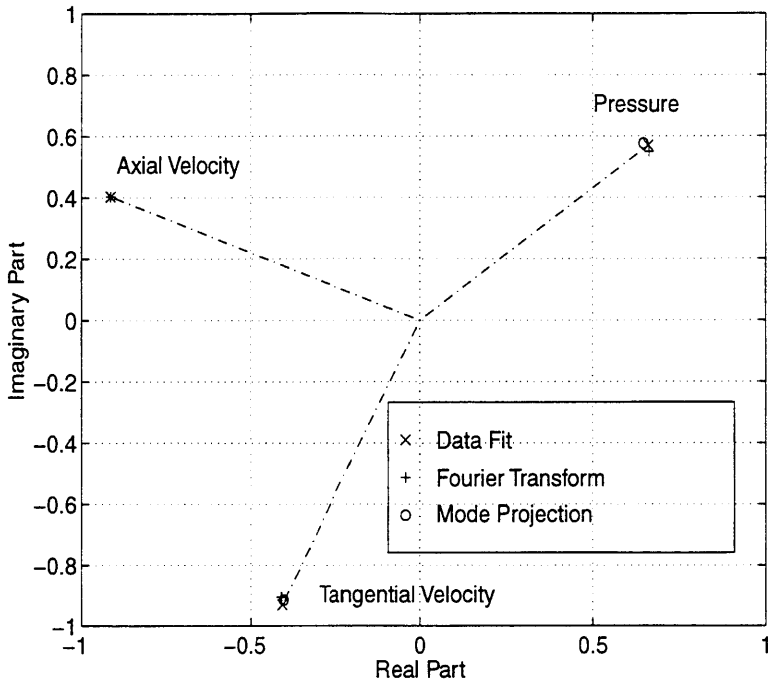

Figure 4.31: Phasers of inlet flow during stall inception

ever, the trace of the downstream pressure shows the presence of a different frequency than the two velocities. For linear disturbances, it is possible to argue that the contents of the pressure signal at a different frequency than the velocities can be ignored. The plot of the FFT of the exit variables given in Figure 4.33 shows that there is a peak in the pressure at the stall frequency obtained from the velocities. The second larger peak in the FFT of the pressure was found to remain at essentially constant magnitude as the stall cell became larger. Therefore, this disturbance does not appear to participate in the development of rotating stall. In addition, the disturbance frequency was found to scale with the number of blades of the compressor and is near the vortex shedding frequency for the rotor blade. Therefore, using the phasers obtained from the FFT's of the velocities and pressure it should once again be possible to show that the flow field can be represented by an eigenmode of the Euler equations. The value for ω was obtained from a data fit of the velocities and was in agreement with that obtained from the inlet flow field. The phasers for the exit flow field are shown in Figure 4.34. There is not agreement between the pressure obtained

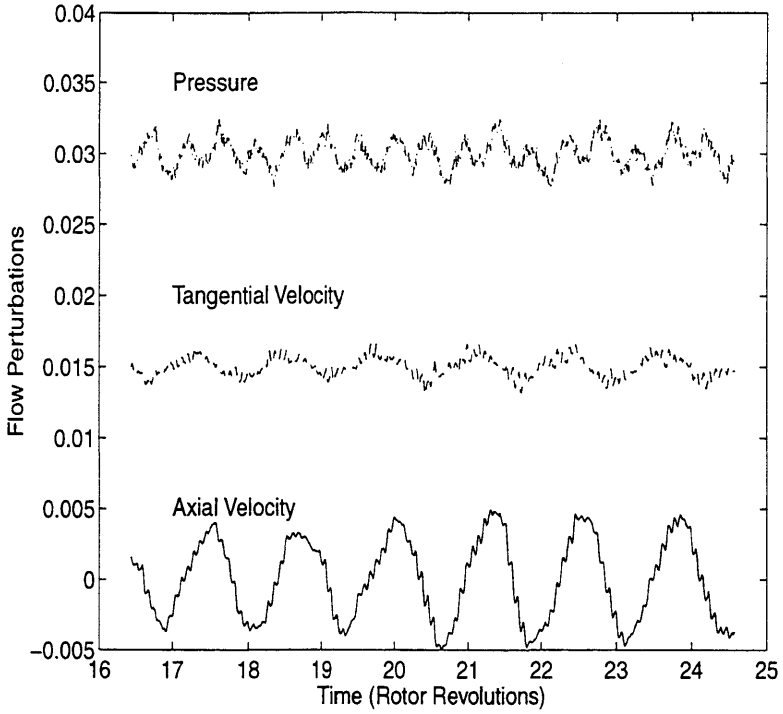

Figure 4.32: Time traces of exit data during initial stall development from the numerical results

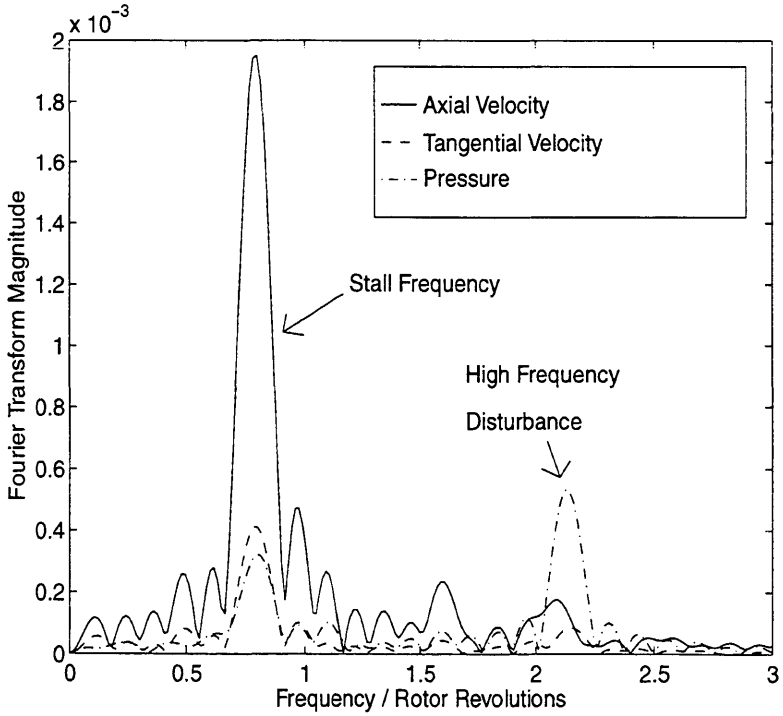

Figure 4.33: FFT of exit flow variables

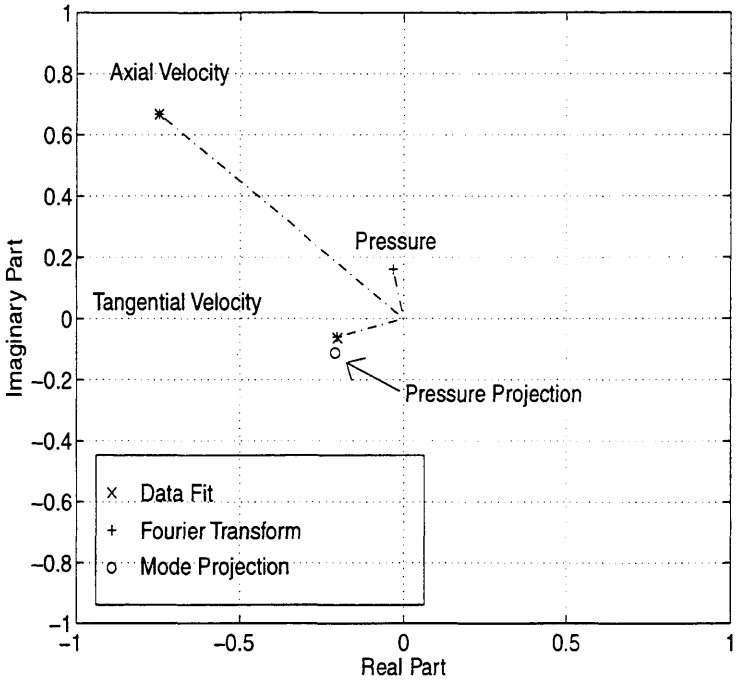

Figure 4.34: Phasers of exit flow during stall inception

from the data (FFT) and that given by the projection from the eigenvectors in the downstream flow field.

It is known that the assumptions upon which the eigenvalue analysis is based have been violated in the downstream duct. It can be seen in the plots of the compressor flow field given in the previous section that the flow is neither uniform nor steady in the downstream region. Since the this analysis could have been conducted in the rotating reference frame where the flow is essentially steady, with no loss in generality, the unsteadiness is not the cause of the discrepancy. Thus, the difference is attributable to the non-uniformity of the flow field. Another difference between the actual flow field and the form assumed by the linear model, which was noted by Marble [34], is that the vorticity of the background flow is not uniformly distributed, but rather is concentrated in the blade wakes. For lack of a simple alternative, this exit flow field model will be used in the subsequent analysis (without any apparent detrimental effect on the results).

4.4.3 Blade Row Modeling Assumptions

The blade row model is the portion of the stability model which relates the upstream and downstream flow quantities. The three required matching conditions are continuity, pressure rise (or losses), and turning.

Essentially all the models predict that the compressor flow will initially become unstable near the peak of its total-to-static pressure rise characteristic, and they yield relatively similar results for the rotation rate of the instability. The key difference between the various stability models is the relative position of the eigenvalues for the different harmonic numbers. Models which assume that the compressor responds instantaneously to changes in the flow show all of the eigenmodes becoming unstable at the same flow coefficient. The inclusion of a lag in the compressor response changes the relative stability of these eigenmodes. Typically, models which utilize a lag in the compressor response show that the lowest harmonic will become unstable at a higher flow coefficient than the higher order modes.

It is the goal of this section to utilize the computed rotating stall event to evaluate the assumptions commonly used in the formation of a blade row model. For this study, the form of the blade model was the same as the incompressible model used by Nagano, Machida and Takata [42], which can be summarized as follows.

$$u_1 = u_2 \tag{4.6}$$

$$p_{t,1} - p_{t,2} - \lambda \left(\frac{\partial u}{\partial t} \right)_{\text{relative}} = \frac{1}{2} \left(u_1^2 + v_1^2 \right) X \tag{4.7}$$

$$\tau_X \left(\frac{\partial X}{\partial t} \right)_{\text{relative}} = X_{SS} - X \tag{4.8}$$

$$\tau_\beta \left(\frac{\partial \beta_2}{\partial t} \right)_{\text{relative}} = \beta_{2,SS} - \beta_2 \tag{4.9}$$

The locations of stations 1 and 2 as well as the flow angle convention are shown in Figure 4.35. In these equations, λ represents the inertia of the fluid in the blade passage as shown in Appendix A. The term X is the total pressure loss coefficient. The two lag terms, τ_X and τ_β give the time constant of a first order lag response of

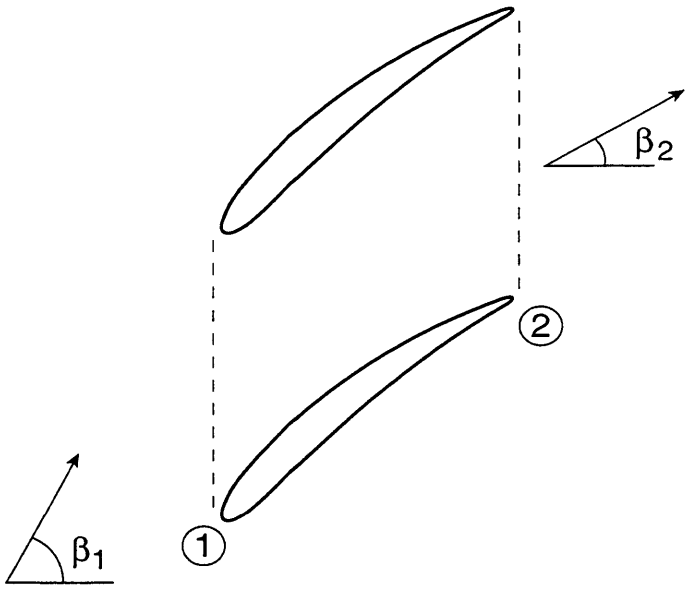

Figure 4.35: Measurement locations for the blade model study

the losses and turning to the inlet flow conditions. The two lag equations allow the instantaneous loss and turning to deviate from the steady state values given by X_{SS} and $\beta_{2,SS}$. To close these relations it is necessary to specify the form of the steady state loss and turning functions. For low speed flows it is reasonable to assume that both the steady state loss and turning should be functions of the inlet flow angle. Thus in the linearized form, these terms can be replaced by the their steady state derivatives.

$$\delta X_{SS} = \left(\frac{\partial X}{\partial \beta_1}\right)_{SS} \delta\beta_1 \tag{4.10}$$

$$\delta \beta_{2,SS} = \left(\frac{\partial \beta_2}{\partial \beta_1}\right)_{SS} \delta\beta_1 \tag{4.11}$$

All the quantities shown here are relative to the blade row in question. (The equations will look slightly different when written for a rotor as compared to a stator blade row due to a change in reference frame.)

For an incompressible flow field of a compressor with many blades, continuity is satisfied at each point on the circumference by the physical restriction of the flow

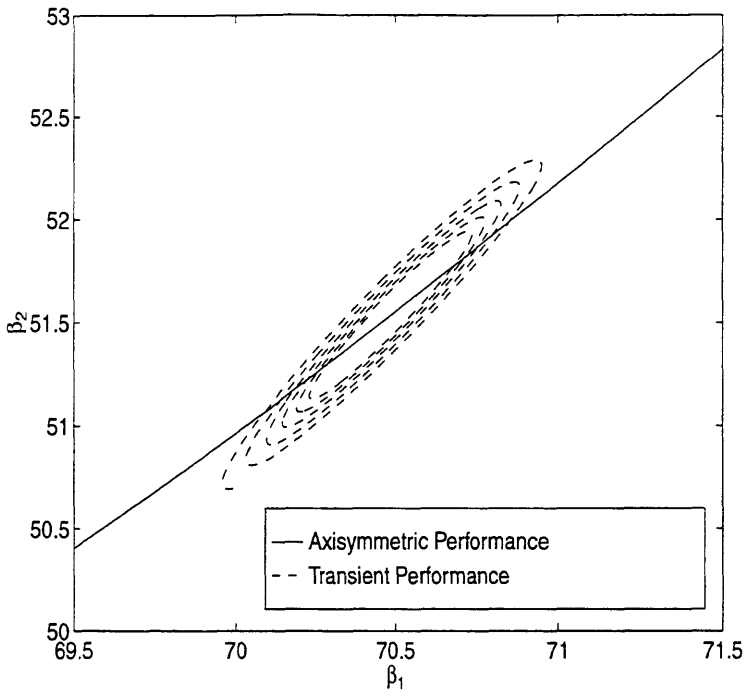

Figure 4.36: Comparison of unsteady turning with steady state response

through the blades. However, the stagger of the blades will provide an offset to this relation in the circumferential direction.

The turning relation can be checked directly since the inlet and exit flow angles are directly measurable quantities. To see the effect of unsteady turning variations, the response of the compressor blade row can be plotted with the steady-state axisymmetric response as shown in Figure 4.36. This comparison was made using results from the numerical computation of rotating stall in a single blade row rotor-only compressor. The steady state response is equivalent to $\beta_{2,SS}$ in Equation 4.9. The unsteady response deviates from the steady response in the mean slope of the curve. In addition, hysteresis is clearly evident in the unsteady response.

Using these results, the relation given by Equations 4.9 and 4.11 can be fit to the data to provide an estimate to τ_β by minimizing the square of the errors between the measured value of β_2 and that given by integrating Equation 4.9 in time. The resulting best fit to the data is shown in Figure 4.37; a value of τ_β equal to 1.0 times the flow through time of the blade row gave the best fit. This value is in agreement

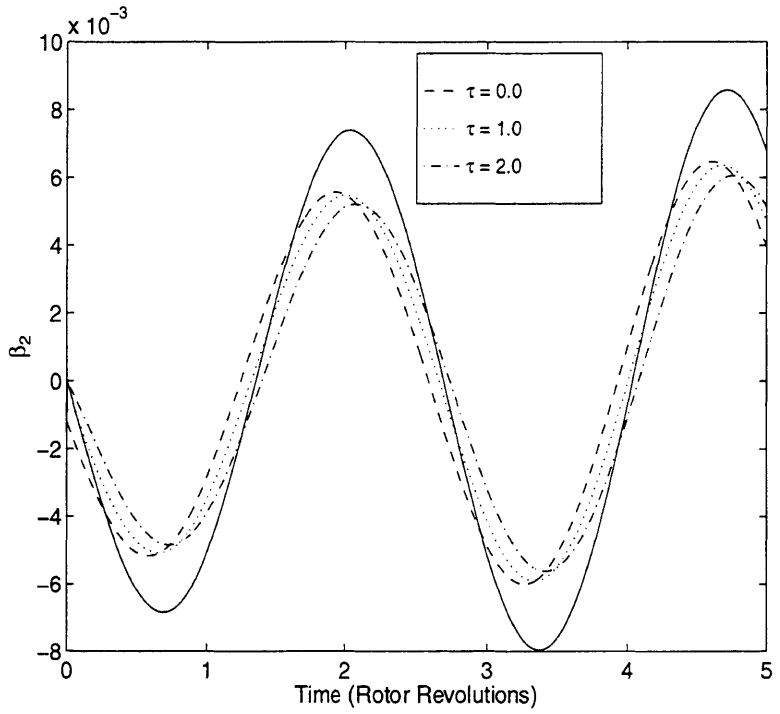

Figure 4.37: Fit of β_2 using first order lag equation compared to numerical results

with that given by Nagano, Machida, and Takata [42]. In Figure 4.37 a noticeable difference is seen in the magnitude of the measured and modeled response of β_2. This is likely attributable to the over simplification implied by the first order lag model. The data fit does do a good job in fitting the phase lag of the response. Nagano et al. [42] argued that both the lag time constant and the shape of the steady state response curve could be derived by fitting the lag equation to the data. However, this method does not necessarily give a unique solution.

A similar process was used to fit the losses to the relations given by Equations 4.8 and 4.10. The measurement of the loss coefficient is not as straightforward as the turning since the loss coefficient is not directly measurable. To arrive at a value for the magnitude and phase of X a linearized form of Equation 4.7 was used. A comparison of the unsteady and steady response of the loss coefficient is shown in Figure 4.38. The loss coefficient was found to compare more closely between the steady and unsteady response than the turning. By fitting the value of the loss coefficient in the same way as the turning, a value of τ_X equal to 0.45 flow through times was obtained.

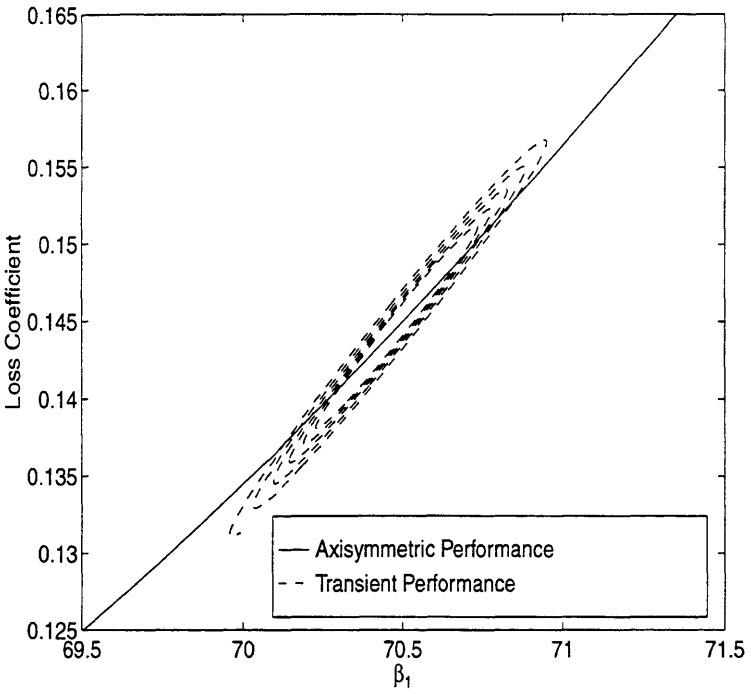

Figure 4.38: Comparison of unsteady loss coefficient with steady state response

Agreement of the fit between the data and the lag relation was very similar to that shown for the turning in Figure 4.37.

To confirm the assumption that the time lag constant (τ) was independent of the length scale of the disturbance, an identical analysis was performed for compressors consisting of 12, 8, and 4 blades. In each of these cases the same blade geometry was used and a modal stall of the first harmonic was seen. The values for both τ_β and τ_X were found to be independent of the number of blades (length scale of the disturbance) when non-dimensionalized by the flow through time of the compressor blade row.

4.4.4 Linear Stability Model Results

Utilizing the analysis of the previous section a linear stability model can be constructed based on Equations 4.6-4.9. The following set of linearized relations were

obtained for a rotor blade row ($U = 0$ for a stator blade row).

$$u'_1 = u'_2 \tag{4.12}$$

$$p'_1 + \overline{u}_1 u'_1 + \overline{v}_1 v'_1 - p'_2 - \overline{u}_2 u'_2 - \overline{v}_2 v'_2 - \lambda \left(\omega + \frac{U}{R}\imath n\right) u'_1 = \overline{u}_1 \overline{X} u'_1 + \overline{v}_1 \overline{X} v'_1 + \frac{1}{2}\left(\overline{u}_1^2 + \overline{v}_1^2\right) X' \tag{4.13}$$

$$\tau_X \left(\omega + \frac{U}{R}\imath n\right) X' = \frac{\partial X}{\partial \beta_1}\beta'_1 - X' \tag{4.14}$$

$$\tau_\beta \left(\omega + \frac{U}{R}\imath n\right) \beta'_2 = \frac{\partial \beta_2}{\partial \beta_1}\beta'_1 - \beta'_2 \tag{4.15}$$

In these equations the over-barred quantities represent the mean values and the primed quantities represent perturbations about the mean values. The values for the time constants in the lag equations were taken from the data fit done in the previous section ($\tau_\beta = 1.0$ and $\tau_X = 0.45$). The mean flow quantities and the steady state performance derivatives could all be determined from the axisymmetric performance.

Using this model the eigenvalues shown in Figure 4.39 were obtained for the sixteen bladed rotor-only compressor. In the computation a modal stall of the second harmonic was observed at a flow coefficient of 0.353. At this point the stability model predicts that the eigenvalues for all the modes are unstable. The linear model predicts that the highest order modes will become unstable before the lower ones. Using the criteria of at least eight blades per harmonic, only the first two harmonics can be compared with the model. When so restricted, the linear model correctly predicts that the second harmonic will be the least stable mode of the system.

Using the combined results of the four, eight, and sixteen bladed compressors, it was possible to estimate the position of several of the eigenvalues for the sixteen bladed compressor at its stall point. The advantage of using the four and eight bladed compressor results, is that the geometry of the compressor is identical to the sixteen bladed one, but the lower harmonics are removed from consideration. Specifically, it was possible to measure three of the eigenvalues of the sixteen bladed compressor for the operating point of $\phi = 0.353$. Since the sixteen bladed compressor stalled in the second mode, and the eight bladed compressor stalled in the first mode, there

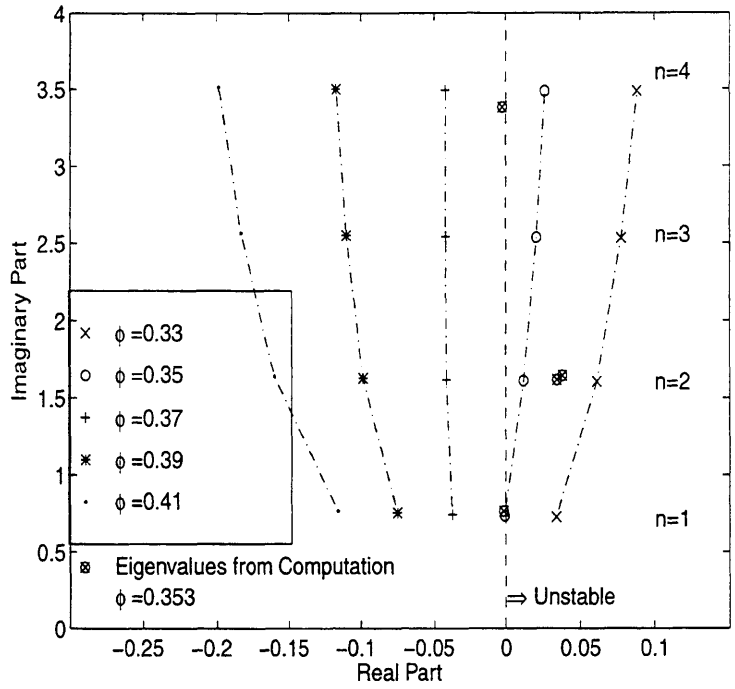

Figure 4.39: Predicted eigenvalues for the sixteen bladed compressor

exists two equivalent measurements of this mode. In addition, the first harmonic was the dominant mode for a short period of time before the second harmonic overtook it in the sixteen bladed stall event. This allowed the first harmonic eigenvalue to be estimated as well. The four bladed compressor was found to stall at a lower flow coefficient than the other two configurations, but by using the amount by which the eigenvalues change due to a change in the flow coefficient in the linear model, the change in flow coefficient at stall could be approximately corrected for.

The end result is the comparison of the measured and predicted eigenvalues for the sixteen bladed compressor at a flow coefficient of 0.353 as shown in Figure 4.39. Due to the length scale limitations of the model, only the first two harmonics are considered reliable. For these two harmonics, the frequencies agree to within 3% and the absolute level of stability is also captured reasonably well. More importantly, the trend in the relative stability between the modes is correctly represented. For the fourth harmonic, the rotational speed is not captured as well as the lower order modes, Also, there appears to be an increased level of damping which is not captured

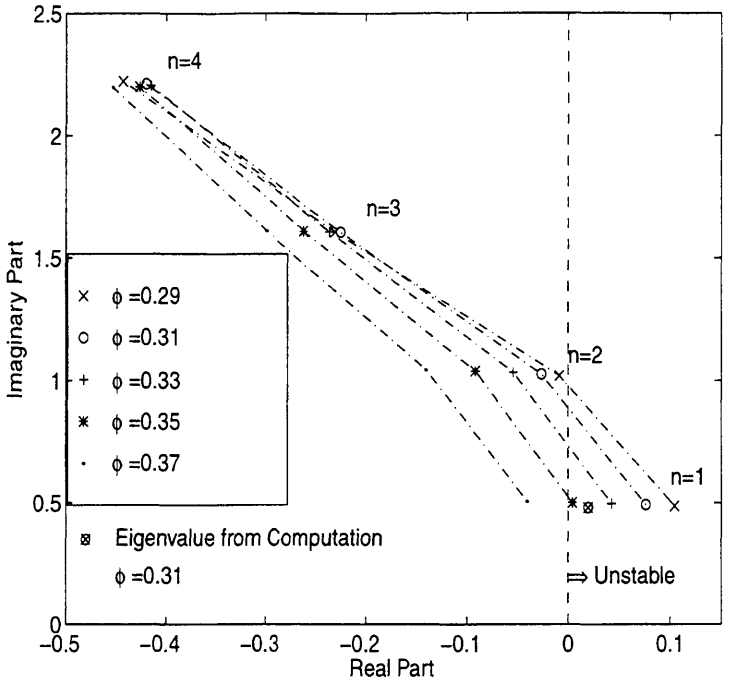

Figure 4.40: Predicted eigenvalues for the single stage compressor

by the linear model for such a small number of blades per harmonic.

The shape of the eigenvalue map presented for the single blade row compressor is contrary to the conventional view that the lowest harmonic will be the least stable. However, this case is somewhat unusual in that there is only one blade row. The eigenvalue map did regain its more familiar shape when a single stage compressor was analyzed.

For the single stage compressor discussed in Section 4.3 an eigenvalue analysis was conducted using the lag parameters determined for the rotor-only case. The model for the single stage compressor was constructed by using a separate model for each blade row and joining them in series. The resulting eigenvalues are shown in Figure 4.40. At the numerically determined stalling point ($\phi = .31$), the first harmonic is the only predicted unstable mode of the system. This is in qualitative agreement with the numerical results shown in Figure 4.19. For this case all of the higher harmonics do not increase above their background levels until after the first harmonic has reached 10% of its in-stall magnitude. The predicted rotational rate of the stalling harmonic

of 48% is in good agreement with the measured speed of between 45% and 50%.

The primary discrepancy seen between the numerical results and the linear model is the flow coefficient at which the compressor becomes unstable. However, this is not a direct comparison since the information used for the linear model came from the axisymmetric speedline computation rather than the actual stall computation. For the single stage compressor it was impossible to exactly preserve the blade count ratio between the axisymmetric calculation and the full rotating stall case which results in a difference in the performance as shown in Figure 4.17. From this figure it can be seen that the axisymmetric speedline exhibits a positive slope at a higher flow coefficient than the full compressor case. The predicted stalling flow coefficient of the linear model ($\phi = 0.35$) is in good agreement with the peak of the axisymmetric speedline shown in Figure 4.17.

4.4.5 Effects of Modeling Assumptions on Stability Predictions

Using this validated stability model, various portions of the model can be modified to assess their effects on the overall results. It is especially important to assess the effects of the assumed form of the exit static pressure since it did not to conform to numerical results. To do this the exit pressure perturbations were set to zero in the model. The results are compared in Figure 4.41 for the rotor-only case with sixteen blades (reference Figure 4.39). The effect was to decrease the change in the stability per change in flow coefficient, and to increase the rotational speeds by about 5%. Both sets of eigenvalues have the same structure, and the effect of setting the exit pressure to zero appears to be minor. Therefore, the use of the exit flow field model presented earlier appears to be adequate.

The measured parameters used to fit the linear model to the numerical results are the two lag time constants. The influence of these parameters on the eigenvalues of the system can be seen in the following results. Figure 4.42 shows the eigenvalue map with both lag parameters set to zero. Consistent with models that assume that

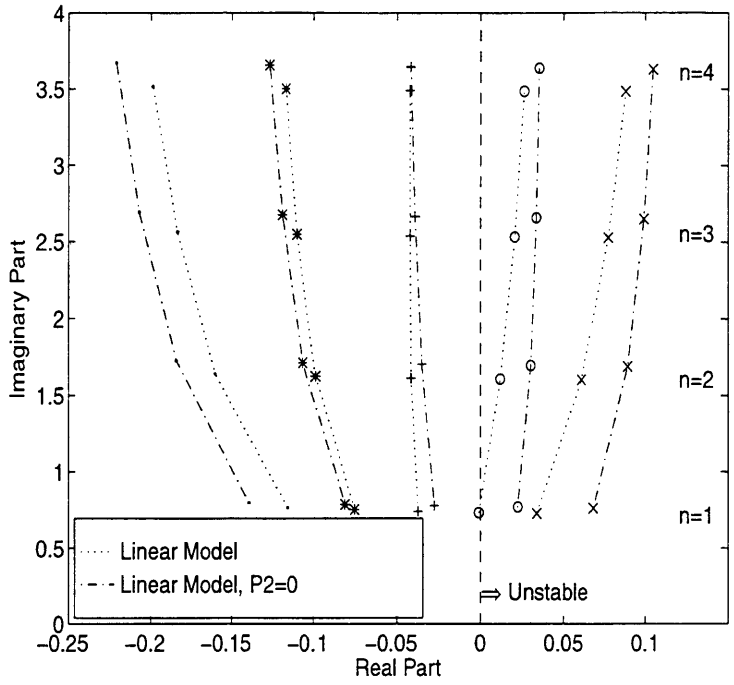

Figure 4.41: Comparison of eigenvalues for the linear model with $p_2 = 0$ for the sixteen bladed compressor

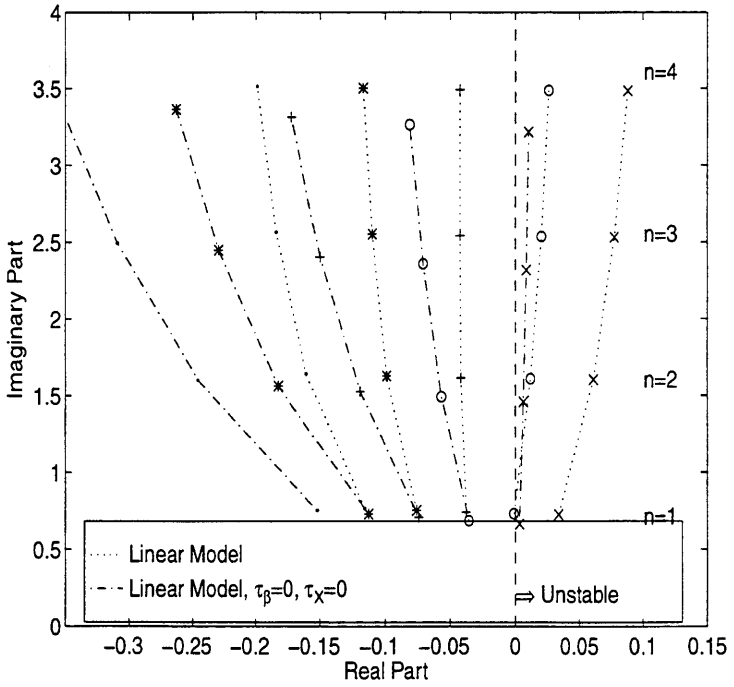

Figure 4.42: Comparison of eigenvalues for the linear model with $\tau_\beta = 0$ and $\tau_X = 0$ for the sixteen bladed compressor

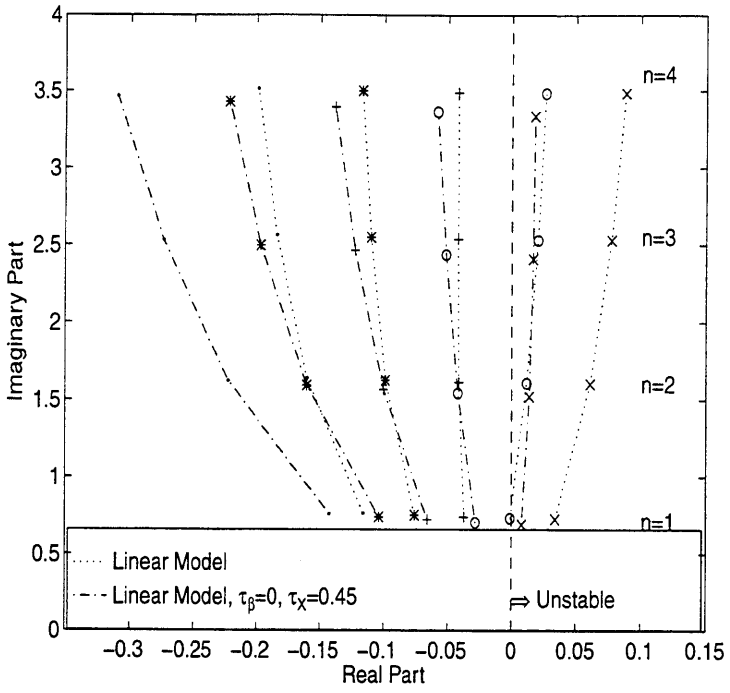

Figure 4.43: Comparison of eigenvalues for the linear model with $\tau_\beta = 0$ and $\tau_X = 0.45$ for the sixteen bladed compressor

the compressor responds according to its steady state performance, the eigenvalues nearly line up on the imaginary axis at the critical flow condition when the lag was removed. When the lag parameters were set to zero one at a time, the results given in Figures 4.43 and 4.44 were obtained. The unsteady response of the turning constituted the largest part of the effect of the unsteady blade response. As shown by Longley [32], both the unsteady turning and losses affect the results in essentially the same manner.

The same changes were also made for the single stage compressor. The results for setting the exit pressure to zero are shown in Figure 4.45. As in the rotor-only case, the stability and the rotational speed were modified by this change (10% in speed for n=1), but the overall shape of the eigenvalue map remained about the same. A greater difference was seen when the lags were neglected. Since the system matrix became poorly conditioned for very small lags, a value of 0.1 was used instead of zero. This result is given in Figure 4.46. Again, the eigenvalues at the critical flow coefficient tend to line up on the imaginary axis, as predicted by the form of the linear

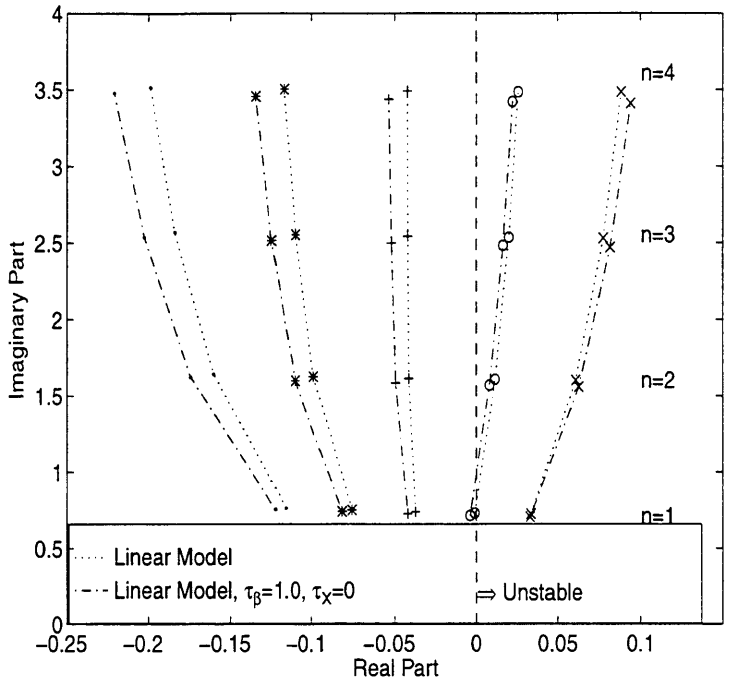

Figure 4.44: Comparison of eigenvalues for the linear model with $\tau_\beta = 1.0$ and $\tau_X = 0$ for the sixteen bladed compressor

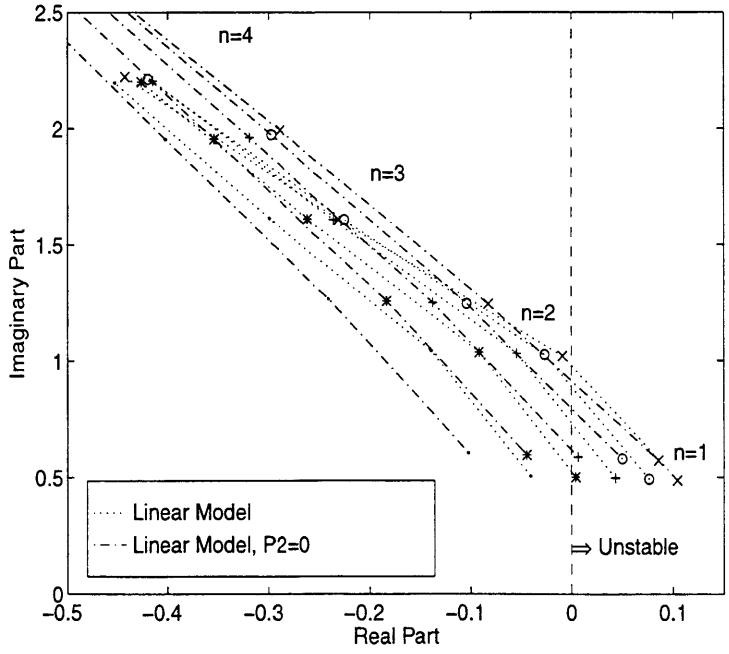

Figure 4.45: Comparison of eigenvalues for the linear model with $p_2 = 0$ for the single stage compressor

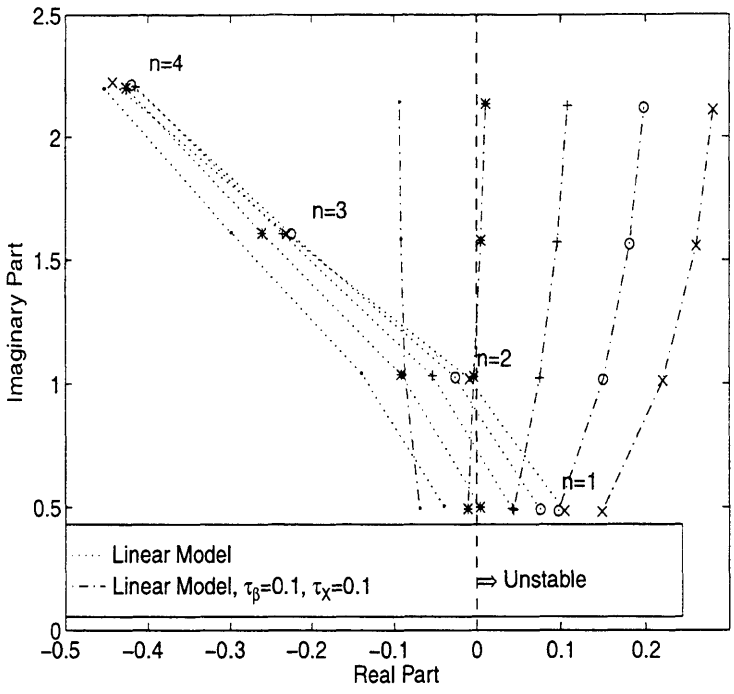

Figure 4.46: Comparison of eigenvalues for the linear model with $\tau_\beta = 0.1$ and $\tau_X = 0.1$ for the single stage compressor

model without lags. This result confirms the initial expectation that the inclusion of an unsteady blade response would stabilize the higher modes of the system.

4.4.6 Discrete Blade Effects

The final assumption of the analytic stability models to be assessed is the assumption that the wavelength of the disturbance is much longer than the blade spacing. This assumption can be evaluated directly by varying the number of compressor blades. Section 4.1 presented the stalling behavior for a rotor-only compressor with eight blades. For comparison, the same conditions were used to compute the development of rotating stall for a four bladed compressor. Each of the compressors used the same blade geometry and each compressor exhibited a first harmonic modal stall. Therefore, the number of blades per disturbance wavelength was equal to the number of blades for each compressor.

Figures 4.47 and 4.48 display the time histories of the magnitude of the Fourier

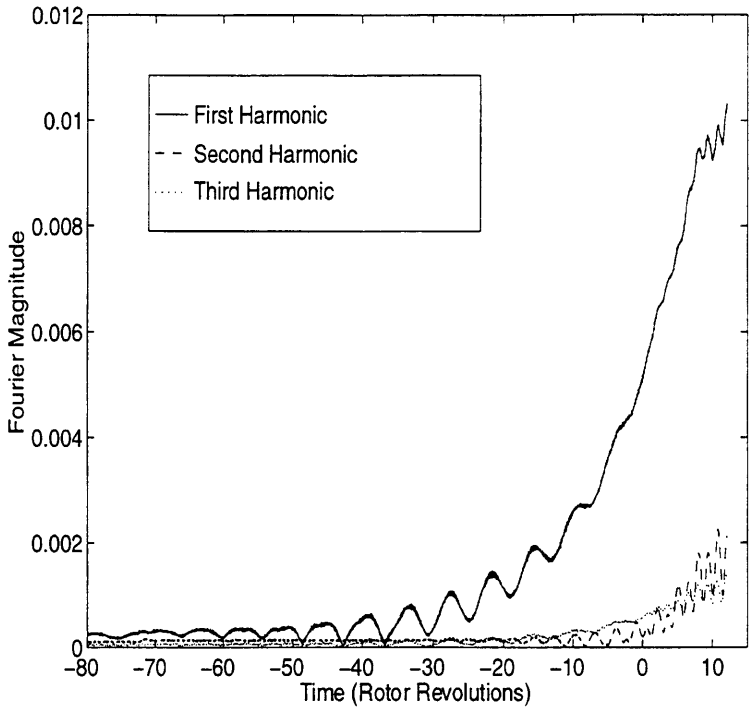

Figure 4.47: Time traces of the magnitude of the Fourier harmonics of the inlet axial velocity for the four bladed compressor

harmonics of the inlet axial velocity as the compressors entered into rotating stall. Only the initial development of rotating stall is shown in these figures. One item that is evident is the modulation of the magnitude of the first harmonic for the four bladed compressor. The frequency of this modulation corresponds to the difference of the first harmonic frequency and the blade passing frequency. Thus, the variation in the magnitude of the first harmonic is due to the disturbance passing through the flow variations of the individual blades. This is precisely the effect that is neglected in the analytic stall models. Since this effect is not evident in the eight bladed compressor case, the minimum number of blades per harmonic which are required for the stability model is eight or less.

4.5 Summary

For the two-dimensional representation of the stalling process all of the instabilities were found to be modal in nature and well predicted by the current compressor

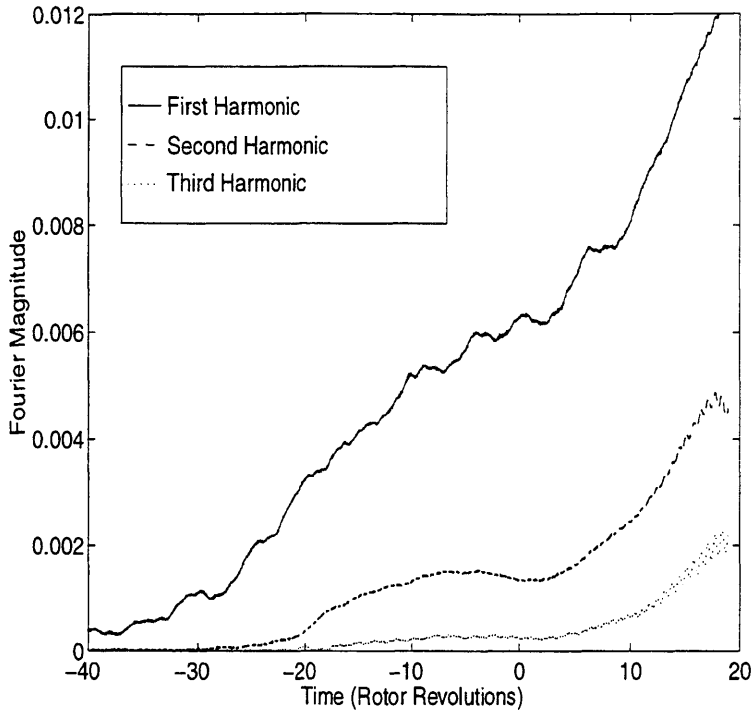

Figure 4.48: Time traces of the magnitude of the Fourier harmonics of the inlet axial velocity for the eight bladed compressor

stability models. Taken together, these results confirm that the development of a modal stall takes place according to the hypotheses used to formulate these models. In particular, the response of the blade row behaves in the following way.

- The unsteady compressor performance does not deviate substantially from the steady state performance which allows the unsteady performance to be described adequately as a linear functions of the inlet conditions with a first order differential lag.

- The instantaneous performance lags the steady-state performance with a time scale of the order of the flow through time of the blade row.

  - This response can be reasonably well approximated by a simple first order lag equation.

  - These lag parameters have been directly measured.

When coupled with the exterior flow field, these conditions yield a stability model which has been shown to accurately capture the modal development of rotating stall.

Chapter 5

Three-Dimensional Results and Analysis

Experimental results have shown that the development of rotating stall can be three-dimensional in nature. It is the goal of this portion of the study to assess the effects of three-dimensional flow structures on the development of rotating stall.

5.1 Three-Dimensional Stall

A single blade row compressor geometry with eight blades was examined. This was considered the minimum number of blades that was capable of demonstrating either a modal or short length-scale type of stall inception.

The compressor geometry, shown in Figure 5.1, was the three-dimensional version of that used for the two-dimensional study. The performance of the compressor from which this geometry was taken is presented by Wisler [55]. The details of the experimentally observed stall inception for this compressor are presented by Silkowski [45] and Park [44]. In these experiments the compressor exhibited a short length-scale type of stall inception which was located primarily in the first stage rotor. In the experiments the compressor consisted of four stages with a set of inlet guide vanes, but only the rotor blade row was used for this computational study.

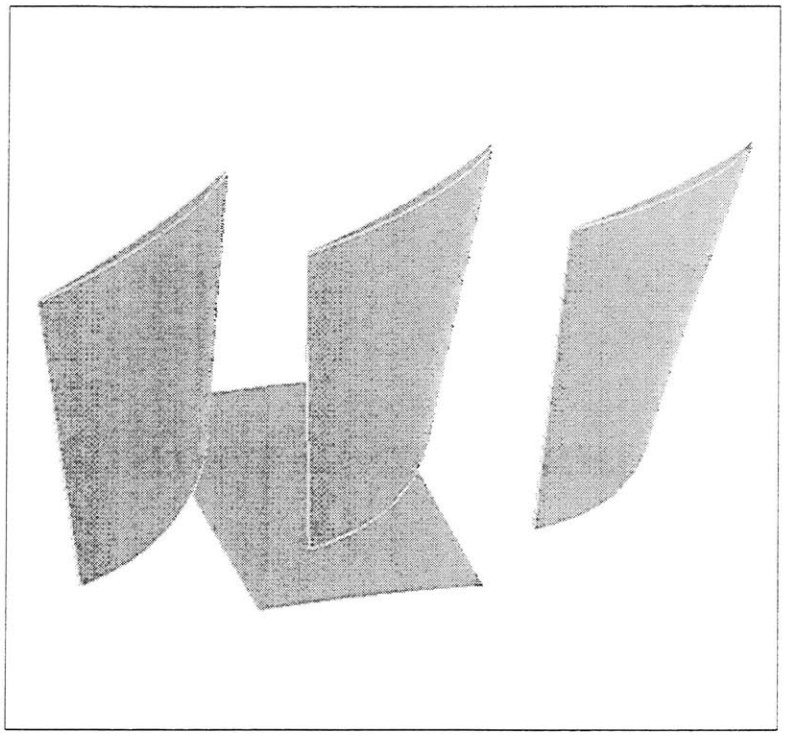

Figure 5.1: E^3 Blades used for three-dimensional study of rotating stall

5.1.1 Characterization of Three-Dimensional Stall

The geometry used for the computation is shown in Figure 5.2. Because eight blades were used, this required that only a fraction of the annulus be used in order to preserve the three-dimensional shape of the blade. This constraint limits the maximum wavelength of any non-axisymmetric disturbance to eight blades spacings in length. In addition, the length of time over which periodicity is imposed is not the same as the amount of time for a physical revolution to occur. To avoid confusion, the time it takes for the eight blades to traverse the domain once will be referred to as a *period* rather than a *revolution.*

A 3.0% tip clearance (as a percent of chord) configuration was used for this computation. Before the compressor was throttled to stall, a steady state solution was obtained near the peak of the characteristic. The compressor was then throttled from a flow coefficient of 0.335 to a value of 0.300 in 5 periods and then held at a constant throttle setting while the rotating stall pattern developed. This large throttle change was made to prevent the need to make multiple throttle changes due to the

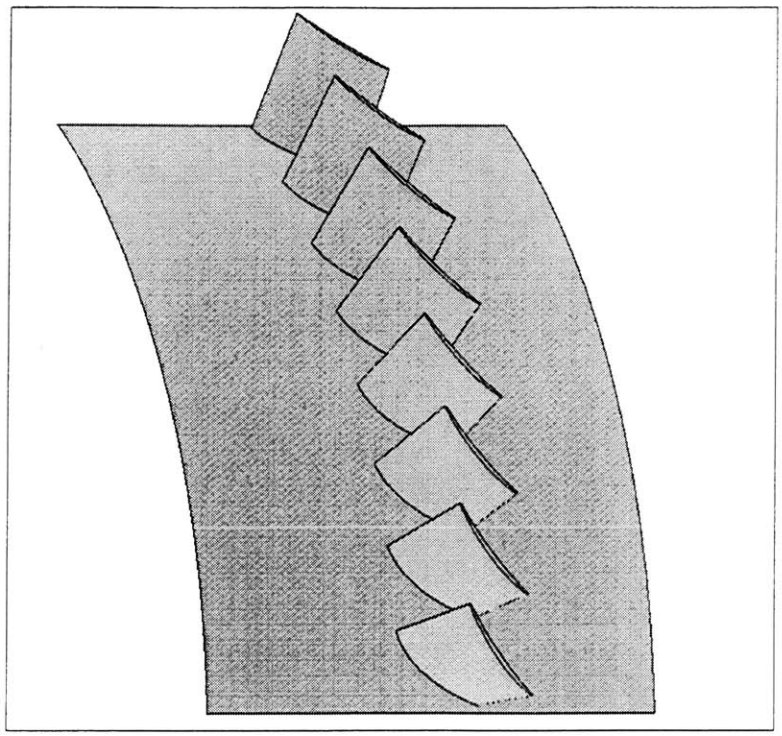

Figure 5.2: Compressor geometry used for three-dimensional rotating stall investigation

long computational time required to produce a solution. Figure 5.3 shows the characteristics for both the steady state single blade configuration and the transient eight bladed computation. Because of the finite rate at which the mass flow was reduced in the compressor, the measured transient pressure rise appears greater than the steady state value for a given flow coefficient due to the unsteady effect of the inertia of the fluid in the blade passage. Non-axisymmetric flow was observed to occur at at flow coefficient of 0.32. This corresponds with the flow coefficient at which the single passage pressure rise was maximum.

The development of the stalling flow pattern can be seen in traces of the axial velocity from eight evenly spaced locations around the annulus taken near the tip, 1/4 chord upstream of the compressor, as shown in Figure 5.4. An artificial offset has been added to all of the traces except the bottom one to allow them to be viewed together. The traces show the rapid growth of several small amplitude disturbances which then give way to one large magnitude short length-scale disturbance.

An entropy contour at the leading edge of the compressor taken during the de-

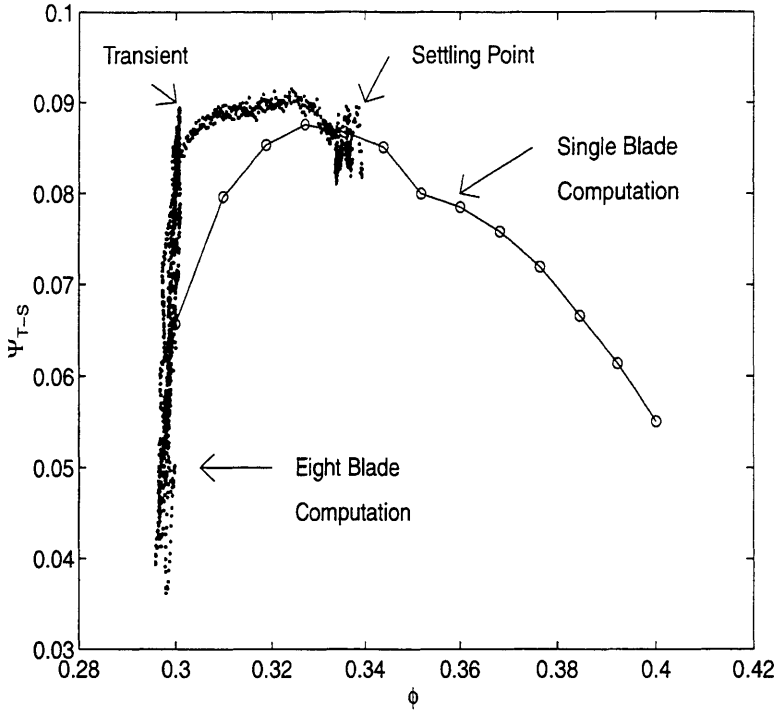

Figure 5.3: Pressure rise characteristic for the E^3 rotor with 3.0% tip clearance during a transient to stall

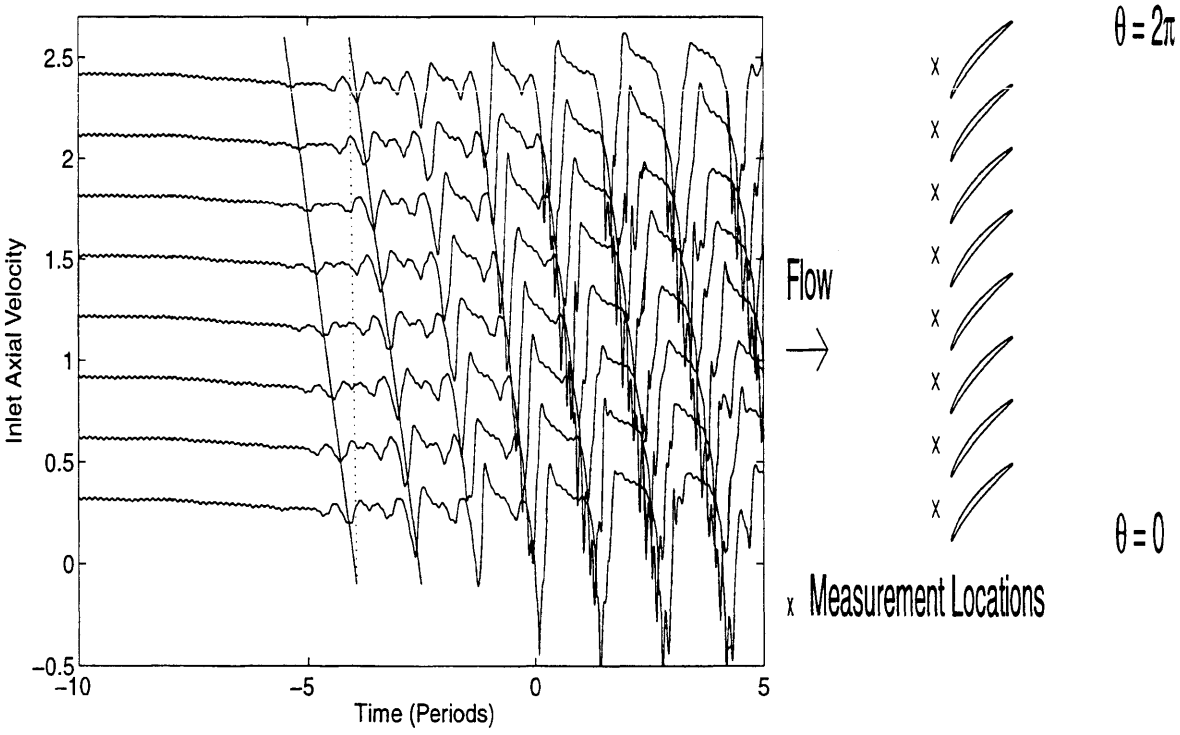

Figure 5.4: Traces of the inlet axial velocity for the E^3 rotor with 3.0% tip clearance during a transient to stall

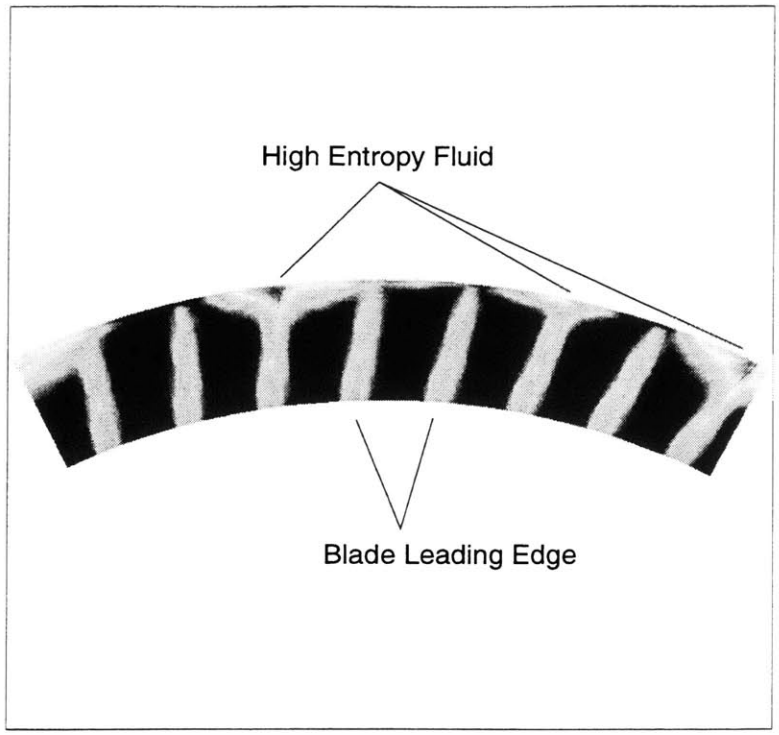

Figure 5.5: Entropy contour of the leading edge of the E^3 compressor with 3.0% clearance (Time = -4.1)

velopment of these disturbances, given in Figure 5.5, shows two important features. The first is the presence of flow spilling forward of the compressor as evidenced by the high entropy fluid in the blade passage at the leading edge. The second is that the reversed flow region is confined to the tip of the compressor.

To show that the disturbance seen in this computation is the same phenomena as that seen in experiment, the numerical results have been compared to the available experimental data. It is not possible to perform a direct back-to-back comparison with the multi-stage compressor data, but the defining characteristics of a short length-scale stall inception can be compared. One limitation is that the comparison must be done for times when the stalling disturbance is relatively small in size. In the experiment the effect of other blade rows on the disturbance in the rotor becomes stronger as the disturbance grows in size.

The defining characteristics of a short length-scale stalling disturbance are a small circumferential extent, high rate of rotation, high growth rate [7], and a localization near the tip [45]. The position of the disturbance at the tip of the blades has already

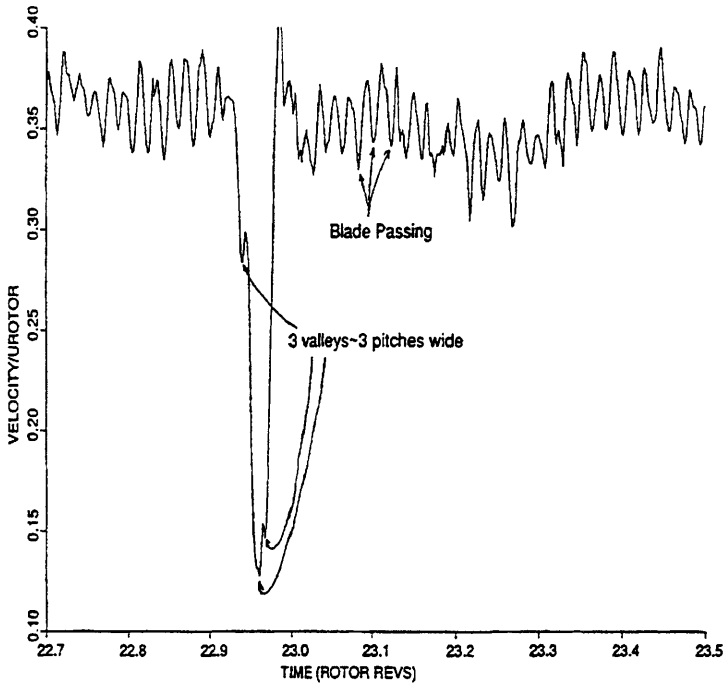

Figure 5.6: Trace of the inlet axial velocity for the compressor tested by Silkowski during a transient to stall

been demonstrated. To compare the size and shape of the disturbance, the upstream velocity near the tip has been compared with the experimental measurements. The experimental result is from the report by Silkowski [45] and is shown in Figure 5.6. The result from the computation is shown over the same corresponding period of time in Figure 5.7. The experimental result shows a single disturbance that is approximately three blade pitches wide. The numerical result shows several disturbances which are also approximately three blade pitches wide. Because other experiments have shown the development of more than one short length-scale stall cell [7], this difference in the number of stall cells is not considered important. However, the shape of the disturbances are in accord with experiment. The rotational speed of the disturbance of 70% of the rotor speed also matches the experimental result. To compare the growth rate of the disturbance it is necessary to consider that the computation represents only a fraction of the total compressor annulus. The data of Silkowski [45] show that the disturbance takes just over one rotor revolution to grow from small scale to the magnitude of the fully developed stall. In the computation, this growth

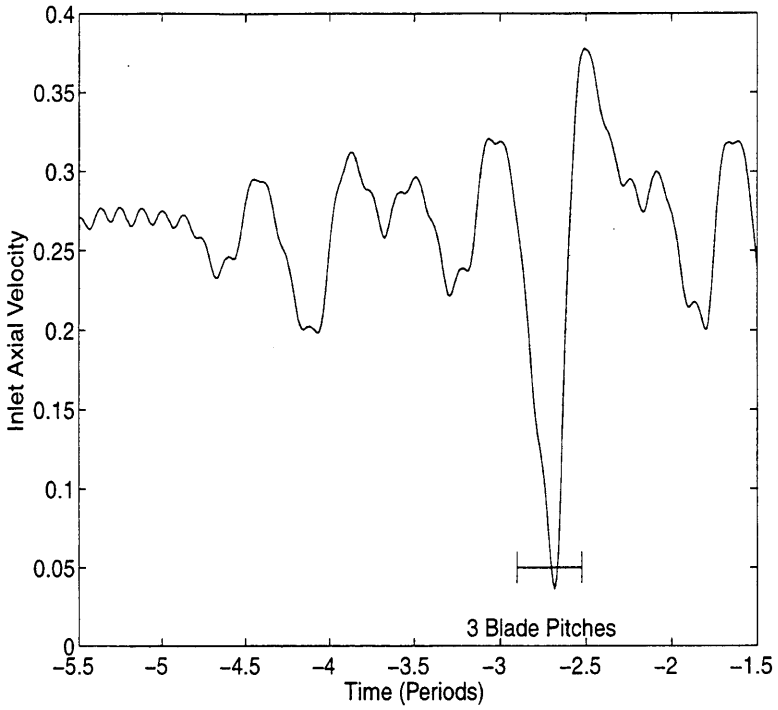

Figure 5.7: Trace of the inlet axial velocity for the E^3 rotor with 3.0% tip clearance during a transient to stall

takes about seven periods, which corresponds to one full rotor revolution.

Therefore to the extent to which data for comparison exist, the results show that this is the type of short length-scale stalling disturbance observed in experiments.

5.1.2 Short Length-Scale Stalling Mechanism

Examination of the flow in the tip region of the compressor during the development of the short length-scale stall showed that motion of the tip clearance vortex was a prominent feature in this process. At the operating point where non-axisymmetric flow began to develop, it was observed that the tip clearance vortex was located at the leading edge of the compressor with a trajectory which was perpendicular to the axial direction During the development of rotating stall, the vortex was seen to move upstream of the compressor to form the forward boundary of the reversed flow region of the stall cell. To view the course that this vortex takes during the development of rotating stall a sequence of plots of the magnitude of the vorticity in the tip region

of the compressor are presented in Figures 5.8-5.11. Just before stall (Figure 5.8) the tip clearance vortex can be seen to stretch from the leading edge of each rotor blade to the leading edge of its nearest neighbor. Figure 5.9 shows the state of these vortices after non-axisymmetric flow has begun to develop. At this point, the flow in the lower 3/4 span of the compressor is relatively undisturbed even though substantial non-uniformity exists at the tip as shown in Figure 5.5. At least two short length-scale stall cells can be seen developing as evidenced by the presence of the tip clearance vortex forward of the leading edge of the compressor. At a later time one of these stall cells becomes dominant as shown in Figure 5.10. At the leading edge of this disturbance the tip clearance vortex is evident. In Figure 5.11 the stall cell can be seen in its near-final state. This flow field is similar to that seen in Figure 5.10 but the disturbance has propagated farther upstream and the width of the stall cell has increased. These features were evident throughout the outer 10-15% of the span (an immersion of 8% was found to give the best overall view of the stalling process).

A side view of the flow during the early stages of this process is shown in Figure 5.12. This figure presents a contour of the vorticity magnitude along with arrows denoting the flow velocity for a plane of constant circumferential angular position. The position of the clearance vortex ahead of the blades near the casing can be seen.

5.1.3 Role of the Tip Clearance Vortex in Short Length-Scale Stall

To understand the role of the tip clearance vortex in the formation of a short length-scale stall cell, the steady state positioning and transient motion of the vortex were considered. As previously stated, the position of the tip clearance vortex was seen to be perpendicular to the axial direction at the leading edge of the compressor just prior to the development of asymmetric flow. For higher flow coefficients, the trajectory of the vortex lies farther back in the blade passage. This can be seen in the plots of the magnitude of the vorticity in the tip region presented in Figure 5.13 for a near-design point and in Figure 5.14 for the stalling point. At a flow coefficient near

Figure 5.8: Vorticity contour at 8% immersion of the E^3 compressor with 3.0% clearance (Time = -5.9)

Figure 5.9: Vorticity contour at 8% immersion of the E^3 compressor with 3.0% clearance (Time = -4.1)

Figure 5.10: Vorticity contour at 8% immersion of the E^3 compressor with 3.0% clearance (Time = -1.9)

Figure 5.11: Vorticity contour at 8% immersion of the E^3 compressor with 3.0% clearance (Time = 1.0)

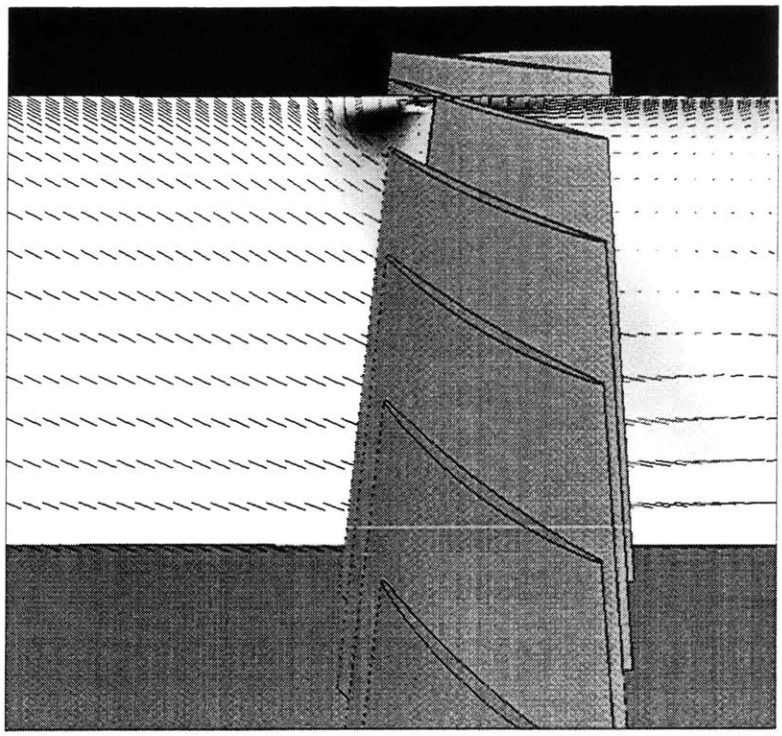

Figure 5.12: Vorticity contour at constant θ of the E^3 compressor with 3.0% clearance (Time = -3.3)

the design point the tip clearance vortex rolls up at about the quarter chord position with a trajectory that extends across the blade passage and then follows the stagger of the neighboring blade as shown in Figure 5.13. At the peak of the pressure rise characteristic, the vortex rolls up near the leading edge and has a trajectory which is perpendicular to the axial direction as shown in Figure 5.14.

A simpler view of the vortex trajectory for different flow coefficients is given in Figure 5.15. The positions shown in this figure were taken from the steady state single blade computations. As the flow coefficient is reduced the clearance vortex trajectory becomes closer to being perpendicular to the axial direction. The equilibrium position of this vortex can be described using a description of the flow based on vortex dynamics. Because the vortex is near a solid boundary, it will possess a self induced velocity which can be explained through the use of an image vortex as shown in Figure 5.16. This induced velocity will be towards the upstream axial direction. For a given strength of the vortex and value of the mean flow there will, in general, be a vortex trajectory at which the induced velocity is balanced by the component

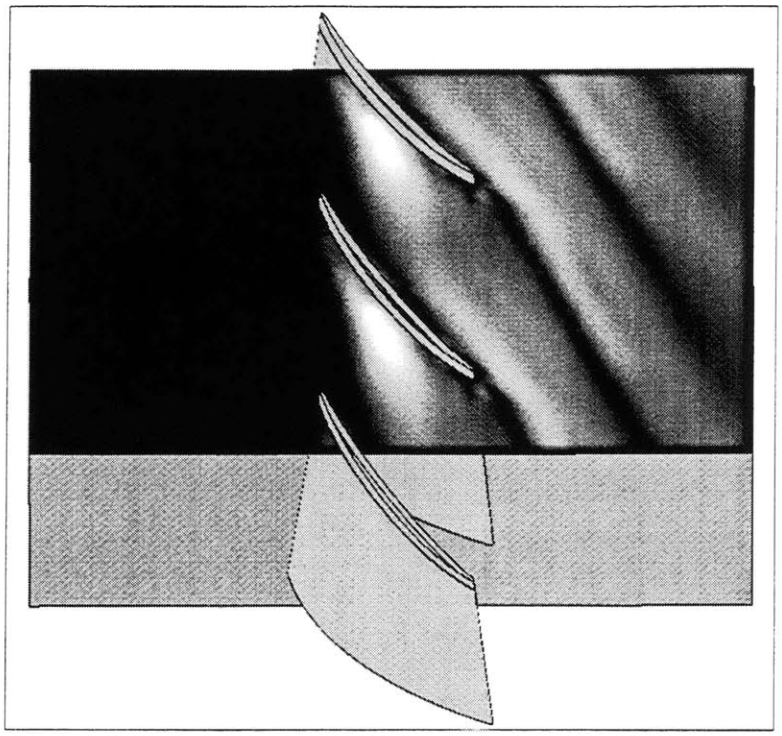

Figure 5.13: Vorticity contour at 6% immersion of the E^3 compressor with 3.0% clearance ($\phi = 0.37$)

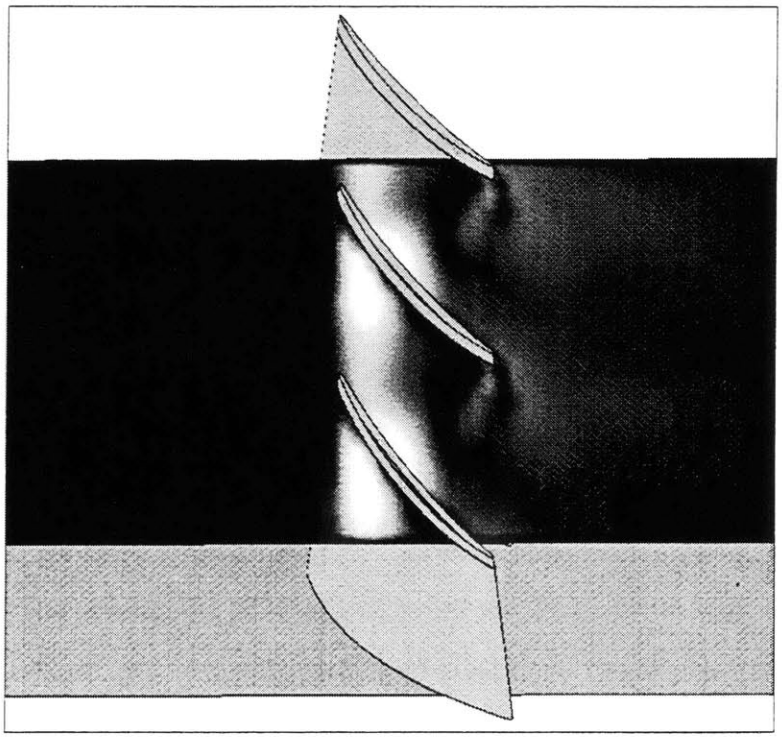

Figure 5.14: Vorticity contour at 6% immersion of the E^3 compressor with 3.0% clearance ($\phi = 0.32$)

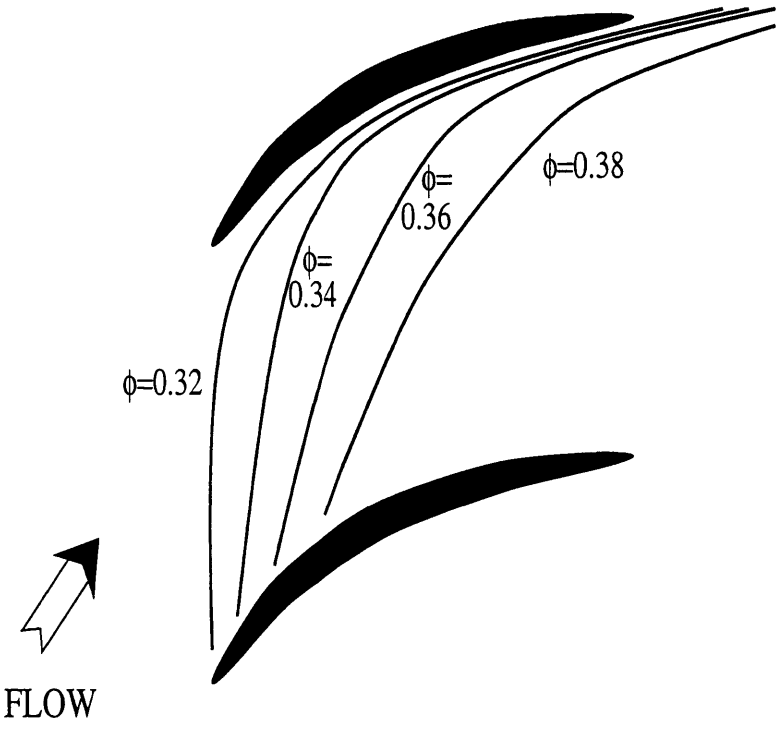

Figure 5.15: Trajectories of the tip clearance vortex for the E^3 rotor with 3.0% tip clearance for different flow coefficients

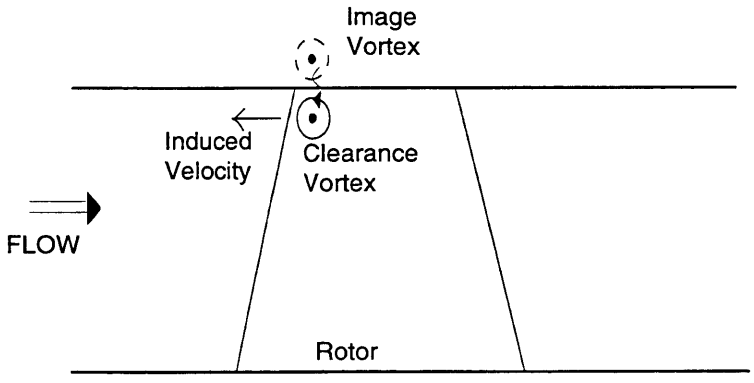

Figure 5.16: Velocity induced by image vortex

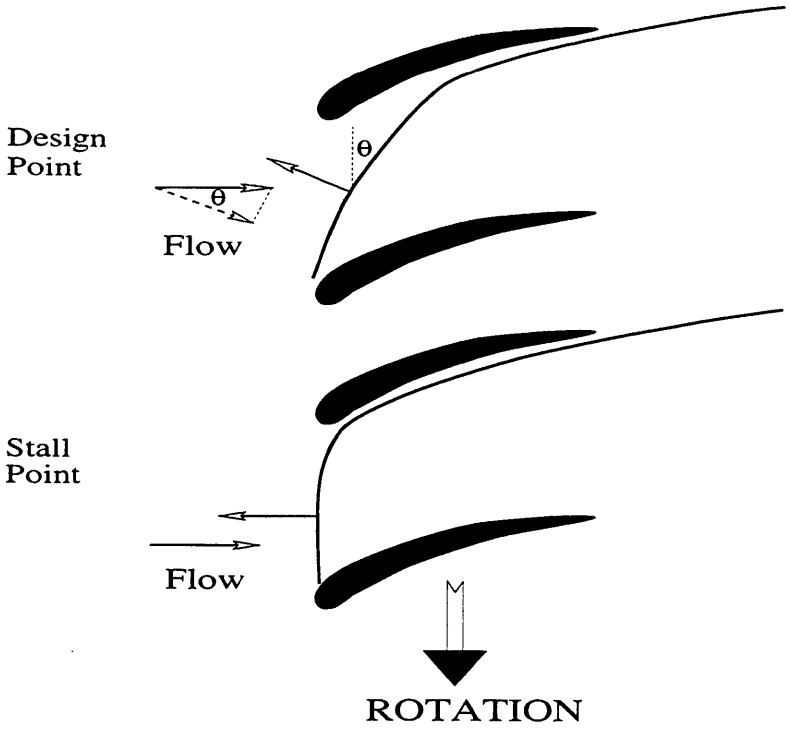

Figure 5.17: Trajectory and induced velocity for the tip clearance vortex at different loading conditions

of the mean flow normal to the vortex. As the compressor is throttled towards stall, the strength of the clearance vortex will increase (due to increased blade loading) and the mean flow velocity will decrease. This will result in the trajectory of the vortex becoming closer to being perpendicular to the mean flow direction. This simplified description of the vortex trajectory assumes that the self induced velocity of the vortex can be described as if the vortex extended to infinity. Because the distance of the vortex from the wall is much less than the span of the vortex ($\sim$ one blade spacing), the self induced velocity can be approximated using only the local strength and orientation of the vortex.

At an operating point such as the design point, the trajectory will be in an equilibrium position such as that shown in Figure 5.17. The stability of this trajectory can be analyzed by considering a displacement of the vortex from this position. If the vortex were moved forward of this equilibrium position, the angle the vortex makes with the perpendicular to the mean flow (θ) would decrease resulting in an increased value of the normal component of the mean flow. When the induced velocity is then

subtracted from this increased normal component of the mean flow, the net velocity of the vortex will be such that it will return towards the equilibrium position. Thus, this position is stable.

For lower flow coefficients the equilibrium trajectory of the vortex becomes increasingly closer to being perpendicular to the mean flow direction. A stable equilibrium position no longer exists when the vortex trajectory becomes perpendicular to the mean flow direction. At this position, the correcting action of an increased normal component of the mean flow is lost. (This point was reached at the peak of the pressure rise characteristic.) When the compressor is throttled past this point, the vortex will possess a sufficient self induced velocity to cause it to propagate forward of the compressor. Once the vortex is able to move out of the blade passage, the circulation of the vortex will remain unchanged (neglecting viscous effects), so the vortex will be able to continue propagating forward of the compressor.

Although the formation of the tip clearance vortex is the result of viscous features of the flow, the subsequent description of the trajectory and motion of this vortex is entirely inviscid. This point should allow the formulation of simple models to describe the occurrence and development of this stalling process.

This description, by itself, does not explain why the flow breaks down into a non-axisymmetric short length-scale stall cell, but a further consideration of the vortex motion can be used. Prior to the development of rotating stall, the tip clearance vortex is connected to the tip of one blade and, after traversing across the blade passage, it is turned into the downstream direction. Because a vortex line cannot end in the fluid, the tip clearance vortex must remain connected to the circulation about a compressor blade and to the downstream trail, as shown in Figure 5.18. Thus, when the vortex begins to propagate forward of the compressor it must do so by bowing forward. The portion of the vortex in the center of the bowed region will remain perpendicular to the flow direction. However, the remainder of the vortex will be turned away from the main flow direction and will therefore have its upstream self induced velocity reduced. This will thus increase the amount which the vortex is bowed. In this way, the shape of an upstream propagating vortex is unstable.

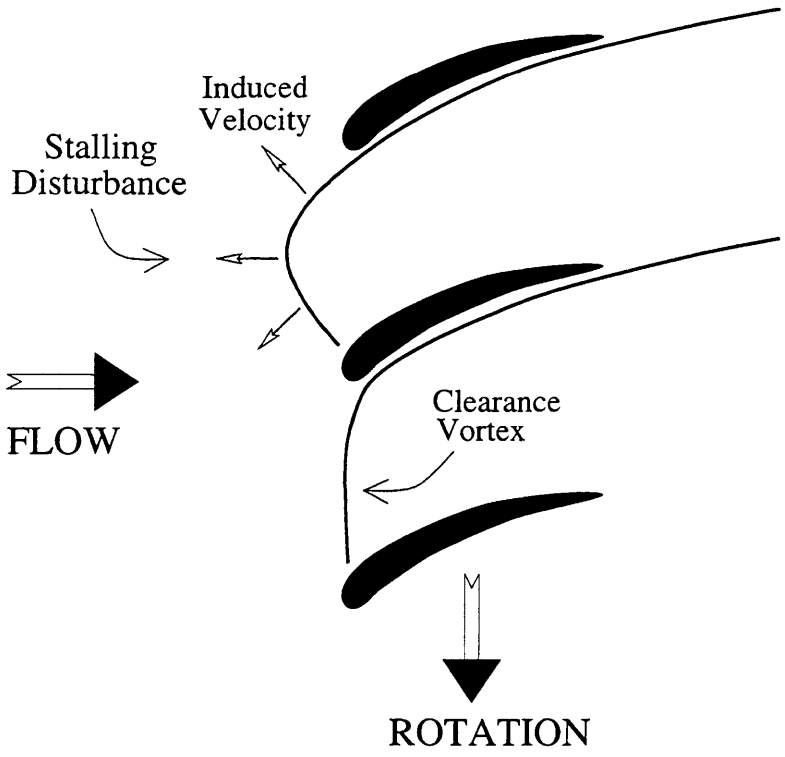

Figure 5.18: Initial shape of clearance vortex motion

Therefore this type of a stall inception will develop into a localized disturbance. In addition, because the initial size of the clearance vortex is one blade pitch long in the circumferential direction, the size of the resulting stall cell will be on the order of the blade spacing; as has been shown in experiment [7] [45].

An interesting consequence of this type of stall inception is that a description of the entire compression system was not required to demonstrate that an unstable flow situation could exist. Of course this process does not take place in isolation, and at some point the influence of the remainder of the compression system will be felt. However, the breakdown of the flow described has been shown to remain local to the tip region of one blade row even though it had reached a considerable magnitude (regions of upstream negative axial velocity). Therefore, this stalling pattern is not likely to be affected by the rest of the compression system during its initial development, and the single blade row results should also apply to the initial development of a short length-scale stall in multi-blade row compressors. For a well matched compressor operating near the peak of its characteristic, such a disturbance has the potential to

induce rotating stall to occur in the entire compressor [45].

5.1.4 Axisymmetric Performance

The development of the short length-scale stall was shown to arise out of a blade passage flow structure with a local inception criteria. Therefore the possibility exists for an axisymmetric flow situation in which the tip clearance vortex also moves forward of the compressor. Unsteady flow calculations of a periodic single blade passage were used to investigate this point. It was found that the once the tip clearance vortex reached the critical position at the leading edge of the blade row, it remained at the same position while the flow coefficient was further reduced. For this to be the case, it is required that the strength of the tip clearance vortex must decrease. A corresponding decrease in the circulation of the blade is also to be expected. This was evidenced by a decrease in the pressure rise of the single blade calculation (see Figure 5.3) for decreases in the flow coefficient past the critical point (peak of the single blade characteristic). Therefore, for the single blade computations, the flow coefficient for which the vortex becomes perpendicular to the mean flow direction would be expected to correspond to the peak of the pressure rise characteristic, which was observed to be the case.

It thus appears that in the axisymmetric case, the forward movement of the tip clearance vortex causes enough of a reduction in the pressure rise of the compressor to allow a sufficient decrease in the strength of the vortex to allow it to remain in the blade passage. This effect was ignored in the previous short length-scale stability argument. However, for stalling disturbances which occupy a small enough region of the compressor, the overall pressure rise should not be substantially decreased. Therefore, the stability criteria presented should be applied only to disturbances which represent a small fraction of the annulus. Because the computation performed here using eight blades was seen to be capable of demonstrating a short length-scale stall, the assumption that compressor performance is relatively unaffected by an initial short length-scale disturbance should be suitable for actual compressors which have an order of magnitude more blades.

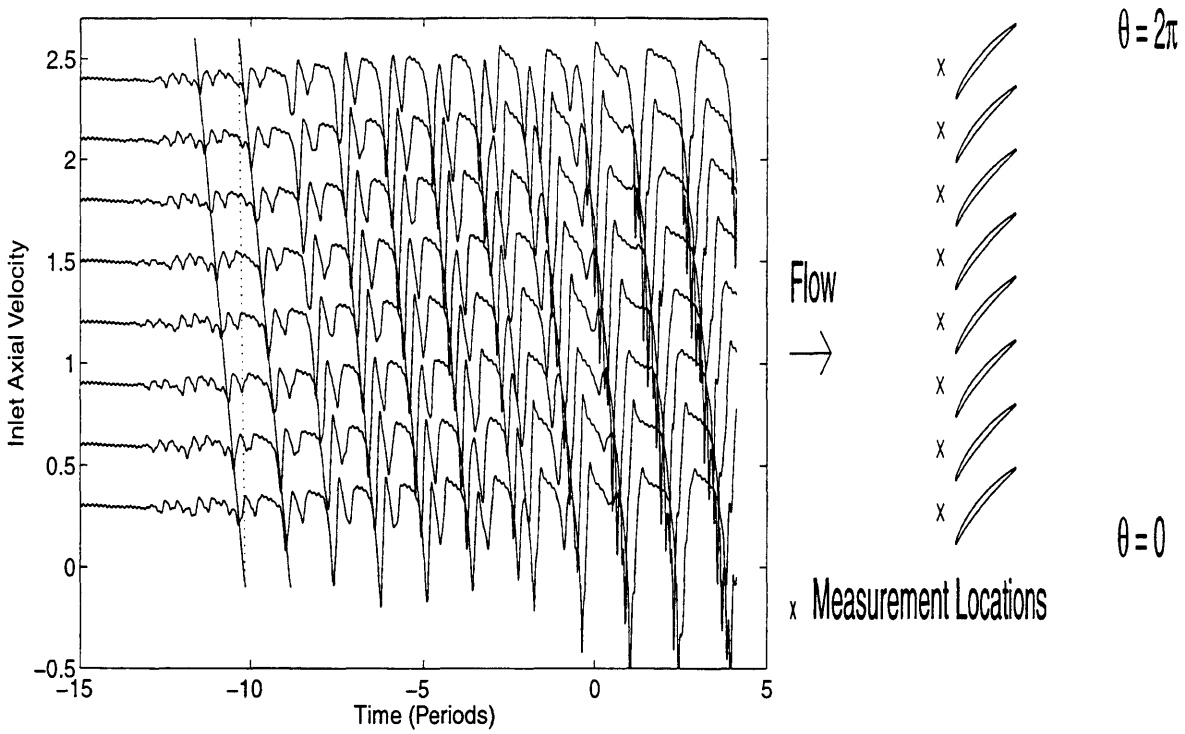

Figure 5.19: Traces of the inlet axial velocity for the E^3 rotor with 1.4% tip clearance during a transient to stall

5.2 Effect of Tip Clearance Size on Stall Inception

Because of the importance of the the tip clearance flow in the development of the short length-scale stalling event, the effect of changes in the tip clearance have been studied. The same compressor geometry was used, but with a tip clearance of 1.4%.

The results were similar to the larger tip clearance case. The stall pattern was one of short length-scale stall cells localized near the tip. Two cells of comparable magnitude coexisted for over 10 periods, but as in the large tip clearance case, eventually only one stall cell remained. A plot of the traces of the inlet axial velocity are given in Figure 5.19. As in the previous case, the initial stalling disturbances have the same shape, size, speed of rotation, and growth rate as seen in the experimental data. Again these short length-scale disturbances were observed to develop when the tip clearance vortex began to propagate forward of the compressor.

For the two different sizes of tip clearance computed, the development of rotating stall occurred in the same manner, and resulted in the same type of stall.

5.3 Summary

The results from the three-dimensional study of rotating stall show the development of a short length-scale rotating stall inception which is fundamentally different from the modal stalling case. For the short length-scale stalling case, the instability was shown to develop directly out of a blade passage flow field structure; namely the tip clearance vortex. In the modal stalling case, a description of the flow structures within the blade passages were unnecessary to describe the development of rotating stall.

These results imply that the resulting stability criteria is local in nature. This is contrary to the idea of a modal stall inception which relies on a description of the entire compression system to predict an instability. The recent experimental results of Camp [4] serve to corroborate this point. In Camp's experiment the axial loading of the compressor was modified by changing the blade angles of the stators and inlet guide vanes. When this was done, the stalling mode of the compressor was seen to change from a modal stall to a short length-scale stall. Further analysis showed that the inception of the short length-scale stall occurred when the first stage rotor incidence reached a critical value. Thus, when a modal stall was encountered, the compressor stability was found to be well predicted by the modal model used by Camp, while the inception of a short length-scale stall was predicted by a critical incidence at one location within the compressor.

The conclusion of this study is that a second stall inception criteria has been identified for axial compressors. Because this criteria has been shown to be local in nature, single blade passage calculations can be used to predict the conditions at which a short length-scale disturbance may occur; rather than computing the entire annulus. This represents an order of magnitude reduction in the computational requirements needed to predict the onset of a short length-scale disturbance.

Chapter 6

Conclusions

6.1 Conclusions from the Three-Dimensional Study of Rotating Stall

Three-dimensional computations showed rotating stall inception of the short length-scale type. An analysis of the flow structures within the blade passages showed that the tip clearance flow structure was fundamental to the development of the short length-scale stall. A new description based on vortex kinematics has been used to describe the evolution of this stalling process. The specific conclusions are:

- The formation of this type of stall inception is a result of the tip clearance vortex moving forward of the compressor blade row. It was shown that once the vortex began to move forward of the blade row it would continue to do so.

- The resulting criteria (trajectory of the tip clearance vortex perpendicular to the mean flow direction) for the development of non-axisymmetric flow is local in nature. This is fundamentally different than the modal case where the entire flow field must be considered in order to analyze its stability.

- The process by which the short length-scale disturbance develops is general to axial compressors with tip-critical flow fields. Because of its local nature, in any compressor which experiences a spilling forward of the tip clearance vortex, a

similar breakdown of the compressor flow field is to be expected.

- The use of a computational method to study rotating stall provided a level of detail, not possible in experiments, which has allowed a description of the inception of a short length-scale rotating stall inception.

- Because the inception criteria is local in nature, full annulus computations are not required to predict the flow conditions at which a short length-scale stall may occur.

6.2 Conclusions from the Two-Dimensional Study of Rotating Stall

The general conclusion from the two-dimensional study of rotating stall inception is that the modal rotating stall inception process is well described by existing stability models. The basic modeling assumptions of the stability models have been verified and calibrated. Although this is not the first study to conclude that the current compressor stability models are capable of predicting a modal rotating stall inception, the criteria used in past studies to verify the models is that the output (eigenvalues) agreed with the experimental evidence. In this study, the details of each of the major flow field assumptions which make up these stability models have been tested and verified directly. Specific conclusions are:

- The two-dimensional development of modal rotating stall has been shown to be the result of the growth of a linearly unstable eigenmode of the compression system. Through the use of a compressor stability model, the key aspects of the compressor flow field which contribute to the development of a modal stall were shown to be a description of the losses and turning functions through the blade row. This description does not require the details of the loss and turning mechanisms. Hence, this result applies to the general class of compressors used in axial turbomachinery including three-dimensional geometries.

- The unsteady performance of a compressor blade row can be reasonably well described by using a first order lag equation. By fitting the results of a first order lag equation to the numerical results, a time constant of 1.0 flow through times was found for the turning and 0.45 flow through times for the losses. These parameters were shown to be unaffected by the length scale of the stalling disturbance.

- The assumptions of the simple flow field model for the compressor ducts were found to be well verified for the inlet, but not for the exit. However, the eigenvalues obtained from the linearized model were found to be insensitive to this modeling error.

- The resulting linearized stability model was able to accurately predict the absolute stability of the compressor, the relative stability of the various modes, and the rotational speed of the modes for both a single and multi-blade row compressor.

6.3 Recommendations for Future Research

For the short length-scale stall inception questions remain to be answered. Recommendations for future research are as follows.

- Obtain experimental verification of the presence of forward propagation of the tip clearance vortex during the development of a short length-scale stall inception.

- Develop a simple fluid dynamic model to describe the growth and development of the short length-scale stalling disturbance in order to investigate the (nonlinear) effect that this type of disturbance will have on the stability of the entire compression system.

Ultimately the goal of this enhanced understanding of the short length-scale stall inception is the ability to create a compressor with an improved stability character.

Therefore, in conjunction with a more detailed study of this event, efforts should be made to find ways to manage this flow situation.

Bibliography

[1] Adamczyk, J. J., M. L. Celestina, T. A. Beach, and M. Barnett. "Simulation of Three-Dimensional Viscous Flow within a Multistage Turbine." *Journal of Turbomachinery.* Vol. 112. 1989. 370-376.

[2] Anderson, D. A., J. C. Tannehill, and R. H. Pletcher. *Computational Fluid Mechanics and Heat Transfer.* Hemisphere Publishing Corporation. New York. 1984.

[3] Baldwin, B. S. and H. Lomax. "Thin Layer Approximation and Algebraic Model for Separated Turbulent Flows." AIAA Paper 78-257. Huntsville, Alabama. 1978.

[4] Camp T. R. *Aspects of the Off-Design Performance of Axial Flow Compressors.* PhD Thesis, University of Cambridge. July 1995.

[5] Chieng, C. C. and B. E. Launder. "On the Calculation of Turbulent Heat Transport Downstream from an Abrupt Pipe Expansion." *Numerical Heat Transfer.* Vol. 3. 1980. 189-207.

[6] Davis, R. L., D. E. Hobbs, and H. D. Weingold. "Prediction of Compressor Cascade Performance Using a Navier-Stokes Technique." *Journal of Turbomachinery.* Vol. 110. October 1988. 520-531.

[7] Day, I. J. "Stall Inception in Axial Flow Compressors." *Journal of Turbomachinery.* Vol. 115. January 1993. 1-9.

[8] Dunham, J. "Non-Axisymmetric Flows in Axial Compressors." *Mechanical Engineering Science.* Monograph No. 3. October 1965. 1-31.

[9] Emmons, H. W., C. E. Pearson, and H. P. Grant. "Compressor Surge and Stall Propagation." *Transactions of the ASME.* Vol. 79. April 1955. 455-469.

[10] Epstein, A. H., J. E. Ffowcs Williams, and E. M. Greitzer. "Active Suppression of Aerodynamic Instabilities in Turbomachines." *Journal of Propulsion and Power.* Vol. 5. March 1989. 204-211.

[11] Fullner, M. *Modeling and Control of Rotating Stall in High Speed Multi-Stage Axial Compressors.* PhD Thesis, Massachusetts Institute of Technology. May 1994.

[12] Garnier, V. H, A. H. Epstein, E. M. Greitzer. "Rotating Waves as a Stall Inception Indication in Axial Compressors." *Journal of Turbomachinery.* Vol. 113 No. 2. April 1991. 290-302.

[13] Giles, M. B. *Non-Reflecting Boundary Conditions for the Euler Equations.* CFDL-TR-88-1. Computational Fluid Dynamics Laboratory, Massachusetts Institute of Technology. February 1988.

[14] Giles, M. B. "Nonreflecting Boundary Conditions for Euler Equation Calculations." *AIAA Journal.* Vol. 28. 1990. 2050-2058.

[15] Giles, M. B. *UNSFLO: A Numerical Method for the Calculation of Unsteady Flow in Turbomachinery.* GTL Report No. 205. Gas Turbine Laboratory, Massachusetts Institute of Technology. May 1991.

[16] Greitzer E. M. "The Stability of Pumping Systems - The 1980 Freeman Scholar Lecture." *Journal of Fluids Engineering.* Vol. 103. June 1981. 193-242.

[17] Halstead, D. E., D. C. Wisler, T. O. Okishi, G. J. Walker, H. P. Hodson, and H. Shin. "Boundary Layer Development in Axial Compressors and Turbines, Parts 1-4." ASME Paper 95-GT-462. Houston, Texas. June 1995.

[18] Haynes, J. M. *Active Control of Rotating Stall in a Three-Stage Axial Compressor.* GTL Report No. 218. Gas Turbine Laboratory, Massachusetts Institute of Technology. June 1993.

[19] Haynes, J. M., G. J. Hendricks, and A. H. Epstein. "Active Stabilization of Rotating Stall in a Three-Stage Axial Compressor." *Journal of Turbomachinery.* Vol. 116. April 1994. 226-239.

[20] He, L. "Computational Study of Rotating Stall Inception in Axial Compressors." *Journal of Propulsion and Power.* Publication Pending.

[21] Hindman, R. G. "Geometrically Induced Errors and Their Relationship to the Form of the Governing Equations and the Treatment of Generalized Mappings." AIAA Paper 81-1008. Palo Alto, California. 1981.

[22] Hobbs, D. E. and H. D. Weingold. "Development of Controlled Diffusion Airfoils for Multistage Compressor Application." *Journal of Engineering for Gas Turbines and Power.* Vol. 106. April 1984. 271-278.

[23] Holmes, D. G. and S. D. Connell. "Solution of the 2-D Navier-Stokes Equations on Unstructured Adaptive Grids." AIAA Paper 89-1932. Presented at the 9th AIAA Computational Fluid Dynamics Conference, Buffalo, NY. June 1989.

[24] Hoying, D. A. "Stall Inception in a Multistage High-Speed Axial Compressor." *Journal of Propulsion and Power.* Vol. 11, No. 5. September 1995. 915-922.

[25] Hynes, T. P. and E. M. Greitzer. "A Method for Assessing Effects of Circumferential Flow Distortion on Compressor Stability." *Journal of Turbomachinery.* Vol. 109. July 1987. 371-379.

[26] Jackson, A. D. *Stall Inception in Axial Compressor.* M. Sc. Thesis, Cambridge University. 1985.

[27] Khalid, S. A. *The Effects of Tip Clearance on Axial Compressor Pressure Rise.* PhD Thesis, Massachusetts Institute of Technology. February 1995.

[28] Koch, C. C. "Stalling Pressure Rise Capability of Axial Flow Compressor Stages." *ASME Journal of Engineering for Power.* Vol. 103. 1981. 645-656.

[29] Launder, B. E. and D. B. Spalding. "The Numerical Computation of Turbulent Flows." *Computer Methods in Applied Mechanics and Engineering.* Vol. 3. 1974. 269-289.

[30] Lee, Y. T., C. Hah, and J. Loellbach. "Flow Analyses in a Single-Stage Propulsion Pump." ASME 94-GT-139. Presented at the International Gas Turbine and Aeroengine Congress and Exposition, The Hague, Netherlands. June 1994.

[31] Lighthill, M. J. "On Displacement Thickness." *Journal of Fluid Mechanics.* Vol. 4. 1958. 383.

[32] Longley, J. P. "A Review of Nonsteady Flow Models for Compressor Stability." *Transactions of the ASME, Journal of Turbomachinery.* Vol. 116. April 1994. 202-215.

[33] MacCormack, R. W. *Numerical Computation of Compressible Viscous Flow.* Course Notes. Stanford University. 1991.

[34] Marble, F. E. Personal Communication. May 1, 1996.

[35] McDougall, N. M. *Stall Inception in Axial Compressors.* PhD Thesis, Queens' College, University of Cambridge. March 1988.

[36] McDougall, N. M., N. A. Cumpsty, and T. P. Hynes. "Stall Inception in Axial Compressors." *Transactions of the ASME.* Vol. 112. January 1990. 116-125.

[37] Moore, F. K. "Theory of Rotating Stall of Multistage Axial Compressors: Part I - Small Disturbances." *Journal of Engineering for Gas Turbines and Power.* Vol. 106. April 1984. 313-320.

[38] Moore, F. K. "A Theory of Rotating Stall of Multistage Axial Compressors: Part II - Finite Disturbances." *Journal of Engineering for Gas Turbines and Power.* Vol. 106. April 1984. 321-326.

[39] Moore, F. K. "A Theory of Rotating Stall of Multistage Axial Compressors: Part III - Limit Cycles." *Journal of Engineering for Gas Turbines and Power.* Vol. 106. April 1984. 327-336.

[40] Moore, F. K. and E. M. Greitzer. "A Theory of Post-Stall Transients in Axial Compression Systems: Part I - Development of Equations." *Journal of Engineering for Gas Turbines and Power.* Vol. 108. January 1986. 68-76.

[41] Moore, F. K. and E. M. Greitzer. "A Theory of Post-Stall Transients in Axial Compression Systems: Part II - Application." *Journal of Engineering for Gas Turbines and Power.* Vol. 108. April 1986. 231-239.

[42] Nagano, S., Y. Machida, and H. Takata. "Dynamic Performance of Stalled Blade Rows." Japan Society of Mech. Eng. Paper #JSME 11. Presented at Tokyo Joint International Gas Turbine Conference, Tokyo, Japan. October 1971.

[43] Nishizawa, T. and H. Takata. "Numerical Study on Rotating Stall in Finite Pitch Cascades." ASME Paper. Presented at Proceedings of the International Gas Turbine and Aeroengine Congress and Exposition, The Hague, Netherlands. June 1994.

[44] Park, H. G. *Unsteady Disturbance Structures in Axial Flow Compressor Stall Inception.* Master's Thesis, Massachusetts Institute of Technology. May 1994.

[45] Silkowski, P. D. *Measurements of Rotor Stalling in a Matched and a Mismatched Multistage Compressor.* GTL Report No. 221. Gas Turbine Laboratory, Massachusetts Institute of Technology. April 1995.

[46] Sovran, G. "The Measured and Visualized Behavior of Rotating Stall in an Axial-Flow Compressor and in a Two-Dimensional Cascade." *Journal of Engineering for Power.* Vol. 81. January 1959. 24-34.

[47] Steger, J. L. and R. L. Sorenson. "Automatic Mesh-Point Clustering Near a Boundary in Grid Generation with Elliptic Partial Differential Equations." *Journal of Computational Physics.* Vol. 33. 1979. 405-410.

[48] Stenning, A. H. and A. R. Kriebel. "Stall Propagation in a Cascade of Airfoils." *Transactions of the ASME.* Vol. 80. May 1958. 777-790.

[49] Storer, J. A. and N. A. Cumpsty. "Tip Leakage Flows in Axial Compressors." *Transactions of the ASME.* Vol. 113. 1991. 252-259.

[50] Tam, C. K. W. and J. C. Webb. "Dispersion-Relation-Preserving Finite Difference Schemes for Computational Acoustics." *Journal of Computational Physics.* Vol 107. 1993. 262-281.

[51] Tam, C. K. W., J. C. Webb, and Z. Dong. "A study of the short wave components in computational acoustics." *Journal of Computational Acoustics.* Vol. 1. 1993. 1-30.

[52] Thomas, P. D. and C. K. Lombard. "The Geometric Conservation Law - A Link Between Finite-Difference and Finite-Volume Methods of Flow Computation on Moving Grids." AIAA Paper 78-1208. AIAA 11th Fluid and Plasma Dynamics Conference, Seattle, Washington. July 10-12, 1978.

[53] Tryfonidis, M., O. Etchevers, J. D. Paduano, G. F. Hendricks, and A. H. Epstein. "Pre-Stall Behavior of Several High-Speed Compressors." *Journal of Turbomachinery.* Vol. 117. January 1995. 62-80.

[54] White, F. M. *Viscous Fluid Flow.* McGraw-Hill Book Company. New York. 1974.

[55] Wisler, D. C. *Core Compressor Exit Stage Study, Volume IV - Data and Performance Report for the Best Stage Configuration.* NASA CR-165357. NASA Lewis Research Center. April 1981.

Appendix A

Two-Dimensional Linear Stability Model

A simple linear model can be constructed to provide an estimate of the frequency of rotating stall and the operating point at which stall occurs.

The linear stability model looks for possible solutions to the governing equations and provides their nature in both time and space. The starting point for the model is an equilibrium background flow solution for the problem of interest. Then, allowable small amplitude wave-like perturbational solutions to the background flow will be sought. In this case, the background flow solution will be uniform flow in a two-dimensional duct both upstream and downstream of the compressor. A general perturbational solution will be derived, and then the boundary conditions will be implemented in order to yield the final form of the solution.

The development of the linear stability model begins with the linearized non-dimensional form of the two-dimensional incompressible Euler equations (and continuity).

$$\begin{aligned} \frac{\partial u'}{\partial x} + \frac{\partial v'}{\partial y} &= 0 \\ \frac{\partial u'}{\partial t} + \overline{u}\frac{\partial u'}{\partial x} + \overline{v}\frac{\partial u'}{\partial y} &= -\frac{\partial p'}{\partial x} \\ \frac{\partial v'}{\partial t} + \overline{u}\frac{\partial v'}{\partial x} + \overline{v}\frac{\partial v'}{\partial y} &= -\frac{\partial p'}{\partial y} \end{aligned} \tag{A.1}$$

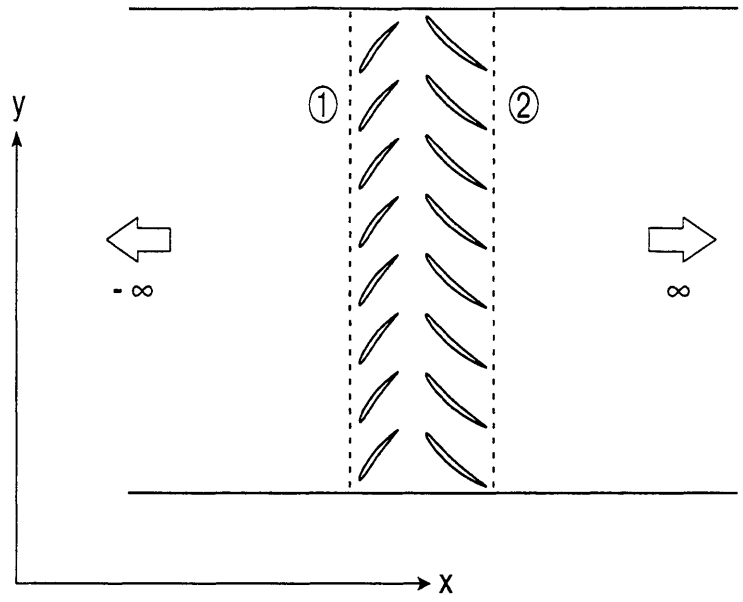

Figure A.1: Diagram of compressor coordinates for the linear model

Where the primed quantities represent perturbations from an equilibrium background flow, and the over-barred quantities represent the magnitude of the equilibrium flow such that $u = \overline{u} + u'$. The main axial flow direction corresponds to the x direction, and the tangential flow direction is given by y. The coordinate directions and the numbering scheme for the upstream and downstream regions is shown in Figure A.1. In a real compressor, the second direction would be the circumferential coordinate (ie. θ), but for the simple two-dimensional case the equations can be expressed in cartesian coordinates with no loss in generality. These equations are non-dimensionalized by the rotor speed and the radius of the compressor.

In order to represent the wave-like solutions of Equation A.1, a periodic solution in y of the following form is assumed.

$$\begin{pmatrix} u' \\ v' \\ p' \end{pmatrix} = \begin{pmatrix} \tilde{u} \\ \tilde{v} \\ \tilde{p} \end{pmatrix} e^{\imath kx + \imath ny + \omega t}, \quad n = 1 \ldots \infty \tag{A.2}$$

Where the quantities with a tilde are unknown constants which are required to yield a solution. In order for $n = 1$ to correspond to the first complete mode, the coordinates have been non-dimensionalized so that $0 \leq y \leq 2\pi$.

In general, a choice of $\tilde{u}$, $\tilde{v}$, and $\tilde{p}$ does not represent a solution to the Euler equations. By substituting the assumed solution A.2 into the Euler equations A.1, the following result is obtained.

$$\begin{bmatrix} \imath k & \imath n & 0 \\ \omega + \overline{u}\imath k + \overline{v}\imath n & 0 & \imath k \\ 0 & \omega + \overline{u}\imath k + \overline{v}\imath n & \imath n \end{bmatrix} \begin{pmatrix} \tilde{u} \\ \tilde{v} \\ \tilde{p} \end{pmatrix} = \begin{pmatrix} 0 \\ 0 \\ 0 \end{pmatrix} \tag{A.3}$$

In order for a non-trivial solution to exist, the determinant of this matrix must be zero. Using this fact, the relation between k, n, and ω can be determined. When solved for k, three such solutions exist.

$$k_1 = -\imath n\,, \quad k_2 = \imath n\,, \quad k_3 = \frac{\omega}{\overline{u}}\imath - \frac{\overline{v}}{\overline{u}}n \tag{A.4}$$

Using these values for k, the form of the solutions for $\tilde{u}, \tilde{v}$, and $\tilde{p}$ can be found as multiples of the three right eigenvectors of the matrix given in Equation A.3. The right eigenvectors are as follows.

$$\vec{x}_1 = \begin{pmatrix} 1 \\ \imath \\ -\frac{\omega}{n} - \overline{u} - \overline{v}\imath \end{pmatrix}, \quad \vec{x}_2 = \begin{pmatrix} 1 \\ -\imath \\ \frac{\omega}{n} - \overline{u} + \overline{v}\imath \end{pmatrix}, \quad \vec{x}_3 = \begin{pmatrix} 1 \\ \frac{\overline{v}}{\overline{u}} - \frac{\omega}{\overline{u}n}\imath \\ 0 \end{pmatrix} \tag{A.5}$$

Combining the eigenvectors with their associated eigenvalues, the complete form of the linearized solution can be found.

$$\begin{pmatrix} u' \\ v' \\ p' \end{pmatrix} = C_1\vec{x}_1 e^{nx+\imath ny+\omega t} + C_2\vec{x}_2 e^{-nx+\imath ny+\omega t} + C_3\vec{x}_3 e^{-\frac{\omega}{\overline{u}}x - \frac{\overline{v}}{\overline{u}}n\imath x + \imath ny + \omega t} \tag{A.6}$$

What remains is to solve for the unknown coefficients (C_1, C_2, C_3) for given values of n and ω. However, to find the linear limit of stability, actual values for these constants are not required. What is required is that the constants not all be zero. This requirement will yield a relation for ω in terms of n and other flow quantities. The real part of ω will thus determine whether the solution is growing (unstable) or decaying (stable) with time.

In a compressor, the solution given in Equation A.6 is appropriate in both the upstream and downstream flow regions. Initially this gives six unknown coefficients. A consideration of the structure of the eigenvectors is helpful in eliminating some of these constants. An examination of the eigenvectors shows that the first two eigenvectors correspond to the two potential modes of the Euler equations, and the third corresponds to the vortical mode. For this problem the flow field can be specified to have no vorticity far upstream. Since vortical information can only propagate in the (assumed positive) flow direction, no vorticity will be present in the entire upstream region. Therefore, for this case, it is appropriate to set $C_3 = 0$ in the upstream region. The remaining two eigenvectors correspond to the potential (pressure) modes of the system. Potential perturbations which grow with distance from the compressor are inappropriate since the compressor is the only source of wave energy being considered in this analysis. Therefore, only pressure modes which decay with distance from the compressor will be considered. This removes one of the first two eigenvectors from the solution in both the upstream and downstream regions of the flow field. The resulting analysis leaves one non-zero mode present in the upstream region, and two in the downstream region.

Using this reduction in unknowns, the quantities to be solved for can be written as

$$\begin{pmatrix} u_1' \\ v_1' \\ p_1' \end{pmatrix} = A \begin{pmatrix} 1 \\ \imath \\ -\frac{\omega}{n} - \overline{u} - \overline{v}\imath \end{pmatrix} e^{nx+\imath ny+\omega t} \tag{A.7}$$

for the upstream quantities, and

$$\begin{pmatrix} u_2' \\ v_2' \\ p_2' \end{pmatrix} = B \begin{pmatrix} 1 \\ -\imath \\ \frac{\omega}{n} - \overline{u} + \overline{v}\imath \end{pmatrix} e^{-n x + \imath n y + \omega t} + C \begin{pmatrix} 1 \\ \frac{\overline{v}}{\overline{u}} - \frac{\omega}{\overline{u}n}\imath \\ 0 \end{pmatrix} e^{-\frac{\omega}{\overline{u}}x - \frac{\overline{v}}{\overline{u}}n x\imath + \imath n y + \omega t} \quad \text{(A.8)}$$

for the downstream quantities.

Three conditions are still required to solve for the remaining unknowns. The consideration of mass, momentum, and tangential velocity across the compressor will form the remaining relations.

Mass conservation will provide the first constraint. Owing to the presence of the compressor blades, flow may not redistribute in the tangential direction as it passes through the compressor. Therefore, the statement of continuity reduces to the following.

$$u_1' = u_2' \quad \text{(A.9)}$$

In this case the subscript 1 refers to the inlet of the compressor, and 2 refers to the exit as shown in Figure A.1.

The momentum equation is used to form the next matching condition. By integrating along the flow direction through the blade passage and using continuity to remove the convective term the following form of the Euler equation is found.

$$\frac{\partial u}{\partial t} = -\frac{p_2 - p_1}{l_{\text{effective}}} + \psi \quad \text{(A.10)}$$

Since u is conserved by continuity, it remains constant during the integration. The variable ψ represents the static-to-static pressure rise through the blade row. The use of an effective length $\left(l_{\text{effective}}\right)$ accounts for the total blade passage channel length and the fact that the inlet and exit planes on which the pressure acts are not necessarily perpendicular to the blade passage channel. A reasonable estimate of this

quantity is given by Hynes and Greitzer [25] as

$$l_{\text{effective}} = \frac{b}{\cos^2 \gamma} \tag{A.11}$$

where b is the axial chord length, and γ is the stagger angle of the blade row.

As written, Equation A.10 is valid only for a stator blade row. Due to the motion of the rotor, the change in u with respect to time seen by the rotor is the sum of the change with respect to time in the absolute system plus the convective change due to the rotor motion. Thus the momentum equation for a rotor becomes.

$$\frac{\partial u}{\partial t} + U\frac{\partial u}{\partial y} = -\frac{p_2 - p_1}{l_{\text{effective}}} + \psi \tag{A.12}$$

With U being the rotor speed (typically equal to one in non-dimensional variables). In general, the momentum equation can be written in a simple form for the entire compressor.

$$\mu\frac{\partial u}{\partial t} + \lambda U\frac{\partial u}{\partial y} = -p_2 + p_1 + \psi \tag{A.13}$$

$$\mu = \sum_{\text{all blade rows}} l_{\text{effective}}$$

$$\lambda = \sum_{\text{rotors}} l_{\text{effective}}$$

Prior experience has shown that the use of a total-to-static pressure rise coefficient is more convenient than the static-to-static one. The use of the total-to-static coefficient (Ψ) requires that the inlet dynamic head be added to the relation.

$$\mu\frac{\partial u}{\partial t} + \lambda U\frac{\partial u}{\partial y} = -p_2 + p_1 + \Psi + 1/2\left(u_1^2 + v_1^2\right) \tag{A.14}$$

This equation is complete except for the step of writing it in perturbational form. For this analysis, the pressure rise coefficient is assumed to be a function of u_1 and v_1. The final form of the momentum matching condition becomes,

$$\mu\omega u_1' + \lambda\imath n u_1' = p_1' - p_2' + \Psi_u u_1' + \Psi_v v_1' + \overline{u}_1 u_1' + \overline{v}_1 v_1' \tag{A.15}$$

where Ψ_u and Ψ_v represent the derivatives of Ψ with respect to u_1 and v_1 respectively.

The third matching condition requires some information regarding the tangential velocity. An empirical relation is generally used. The simplest of which is to specify a constant leaving angle for the compressor exit. This is a reasonable constraint for compressors with relatively high solidity blading. A first order correction can be made by assuming that the outlet flow angle is a function of the inlet velocity. For compressors with a stator as the last blade row the relation is.

$$v_2' = \frac{\overline{v}_2}{\overline{u}_2} u_2' + \frac{\partial \left(v_2/u_2 \right)}{\partial u_1} \overline{u}_2 u_1' \tag{A.16}$$

To find the final form of the solution A.7 and A.8 are substituted into the matching conditions A.9, A.15, A.16. This will yield a system of equations in the unknowns A, B, and C in the following form.

$$\begin{bmatrix} x_{11} & x_{12} & x_{13} \\ x_{21} & x_{22} & x_{23} \\ x_{31} & x_{32} & x_{33} \end{bmatrix} \begin{pmatrix} A \\ B \\ C \end{pmatrix} = \begin{pmatrix} 0 \\ 0 \\ 0 \end{pmatrix} \tag{A.17}$$

This has a non-trivial solution only if the matrix has a determinant equal to zero. The method shown tends to contain more algebraic steps than those presented in other references such as Hynes and Greitzer [25], but the result is the same. For more complicated matching conditions this general method is probably better suited.

By making one additional assumption, the system of equations results in a simple analytic result. This is obtained by specifying that the exit angle from the compressor will be zero ($\frac{\partial(v_2/u_2)}{\partial u_1} = 0$ and $\overline{v}_2 = 0$). Continuity will prescribe that $\overline{u}_2 = \overline{u}_1$. For this case, two mathematical solutions exist. The first eigenvalue,

$$\frac{\omega}{n} = \overline{u}_2 - \imath \overline{v}_2 \tag{A.18}$$

results in a solution for which the second eigenvector becomes degenerate. As a result, the only possible solution is one in which A, B, and C are all zero.

The only physically valid solution results from the second root to the characteristic equation.

$$\frac{\omega}{n} = \frac{\Psi_u + \imath\,(\Psi_v - \lambda n)}{2 + \mu n} \tag{A.19}$$

Clearly, the real part of ω becomes positive (unstable) when the slope of the total-to-static compressor characteristic becomes positive. (Hence the choice of total-to-static pressure rise characteristic.) The imaginary part of ω provides the speed at which the disturbance will rotate. This speed is a function of the wave number, effective compressor lengths (inertias), and the inlet swirl sensitivity (Ψ_v).

Appendix B

Development of Three-Dimensional Navier-Stokes Equations in Cylindrical Coordinates with Rotation

To solve for three-dimensional flows in turbomachines, it becomes convenient to write the equations of motion in cylindrical coordinates. This allows substantial simplification of the geometrical description of the compressor in the grid coordinate system. Fortunately, the general form of the equations is unchanged from the cartesian form of the Navier-Stokes equations with the exception of source terms. This allows the same numerical method to be used for either a cartesian or cylindrical system.

B.1 Generalized Curvilinear Coordinates

The derivation begins by expressing the equations of motion in vector notation. Then, using generalized curvilinear coordinates, the equations can be written in any curvilinear coordinate system by replacing the vector notation with the appropriate form of the derivative. This method is outlined in Anderson, Tannehill, and Pletcher [2].

Using generalized curvilinear coordinates, the following operators take the form.

$$\nabla\phi = \frac{1}{h_1}\frac{\partial\phi}{\partial x_1}\hat{i_1} + \frac{1}{h_2}\frac{\partial\phi}{\partial x_2}\hat{i_2} + \frac{1}{h_3}\frac{\partial\phi}{\partial x_3}\hat{i_3} \tag{B.1}$$

$$\nabla\cdot\vec{A} = \frac{1}{h_1h_2h_3}\left[\frac{\partial h_2h_3A_1}{\partial x_1} + \frac{\partial h_3h_1A_2}{\partial x_2} + \frac{\partial h_1h_2A_3}{\partial x_3}\right] \tag{B.2}$$

$$\nabla\times\vec{A} = \frac{1}{h_1h_2h_3}\begin{bmatrix} h_1\left(\frac{\partial h_3A_3}{\partial x_2} - \frac{\partial h_2A_2}{\partial x_3}\right)\hat{i_1} \\ h_2\left(\frac{\partial h_1A_1}{\partial x_3} - \frac{\partial h_3A_3}{\partial x_1}\right)\hat{i_2} \\ h_3\left(\frac{\partial h_2A_2}{\partial x_1} - \frac{\partial h_1A_1}{\partial x_2}\right)\hat{i_3} \end{bmatrix} \tag{B.3}$$

$$\nabla^2\phi = \frac{1}{h_1h_2h_3}\left[\frac{\partial}{x_1}\left(\frac{h_2h_3}{h_1}\frac{\partial\phi}{\partial x_1}\right) + \frac{\partial}{x_2}\left(\frac{h_3h_1}{h_2}\frac{\partial\phi}{\partial x_2}\right) + \frac{\partial}{x_3}\left(\frac{h_1h_2}{h_3}\frac{\partial\phi}{\partial x_3}\right)\right] \tag{B.4}$$

For a cylindrical coordinate system, the metric terms take the following values.

$$\begin{aligned} x_1 = x \quad x_2 = \theta \quad x_3 = r \\ h_1 = 1 \quad h_2 = r \quad h_3 = 1 \\ \hat{i}_1 = \hat{x} \quad \hat{i}_2 = \hat{\theta} \quad \hat{i}_3 = \hat{r} \end{aligned} \tag{B.5}$$

Thus, the velocity vector becomes.

$$\vec{V} = u_x\hat{x} + u_\theta\hat{\theta} + u_r\hat{r} \tag{B.6}$$

Substitution of these operators into the vector forms of the equations will yield the cylindrical forms.

B.2 Continuity Equation

The continuity equation possesses the following general form [2].

$$\frac{\partial\rho}{\partial t} + \vec{V}\cdot\nabla\rho + \rho\left(\nabla\cdot\vec{V}\right) = 0 \tag{B.7}$$

Substituting in the above forms of the vector derivatives yields.

$$\frac{\partial \rho}{\partial t} + u_x \frac{\partial \rho}{\partial x} + \frac{u_\theta}{r}\frac{\partial \rho}{\partial \theta} + u_r \frac{\partial \rho}{\partial r} + \frac{\rho}{r}\frac{\partial r u_x}{\partial x} + \frac{\rho}{r}\frac{\partial u_\theta}{\partial \theta} + \frac{\rho}{r}\frac{\partial r u_r}{\partial r} = 0 \tag{B.8}$$

After combining partial derivative terms, a simplified (conservative) form is obtained.

$$\frac{\partial \rho}{\partial t} + \frac{\partial \rho u_x}{\partial x} + \frac{1}{r}\frac{\partial \rho u_\theta}{\partial \theta} + \frac{1}{r}\frac{\partial r \rho u_r}{\partial r} = 0 \tag{B.9}$$

B.3 Momentum Equation

In general vector notation, the momentum equation can be written as [2],

$$\rho\left(\frac{\partial \vec{V}}{\partial t} + \vec{V}\cdot\nabla\vec{V}\right) = \nabla\cdot\Pi_{ij} \tag{B.10}$$

where Π_{ij} is the generalized stress tensor (including pressure). For a constant viscosity fluid, this tensor takes the following form,

$$\Pi_{ij} = -p\delta_{ij} + \mu\left[\left(\frac{\partial u_i}{\partial x_j} + \frac{\partial u_j}{\partial x_i}\right) - \frac{2}{3}\delta_{ij}\frac{\partial u_k}{\partial x_k}\right] \tag{B.11}$$

and is clearly symmetric. The term δ_{ij} refers to the Kroniker delta. Expanding the terms of the momentum equation in cylindrical coordinates yields.

$$\begin{aligned}
\vec{V}\cdot\nabla\vec{V} &= \left(u_x\frac{\partial u_x}{\partial x} + \frac{u_\theta}{r}\frac{\partial u_x}{\partial \theta} + u_r\frac{\partial u_x}{\partial r}\right)\hat{x} \\
&+ \left(u_x\frac{\partial u_\theta}{\partial x} + \frac{u_\theta}{r}\frac{\partial u_\theta}{\partial \theta} + u_r\frac{\partial u_\theta}{\partial r} + \frac{u_\theta u_r}{r}\right)\hat{\theta} \\
&+ \left(u_x\frac{\partial u_r}{\partial x} + \frac{u_\theta}{r}\frac{\partial u_r}{\partial \theta} + u_r\frac{\partial u_r}{\partial r} - \frac{u_\theta^2}{r}\right)\hat{r}
\end{aligned} \tag{B.12}$$

$$\begin{aligned}
\nabla\cdot\Pi_{ij} &= \frac{1}{r}\left(\frac{\partial r\Pi_{11}}{\partial x} + \frac{\partial \Pi_{12}}{\partial \theta} + \frac{\partial r\Pi_{13}}{\partial r}\right)\hat{x} \\
&+ \frac{1}{r}\left(\frac{\partial r\Pi_{12}}{\partial x} + \frac{\partial \Pi_{22}}{\partial \theta} + \frac{\partial r\Pi_{23}}{\partial r} + \Pi_{23}\right)\hat{\theta}
\end{aligned} \tag{B.13}$$

$$+ \quad \left(\frac{\partial r \Pi_{13}}{\partial x} + \frac{\partial \Pi_{23}}{\partial \theta} + \frac{\partial r \Pi_{33}}{\partial r} - \Pi_{22} \right) \hat{r}$$

In cylindrical coordinates, the stress tensor given by Equation B.11 is written.

$$\begin{aligned}
\Pi_{11} &= -p + \frac{2}{3}\mu \left(2e_{11} - e_{22} - e_{33}\right) \\
\Pi_{22} &= -p + \frac{2}{3}\mu \left(2e_{22} - e_{11} - e_{33}\right) \\
\Pi_{33} &= -p + \frac{2}{3}\mu \left(2e_{33} - e_{11} - e_{22}\right) \\
\Pi_{12} &= \mu e_{12} \\
\Pi_{13} &= \mu e_{13} \\
\Pi_{23} &= \mu e_{23} \\
e_{11} &= \frac{\partial u_x}{\partial x} \\
e_{22} &= \frac{1}{r}\frac{\partial u_\theta}{\partial \theta} + \frac{u_r}{r} \\
e_{33} &= \frac{\partial u_r}{\partial r} \\
e_{12} &= r\frac{\partial}{\partial x}\left(\frac{u_\theta}{r}\right) + \frac{1}{r}\frac{\partial u_x}{\partial \theta} \\
e_{13} &= \frac{\partial u_x}{\partial r} + \frac{\partial u_r}{\partial x} \\
e_{23} &= r\frac{\partial}{\partial r}\left(\frac{u_\theta}{r}\right) + \frac{1}{r}\frac{\partial u_r}{\partial \theta}
\end{aligned} \tag{B.14}$$

For clarity, the viscous terms can be separated from the pressure to define a viscous stress tensor (Γ).

$$\Gamma_{ij} = \Pi_{ij} + p\delta_{ij} \tag{B.15}$$

By combining all of the above terms, the momentum equations in cylindrical coordinates are obtained. Beginning with the x-momentum equation, this results in the following form.

$$\begin{aligned}
&\rho\frac{\partial u_x}{\partial t} + \rho u_x\frac{\partial u_x}{\partial x} + \rho\frac{u_\theta}{r}\frac{\partial u_x}{\partial \theta} + \rho u_r\frac{\partial u_x}{\partial r} = \\
&\frac{1}{r}\left(-\frac{\partial rp}{\partial x} + \frac{\partial r\Gamma_{11}}{\partial x} + \frac{\partial \Gamma_{12}}{\partial \theta} + \frac{\partial r\Gamma_{13}}{\partial r}\right)
\end{aligned} \tag{B.16}$$

This form is not the most desirable form to solve numerically due to the need to evaluate many derivatives. What is desired is to collect all of the derivative terms together so that they can be evaluated simultaneously. This is done by rewriting the time derivative term to obtain a $\frac{\partial \rho}{\partial t}$ term which is then substituted for using the continuity equation. The first step involves writing the time derivative term as.

$$\rho \frac{\partial u_x}{\partial t} = \frac{\partial \rho u_x}{\partial t} - u_x \frac{\partial \rho}{\partial t} \tag{B.17}$$

After using the continuity equation to eliminate the $\frac{\partial \rho}{\partial t}$ term, the remaining terms can be collected to yield the conservative form of the x-momentum equation.

$$\frac{\partial \rho u_x}{\partial t} + \frac{\partial}{\partial x}\left(\rho u_x^2 + p - \Gamma_{11}\right) + \frac{1}{r}\frac{\partial}{\partial \theta}\left(\rho u_x u_\theta - \Gamma_{12}\right) + \frac{1}{r}\frac{\partial}{\partial r}\left(r\rho u_x u_r - r\Gamma_{13}\right) = 0 \tag{B.18}$$

Following identical procedures, the θ and r momentum equations can be written in conservative form.

$$\begin{aligned} &\frac{\partial \rho u_\theta}{\partial t} + \frac{\partial}{\partial x}\left(\rho u_x u_\theta - \Gamma_{12}\right) + \frac{1}{r}\frac{\partial}{\partial \theta}\left(\rho u_\theta^2 + p - \Gamma_{22}\right) \\ &\quad + \frac{1}{r}\frac{\partial}{\partial r}\left(r\rho u_\theta u_r - r\Gamma_{23}\right) = \frac{1}{r}\left(-\rho u_\theta u_r + \Gamma_{23}\right) \end{aligned} \tag{B.19}$$

$$\begin{aligned} &\frac{\partial \rho u_r}{\partial t} + \frac{\partial}{\partial x}\left(\rho u_x u_r - \Gamma_{13}\right) + \frac{1}{r}\frac{\partial}{\partial \theta}\left(\rho u_\theta u_r - \Gamma_{23}\right) \\ &+ \frac{1}{r}\frac{\partial}{\partial r}\left(r\rho u_r^2 + rp - r\Gamma_{33}\right) = \frac{1}{r}\left(\rho u_\theta^2 + p - \Gamma_{22}\right) \end{aligned} \tag{B.20}$$

B.4 Energy Equation

The general form of the energy equation without heat addition and neglecting external body forces is used [2].

$$\frac{\partial E_t}{\partial t} + \nabla \cdot E_t \vec{V} = -\nabla \cdot \vec{q} + \nabla \cdot \left(\Pi_{ij} \cdot \vec{V}\right) \tag{B.21}$$

To complete the relation, the following definitions and the equation of state are required.

$$E_t = \rho\left(e + \frac{u_x^2 + u_\theta^2 + u_r^2}{2}\right) \tag{B.22}$$

$$\vec{q} = -k\nabla T \tag{B.23}$$

$$T = \frac{(\gamma - 1)\, e}{R} \tag{B.24}$$

$$p = (\gamma - 1)\, \rho e \tag{B.25}$$

After a direct substitution of the vector terms written in cylindrical coordinates, the energy equation becomes.

$$\begin{aligned} &\frac{\partial E_t}{\partial t} + \frac{\partial}{\partial x}\left(E_t u_x + p u_x - k\frac{\partial T}{\partial x} - \Gamma_{11}u_x - \Gamma_{12}u_\theta - \Gamma_{13}u_r\right) \\ &\quad + \frac{1}{r}\frac{\partial}{\partial \theta}\left(E_t u_\theta + p u_\theta - \frac{k}{r}\frac{\partial T}{\partial \theta} - \Gamma_{12}u_x - \Gamma_{22}u_\theta - \Gamma_{23}u_r\right) \\ &+ \frac{1}{r}\frac{\partial}{\partial r}\left(rE_t u_r + rpu_r - rk\frac{\partial T}{\partial r} - r\Gamma_{13}u_x - r\Gamma_{23}u_\theta - r\Gamma_{33}u_r\right) = 0 \end{aligned} \tag{B.26}$$

B.5 Rotational Terms

Due to the presence of rotating geometries within an axial compressor, it is often convenient to solve the equations of motion in a rotating frame of reference. Two main differences are involved in using a moving frame of reference. The most obvious is that the velocities will have different values than in the stationary system. For this case, a constant rate of rotation (Ω) about the x axis is assumed throughout. Thus, the translation from the stationary system ($\vec{u}$) to the rotating one ($\vec{w}$) becomes.

$$\begin{aligned} w_x &= u_x \\ w_\theta &= u_\theta + \Omega r \\ w_r &= u_r \end{aligned} \tag{B.27}$$

The other difference is that differentiation will be performed in a different system of coordinates. Since the physical coordinates are the same in both systems, there is no difference between the spatial derivatives in each frame of reference. However, the derivatives with respect to time will be modified due to the relative movement between the rotating and stationary frames. This can be stated as,

$$\left.\frac{\partial \phi}{\partial t}\right|_{stationary} = \left.\frac{\partial \phi}{\partial t}\right|_{moving} - \vec{U} \cdot \nabla \phi \tag{B.28}$$

for the derivative of the scalar ϕ with respect to time , where $\vec{U}$ represents the velocity of the moving system with respect to the stationary one. For the case of constant rotation about the x-axis, this becomes.

$$\left.\frac{\partial \phi}{\partial t}\right|_{stationary} = \left.\frac{\partial \phi}{\partial t}\right|_{moving} + \Omega r \frac{1}{r}\frac{\partial \phi}{\partial \theta} \tag{B.29}$$

In order to write the equations in the rotating frame of reference, it is then necessary to replace the values of velocity using Equation B.27 and replace the time time derivatives with the formula given in Equation B.29. This will introduce new terms in each equation, many of which will cancel out. The specific results are given below for each equation.

B.5.1 Continuity Equation in Rotating Coordinates

Substituting Equations B.27 and B.29 into B.9 yields the continuity equation which has the identical form as the original.

$$\frac{\partial \rho}{\partial t} + \frac{\partial \rho w_x}{\partial x} + \frac{1}{r}\frac{\partial \rho w_\theta}{\partial \theta} + \frac{1}{r}\frac{\partial r \rho w_r}{\partial r} = 0 \tag{B.30}$$

B.5.2 The X-Momentum Equation in Rotating Coordinates

Just as in the case of the continuity equation, the transformation of the x-momentum equation (B.18) yields an identical form of the equation.

$$\frac{\partial \rho w_x}{\partial t}+\frac{\partial}{\partial x}\left(\rho w_x^2+p-\Gamma_{11}\right)+\frac{1}{r}\frac{\partial}{\partial \theta}\left(\rho w_x w_\theta-\Gamma_{12}\right)+\frac{1}{r}\frac{\partial}{\partial r}\left(r\rho w_x w_r-r\Gamma_{13}\right)=0 \quad \text{(B.31)}$$

B.5.3 The θ-Momentum Equation in Rotating Coordinates

The transformation of the θ-momentum equation results in several additional terms. However, several of the terms combine (when divided by Ωr) to yield the continuity equation (B.30). After these terms are canceled, the resulting equation has an additional source term.

$$\begin{aligned}\frac{\partial \rho w_\theta}{\partial t}+\frac{\partial}{\partial x}\left(\rho w_x w_\theta-\Gamma_{12}\right)+\frac{1}{r}\frac{\partial}{\partial \theta}\left(\rho w_\theta^2+p-\Gamma_{22}\right) \quad \text{(B.32)}\\ +\frac{1}{r}\frac{\partial}{\partial r}\left(r\rho w_\theta w_r-r\Gamma_{23}\right)=\frac{1}{r}\left(-\rho w_\theta w_r+2\Omega r\rho w_r+\Gamma_{23}\right)\end{aligned}$$

B.5.4 The R-Momentum Equation in Rotating Coordinates

The transformation of the r-momentum equation (B.20) results in two additional source terms.

$$\begin{aligned}\frac{\partial \rho w_r}{\partial t}+\frac{\partial}{\partial x}\left(\rho w_x w_r-\Gamma_{13}\right)+\frac{1}{r}\frac{\partial}{\partial \theta}\left(\rho w_\theta w_r-\Gamma_{23}\right) \quad \text{(B.33)}\\ +\frac{1}{r}\frac{\partial}{\partial r}\left(r\rho w_r^2+rp-r\Gamma_{33}\right)=\frac{1}{r}\left(\rho w_\theta^2+p-2\Omega r\rho u_\theta+\Omega^2 r^2\rho-\Gamma_{22}\right)\end{aligned}$$

B.5.5 Energy Equation in Rotating Coordinates

The transformation of the energy equation using this method is more tedious, but involves no new methods. The only difference from the previous transformations to rotating coordinates is the user's choice of a definition for the total energy. For consistency with the equations in a stationary frame, a rotating total energy (E_t') has

been defined.

$$E'_t = \rho\left(e + \frac{w_x^2 + w_\theta^2 + w_r^2}{2}\right) \tag{B.34}$$

$$E'_t = E_t - \rho w_\theta \Omega r + \rho\frac{\Omega^2 r^2}{2} \tag{B.35}$$

By once again making the substitutions to the rotating frame of reference, the same equation is obtained along with many additional terms. As with the θ-momentum equation, the continuity equation (B.30) can be used to cancel several terms. In addition, the θ-momentum equation (B.32) can be substituted into the equation. This last substitution will not be a direct cancellation, and will thus provide some additional terms. The end result is the addition of a single source term.

$$\begin{aligned} &\frac{\partial E'_t}{\partial t} + \frac{\partial}{\partial x}\left(E'_t w_x + p w_x - k\frac{\partial T}{\partial x} - \Gamma_{11} w_x - \Gamma_{12} w_\theta - \Gamma_{13} w_r\right) \\ &\quad + \frac{1}{r}\frac{\partial}{\partial \theta}\left(E'_t w_\theta + p w_\theta - \frac{k}{r}\frac{\partial T}{\partial \theta} - \Gamma_{12} w_x - \Gamma_{22} w_\theta - \Gamma_{23} w_r\right) \\ &+ \frac{1}{r}\frac{\partial}{\partial r}\left(r E'_t w_r + r p w_r - r k\frac{\partial T}{\partial r} - r\Gamma_{13} w_x - r\Gamma_{23} w_\theta - r\Gamma_{33} w_r\right) = \Omega^2 r \rho w_r \end{aligned} \tag{B.36}$$

B.6 Vector Form of the Equations of Motion

In order to implement the numerical solution of these equations, is is advantageous to write them in a simple form. Since all of the equations possess nearly the same format, it is easy to stack them into a vector format. The general form of the equations will take the form.

$$\frac{\partial \vec{U}}{\partial t} + \frac{\partial \vec{E}}{\partial x} + \frac{1}{r}\frac{\partial \vec{F}}{\partial \theta} + \frac{1}{r}\frac{\partial r\vec{G}}{\partial r} = \frac{1}{r}\vec{S} \tag{B.37}$$

B.6.1 Three-Dimensional Navier-Stokes Equations in Cylindrical Coordinates

Using the form of the equations given by Equation B.37, the three-dimensional Navier-Stokes equations can be written in cylindrical coordinates in the following way.

$$\vec{U} = \begin{pmatrix} \rho \\ \rho u_x \\ \rho u_\theta \\ \rho u_r \\ E_t \end{pmatrix} \tag{B.38}$$

$$\vec{E} = \begin{pmatrix} \rho u_x \\ \rho u_x^2 + p - \Gamma_{11} \\ \rho u_x u_\theta - \Gamma_{12} \\ \rho u_x u_r - \Gamma_{13} \\ E_t u_x + p u_x - q_x - \Gamma_{11} u_x - \Gamma_{12} u_\theta - \Gamma_{13} u_r \end{pmatrix} \tag{B.39}$$

$$\vec{F} = \begin{pmatrix} \rho u_\theta \\ \rho u_x u_\theta - \Gamma_{12} \\ \rho u_\theta^2 + p - \Gamma_{22} \\ \rho u_\theta u_r - \Gamma_{23} \\ E_t u_\theta + p u_\theta - q_\theta - \Gamma_{12} u_x - \Gamma_{22} u_\theta - \Gamma_{23} u_r \end{pmatrix} \tag{B.40}$$

$$\vec{G} = \begin{pmatrix} \rho u_r \\ \rho u_x u_r - \Gamma_{13} \\ \rho u_\theta u_r - \Gamma_{23} \\ \rho u_r^2 + p - \Gamma_{33} \\ E_t u_r + p u_r - q_r - \Gamma_{13} u_x - \Gamma_{23} u_\theta - \Gamma_{33} u_r \end{pmatrix} \tag{B.41}$$

$$\vec{S} = \begin{pmatrix} 0 \\ 0 \\ -\rho u_\theta u_r + \Gamma_{23} \\ \rho u_\theta^2 + p - \Gamma_{22} \\ 0 \end{pmatrix} \tag{B.42}$$

Closure is obtained using the following relations,

$$E_t = \rho\left(e + \frac{u_x^2 + u_\theta^2 + u_r^2}{2}\right) \tag{B.43}$$

$$q_x = k\frac{\partial T}{\partial x} \quad q_\theta = \frac{k}{r}\frac{\partial T}{\partial \theta} \quad q_r = k\frac{\partial T}{\partial r} \tag{B.44}$$

$$T = \frac{(\gamma - 1)\, e}{R} \tag{B.45}$$

$$p = (\gamma - 1)\, \rho e \tag{B.46}$$

where k, γ, and R are fluid dynamic constants.

B.6.2 Three-Dimensional Navier-Stokes Equations in Rotating Cylindrical Coordinates

Using the form of the equations given by Equation B.37, the three-dimensional Navier-Stokes equations can be written in rotating cylindrical coordinates in the following way.

$$\vec{U} = \begin{pmatrix} \rho \\ \rho w_x \\ \rho w_\theta \\ \rho w_r \\ E_t' \end{pmatrix} \tag{B.47}$$

$$\vec{E} = \begin{pmatrix} \rho w_x \\ \rho w_x^2 + p - \Gamma_{11} \\ \rho w_x w_\theta - \Gamma_{12} \\ \rho w_x w_r - \Gamma_{13} \\ E_t' w_x + p w_x - q_x - \Gamma_{11} w_x - \Gamma_{12} w_\theta - \Gamma_{13} w_r \end{pmatrix} \tag{B.48}$$

$$\vec{F} = \begin{pmatrix} \rho w_\theta \\ \rho w_x w_\theta - \Gamma_{12} \\ \rho w_\theta^2 + p - \Gamma_{22} \\ \rho w_\theta w_r - \Gamma_{23} \\ E_t' w_\theta + p w_\theta - q_\theta - \Gamma_{12} w_x - \Gamma_{22} w_\theta - \Gamma_{23} w_r \end{pmatrix} \tag{B.49}$$

$$\vec{G} = \begin{pmatrix} \rho w_r \\ \rho w_x w_r - \Gamma_{13} \\ \rho w_\theta w_r - \Gamma_{23} \\ \rho w_r^2 + p - \Gamma_{33} \\ E_t' w_r + p w_r - q_r - \Gamma_{13} w_x - \Gamma_{23} w_\theta - \Gamma_{33} w_r \end{pmatrix} \tag{B.50}$$

$$\vec{S} = \begin{pmatrix} 0 \\ 0 \\ -\rho w_\theta w_r + 2\Omega r \rho w_r + \Gamma_{23} \\ \rho w_\theta^2 + p - 2\Omega r \rho w_\theta + \Omega^2 r^2 \rho - \Gamma_{22} \\ \Omega^2 r^2 \rho w_r \end{pmatrix} \tag{B.51}$$

Closure is obtained using the following relations,

$$E_t' = \rho \left(e + \frac{w_x^2 + w_\theta^2 + w_r^2}{2} \right) \tag{B.52}$$

$$q_x = k \frac{\partial T}{\partial x} \quad q_\theta = \frac{k}{r} \frac{\partial T}{\partial \theta} \quad q_r = k \frac{\partial T}{\partial r} \tag{B.53}$$

$$T = \frac{(\gamma - 1)\, e}{R} \tag{B.54}$$

$$p = (\gamma - 1)\, \rho e \tag{B.55}$$

where k, γ, and R are fluid dynamic constants.

B.7 Non-Dimensionalization

The equations of motion were non-dimensionalized using the following reference quantities.

- Length - Blade Spacing (s)
- Velocity - Wheel Speed (U)
- Density - Free Stream Density (ρ_∞)
- Temperature - Free Stream Temperature (T_∞)
- Viscosity - Free Stream Viscosity (μ_∞)
- Pressure - $\rho_\infty U^2$
- Energy - U^2

The non-dimensionalized equations appear almost exactly the same as the dimensional form except that the viscous stresses and the heat fluxes have the following substitutions

$$(\mu + \mu_t) \Rightarrow \frac{\mu + \mu_t}{\mu_\infty} \frac{1}{Re_\infty} \tag{B.56}$$

$$k \Rightarrow \frac{\mu + \mu_t}{\mu_\infty} \frac{1}{(\gamma - 1) M_\infty^2 Re_\infty Pr} \tag{B.57}$$

where,

$$Re_\infty = \frac{\rho_\infty U s}{\mu_\infty}$$

$$M_\infty = \frac{U}{\sqrt{\gamma R T_\infty}}$$

and the equation of state becomes

$$p = (\gamma - 1)\, \rho e \tag{B.58}$$

or,

$$T = \frac{\gamma M_\infty^2 p}{\rho} \tag{B.59}$$

Appendix C

Numerical Method

C.1 Finite Difference Method

Due to the unsteady nature and large range of length scales present in this problem, great care had to be taken in the selection of a numerical method. In order to accurately compute flow structures over a large range of wave numbers, it becomes necessary to formulate the grid requirements with respect to the highest wave number of interest. This results in a grid with many more grid points than would be required to accurately resolve the lower wave numbers. With sufficient grid resolution, virtually any time-accurate numerical method would be acceptable. However, due to the large domain of interest (especially in three dimensions) it becomes very beneficial to consider higher order methods. The added cost associated with computing derivatives using a higher order method is more than offset by the savings in the number of grid points required for the problem. For an unsteady problem, it is important to not only capture the higher wave numbers, but also to propagate them at the correct speeds. Most standard methods are constructed entirely on an order of accuracy analysis basis with the dissipation and dispersion of the method considered after the method has been created. Typical methods for unsteady calculations such as a four-stage Runge-Kutta method have very desirable dissipation characteristics but suffer from a relatively poor dispersive character. Since it is the dissipation and dispersion which truly measures a methods ability to represent the unsteady fluid dynamic equations

correctly, it would be advantageous to consider these points from the onset. Using this idea, Tam and Webb [50] describe a method to create a finite difference method with optimal dissipation and dispersion characteristics. This method is referred to as a Dispersion Relation Preserving (DRP) scheme.

C.1.1 Space Derivatives

Beginning with a general description of a first derivative on a uniform grid at grid point i

$$\left(\frac{\partial f}{\partial x}\right)_i \simeq \frac{1}{\Delta x}\sum_{l=-N}^{M} a_l f\left(x + l\Delta x\right). \tag{C.1}$$

Instead of choosing the coefficients a_l to eliminate terms from the Taylor series expansion of f, the approximation to the derivative given in Equation C.1 is considered in the Fourier transform space. The coefficients will then be chosen to provide the best representation of the derivative over a chosen range of wave numbers. Taking the Fourier transform of Equation C.1 results in

$$\imath\alpha\tilde{f} \simeq \left(\frac{1}{\Delta x}\sum_{l=-N}^{M} a_l e^{\imath\alpha l\Delta x}\right)\tilde{f}. \tag{C.2}$$

From this relation, a numerical approximation to $\alpha\Delta x$ can be defined as follows.

$$\overline{\alpha}\Delta x \equiv -\imath\sum_{l=-N}^{M} a_l e^{\imath\alpha l\Delta x} \simeq \alpha\Delta x \tag{C.3}$$

The quantity $\alpha\Delta x$ represents the range of possible wavelengths which can be propagated on a given grid with $\alpha\Delta x = \pi$ corresponding to the smallest possible wavelength that the grid can support. To provide the best representation of the derivative, it is desired to have $\overline{\alpha}\Delta x = \alpha\Delta x$ over as great a range of wave numbers as possible, where $\overline{\alpha}\Delta x$ represents the finite difference approximation of $\alpha\Delta x$. To achieve this, an error function E can be defined as follows.

$$E = \int_{-\Theta_0}^{\Theta_0} \left|\alpha\Delta x - \overline{\alpha}\Delta x\right|^2 d\left(\alpha\Delta x\right)$$

The variable Θ_0 represents the wave number range over which the error function is to be minimized ($-\pi < \Theta < \pi$). Choosing and even stencil ($N = M$) eliminates the concern of complex values for a_l. Also, for a given value of N, the standard Taylor series order of accuracy analysis can be used to reduce the number of independent coefficients and guarantee a minimum order of accuracy for the method. By allowing only one free parameter the error minimization process becomes very straight forward. For $N = 3$ and $\Theta_0 = 1$ a fourth-order accurate scheme results with an improved dispersive characteristic compared to the standard central difference fourth order scheme. The following values were obtained for the spatial difference coefficients.

$$a_0 = 0.0$$

$$a_1 = -a_{-1} = 0.76685508$$

$$a_2 = -a_{-2} = -0.16348408$$

$$a_3 = -a_{-3} = 0.02003768$$

Since it is possible to construct a sixth order accurate scheme from a 7 point stencil, it is appropriate to compare the new scheme with the sixth order method. It is clear from Figure C.1 that the DRP scheme has an improved range of accuracy compared to both the fourth and sixth order standard schemes. This same data can be plotted in a more suggestive way by dividing the approximate value, $\overline{\alpha}\Delta x$ by the theoretical value. This result is shown in Figure C.2. In this plot the ordinate value gives a ratio of the numerical speed of propagation to the ideal speed. The DRP method correctly captures the propagation speed to well within 1 percent for values of $\alpha\Delta x$ up to 1.0. The standard fourth and sixth order schemes yield a considerably lower range of $\alpha\Delta x$ with accurate wave propagation speeds.

C.1.2 Time Derivative

To provide a complete time-accurate method, it is necessary to generate a method for time discretization as well. This is done in a very similar way to the space derivative except it is appropriate to take the Laplace transform instead of the Fourier transform.

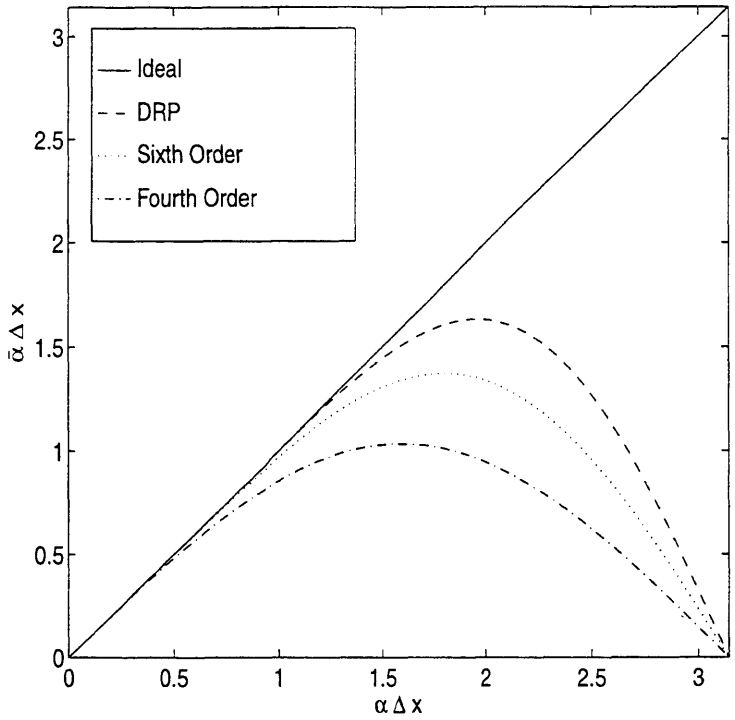

Figure C.1: Comparison of $\overline{\alpha}\Delta x$ for DRP scheme and standard fourth and sixth order schemes.

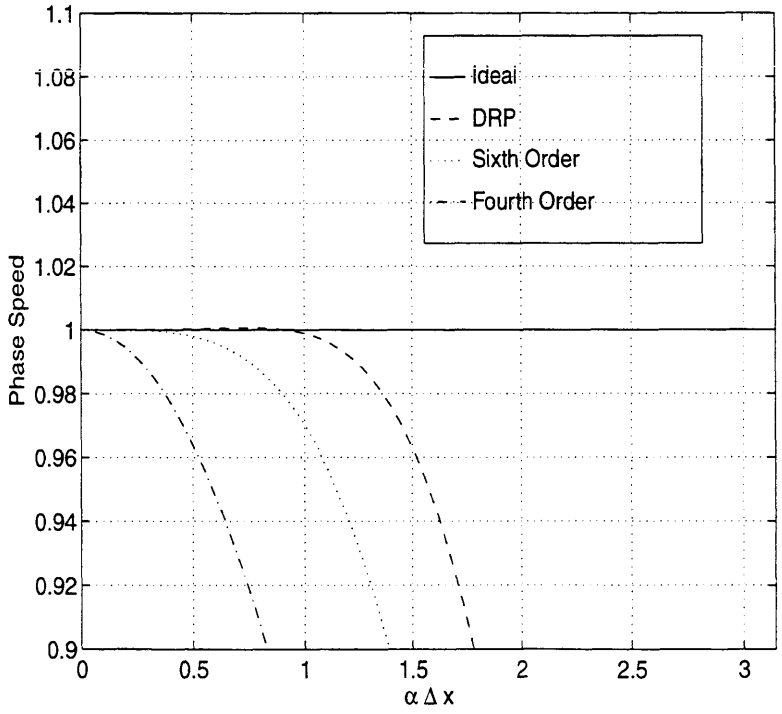

Figure C.2: Comparison of wave propagation speed for DRP scheme and standard fourth and sixth order schemes.

In the construction of a higher order method, data from more than one previous time will be used in updating the current time step. Two basic formulations are possible; either the values of the unknown or its derivative can be saved. In this formulation, the value of the time derivative will be saved from previous time steps. This value comes from the evaluation of the space derivatives (and any source terms), and is known at the current time step as well as previous time steps. In general, the time derivative can be written as

$$\frac{U^{(n+1)} - U^{(n)}}{\Delta t} \simeq \sum_{j=0}^{N} b_j \left(\frac{dU}{dt}\right)^{(n-j)} \tag{C.4}$$

where $\left(\frac{dU}{dt}\right)^{(n)}$ represents the value computed from the evaluation of the space terms in the equation (right-hand side) to be solved at time step n. Taking the Laplace transform yields the following form of Equation C.4.

$$\frac{\imath\left(e^{\imath\omega\Delta t} - 1\right)}{\imath\Delta t \sum_{j=0}^{N} b_j e^{\imath j\omega\Delta t}} \tilde{U} \simeq \frac{d\tilde{U}}{dt} = -\imath\omega\tilde{U} \tag{C.5}$$

A numerical approximation to the ideal variable ω can be defined as follows.

$$\overline{\omega}\Delta t \equiv \frac{\imath\left(e^{\imath\omega\Delta t} - 1\right)}{\sum_{j=0}^{N} b_j e^{\imath j\omega\Delta t}} \simeq \omega\Delta t \tag{C.6}$$

Once again, the numerical approximation, $\overline{\omega}\Delta t$, can be optimized with respect to the ideal quantity ($\omega\Delta t$). An error function is once again defined over a specified range of $\omega\Delta t$.

$$E = \int_0^{\Theta_0} \left\{\sigma \left[Re\left(\overline{\omega}\Delta t - \omega\Delta t\right)\right]^2 + (1-\sigma)\left[Im\left(\overline{\omega}\Delta t - \omega\Delta t\right)\right]^2\right\} d\left(\omega\Delta t\right) \tag{C.7}$$

The variable σ is used to provide weighting between the wave propagation characteristics (real part) and the dissipation (imaginary part). The range of $\omega\Delta t$ over which the method is optimized is specified by Θ_0. Once again, a Taylor series order of accuracy analysis can be used to reduce the number of free parameters (b_j) in the

minimization process. A measure of the quality of this method can be shown in plots of the real and imaginary parts of $\overline{\omega}\Delta t$ versus $\omega\Delta t$. However, for a high-order method ($N > 1$), for each $\omega\Delta t$ there exists $N + 1$ roots. For $N = 3$, $\Theta_0 = 0.5$, and $\sigma = 0.36$ with an order of accuracy of $(\Delta t)^3$ (one free parameter) the values obtained are.

$$b_0 = 2.30255809$$

$$b_1 = -2.49100760$$

$$b_2 = 1.57435093$$

$$b_3 = -0.38589142$$

Plots of the four roots of Equation C.6 are shown in Figures C.3 and C.4 along with the theoretical value. Clearly, only one of these roots represents the desired value. The numerical method is capable of capturing the behavior of all of these roots with no clear way of distinguishing between them. Fortunately, in the lower range of $\omega\Delta t$, only the one desirable root has an imaginary part near zero. This results in all of the remaining (spurious) roots being heavily damped so that their presence will not be seen in the numerical result. However, it is one of the spurious roots which first displays a positive imaginary part. This point then becomes the numerical stability limit since any wave with $\omega\Delta t$ above this limiting value will grow without bound. It is a rather fortunate occurrence that this limiting value occurs just at the point where the accuracy of the method (dispersive and dissipative) begins to diminish. Thus, for this particular formulation, any choice of Δt which yields a stable calculation, will also provide one that is time accurate through the range of wave numbers calculated. Plots of the amplification factor and phase speed can be seen in Figures C.5 and C.6 for the principal root. These plots provide a more quantitative representation of the information presented in Figures C.3 and C.4

C.1.3 Equation Form Used

Due to the choice of a higher order method with a multiple point stencil, the use of a structured grid for solving the governing equations is advantageous. In addition, the

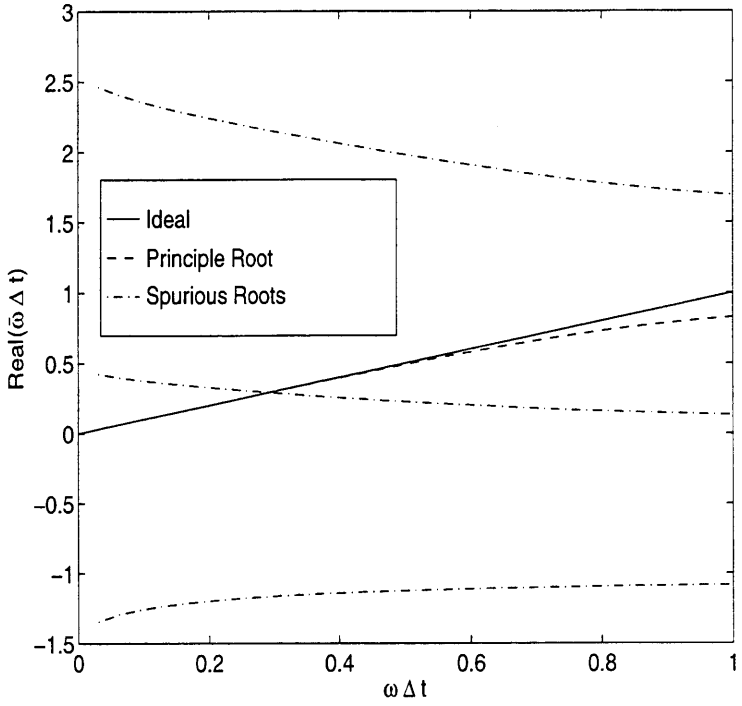

Figure C.3: Comparison of real parts of $\overline{\omega}\Delta t$

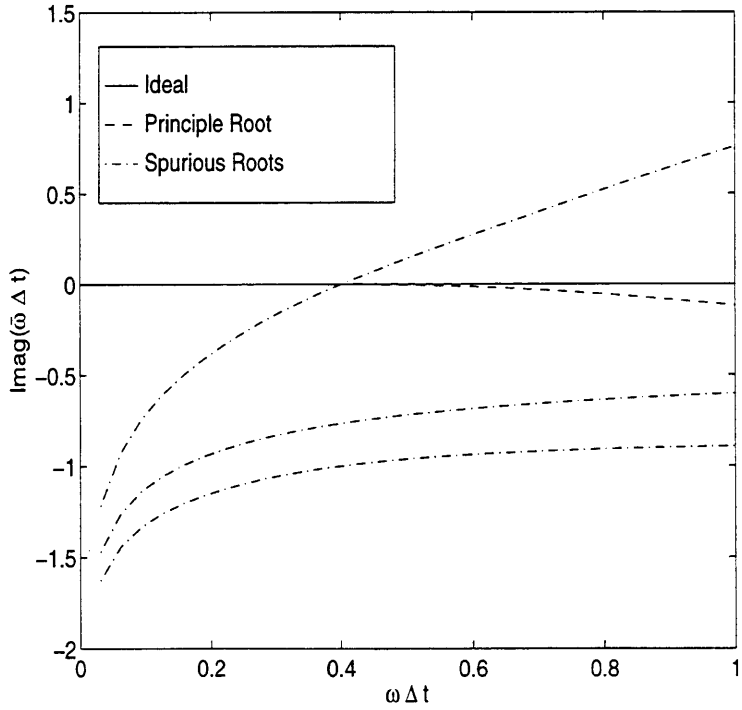

Figure C.4: Comparison of imaginary parts of $\overline{\omega}\Delta t$

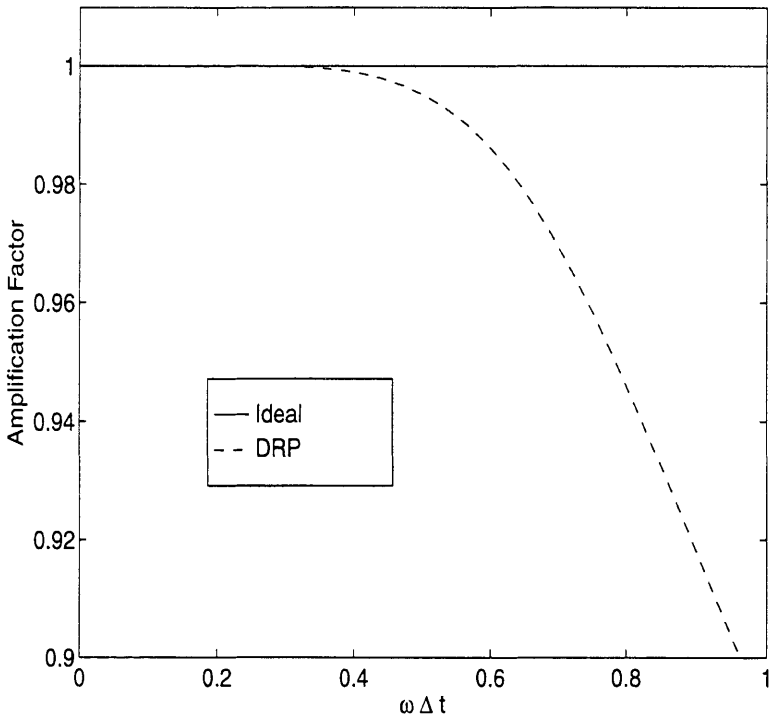

Figure C.5: Amplification factor of time discretization

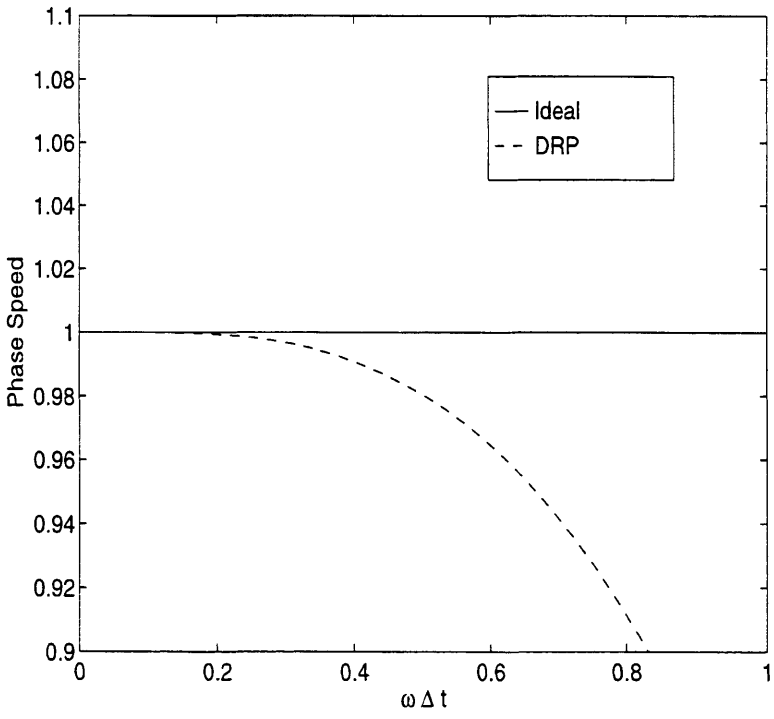

Figure C.6: Normalized Phase Speed of time discretization

application of this method to a finite-difference approach is also more direct. Since a finite-volume approach is not being used, this method does not possess the quality of being strictly conservative. However, due to the high accuracy of the method, errors in conservation were found to be small (typically less than 0.1%).

Care must be taken when choosing the appropriate form of the differential equations to solve. An attractive form to use when solving the Navier-Stokes equations is what is known as the Strong Conservation Law Form. In this form the equation is transformed using the grid metric terms to yield a simpler form of the differential equation to solve numerically [2]. In creating this form, various grid metric terms have been mathematically canceled. However, the numerical implementation of this form may not achieve the exact cancellation of these terms as shown by Thomas and Lombard [52]. If this cancellation is not achieved, this error will act as an unwanted source term in the solution. A more robust method is to use the Chain Rule Conservative Form as described by Hindman [21]. This method does not rely on any such cancellation and therefore allows additional freedom in computing the metric terms needed.

C.1.4 Evaluation of DRP Scheme

In order to verify the expected performance of the DRP method a sample calculation was performed using the one-dimensional convection equation as a model equation. For comparison, a four-stage Runge-Kutta (RK4) method was computed as well. In order to provide a traveling waveform, an oscillating inlet condition was used to launch waves down the duct. The results from these calculations at $\alpha\Delta x = \pi/4$ and $\alpha\Delta x = \pi/3$ are shown in Figures C.7 and C.8 along with the exact solution. Since it was necessary to drop to a lower order scheme near the boundaries, the initial amplitude of the waves traveling down the duct was reduced for both the DRP and Runge-Kutta schemes. The DRP scheme shows near perfect wave speed and no noticeable attenuation away from the boundaries for values of $\alpha\Delta x$ below one. The four-stage Runge-Kutta method, as expected, shows no attenuation of the wave, but the wave speed is noticeably inaccurate.

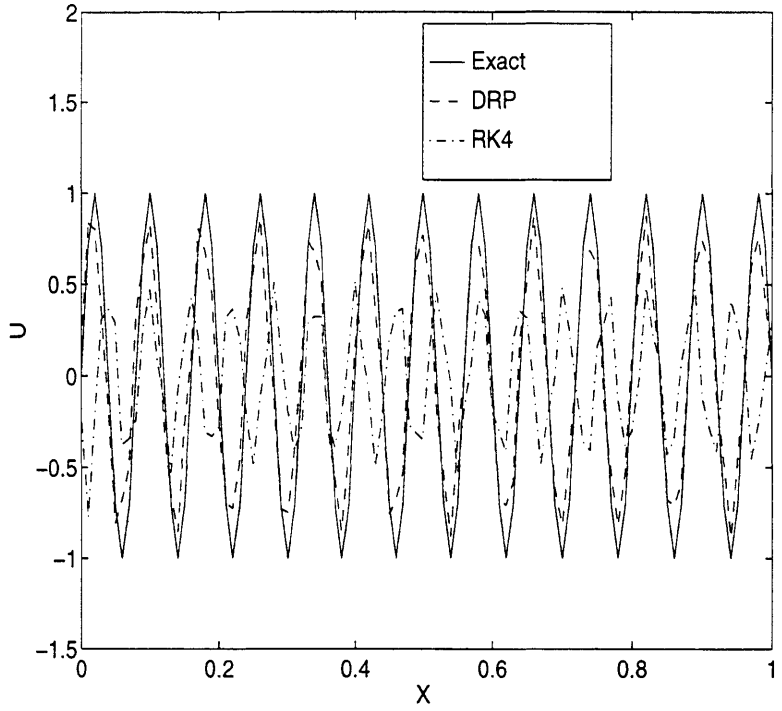

Figure C.7: Comparison of Dispersion Relation Preserving scheme with exact solution and four-stage Runge-Kutta at $\alpha\Delta x = \pi/4$

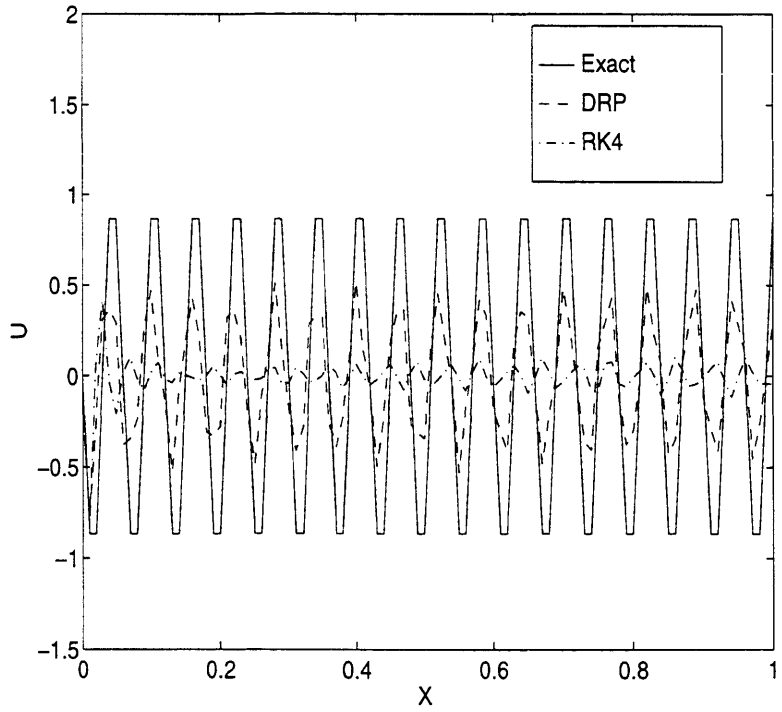

Figure C.8: Comparison of Dispersion Relation Preserving scheme with exact solution and four-stage Runge-Kutta at $\alpha\Delta x = \pi/3$

C.2 Artificial Damping

As with virtually any high-order method, the presence of high frequency waves in the solution is of concern. Although this particular method is not subject to odd-even decoupling, it does well in capturing high frequency waves that unwanted waves will remain in the solution. These waves tend to decay in time, but are easily created at interfaces with solid surfaces and inlet/exit boundaries. It is interesting to note that since the slope of $\overline{\alpha}\Delta x$ (group velocity) is negative for high wave numbers, the unwanted waves may travel in the wrong direction.

The method used is similar in construction to the method used to approximate the space derivatives. However, there is no exact requirement that the smoothing must meet. As long as the method damps high frequency waves and provides a minimum of attenuation for lower frequencies it is a viable method. The artificial damping used takes the following form.

$$U_i^{(n+1)} - U_i^{(n)} = \mu_a \sum_{j=-N}^{M} c_j U_{i+j}^{(n)} \tag{C.8}$$

The variable μ_a is a constant used to adjust the amount of damping present. Just as in the case of the spatial derivative, it is appropriate to analyze this method in the Fourier transform space. The most desirable shape of the damping function in this space is one that is essentially zero in the range of $\alpha\Delta x$ where the solution is desired, and then rises rapidly and remains high for higher values of $\alpha\Delta x$. It is important to remember that any value of the damping function which is even slightly negative will act in a de-stabilizing manner. Tam, Webb, and Dong [51] suggest the use of a Gaussian function centered at π, but any function which meets the above criteria should be suitable. For reasons similar to the spatial derivative, an even stencil was chosen ($N = M$) with symmetric coefficients ($c_j = c_{-j}$). The values obtained are.

$c_0 = 0.351061040$

$c_1 = c_{-1} = -0.242824317$

$c_2 = c_{-2} = 0.074469480$

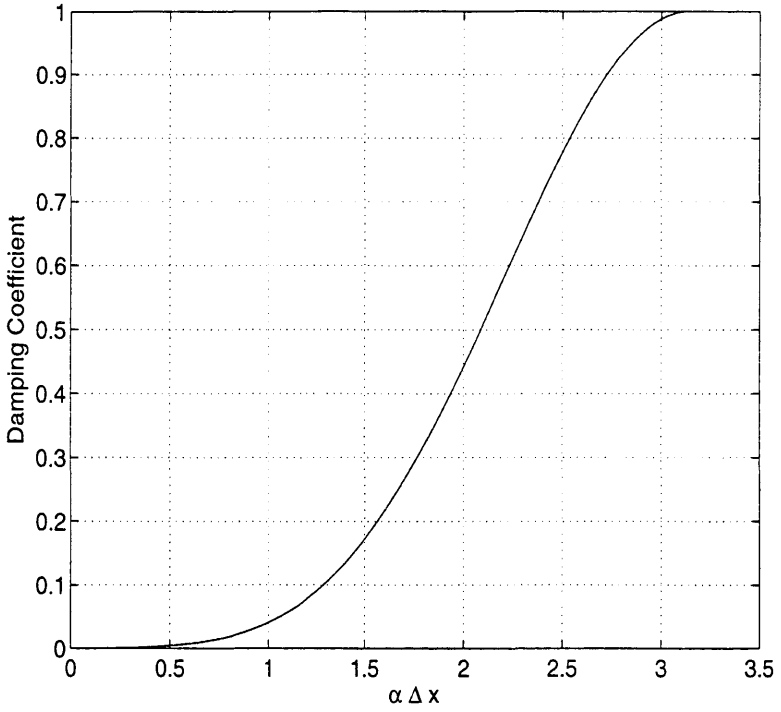

Figure C.9: Normalized Damping function ($N = M = 3$)

$$c_3 = c_{-3} = -0.007175683$$

A plot of the damping function versus $\alpha\Delta x$ is shown in Figure C.9.

Clearly the damping function is not zero through the entire range of interest ($\alpha\Delta x < 1$). Therefore the use of the damping function needs to be applied in a judicious manner. The method chosen for this study was to evaluate the fourth derivative of pressure at each point and use that value to scale μ_a. This method proved to be very effective in selecting and removing unwanted high-frequency waves from the numerical solution without providing excessive damping of the desired waves.

C.3 Coordinate Transformation

For realistic geometries, uniform gridding is not possible. It then becomes advantageous to transform from general curvilinear coordinates (x, θ, r) to a uniform compu-

tational space (ξ, η, ζ). This transformation takes the following form:

$$\begin{aligned} \xi &= \xi(x, \theta, r) \quad x = x(\xi, \eta, \zeta) \\ \eta &= \eta(x, \theta, r) \quad \theta = \theta(\xi, \eta, \zeta) \\ \zeta &= \zeta(x, \theta, r) \quad r = r(\xi, \eta, \zeta) \end{aligned} \tag{C.9}$$

In this way, when derivatives are computed on the mesh, the non-orthogonality of the grid will yield several cross terms.

$$\begin{aligned} \frac{\partial}{\partial x} &= \xi_x \frac{\partial}{\partial \xi} + \eta_x \frac{\partial}{\partial \eta} + \zeta_x \frac{\partial}{\partial \zeta} \\ \frac{\partial}{\partial \theta} &= \xi_\theta \frac{\partial}{\partial \xi} + \eta_\theta \frac{\partial}{\partial \eta} + \zeta_\theta \frac{\partial}{\partial \zeta} \\ \frac{\partial}{\partial r} &= \xi_r \frac{\partial}{\partial \xi} + \eta_r \frac{\partial}{\partial \eta} + \zeta_r \frac{\partial}{\partial \zeta} \end{aligned} \tag{C.10}$$

The transformation can be written in the following forms:

$$\begin{bmatrix} d\xi \\ d\eta \\ d\zeta \end{bmatrix} = \begin{bmatrix} \xi_x & \xi_\theta & \xi_r \\ \eta_x & \eta_\theta & \eta_r \\ \zeta_x & \zeta_\theta & \zeta_r \end{bmatrix} \begin{bmatrix} dx \\ d\theta \\ dr \end{bmatrix}$$

or

$$\begin{bmatrix} dx \\ d\theta \\ dr \end{bmatrix} = \begin{bmatrix} x_\xi & x_\eta & x_\zeta \\ \theta_\xi & \theta_\eta & \theta_\zeta \\ r_\xi & r_\eta & r_\zeta \end{bmatrix} \begin{bmatrix} d\xi \\ d\eta \\ d\zeta \end{bmatrix} \tag{C.11}$$

Although the terms required to transform the derivatives on the grid to the desired curvilinear coordinates are contained in the first matrix, only the second matrix can be computed directly. Since the matrices are inverses of each other, the desired terms can be found by inverting the second matrix as follows:

$$\xi_x = J(\theta_\eta r_\zeta - \theta_\zeta r_\eta)$$

$$\xi_\theta = -J(x_\eta r_\zeta - x_\zeta r_\eta)$$

$$\xi_r = J\left(x_\eta \theta_\zeta - x_\zeta \theta_\eta\right)$$
$$\eta_x = -J\left(\theta_\xi r_\zeta - \theta_\zeta r_\xi\right)$$
$$\eta_\theta = J\left(x_\xi r_\zeta - x_\zeta r_\xi\right)$$
$$\eta_r = -J\left(x_\xi \theta_\zeta - x_\zeta \theta_\xi\right)$$
$$\zeta_x = J\left(\theta_\xi r_\eta - \theta_\eta r_\xi\right)$$
$$\zeta_\theta = -J\left(x_\xi r_\eta - x_\eta r_\xi\right)$$
$$\zeta_r = J\left(x_\xi \theta_\eta - x_\eta \theta_\xi\right)$$

where

$$J = \frac{\partial\left(\xi, \eta, \zeta\right)}{\partial\left(x, \theta, r\right)} = 1/\begin{vmatrix} x_\xi & x_\eta & x_\zeta \\ \theta_\xi & \theta_\eta & \theta_\zeta \\ r_\xi & r_\eta & r_\zeta \end{vmatrix}$$

Some simplification of the evaluation of derivatives (C.11) can be made when the grid lines are coincident with the coordinate axes. For the case of the H-Grid, the grid lines have been constructed to lie precisely on the coordinate axes in all three directions. For this case equation C.11 reduces to:

$$\frac{\partial}{\partial x} = \xi_x \frac{\partial}{\partial \xi}$$
$$\frac{\partial}{\partial \theta} = \eta_\theta \frac{\partial}{\partial \eta}$$
$$\frac{\partial}{\partial r} = \zeta_r \frac{\partial}{\partial \zeta}$$

In the case of the O-grid, the grid is constructed of two-dimensional slices which fall on surfaces of constant r. Such a constant radius surface is shown in Figure C.10. For this case equation C.11 reduces to:

$$\frac{\partial}{\partial x} = \xi_x \frac{\partial}{\partial \xi} + \eta_x \frac{\partial}{\partial \eta}$$
$$\frac{\partial}{\partial \theta} = \xi_\theta \frac{\partial}{\partial \xi} + \eta_\theta \frac{\partial}{\partial \eta}$$
$$\frac{\partial}{\partial r} = \xi_r \frac{\partial}{\partial \xi} + \eta_r \frac{\partial}{\partial \eta} + \zeta_r \frac{\partial}{\partial \zeta}$$

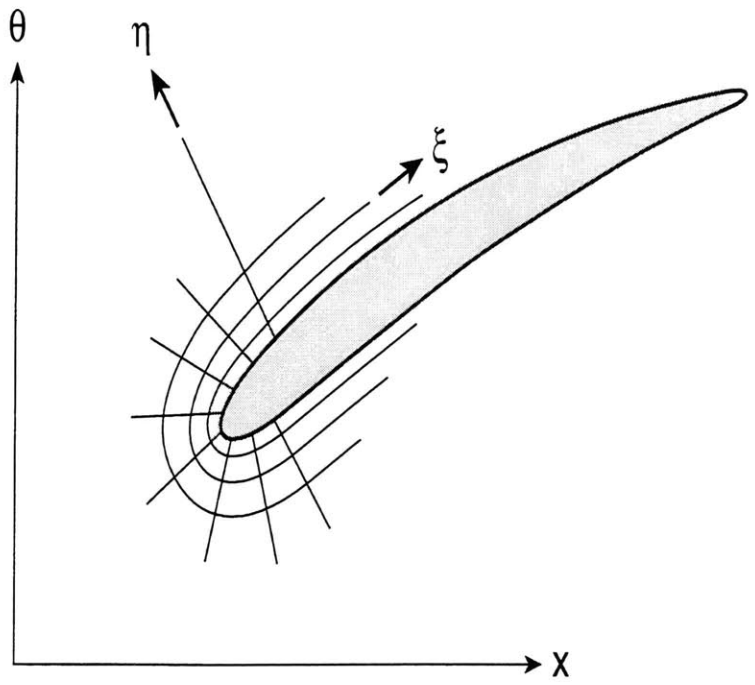

Figure C.10: Grid coordinate directions for O-grid

Finally, one additional simplification can be made in evaluating viscous terms near solid boundaries. Baldwin and Lomax [3] have shown that the primary effect of the viscous terms in the Navier-Stokes equations can be achieved by evaluating only the derivatives normal to solid surfaces. In this case, that corresponds to retaining only the derivatives of η in equation C.11 which then reduces to.

$$\frac{\partial}{\partial x} = \eta_x \frac{\partial}{\partial \eta}$$
$$\frac{\partial}{\partial \theta} = \eta_\theta \frac{\partial}{\partial \eta}$$
$$\frac{\partial}{\partial r} = \eta_r \frac{\partial}{\partial \eta}$$

Appendix D

Computational Grid

When solving the discrete form of the Navier-Stokes equations, the proper choice of gridding technique can be almost as important to the quality of the solution as the numerical method used to solve the equations. Several factors influence the choice of gridding method used for each unique problem. These include the physical geometry, the numerical method being used and the character of the governing equations. This combination of factors led to the use of multiple overlapping grids in this study.

D.1 Use of Multiple Grids

The solution to the problem of rotating stall in axial compressors can be thought of as containing two unique regions of flow. These regions are the flows about the compressor blades, and the flows in the upstream and downstream ducts. These two regions have distinct geometries and even different flow characters. The flow in the ducts is governed almost exclusively by the Euler equations. Since the duct geometry is a simple rectangular shape, a simple grid topology can be used to simplify the computation in this region. Near the blade surfaces, viscous forces become very important in appropriately describing the fluid flow. In this region, it is important that the grid conform to the shape of the body. Having a grid that is orthogonal to the solid surface is advantageous when evaluating the viscous flow terms. The grid must also vary in size in order to resolve the small viscous regions and not consume

excessive computer resources. In order to preserve the accuracy of the numerical method, the grid must also be smooth and not overly distorted or stretched.

To prevent requiring one type of grid to meet the disparate qualities of both regions, the use of multiple grids was selected. This choice came at the added cost of providing a means to interpolate data between the two grids at each time step. However, the formulation of each grid region was simplified greatly, and certain advantages were exploited in both.

D.1.1 H-Grid

The geometry of the compressor duct is exceedingly simple. For this region a rectangular H-grid was chosen. For duct geometries with no radial variations, the grid lines were able to coincide exactly with the coordinate directions. This resulted in a considerable simplification when evaluating the numerical derivatives as shown in Appendix C. Additionally, the use of a simple grid geometry allows for a simpler evaluation of flow quantities used for subsequent analysis.

D.1.2 O-Grid

Near the blade surfaces, it is desirable to have a grid that wraps around the blade. In this region a circular O-grid was used. As stated previously, it is desirable for the grid in this region to be closely packed near the surface and less so away from the blade. Grid orthogonality at the surface is also advantageous. Finally, it is desirable to have a grid that varies in a smooth manner. In general it is difficult to fulfill all of these requirements simultaneously. Analytic methods may work for a problem such as this, but tend to be best suited for a narrow range of geometries. For this problem, an elliptic partial differential equation method was used to generate the O-grid. The grid generation code used directly follows the method presented by Steger and Sorenson [47]. In using this method, grid orthogonality at the surface could be controlled directly and grid spacing was specified in an approximate manner. The use of an elliptic partial differential equation assures that the resulting grid will be smooth

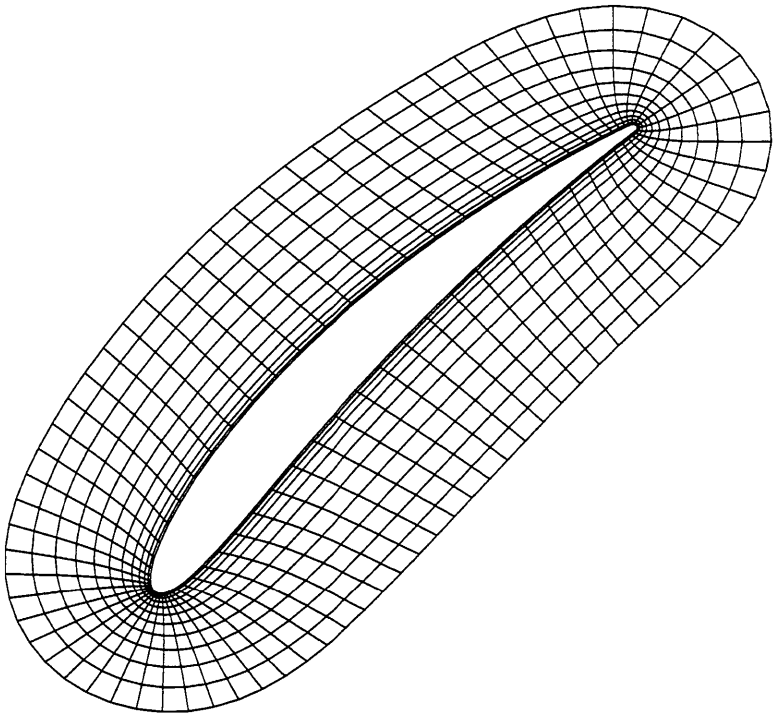

Figure D.1: Typical O-Grid used

and tends to yield grids with nearly orthogonal lines. Figure D.1 demonstrates the grid clustering near the blade surface. A closer view of the grid near the blade is shown in Figure D.2. This view clearly shows the orthogonality of the grid near the blade surface as well as the near orthogonality of the grid in the rest of the grid. All O-Grids were constructed using two-dimensional sections of the compressor blades.

D.1.3 Grid Interpolation Scheme

Inherent in the use of multiple grids is the need to pass flow information between them. Since the grids used share no common boundaries, it is necessary to use interpolation to pass the data between grids. In order to reduce the code complexity, a method of interpolation that was suitable for both rotors and stators was sought. In general, the relative motion of two grids requires that all new interpolation coefficients be computed for each time step. By taking advantage of the simplified geometry of the H-grid, it was possible to compute new interpolation coefficients in a quick analytical way. The method used is somewhat different depending upon which direction the

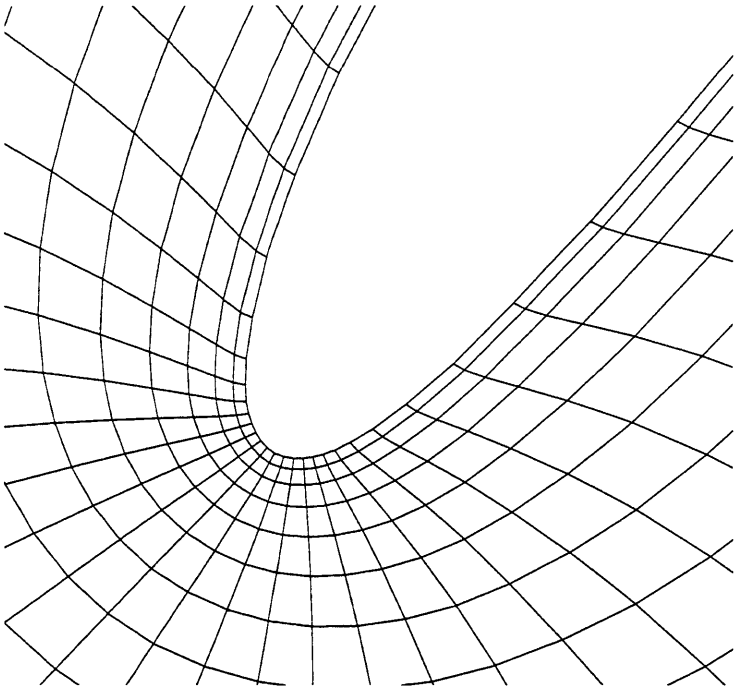

Figure D.2: Closeup of typical O-Grid

data is being transferred between the two grids.

The most difficult part in computing the interpolation coefficients from one grid to the other is locating which points in one grid form the nearest neighbors to the specified point in the other grid. The neighboring points were chosen by finding the rectangular cluster of points in the other grid that formed the cell in which the specified point was contained. After these neighboring points were found, their coordinates were used to compute the bilinear interpolation coefficients. Since the governing equations were solved using the conservative form, the conservative variables were used for interpolation.

H-Grid to O-Grid Interpolation

The principal fact that allows a simple calculation of the interpolation coefficients is that the H-grid used in perfectly rectangular and uniform. This makes it possible to find which grid cell in the H-grid a given point in the O-grid lies in by using a simple analytic formula. Once the proper cell is located, it is a simple task to

calculate the interpolation coefficients for the points which form the boundary of that cell. Movement of the O-grid over the H-grid does not complicate this process in any substantial way.

O-Grid to H-Grid Interpolation

A more difficult task is to transfer the data from the O-grid to the H-grid. Since the O-grid is not uniform, it is not possible to locate the appropriate cell in the O-grid analytically. Instead an intermediate uniform grid is formed. Since the intermediate grid moves with the blade (in the case of a rotor), these interpolation coefficients never change. It then remains to locate the points in the intermediate grid which are the nearest neighbors to the specified point in the H-grid.

A remaining task is to determine which points in the H-grid need values interpolated from the O-grid. This is accomplished by defining a boundary which moves with the O-grid. When a point in the H-grid lies inside the boundary, it then has the values from the O-grid interpolated to it. Since the path of the rotor is well defined in this case, this determination is not difficult.

Numerous implementation details have been left out in this description, but the overall method is no more complex than has been described. One potential cause of difficulty, however, is the treatment of the periodic boundary. Since the blades move across this boundary it is necessary to allow the interpolation to stretch across this boundary as well. No new methods are required other than careful bookkeeping.

D.2 Grid Construction

The use of overlapping grids makes the construction of the complete grid relatively simple. In addition, all three-dimensional grids are constructed out of two-dimensional grids stacked on planes of constant radius. The grid is constructed essentially by placing the O-grids in the proper place on top of an underlying H-Grid. Since the H-grid is evenly spaced and rectangular, it is trivial to construct. For computational efficiency, the grid is allowed to stretch in the axial direction in the upstream and

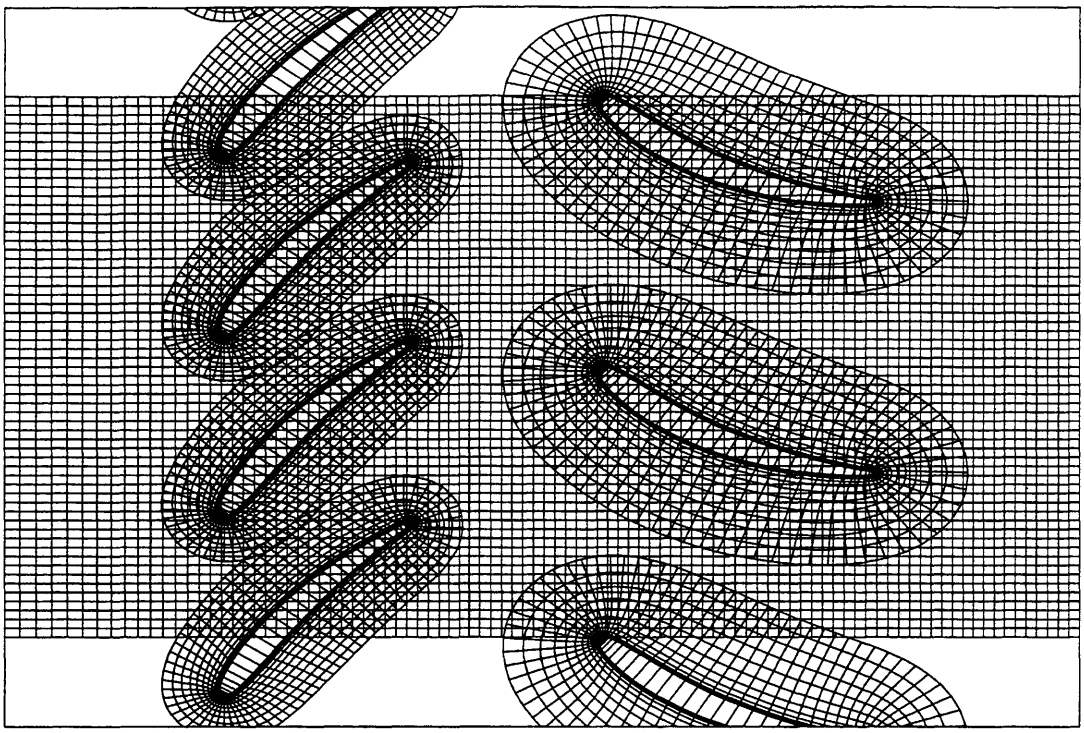

Figure D.3: Two-dimensional computational grid

downstream duct portions. A view of one of the two-dimensional grids is shown in Figure D.3. Additional blades are drawn in order to show periodicity.

Appendix E

Tip Clearance Model

One of the important flow features in a three-dimensional description of an axial compressor is the presence of a tip gap leakage flow. The flow through the tip gap leads to the tip leakage vortex. The effect the leakage vortex has on the compressor performance is discussed in detail by Khalid [27]. Several points are relevant for the implementation of a model for the tip gap flow in this investigation. Storer and Cumpsty [49] found that the flow in the gap is primarily pressure driven (ie: can be described by Bernoulli's Eq.). The subsequent losses which yield lower total pressure in the leakage vortex are the result of mixing which occurs after the flow has emerged from the tip gap. Considering these points, a tip gap model which satisfies the Euler equations will satisfy these requirements, and will also be appropriate for unsteady flow situations. Due to the presence of the compressor case, the flow local to the tip gap should also be two-dimensional. As recommended by Storer and Cumpsty [49], a discharge coefficient of 0.8 is used to approximate the reduction in tip clearance flow area due to the flow contraction arising from viscous effects. Thus the computational tip gap used was smaller than the actual valued being modeled.

The tip gap model which has been implemented for this investigation is a two-dimensional finite-volume Euler method. A simple grid of volumes within the tip gap where defined, and fluxes were computed as a combination of fluxes from the blade passage flow and from neighboring tip gap volumes. By allowing the volumes within the tip gap to communicate with each other, the problem of trying to determine

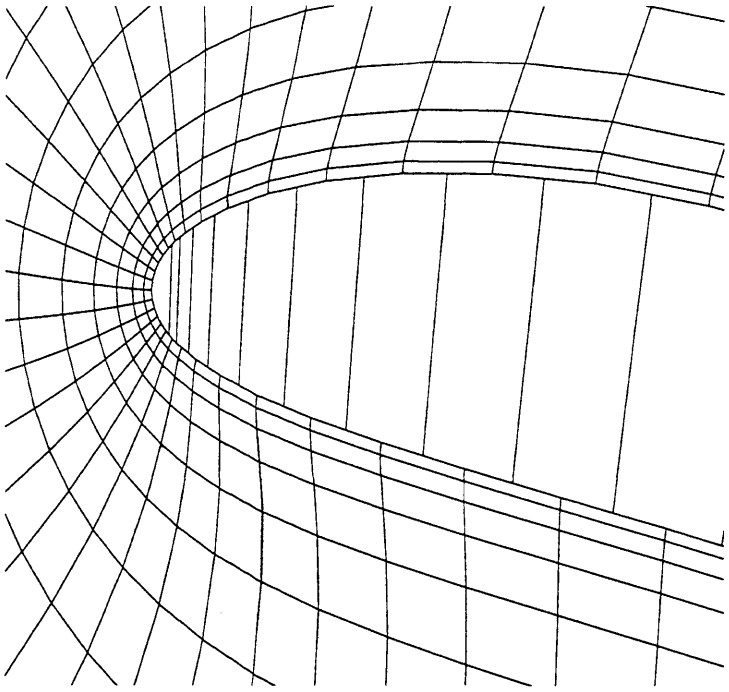

Figure E.1: Grid used to solve for flow in the tip gap region

which points on the pressure and suction sides of the blade should be used to find the pressure difference and subsequent leakage flow velocity has been removed. An example of the grid used in the tip gap region is shown in Figure E.1. The O-grid which envelopes the blade can be seen with the volume of the tip gap filled with simple volumes cut across the thickness of the blade. For most of the blade there exists a one-to-one correspondence between the O-grid boundary points and an adjacent tip gap volume. This correspondence breaks down near the leading and trailing edges. For simplicity, a single larger volume is used in these regions. Because the size of these leading and trailing edge tip gap volumes is still less than the average spacing in the remainder of the tip grid, the ability of the method to resolve flow features such as the tip clearance vortex will not be affected.

A flow solution is obtained for the tip gap region by computing the fluxes into and out of the volumes from the interior and exterior sides. The two-dimensional Euler equations are then used to update the values within each tip gap volume. The points on the boundary between the tip gap volumes and the external flow region are

treated simply as an interface and are not integrated separately. The values on this interface are taken as the average of the interior volume and the first exterior flow grid point in order to compute the fluxes necessary to integrate the Euler equations.

Appendix F

Turbulence Modeling

In the modeling of rotating stall in axial compressors it is necessary to represent the flow at conditions significantly removed from the design point. At these off-design conditions the influence of viscous flow effects becomes very important. It thus becomes necessary to include a viscous model appropriate for the range of flow conditions of interest.

Although the Navier-Stokes are correct (to first order) as written, these equations become excessively stiff when solved directly for viscous flows. Generally, the actual set of equations which are solved numerically are the Reynolds-Averaged Navier-Stokes equations. In these equations, the effects of very small flow structures are represented to the overall flow in the form of an effective viscosity. The remaining task then becomes one of appropriately describing this effective viscosity. In turbomachinery, the viscous effects are generally confined to a very narrow region near the solid surfaces referred to as the boundary layer. A considerable number of methods have been considered by various researchers for solving viscous problems. For the range of Reynolds numbers typically found in gas turbine engines, turbulent viscous flow models are generally used. Two basic types of turbulent flow models exist. Either the viscous flows are solved separately from the outer (inviscid) flow, or the viscous model is integrated directly into the flow solver.

For flows which can be well described by the assumption of a thin, well attached boundary layer, it can be advantageous to solve for the boundary layer flow sepa-

rately from the outer flow. However, it often becomes less clear how to implement these models when the boundary layers becomes separated or when the general flow direction is not well specified. An excellent review of these types of methods can be found in the paper by Lighthill [31].

The second class of methods are those that couple the turbulence model directly with the flow solver. In these methods the turbulence model uses the state of the flow field to calculate what the effective turbulent stresses should be. These effective stresses are then communicated back to the flow solver in the form of an effective coefficient of viscosity. The complexity of these models varies from relatively simple algebraic models up to models which solve a number of partial differential equations. In general, algebraic models are better suited for flows in which the general structure of the flow field is known before hand. This is due to the need to integrate various flow properties in directions which are assumed to correspond to known flow directions. For a less predictable flow field, a rigorous application of these models becomes more difficult. A type of method better suited for less well specified flow fields is the partial differential equation turbulence model. Considerable variety exists in how to implement such a method. A comparison of several popular choices is presented by Launder and Spalding [29]. Following their development, a two-equation k-ϵ turbulence model was implemented for this study.

F.1 The k-ϵ Turbulence Model

The k-ϵ turbulence model computes the evolution of the turbulent kinetic energy (k) and the dissipation rate (ϵ) of turbulent kinetic energy. From these two quantities, an effective turbulent viscosity can be computed as,

$$\mu_t = \rho C_\mu \frac{k^2}{\epsilon} \tag{F.1}$$

where C_μ is an experimentally determined constant. When the governing Navier-Stokes equations are solved, this turbulent viscosity is added to the regular viscosity

and the equations are advanced in the normal way.

Using the notation of Holmes and Connell [23] extended to three-dimensional cylindrical coordinates, the k-ϵ turbulence model can be presented as,

$$\frac{\partial \vec{W}_t}{\partial t} + \frac{\partial \left(\vec{E}_t - \vec{R}_t\right)}{\partial x} + \frac{1}{r}\frac{\partial \left(\vec{F}_t - \vec{S}_t\right)}{\partial \theta} + \frac{1}{r}\frac{\partial r \left(\vec{G}_t - \vec{T}_t\right)}{\partial r} = \vec{H}_t - \vec{I}_t \tag{F.2}$$

$$\vec{W}_t = \begin{pmatrix} \rho k \\ \rho \epsilon \end{pmatrix} \quad \vec{E}_t = \begin{pmatrix} \rho u_x k \\ \rho u_x \epsilon \end{pmatrix} \quad \vec{F}_t = \begin{pmatrix} \rho u_\theta k \\ \rho u_\theta \epsilon \end{pmatrix} \quad \vec{G}_t = \begin{pmatrix} \rho u_r k \\ \rho u_r \epsilon \end{pmatrix} \tag{F.3}$$

$$\vec{R}_t = \begin{pmatrix} \tau^k_{xx} \\ \tau^\epsilon_{xx} \end{pmatrix} \quad \vec{S}_t = \begin{pmatrix} \tau^k_{\theta\theta} \\ \tau^\epsilon_{\theta\theta} \end{pmatrix} \quad \vec{T}_t = \begin{pmatrix} \tau^k_{rr} \\ \tau^\epsilon_{rr} \end{pmatrix} \tag{F.4}$$

$$\vec{H}_t = \begin{pmatrix} \mu_t G \\ C_1 \epsilon \mu_t \frac{G}{k} \end{pmatrix} \quad \vec{I}_t = \begin{pmatrix} \rho \epsilon \\ C_2 \rho \frac{\epsilon^2}{k} \end{pmatrix} \tag{F.5}$$

$$\tau^k_{xx} = \frac{\mu_t}{\sigma_k}\frac{\partial k}{\partial x} \quad \tau^k_{\theta\theta} = \frac{\mu_t}{\sigma_k}\frac{1}{r}\frac{\partial k}{\partial \theta} \quad \tau^k_{rr} = \frac{\mu_t}{\sigma_k}\frac{\partial k}{\partial r} \tag{F.6}$$

$$\tau^\epsilon_{xx} = \frac{\mu_t}{\sigma_\epsilon}\frac{\partial \epsilon}{\partial x} \quad \tau^\epsilon_{\theta\theta} = \frac{\mu_t}{\sigma_\epsilon}\frac{1}{r}\frac{\partial \epsilon}{\partial \theta} \quad \tau^\epsilon_{rr} = \frac{\mu_t}{\sigma_\epsilon}\frac{\partial \epsilon}{\partial r} \tag{F.7}$$

$$G = \left(\frac{\partial u_i}{\partial x_k} + \frac{\partial u_k}{\partial x_i}\right)\frac{\partial u_i}{\partial x_k} \tag{F.8}$$

where C_1, C_2, σ_k, and σ_ϵ are experimentally determined constants. These equations together with Equation F.1 describe the convection $\left(\vec{E}_t, \vec{F}_t, \vec{G}_t\right)$, diffusion $\left(\vec{R}_t, \vec{S}_t, \vec{T}_t\right)$, production $\left(\vec{H}_t\right)$, and destruction $\left(\vec{I}_t\right)$ of the quantities k and ϵ. The following values for the modeling constants have been used.

$$C_\mu = 0.09 \quad C_1 = 1.44 \quad C_2 = 1.92 \quad \sigma_k = 1.0 \quad \sigma_\epsilon = 1.3 \tag{F.9}$$

These constants are the ones presented by Launder and Spalding [29], and are considered appropriate for both free shear flows and flow near solid boundaries.

F.2 Wall Functions

The use of a turbulence model when solving the Navier-Stokes equations reduces the computational requirements by several orders of magnitude when compared to a direct turbulent simulation. Even so, the resulting Reynolds-Averaged Navier-Stokes equations can still be quite stiff. In order to resolve the full details of a turbulent boundary layer, grid points must be placed at values of y^+ as small as 1. This requirement can dictate the need for large computational resources. In order to further reduce the need to calculate the inner portion of the boundary layer in such detail, wall functions can be employed. The use of wall functions permits the first interior computational point to be placed at a value of y^+ in the range of 30-150. Wall functions are the result of approximations to the boundary layer flow that can be made within the "Law-of-the-Wall" region of the flow. Experiments have shown that in this region the shear stress is essentially constant [54]. With the additional assumption of local equilibrium flow, the generation and dissipation of turbulent kinetic energy can be assumed to be equal. Using these assumptions, the turbulent energy equation can then be integrated from the wall to a near-wall point p as shown in Chieng and Launder [5]. This integration yields,

$$\tau_{wall} = \frac{\kappa^* \rho u_p k_p^{1/2}}{\ln\left[\frac{E^* y_p k_p^{1/2}}{\nu}\right]} \tag{F.10}$$

with $E^* = 5.0$ and $\kappa^* = 0.23$, which are consistent with the constants given earlier. With the assumption that ϵ be proportional to the mixing length in the inner region, and the knowledge that ϵ must be zero on the wall, the dissipation equation can be integrated to yield,

$$\epsilon_p = \frac{k_p^{2/3}}{c_l y_p} \tag{F.11}$$

with $c_l = 2.55$. These relations presuppose that the value of k is known at point p. This value can be obtained by solving the regular turbulent energy equation at the near-wall grid point p using the condition that there be no flux through the solid boundary.

One of the consequences of the use of wall functions to describe the flow near a solid boundary is the need to modify the wall boundary condition. Since the wall shear stress has been computed by using the wall function it is no longer appropriate to specify a zero velocity condition at the wall. What is most important is that the Navier-Stokes flow solver "feel" the correct wall shear stress. Therefore, a wall slip velocity is used to represent this information to the governing equations. It is important to note that the implementation of this point is specific to the method being used to solve the flow equations. By using the known wall shear stress and the near-wall velocity and density, the appropriate slip velocity at the wall can then be backed out. This condition does not affect the remaining boundary conditions required by the Navier-Stokes solver as long as the slip velocity remains parallel to the solid boundary. An equivalent way to think of the slip velocity is that it takes on the velocity at the edge of the laminar sub-layer while the thickness of this sub-layer is disregarded.

F.3 Implementation of the Turbulent Model

Due to the similarity in structure between the turbulent model equations and the Navier-Stokes equations, standard numerical methods used for fluid dynamics can be used to solve them. Since the flow of information for the turbulent model equations moves at the convective speed, for a low Mach number flow a less accurate time marching scheme is required than the one used for the Navier-Stokes equations (where waves move at the speed of sound). Also, since the grid tends to be more dense in the viscous regions of the flow, the spatial accuracy may also be lower. For simplicity and robustness, a two-stage MacCormack Predictor-Corrector method was chosen to integrate the turbulent model equations. The turbulent equations are then integrated separately from the flow equations, but at the same rate, in a time-accurate manner.

Additional consideration must also be given to the specification of the turbulent model values at the boundaries of the turbulent calculation. On solid surfaces, no values are needed since no fluxes are permitted at the surface. As stated in Chapter 3,

the turbulent flow model is only applied to the grid regions surrounding the blades. Therefore, it is necessary to specify values for the turbulent quantities at the free edge. This specification is complicated by the fact that some portions of this boundary are inflow boundaries and other portions are outflow boundaries. In addition, there is no way to know which type the boundaries will be a priori. A simple solution was to extrapolate the values from the next-to-last grid point out to the edge point. In this way, the effect of the turbulent kinetic energy and dissipation convecting with the flow is approximated for an outlet boundary. At an inlet boundary, the lack of sources of production of turbulent kinetic energy, coupled with its destruction, tended to drive these edge values of k and ϵ to zero as desired. In this way, this simple method of extrapolation produced the desired physical effect at both inlet and exit boundaries.

Appendix G

One-Dimensional Characteristic Boundary Conditions for the Three-Dimensional Euler Equations in Cylindrical Coordinates

At the boundary of a numerical domain, it is no longer possible to employ the same solution technique as the one used for the interior region. For solid boundaries, it is usually possible to calculate values for the boundary points by extracting information from the nearby interior points. This task is not as simple at a free boundary since the specification of the values on this boundary requires more information than can be obtained from the interior flow solution alone. On free boundaries, the influence of the fluid from outside the computational domain must be represented. This will require that the form of the exterior flow field be specified beforehand. What is needed is to separate the governing equations into parts which represent the flow of information into and out of the computational domain. For each piece of information required from outside of the domain, an exterior boundary condition will need to be

specified. The remaining pieces of information will come from the interior flow field. These two sources of information can then be combined to yield a solution at a free boundary.

G.1 Theory

The method used to separate the governing equations into incoming and outgoing parts is the method of characteristics. The theory and its application to the Euler equations are taken from the notes of MacCormack [33].

To begin, consider a one-dimensional unsteady set of equations in the following form,

$$\frac{\partial \vec{U}}{\partial t} + A\frac{\partial \vec{U}}{\partial x} = \vec{Q} \tag{G.1}$$

where A is a constant coefficient matrix. These equations can be written in a different form by applying a similarity transformation to the matrix A. When this is done, the equations become.

$$\frac{\partial \vec{V}}{\partial t} + \Lambda\frac{\partial \vec{V}}{\partial x} = \vec{R} \tag{G.2}$$

$$\vec{V} = S\vec{U}$$

$$\vec{R} = S\vec{Q}$$

The matrices S and Λ correspond to the left eigenvector and the eigenvalue matrices of A respectively. These matrices satisfy the following relation,

$$SAS^{-1} = \Lambda = \begin{bmatrix} \lambda_1 & & 0 \\ & \ddots & \\ 0 & & \lambda_n \end{bmatrix} \tag{G.3}$$

where Λ is a diagonal matrix containing the eigenvalues of A. Since Λ is diagonal, these equations are now decoupled and each equation can be written individually.

$$\frac{\partial V_i}{\partial t} + \lambda_i\frac{\partial V_i}{\partial x} = R_i \tag{G.4}$$

The equation now has the simple form of a (inhomogeneous) convection equation where the quantity V_i is convected at speed λ_i. Thus, the sign of λ_i will determine the direction this equation must be integrated.

Given a free boundary at some x location, there will be, in general, some number of transformed equations with positive λ_i and the remainder with negative λ_i. Each equation for which the flow of information is into the computational domain must be accompanied by a specification of the exterior flow field. The equations which are integrated from the interior can be solved in the form given in equation G.4.

The implementation of this method becomes clearer when a specific case is considered.

G.2 Similarity Transformation of the Simplified Three-Dimensional Euler Equations

For the three-dimensional Euler equations in cylindrical coordinates, the variables in equation G.1 take on the following values.

$$\vec{U} = \begin{pmatrix} \rho \\ u \\ v \\ w \\ p \end{pmatrix} \tag{G.5}$$

$$A = \begin{bmatrix} \bar{u} & \bar{\rho} & 0 & 0 & 0 \\ 0 & \bar{u} & 0 & 0 & 1/\bar{\rho} \\ 0 & 0 & \bar{u} & 0 & 0 \\ 0 & 0 & 0 & \bar{u} & 0 \\ 0 & \gamma\bar{p} & 0 & 0 & \bar{u} \end{bmatrix} \tag{G.6}$$

$$\vec{Q} = \begin{pmatrix} 0 \\ 0 \\ \frac{-\bar{v}\bar{w}}{r} \\ \frac{\bar{v}^2}{r} \\ 0 \end{pmatrix} \tag{G.7}$$

Obviously, this does not give the entire form of the three-dimensional Euler equations. In order to utilize the theory presented in the previous section, the derivatives with respect to θ and r have been ignored. This will result in a method that only allows for solutions which are uniform in θ and r to exist at the exit. This deficiency will be addressed in the section on three-dimensional non-reflecting boundary conditions. In addition to neglecting certain derivatives, other concessions must be made in order to use this form of the boundary equations. First, the matrix A must be treated as a constant throughout the analysis (note the use of over-bars to distinguish the constant values from the variables). This is a reasonable approximation if the variations at the exit are small. Second, the inlet and exit boundaries must be perpendicular to the x axis (or the determination of incoming and outgoing waves must be modified).

For the given A matrix, the S matrix is:

$$S = \begin{bmatrix} 1 & 0 & 0 & 0 & -1/\bar{c}^2 \\ 0 & 0 & 1 & 0 & 0 \\ 0 & 0 & 0 & 1 & 0 \\ 0 & \bar{\rho}\bar{c} & 0 & 0 & 1 \\ 0 & -\bar{\rho}\bar{c} & 0 & 0 & 1 \end{bmatrix} \tag{G.8}$$

and the corresponding eigenvalues are.

$$\Lambda = \begin{bmatrix} \bar{u} & 0 & 0 & 0 & 0 \\ 0 & \bar{u} & 0 & 0 & 0 \\ 0 & 0 & \bar{u} & 0 & 0 \\ 0 & 0 & 0 & \bar{u}+\bar{c} & 0 \\ 0 & 0 & 0 & 0 & \bar{u}-\bar{c} \end{bmatrix} \tag{G.9}$$

By applying this transformation, the following relations are found.

$$\delta\rho - \frac{1}{\bar{c}^2}\delta p = -\bar{u}\frac{\Delta t}{\Delta x}\left(\Delta\rho - \frac{1}{\bar{c}^2}\Delta p\right) \tag{G.10}$$

$$\delta v = -\bar{u}\frac{\Delta t}{\Delta x}(\Delta v) - \frac{\bar{v}\bar{w}}{r}\Delta t \tag{G.11}$$

$$\delta w = -\bar{u}\frac{\Delta t}{\Delta x}(\Delta w) + \frac{\bar{v}^2}{r}\Delta t \tag{G.12}$$

$$\bar{\rho}\bar{c}\delta u + \delta p = -(\bar{u} + \bar{c})\frac{\Delta t}{\Delta x}(\bar{\rho}\bar{c}\Delta u + \Delta p) \tag{G.13}$$

$$-\bar{\rho}\bar{c}\delta u + \delta p = -(\bar{u} - \bar{c})\frac{\Delta t}{\Delta x}(-\bar{\rho}\bar{c}\Delta u + \Delta p) \tag{G.14}$$

$$\delta(\ ) = (\ )^{(n+1)} - (\ )^{(n)}$$

$$\Delta(\ ) = (\ )_{(i+1)} - (\ )_{(i)}$$

The operators δ and Δ represent difference operators in time and space respectively. A simple one sided difference has been indicated, but higher order difference operators may be used. It is important that the spatial difference terms be taken in the proper direction (upwind or downwind) in agreement with the flow of information dictated by the differential equation. A closer inspection of these relations shows that the first three equations represent the convection of one entropy and two vorticity modes at the speed of the flow. The fourth and fifth equations give the convection of the potential modes at their respective convective velocities.

Consistent with the properties of compressible supersonic flow, no information will travel in the upstream direction. This requires the user to supply all of the flow quantities at the inlet, and none at the exit. The subsonic case is more difficult since a mixture of information from the interior and exterior of the flow domain must be used to form the boundary conditions. It is this subsonic case which will be considered in the next two sections.

G.3 Inlet Boundary

For the subsonic inlet case only one of the characteristic relations can be used to provide information from the interior of the flow solution (G.14). This requires that the user specify four pieces of flow information to complete the description of the flow at the inlet. The form of the user specified information is open to some interpretation. By consideration of equation G.14, the minimum requirement of the user specified conditions is that a relation between pressure and axial velocity be given. The user is free to specify the remaining quantities. However, it is generally advantageous to try to specify the same quantities which are possible to specify in real flow situations. The case shown here will be for the specification of the total pressure, total temperature, tangential and radial velocity. The specification of the inlet flow angles is also appropriate in many cases. For this case, the relation between pressure and axial velocity can be derived from the isentropic relations.

$$p_t = p\left(1 + \frac{\gamma - 1}{2} M^2\right)^{\frac{\gamma}{\gamma-1}} = p\left(\frac{T_t}{T}\right)^{\frac{\gamma}{\gamma-1}} \tag{G.15}$$

$$T_t = T + \frac{u^2 + v^2 + w^2}{2C_p} \tag{G.16}$$

Provided that v and w can be specified as a function of u (and possibly time)), the pressure can be written entirely as a function of u using Equations G.15 and G.16. The form of this relation will depend on the method in which the tangential and radial velocities are specified. The end result is the ability to evaluate the partial derivative of pressure with respect to axial velocity ($\frac{\partial p}{\partial u}$). This value can substituted into equation G.14 to yield.

$$-\bar{\rho}\bar{c}\delta u + \frac{\partial p}{\partial u}\delta u = -\left(\bar{u} - \bar{c}\right)\frac{\Delta t}{\Delta x}\left(-\bar{\rho}\bar{c}\Delta u + \Delta p\right) \tag{G.17}$$

$$\Delta(\,) = (\,)_{(i=2)} - (\,)_{(i=1)}$$

Using the data at the current time step, this equation can be evaluated and solved for δu. The axial velocity can then be updated as such.

$$u_{i=1}^{(n+1)} = u_{i=1}^{(n)} + \delta u \tag{G.18}$$

Since v, w, p, and T have been previously expressed in terms of u, all of these terms can be evaluated.

$$\begin{aligned} v_{i=1}^{(n+1)} &= v\left(u_{i=1}^{(n+1)}\right) \\ w_{i=1}^{(n+1)} &= w\left(u_{i=1}^{(n+1)}\right) \\ p_{i=1}^{(n+1)} &= p\left(u_{i=1}^{(n+1)}\right) \\ T_{i=1}^{(n+1)} &= T\left(u_{i=1}^{(n+1)}\right) \end{aligned} \tag{G.19}$$

These five known quantities completely specify the condition at the inlet boundary.

G.4 Exit Boundary

For the exit boundary, four of the characteristic relations are required.

$$\delta\rho - \frac{1}{\bar{c}^2}\delta p = -\bar{u}\frac{\Delta t}{\Delta x}\left(\Delta\rho - \frac{1}{\bar{c}^2}\Delta p\right) \equiv R_1 \tag{G.20}$$

$$\delta v = -\bar{u}\frac{\Delta t}{\Delta x}(\Delta v) - \frac{\bar{v}\bar{w}}{r}\Delta t \equiv R_2 \tag{G.21}$$

$$\delta w = -\bar{u}\frac{\Delta t}{\Delta x}(\Delta w) + \frac{\bar{v}^2}{r}\Delta t \equiv R_3 \tag{G.22}$$

$$\bar{\rho}\bar{c}\delta u + \delta p = -\left(\bar{u} + \bar{c}\right)\frac{\Delta t}{\Delta x}\left(\bar{\rho}\bar{c}\Delta u + \Delta p\right) \equiv R_4 \tag{G.23}$$

$$\Delta\left(\ \right) = \left(\ \right)_{(i=NI)} - \left(\ \right)_{(i=NI-1)}$$

In the case of the exit, less guidance is obtained in how to specify the one remaining quantity. A consideration of the modes of the Euler equations provides some guidance in this area. Since the only mode which permits information to travel upstream in a

subsonic flow is a pressure mode, it is reasonable to assume that the pressure would be an appropriate variable to specify at the exit. For the choice of specifying the exit pressure, the solution to these equations is straightforward.

$$\delta p = p_{\text{specified}} - p_{i=NI}^{(n)} \tag{G.24}$$

$$\delta \rho = R_1 + \frac{\delta p}{\bar{c}^2} \tag{G.25}$$

$$\delta u = \frac{R_4 - \delta p}{\bar{\rho}\bar{c}} \tag{G.26}$$

$$\delta v = R_2 \tag{G.27}$$

$$\delta w = R_3 \tag{G.28}$$

$$\begin{aligned}
p_{i=NI}^{(n+1)} &= p_{i=NI}^{(n)} + \delta p \\
\rho_{i=NI}^{(n+1)} &= \rho_{i=NI}^{(n)} + \delta \rho \\
u_{i=NI}^{(n+1)} &= u_{i=NI}^{(n)} + \delta u \\
v_{i=NI}^{(n+1)} &= v_{i=NI}^{(n)} + \delta v \\
w_{i=NI}^{(n+1)} &= w_{i=NI}^{(n)} + \delta w
\end{aligned} \tag{G.29}$$

These five quantities completely specify the condition for the exit boundary.

Appendix H

Two-Dimensional Non-Reflecting Boundary Conditions

In virtually any numerical solution method to a fluid flow problem, the greatest amount of modeling uncertainty is involved with the specification of boundary conditions. One of the least advanced areas of boundary condition modeling involves entrance and exit flow boundaries. At these boundaries the flow field has been artificially truncated. This results in some ambiguity as to what type of upstream and downstream behavior the boundary is to represent. In many cases, the goal is to allow the interior portion of the numerical flow solver to 'feel' as if the boundaries are very far away. Indeed, what is done in many cases is to place these boundaries at a suitably far distance from the flow region of interest. This solution method becomes unacceptable for many unsteady problems due to the long time required for this large domain to react to any unsteady behavior. In addition, in some problems it is not possible to move the inlet and exit boundaries far enough away. The most challenging situation arises when it is desired to set a specific flow situation (such as a back-pressure) near to the flow region of interest.

Clearly when the boundaries are moved near to the flow field of interest it is not possible to specify constant flow conditions (even for a steady flow). At these points it then becomes more appropriate to specify less specific quantities such as average pressure, temperature, and flow angle. However, the specification of the

average boundary conditions leaves the solution to the boundary values incomplete. The additional information needed to specify the boundary values can be derived from a linearized form of the governing equations. In the case of the linearized Euler equations, there exists four possible eigenmodes which specify the flow solution. Along with these eigenmodes are their associated eigenvalues which will determine the direction in which the information contained in the eigenmodes will travel. The goal of the non-reflecting boundary conditions is to allow all outgoing eigenmodes to exit the flow domain without generating any incoming modes.

H.1 Development of Two-Dimensional Unsteady Non-Reflecting Boundary Conditions

As mentioned previously, the goal of the non-reflecting boundary conditions is to allow all out-going modes of the flow solution to propagate out of the numerical domain without introducing any unwanted incoming modes. It is theoretically possible to derive a universal method that would work for all problems, whether they be steady, unsteady, of known frequency or not. Specific methods have unique advantages and drawbacks. As a result, the type of method used to achieve non-reflecting boundary conditions depends upon the type of solution desired. A description of the common methods is contained in the report by Giles [13]. For this study the approximate unsteady method, presented in the same report by Giles, will be used. This method will be used because of the inherently unsteady nature of rotating stall and the inability to know the frequency of rotating stall a priori.

Because the details of this method are contained in the report by Giles [13], only the important results will be presented here. In Appendix I the three-dimensional non-reflecting boundary conditions are derived in detail. To further examine the steps involved in constructing such a method, either of these references should suffice.

H.1.1 Theory

In order to apply a linear analysis, it is first useful to write the two-dimensional linearized Euler equations in primitive form.

$$\frac{\partial \vec{U}}{\partial t} + A\frac{\partial \vec{U}}{\partial x} + B\frac{\partial \vec{U}}{\partial y} = 0 \tag{H.1}$$

$$\vec{U} = \begin{pmatrix} \delta\rho \\ \delta u \\ \delta v \\ \delta p \end{pmatrix} = \begin{pmatrix} \rho - \bar{\rho} \\ u - \bar{u} \\ v - \bar{v} \\ p - \bar{p} \end{pmatrix}$$

$$A = \begin{bmatrix} \bar{u} & \bar{\rho} & 0 & 0 \\ 0 & \bar{u} & 0 & 1/\bar{\rho} \\ 0 & 0 & \bar{u} & 0 \\ 0 & \gamma\bar{p} & 0 & \bar{u} \end{bmatrix} \quad B = \begin{bmatrix} \bar{v} & 0 & \bar{\rho} & 0 \\ 0 & \bar{v} & 0 & 0 \\ 0 & 0 & \bar{v} & 1/\bar{\rho} \\ 0 & 0 & \gamma\bar{p} & \bar{v} \end{bmatrix}$$

The matrices A and B are treated as constants in the analysis. This is denoted by placing over-bars on the variables to represent the mean quantities of the values. The quantities in the $\vec{U}$ vector are perturbations from the mean quantities. As long as these perturbations are relatively small, linear analysis will apply.

In general, the variables in the vector $\vec{U}$ can be written as the Fourier-Laplace transform of $\tilde{u}$.

$$\vec{U}(x, y, t) = \sum \tilde{u}(k, l, \omega)\, e^{\imath(kx+ly-\omega t)} \tag{H.2}$$

Substitution of this form of the solution into the linearized Euler equations (H.1)gives.

$$(-\omega I + kA + lB)\sum \tilde{u} = 0 \tag{H.3}$$

The problem is now in the form of a standard eigenvalue problem. Having decomposed the general solution into one involving eigenmodes yields the following form of the

solution.

$$\sum \tilde{u} = \sum_{i=1}^{N} a_i \tilde{u}_i^R \tag{H.4}$$

The sum of system modes has been reduced to a sum of four right hand eigenvectors ($\tilde{u}_i^R$) of unknown magnitude (a_i). These eigenvectors are the right hand null vectors to the coefficient matrix $[-\omega I + kA + lB]$ evaluated at the appropriate eigenvalue. A set of left eigenvectors will be required as well. Since the form of the eigenvalues will change the left eigenvectors, this should wait until the eigenvalue have been determined.

One of the problems involved in implementing a non-reflecting boundary condition is the determination of which modes are entering, and which modes are leaving the numerical domain. This determination is simplified considerably if the inlet and exit boundaries are oriented perpendicular to a coordinate axis. For example, if the inlet/exit boundary is perpendicular to the x axis, it is convenient to choose k as the choice of eigenvalue to solve for. This choice makes the determination of the direction of motion of the various modes straight forward. For subsonic axial flow in the positive flow direction, three of these eigenmodes will be entering at an inlet boundary and one at an exit boundary. The remaining eigenmodes will be leaving the computational domain. It is the goal of this method to allow these modes to leave without exciting any unwanted entering modes.

Now that a choice has been made for the required eigenvalue (k), it is possible to define the left hand eigenvectors. These eigenvectors will be the left null vectors of the matrix $A^{-1}[-\omega I + kA + lB]$, and will be denoted by $\tilde{v}_j^L$. By defining the eigenvectors in this manner, the right hand eigenvectors ($\tilde{u}_i^R$) will be orthogonal to the left hand eigenvectors ($\tilde{v}_j^L$) except when $i = j$. (Note: Some additional care must be taken if there are repeated eigenvalues, but it will still be possible to construct a set of orthogonal eigenvectors.)

Using the orthogonality relationship, the statement of non-reflectivity can now be constructed. Since the solution (in the Fourier-Laplace space) can be written as a summation of the right hand eigenvectors, a particular mode can be selected out and

set to zero by pre-multiplying the entire solution by the corresponding left eigenvalue.

$$\tilde{u}_j^L \sum \tilde{u} = \tilde{u}_j^L \sum_{i=1}^{N} a_i \tilde{u}_i^R = a_j \tilde{u}_j^L \tilde{u}_j^R \stackrel{\text{set}}{=} 0 \tag{H.5}$$

Ideally this would set a_j to zero, which when substituted into Equation H.4 would eliminate this mode. However, the possibility of $\tilde{u}_j^L \tilde{u}_j^R = 0$ still remains. Even if this term is indeed zero, the equation may still be valid depending on the form of the non-zero condition. For the two-dimensional Euler equations, there exists one of these 'ill-posed' modes. Giles [13] describes this consideration in more detail and offers a solution to the problem. The result is a modified left eigenvector. This modification causes the eigenvectors to no longer be orthogonal, but Giles shows that the error induced by this modification can be minimized and that the equations are now well-posed. In addition to the modification required for well posedness, the left eigenvectors must also be approximated to low order in l and ω. The reduction of order is required to provide a low order differential equation when the non-reflecting boundary conditions are transformed back from the Fourier-Laplace space. The modified set of left eigenvectors approximated to first order is as follows.

$$\tilde{v}_1^L = \begin{pmatrix} -\bar{c}^2 & 0 & 0 & 1 \end{pmatrix} \tag{H.6}$$

$$\tilde{v}_2^L = \begin{pmatrix} 0 & \bar{\rho}\bar{c}\bar{u}\lambda & \bar{\rho}\bar{c} + \bar{\rho}\bar{c}\bar{v}\lambda & \bar{c}\lambda \end{pmatrix} \tag{H.7}$$

$$\tilde{v}_3^L = \begin{pmatrix} 0 & \bar{\rho}\bar{c} + \bar{\rho}\bar{c}\bar{v}\lambda & \frac{1}{2}\bar{\rho}\bar{c}\left(\bar{c} - \bar{u}\right)\lambda & 1 + \bar{v}\lambda \end{pmatrix} \tag{H.8}$$

$$\tilde{v}_4^L = \begin{pmatrix} 0 & -\bar{\rho}\bar{c} - \bar{\rho}\bar{c}\bar{v}\lambda & \frac{1}{2}\bar{\rho}\bar{c}\left(\bar{c} + \bar{u}\right)\lambda & 1 + \bar{v}\lambda \end{pmatrix} \tag{H.9}$$

The variable λ is equal to l/ω.

With these approximate, modified left eigenvectors, the statement of non-reflectivity given in Equation H.5 can be transformed back from Fourier-Laplace space. When this is done, all of the leading order terms will transform into time derivatives while the terms multiplying λ will become space derivatives. The set of four non-reflecting

boundary equations can thus be written in the following form.

$$A^*_{mod}\frac{\partial \vec{U}}{\partial t} + B^*_{mod}\frac{\partial \vec{U}}{\partial y} = \vec{0} \tag{H.10}$$

$$A^*_{\text{mod}} = \begin{bmatrix} -\bar{c}^2 & 0 & 0 & 1 \\ 0 & 0 & \bar{\rho}\bar{c} & 0 \\ 0 & \bar{\rho}\bar{c} & 0 & 1 \\ 0 & -\bar{\rho}\bar{c} & 0 & 1 \end{bmatrix} B^*_{\text{mod}} = \begin{bmatrix} 0 & 0 & 0 & 0 \\ 0 & \bar{\rho}\bar{c}\bar{u} & \bar{\rho}\bar{c}\bar{v} & \bar{c} \\ 0 & \bar{\rho}\bar{c}\bar{v} & \bar{\rho}\bar{c}\frac{1}{2}(\bar{c}+\bar{u}) & \bar{v} \\ 0 & -\bar{\rho}\bar{c}\bar{v} & \bar{\rho}\bar{c}\frac{1}{2}(\bar{c}+\bar{u}) & \bar{v} \end{bmatrix}$$

In order to cast these equations into a simpler form to solve, a new vector of unknowns is defined as follows.

$$\vec{c} = A^*_{\text{mod}}\vec{U} \tag{H.11}$$

Using this transformation, Equation H.10 becomes:

$$\frac{\partial \vec{c}}{\partial t} + E\frac{\partial \vec{c}}{\partial y} = \vec{0} \tag{H.12}$$

$$E = B^*_{\text{mod}}{A^*_{\text{mod}}}^{-1} = \begin{bmatrix} 0 & 0 & 0 & 0 \\ 0 & \bar{v} & \frac{1}{2}(c+\bar{u}) & \frac{1}{2}(\bar{c}-\bar{u}) \\ 0 & \frac{1}{2}(\bar{c}-\bar{u}) & \bar{v} & 0 \\ 0 & \bar{u} & 0 & \bar{v} \end{bmatrix}$$

The new set of unknowns ($\vec{c}$) are called the characteristic variables. The set of equations contained in H.12 describe the condition of non-reflectivity for all four eigenmodes.

H.1.2 Implementation

The method of implementation of these equations is no different than in the three-dimensional case presented in Appendix I.

In the case of a subsonic inlet boundary, the first three equations of the set given in H.12 are solved while the change in the remaining characteristic variable is extrapolated from the interior. By inspection, the first equation of this set has a trivial

solution $\left(\frac{\partial c_1}{\partial t} = 0\right)$. This fact can be used to simplify the procedure. At a subsonic exit, only the last equation of H.12 is used.

One additional piece of information is required to complete the implementation as described in Appendix I. The inverse of the A^*_{mod} matrix is:

$$A^*_{\text{mod}}{}^{-1} = \begin{bmatrix} -\frac{1}{\bar{c}^2} & 0 & \frac{1}{2\bar{c}^2} & \frac{1}{2\bar{c}^2} \\ 0 & 0 & \frac{1}{2\bar{\rho}\bar{c}} & -\frac{1}{2\bar{\rho}\bar{c}} \\ 0 & \frac{1}{\bar{\rho}\bar{c}} & 0 & 0 \\ 0 & 0 & \frac{1}{2} & \frac{1}{2} \end{bmatrix} \tag{H.13}$$

This matrix is required to transform back to the perturbational variables from the characteristic variables.

H.2 Evaluation of Non-Reflecting Boundary Conditions

In order to test the effectiveness of these non-reflecting boundary conditions, a series of runs was made in which the inlet and exit boundaries were brought close to the blade. A rotor blade was chosen in order to test the boundary conditions in an unsteady environment. For comparison, a run was made with the same blade and boundary conditions, but with inlet and exit boundaries four times farther away. Figure H.1 shows a contour plot of static pressure for the case with the boundaries moved farther away. This will be used as the reference case for the subsequent runs.

When the inlet and exit boundaries were brought closer to the blade, and the non-reflecting boundary conditions were used, the flow field remained essentially the same. This case is shown in Figure H.2. The only visible differences between the long and short duct cases are some minor variations at the inlet boundary. No discrepancies can be seen at the exit.

When the one-dimensional boundary conditions are used instead of the non-reflecting ones, the solution looks quite different, as shown in Figure H.3. The effect

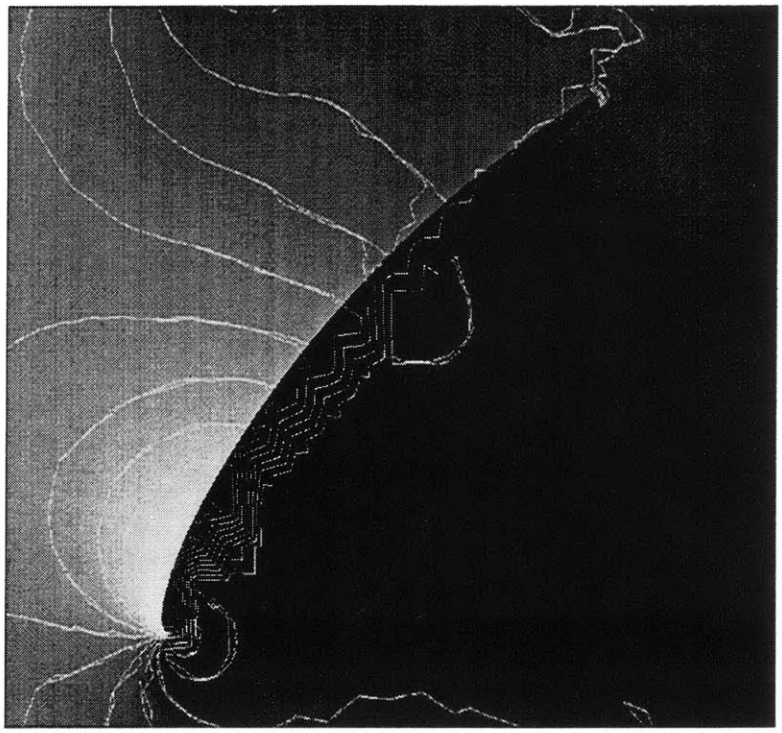

Figure H.1: Non-reflecting boundary condition test case with the duct lengths = 100% of spacing. (pressure)

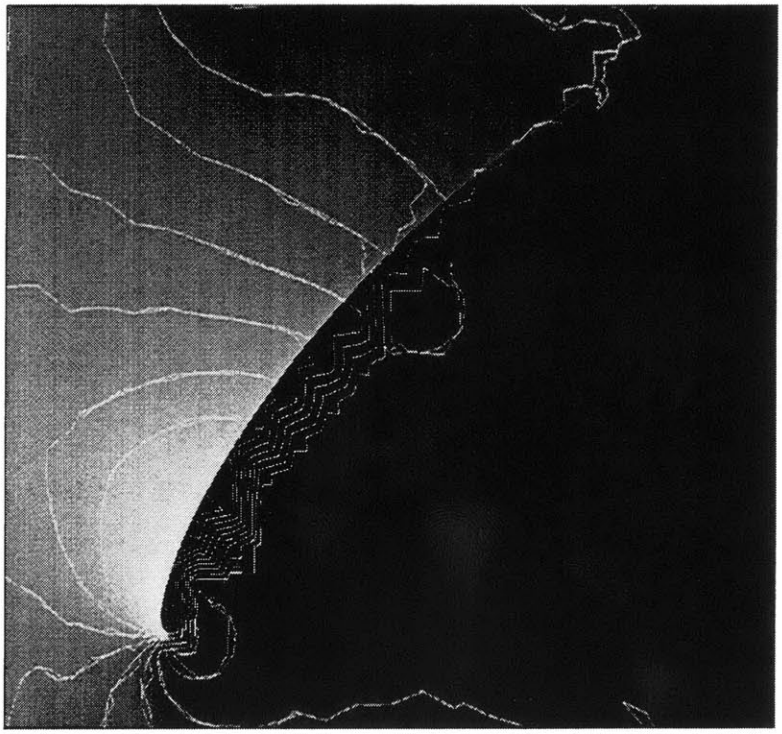

Figure H.2: Non-reflecting boundary condition test case with the duct lengths = 25% of spacing. (pressure)

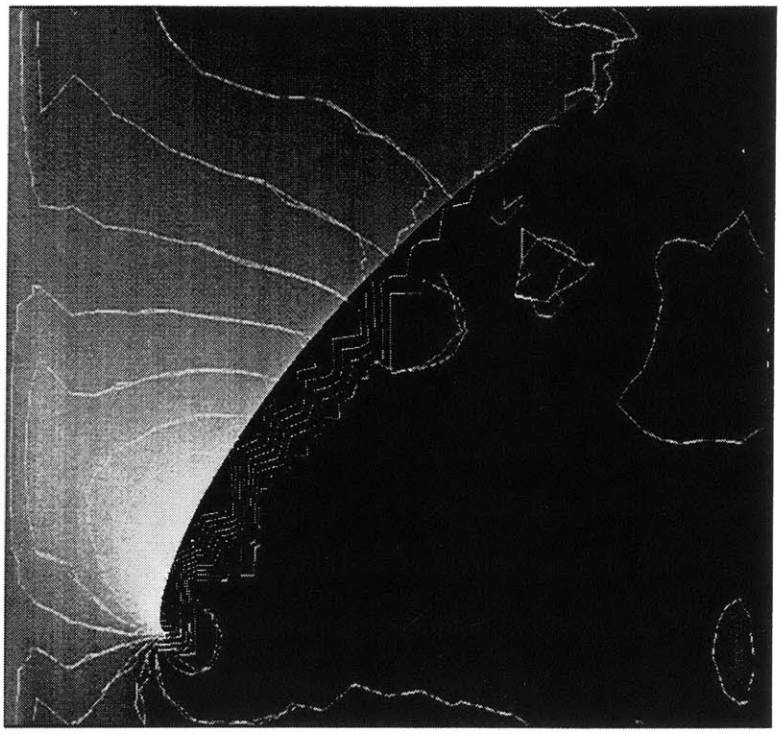

Figure H.3: Average one-dimensional boundary condition test case with the duct lengths = 25% of spacing. (pressure)

of forcing the inlet pressure to be constant is clearly evident. Also, the interaction of the blade wake and the exit boundary condition has produced some non-physical reflections back into the flow domain.

When the one-dimensional boundary conditions were applied locally, instead of in an average sense, the flow field appears similar to the reference case. As seen in Figure H.4, the inlet flow field is similar to the that of Figure H.1. The exit does show some variation from the reference case.

Although the differences in the flow fields between the different types of boundary conditions are evident, the integral quantities (such as flow and pressure rise) were nearly identical in all of these cases. What is most important for this investigation is the effect these boundary conditions have on the inception of rotating stall. This effect was studied by conducting identical computations of rotating stall using the three different boundary conditions represented in Figures H.2-H.4. For this study a twelve bladed rotor-only compressor geometry was used. Analysis of this case showed that the first two modes (harmonics) of the system are both slightly unstable

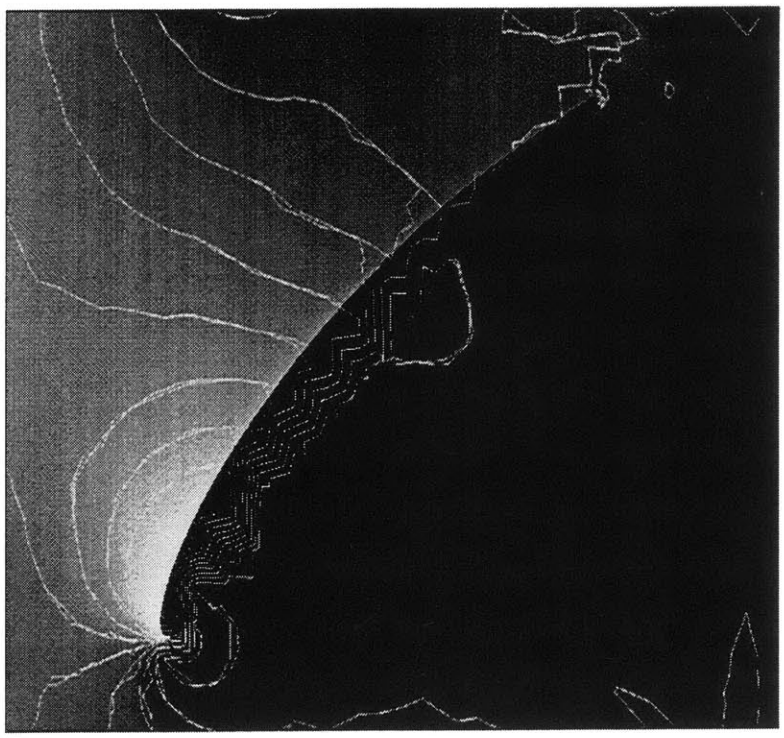

Figure H.4: Local one-dimensional boundary condition test case with the duct lengths = 25% of spacing. (pressure)

at the operating point where this test of the boundary conditions was conducted. Figure H.5 shows the time history of the first four harmonics for the case of the non-reflecting boundary conditions. The various harmonics can be seen growing towards stall, which occurs at approximately 95 rotor revolutions and involves primarily the first and second harmonics. A clipped view of this process is shown in order to allow comparison with the other results. When the purely one-dimensional boundary conditions were used (Reference Figure H.3) the response of the compressor was modified as shown in Figure H.6. As in the case with the non-reflecting boundary conditions, the first and second harmonics represent the majority of the response. However, the stability of the compressor has clearly been modified. All of the modes of the system have been stabilized somewhat. The compressor still appears to be going unstable, but the growth of the instability has been noticeably reduced. When the one-dimensional boundary conditions were applied locally instead of in a mean sense, the results given in Figure H.7 were obtained. For the single blade test case using this boundary condition (Figure H.4) the results appeared quite similar to the

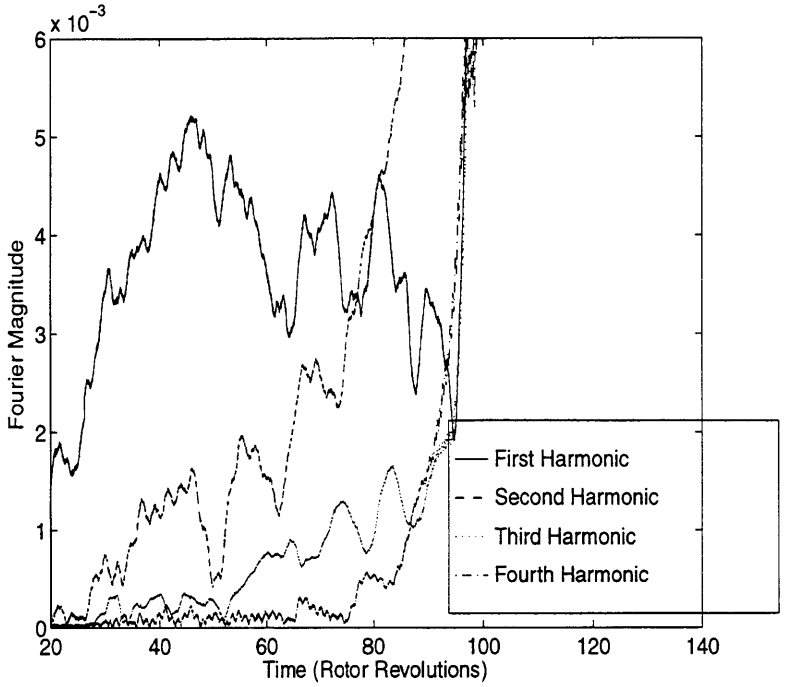

Figure H.5: Time traces of the Fourier harmonics of inlet axial velocity of the twelve bladed compressor with non-reflecting boundary conditions

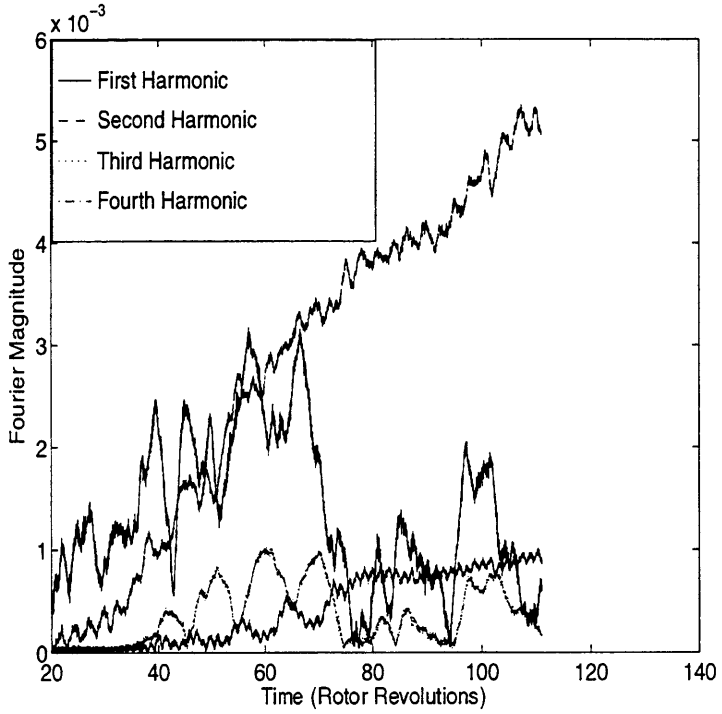

Figure H.6: Time traces of the Fourier harmonics of inlet axial velocity of the twelve bladed compressor with the average one-dimensional boundary conditions

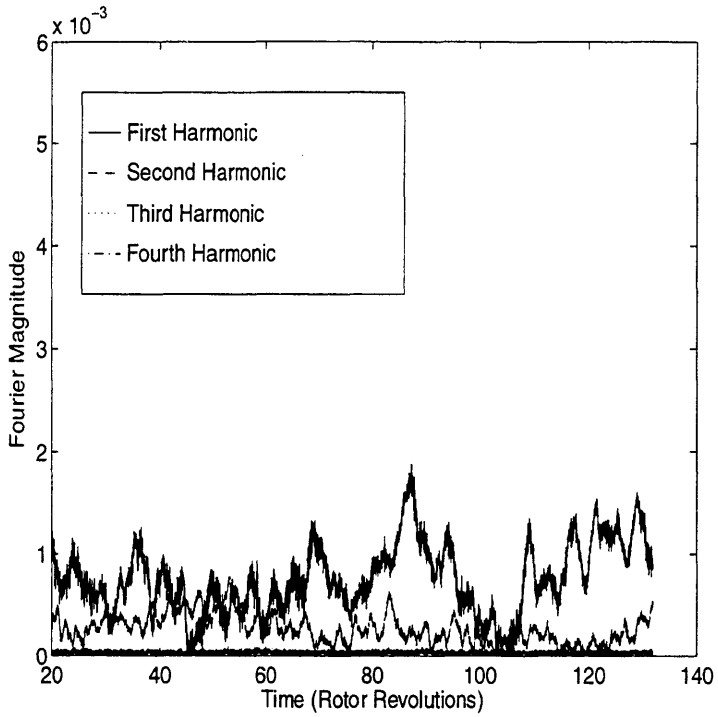

Figure H.7: Time traces of the Fourier harmonics of inlet axial velocity of the twelve bladed compressor with the locally applied one-dimensional boundary conditions

non-reflecting boundary condition. However, for the computation of rotating stall, this boundary condition shows the least agreement with the non-reflecting condition. In this case, the compressor shows no sign entering into rotating stall.

Because of differences such as a longer flow through time of the system, a direct back-to-back comparison of the non-reflecting boundary conditions with a geometry with long ducts cannot be conducted. However, the results presented serve to show that computations of the inception of rotating stall are indeed sensitive to the type of inlet and exit boundary conditions used. Therefore, for the efficient and accurate computation of rotating stall, the non-reflecting type of boundary conditions should be used.

Appendix I

Three-Dimensional Approximate Unsteady Non-Reflecting Boundary Conditions for the Euler Equations

Inherent in any solution to the three-dimensional Euler equations is the need to specify inlet and exit boundary conditions to the flow field of interest. For various reasons it becomes advantageous, or absolutely necessary, to place these boundaries near the flow domain of prime interest. However, when this is done, the variations in the flow field that impinge upon these boundaries will cause undesired non-physical reflections back into the domain of interest. This sections describes a method to construct the boundary conditions in such a way that these unwanted reflections will be minimized. The method described here is a direct extension of the theory presented by Giles [13] with the details of the implementation given in a separate report also by Giles [15]. In Giles' report, he describes four solution methods for the application of non-reflecting boundary conditions for various flow solution methods. In this work, only the approximate unsteady procedure will be considered. However, a large portion of the results are applicable to any one of the solution methods covered

in Giles' paper.

I.1 Theory

I.1.1 Eigenvalue Analysis

The basic idea of the non-reflecting boundary conditions will be to allow waves which are moving out of the computational domain to exit without causing unwanted reflected waves to be created at the boundary. This concept can be stated more exactly when the solution is considered to be composed of a finite number of eigenmodes. Since each eigenmode will have a characteristic speed and direction, the statement of non-reflectivity then becomes one of specifying that the magnitude of eigenmodes entering the domain be zero. In order to construct an Eigen analysis of the equations it is necessary that they first be linearized. Using the linearized form, analysis of the equations in Fourier space can be used to represent the solution as a superposition of eigenmodes. This can be stated as follows

$$\vec{U}(x,y,z,t) = \sum \tilde{u}(k,l,m,\omega)\, e^{i(kx+ly+mz-\omega t)} \tag{I.1}$$

where $\tilde{u}$ is the Fourier-Laplace transform of $\vec{U}$. This form of the solution can then be substituted into the linearized three-dimensional Euler equations (written in primitive form)

$$\frac{\partial \vec{U}}{\partial t} + A\frac{\partial \vec{U}}{\partial x} + B\frac{\partial \vec{U}}{\partial y} + C\frac{\partial \vec{U}}{\partial z} = 0 \tag{I.2}$$

where A, B, and C are constant coefficient matrices and $\vec{U}$ represents perturbations of the flow from the equilibrium solution. After substituting I.1 into I.2, the following dispersion relation is obtained.

$$(-\omega I + kA + lB + mC)\sum \tilde{u} = 0 \tag{I.3}$$

In order for non-trivial solutions for $\tilde{u}$ to exist, the coefficient matrix of Equation I.3 must be singular. This condition yields a relation for ω, k, l, and m. For each solution to the dispersion relation (eigenvalues) there will be associated eigenvectors which are defined as

$$\left(-\underset{\sim}{\omega} I + kA + lB + mC\right)_i \tilde{u}_i^R = 0 \tag{I.4}$$

where the coefficient matrix is evaluated at eigenvalue i. Thus, in Fourier space, the solution to the governing equation becomes.

$$\sum \tilde{u} = \sum_{i=1}^{N} a_i \tilde{u}_i^R \tag{I.5}$$

When written in this form the statement of non-reflectivity becomes rather simple. The goal is to have the coefficient of each eigenmode a_i which is entering the domain equal to zero. Two basic difficulties exist in implementing this idea. First, it is necessary to be able to discern which modes represent solutions which are entering the domain. Second, a method of forcing these coefficients to zero must be created. The first of these problems can be solved directly for specific geometries. The process of forcing the desired coefficients to zero will require constructing a set of equations to solve as well as ensuring that these equations are well posed.

The determination of whether a mode is an entering or exiting the flow domain is relatively straight forward. The group velocity of a mode is given by the following relation.

$$\vec{V}_{group} = \begin{pmatrix} \frac{\partial \omega}{\partial k}\hat{x} \\ \frac{\partial \omega}{\partial l}\hat{y} \\ \frac{\partial \omega}{\partial m}\hat{z} \end{pmatrix} \tag{I.6}$$

If the inlet and exit boundaries are chosen in such a way that they are perpendicular to one of the principal axes, then the determination of whether the mode is entering or exiting the domain is direct. For example, if the inlet/exit plane is perpendicular to the x direction, then the sign of the x component of the group velocity determines whether this mode is entering or exiting the domain. From the form of I.6 it can be seen that the group velocity in the x directions can be found directly if ω has been

solved for in terms of k in the dispersion relation. Since each mode possess its own eigenvalue, this determination can be made for each mode.

Once it has been determined which modes are entering the domain, it remains to specify that the magnitude of each mode is zero. In order to perform this step, an additional set of eigenvectors will be required. The additional eigenvectors are the left eigenvectors of the system which are defined by:

$$\tilde{u}_i^L \left(-\omega I + kA + lB + mC\right)_i = 0 \tag{I.7}$$

The important feature of the left eigenvectors is that they are orthogonal to the right eigenvectors, with the exception of the right eigenvector with the corresponding eigenvalue. This statement will be modified slightly for the case of repeated eigenvalues, but it will still be possible to form orthogonal sets of eigenvectors. The usefulness of this property can be seen when the solution form given in Equation I.5 is pre-multiplied by a given left eigenvector.

$$\tilde{u}_j^L \hat{u} = \tilde{u}_j^L \sum_{i=1}^{N} a_i \tilde{u}_i^R = \tilde{u}_j^L a_j \tilde{u}_j^R \tag{I.8}$$

Using orthogonality, a particular mode can be selected out and set to zero if desired. The result is.

$$\tilde{u}_j^L \hat{u} = a_j \tilde{u}_j^L \tilde{u}_j^R \stackrel{\text{set}}{=} 0 \tag{I.9}$$

I.1.2 Well Posedness

It may seem at this point that the objective of setting the magnitude of the selected mode to zero has been achieved, but one additional concern remains. It still is possible to satisfy this relation, and have a non-zero mode, if the corresponding left and right eigenvectors are orthogonal to each other. In general, this will only occur for specific values of ω, k, l, and m, for a given flow condition. This condition will yield a relation for ω in terms of the various wave numbers and flow variables. Recalling the form of the general solution I.1, it is necessary that any solution of this relation for ω have

an imaginary part that is ≤ 0. If this condition is satisfied, there will be no mode present with an exponentially increasing magnitude in time, and the solution will be well posed. Since these equations will be solved simultaneously with an interior flow solver, one additional constraint must be evaluated to determine whether a mode with the imaginary part of ω greater than zero is a possible solution. The presence of an imaginary part to ω will in general yield a value for k with an imaginary component as well. Once again referring to the form of I.1, this condition will yield an exponentially growing mode in x. Assuming that the interior flow solution method is well posed, only a solution which decays away from the boundary in the x direction is a possible solution. Thus, for values of ω for which the corresponding left and right eigenvectors are orthogonal, if the imaginary part of ω is greater than zero and the mode has a shape which decays away from the boundary (into the computational domain), the solution is ill-posed.

If the relation fails the well posedness condition, it is then necessary to modify the left eigenvectors so that the well posedness condition is satisfied. When this is done, the eigenvectors lose their orthogonality. The end result is that Equation I.9 becomes a matrix times a vector relationship. However, the basic idea remains unchanged. For this case, the relationship for ω is derived from setting the determinant of this matrix to zero.

Up until this point, the discussion of eigenvalues and eigenvectors has been non-specific. It is possible to solve the dispersion relation for ω, k, l, or m. This choice will modify the form of the left eigenvectors. The remainder of the discussion of non-reflecting boundary conditions will assume that the boundary in question is perpendicular to the $\hat{x}$ axis. For this geometry, it is advantageous to choose to solve the dispersion relation for k. This choice will make the appropriate form of the left eigenvectors appear as follows.

$$\tilde{v}_i^L A^{-1} \left(-\omega I + k_i A + lB + mC\right) = 0 \tag{I.10}$$

This point is covered in more detail in the paper be Giles [13]. To avoid confusion,

the notation ($\tilde{v}^L$) has been used to differentiate these eigenvectors from the previous non-specific ones ($\tilde{u}^L$). An important fact is that these new left eigenvectors still possess the same orthogonality property with the original right eigenvectors.

I.1.3 Solution Form

After finding the necessary left eigenvectors for all the modes entering a given boundary and assuring their well posedness, it remains to construct the equations to be implemented at the boundary. The basic idea is to now take the inverse Fourier-Laplace transform of the equations to yield a differential equation in terms of the variables of the governing equations. In general this will yield a relation with high-order derivatives In order to yield a set of equations which can be solved practically, it is advantageous to approximate the left eigenvectors. A linear approximation to the left eigenvectors will yield a set of first-order differential equations to be solved. After taking the inverse Fourier-Laplace transform of the relation with the simplified eigenvectors (replace ω with $-\frac{\partial}{\partial t}$ and, l and m with $\frac{\partial}{\partial y}$ and $\frac{\partial}{\partial z}$), a first-order differential equation will be produced. It should then be possible to integrate this equation with the same numerical procedure used to integrate the governing equations.

I.2 Application to the Euler Equations

The three-dimensional linearized Euler equations can be written in the following primitive variable form.

$$\frac{\partial \vec{U}}{\partial t} + A\frac{\partial \vec{U}}{\partial x} + B\frac{\partial \vec{U}}{\partial y} + C\frac{\partial \vec{U}}{\partial z} = 0 \tag{I.11}$$

$$\vec{U} = \begin{pmatrix} \delta\rho \\ \delta u \\ \delta v \\ \delta w \\ \delta p \end{pmatrix} = \begin{pmatrix} \rho - \bar{\rho} \\ u - \bar{u} \\ v - \bar{v} \\ w - \bar{w} \\ p - \bar{p} \end{pmatrix}$$

$$A = \begin{bmatrix} \bar{u} & \bar{\rho} & 0 & 0 & 0 \\ 0 & \bar{u} & 0 & 0 & 1/\bar{\rho} \\ 0 & 0 & \bar{u} & 0 & 0 \\ 0 & 0 & 0 & \bar{u} & 0 \\ 0 & \gamma\bar{p} & 0 & 0 & \bar{u} \end{bmatrix} \quad B = \begin{bmatrix} \bar{v} & 0 & \bar{\rho} & 0 & 0 \\ 0 & \bar{v} & 0 & 0 & 0 \\ 0 & 0 & \bar{v} & 0 & 1/\bar{\rho} \\ 0 & 0 & 0 & \bar{v} & 0 \\ 0 & 0 & \gamma\bar{p} & 0 & \bar{v} \end{bmatrix} \quad C = \begin{bmatrix} \bar{w} & 0 & 0 & \bar{\rho} & 0 \\ 0 & \bar{w} & 0 & 0 & 0 \\ 0 & 0 & \bar{w} & 0 & 0 \\ 0 & 0 & 0 & \bar{w} & 1/\bar{\rho} \\ 0 & 0 & 0 & \gamma\bar{p} & \bar{w} \end{bmatrix}$$

In the linearized form, the coefficient matrices are computed using the mean flow quantities (denoted by over-bars). These mean values are treated as constants in the subsequent analysis. The quantities contained in the $\vec{U}$ vector are perturbations from the mean values.

The development of the non-reflecting boundary conditions for these equations will directly follow the method described in the previous section. The body of knowledge which has been gained in past analysis of these equations will prove useful in analyzing and describing the results of the application of the non-reflective boundary condition theory.

A great deal of the algebra has been omitted from this description as it tends to distract from the central idea. In many cases the algebraic steps are quite numerous and have been performed using a symbolic mathematics software program. However, most of the results can be verified by simple direct substitution.

I.2.1 Eigenvalue Analysis

Before proceeding directly into the analysis, it is useful to take the additional step of non-dimensionalizing the governing equations. By dividing the equations by the density and speed of sound (based on the mean values), the coefficient matrices become.

$$A = \begin{bmatrix} \bar{u} & 1 & 0 & 0 & 0 \\ 0 & \bar{u} & 0 & 0 & 1 \\ 0 & 0 & \bar{u} & 0 & 0 \\ 0 & 0 & 0 & \bar{u} & 0 \\ 0 & 1 & 0 & 0 & \bar{u} \end{bmatrix} \quad B = \begin{bmatrix} \bar{v} & 0 & 1 & 0 & 0 \\ 0 & \bar{v} & 0 & 0 & 0 \\ 0 & 0 & \bar{v} & 0 & 1 \\ 0 & 0 & 0 & \bar{v} & 0 \\ 0 & 0 & 1 & 0 & \bar{v} \end{bmatrix} \quad C = \begin{bmatrix} \bar{w} & 0 & 0 & 1 & 0 \\ 0 & \bar{w} & 0 & 0 & 0 \\ 0 & 0 & \bar{w} & 0 & 0 \\ 0 & 0 & 0 & \bar{w} & 1 \\ 0 & 0 & 0 & 1 & \bar{w} \end{bmatrix}$$

No distinction has been made in the symbols used for the dimensional and non-dimensional form, since the two forms will not be mixed, and any change between them will be well noted.

The first step in this analysis is to find the eigenvalues of the system. As stated in the Theory section, the dispersion relation will be solved for the variable k; which is consistent with the specification that the boundary of interest will be perpendicular to the $\hat{x}$ direction. This begins by solving the following relation for k.

$$\det\left(-\omega I + kA + lB + mC\right) = 0 \tag{I.12}$$

For this case, there are five roots, of which three of them are a repeated root. They are as follows.

$$\begin{aligned} k_1 = k_2 = k_3 &= \frac{\omega - l\bar{v} - m\bar{w}}{\bar{u}} \\ k_4 &= \frac{\left(\omega - l\bar{v} - m\bar{w}\right)\left(-\bar{u} + S\right)}{1 - \bar{u}^2} \\ k_5 &= \frac{\left(\omega - l\bar{v} - m\bar{w}\right)\left(-\bar{u} - S\right)}{1 - \bar{u}^2} \\ S &\equiv \sqrt{1 - \frac{\left(1 - \bar{u}^2\right)\left(l^2 + m^2\right)}{\left(\omega - l\bar{v} - m\bar{w}\right)^2}} \end{aligned} \tag{I.13}$$

Recalling that the direction of propagation of each eigenmode can be found by evaluating the group velocity, it can be determined which direction these modes will travel. For the first three modes the group velocity is.

$$\frac{\partial \omega}{\partial k_{1,2,3}} = \bar{u} \tag{I.14}$$

So, by definition of an inlet boundary, these modes will always be entering the domain at an inlet. For the fourth and fifth roots the group velocities are.

$$\frac{\partial \omega}{\partial k_4} = \frac{1 - \bar{u}^2}{-\bar{u} + 1/S} \tag{I.15}$$

$$\frac{\partial \omega}{\partial k_5} = \frac{1 - \bar{u}^2}{-\bar{u} - 1/S} \tag{I.16}$$

For solutions with purely real ω and S, the signs of the fourth and fifth group velocities depend upon the value of $\bar{u}$. For $\bar{u} > 1$ (supersonic), both of these velocities are positive. When $0 < \bar{u} < 1$ (subsonic) the group velocity of the fifth eigenvalue changes sign. Some care must be taken in considering complex values for S. Once again, see the paper by Giles [13] for details. The end result is that for subsonic flow, there are four modes which will be entering at the inlet, and one mode will enter the domain at the exit. For the remainder of this work, only this subsonic case will be considered.

The next item to be considered is the determination of the eigenvectors of the system. Technically, only the left eigenvectors are required to create a non-reflecting boundary condition, but the right eigenvectors will also be required to complete the analysis. While this may be one of the more difficult steps algebraically, displaying the steps of this process adds little to its understanding.

The determination of the eigenvectors is a result of the determination of the left and right null-vectors of the following matrix evaluated at the desired eigenvalue. For example, the first left eigenvector is a solution to the this equation.

$$\tilde{v}_1^L A^{-1} \left(-\omega I + k_1 A + l B + m C\right) = 0 \tag{I.17}$$

In applying this relation for all of the eigenvalues, the following set of left eigenvectors was found.

$$\tilde{v}_1^L = \begin{pmatrix} -1 & 0 & 0 & 0 & 1 \end{pmatrix} \tag{I.18}$$

$$\tilde{v}_2^L = \begin{pmatrix} 0 & -\bar{u}\lambda & 1 - \bar{v}\lambda & -\bar{w}\lambda & -\lambda \end{pmatrix} \tag{I.19}$$

$$\tilde{v}_3^L = \begin{pmatrix} 0 & -\bar{u}\lambda & 1 - \bar{v}\lambda - 2\bar{w}\mu & \bar{w}\lambda & -\lambda \end{pmatrix} \tag{I.20}$$

$$\tilde{v}_4^L = \begin{pmatrix} 0 & (1 - \bar{v}\lambda - \bar{w}\mu) & \bar{u}\lambda & \bar{u}\mu & (1 - \bar{v}\lambda - \bar{w}\mu)\, S \end{pmatrix} \tag{I.21}$$

$$\tilde{v}_5^L = \begin{pmatrix} 0 & -(1 - \bar{v}\lambda - \bar{w}\mu) & -\bar{u}\lambda & -\bar{u}\mu & (1 - \bar{v}\lambda - \bar{w}\mu)\, S \end{pmatrix} \tag{I.22}$$

The variables $\lambda = l/\omega$ and $\mu = m/\omega$ have been defined for convenience.

The right null vectors are determined in a similar way to the left null vectors. These vectors must satisfy a relationship such as the one given here for the first eigenvalue.

$$(-\omega I + k_1 A + lB + mC)\,\tilde{u}_1^R = 0 \tag{I.23}$$

In applying this relation for all of the eigenvalues, the following set of right eigenvectors was found.

$$\tilde{u}_1^R = \begin{pmatrix} 1 \\ 0 \\ 0 \\ 0 \\ 0 \end{pmatrix} \quad \tilde{u}_2^R = \begin{pmatrix} 0 \\ -\bar{u}\mu \\ 0 \\ 1-\bar{v}\lambda-\bar{w}\mu \\ 0 \end{pmatrix} \quad \tilde{u}_3^R = \begin{pmatrix} 0 \\ 0 \\ \mu \\ -\lambda \\ 0 \end{pmatrix} \tag{I.24}$$

$$\tilde{u}_4^R = \begin{pmatrix} 1-\bar{v}\lambda-\bar{w}\mu-\frac{(1-\bar{v}\lambda-\bar{w}\mu)(S-\bar{u})\bar{u}}{1-\bar{u}^2} \\ \frac{(1-\bar{v}\lambda-\bar{w}\mu)(S-\bar{u})}{1-\bar{u}^2} \\ \lambda \\ \mu \\ 1-\bar{v}\lambda-\bar{w}\mu-\frac{(1-\bar{v}\lambda-\bar{w}\mu)(S-\bar{u})\bar{u}}{1-\bar{u}^2} \end{pmatrix} \tag{I.25}$$

$$\tilde{u}_5^R = \begin{pmatrix} 1-\bar{v}\lambda-\bar{w}\mu-\frac{(1-\bar{v}\lambda-\bar{w}\mu)(-S-\bar{u})\bar{u}}{1-\bar{u}^2} \\ \frac{(1-\bar{v}\lambda-\bar{w}\mu)(-S-\bar{u})}{1-\bar{u}^2} \\ \lambda \\ \mu \\ 1-\bar{v}\lambda-\bar{w}\mu-\frac{(1-\bar{v}\lambda-\bar{w}\mu)(-S-\bar{u})\bar{u}}{1-\bar{u}^2} \end{pmatrix} \tag{I.26}$$

At this point it is worth stopping to consider the form that these eigenvectors have taken. Since the right eigenvectors give the shapes of the modes, it is possible to describe these modes in terms of the known character of the Euler equations. The first mode contains only density variations, and thus describes the presence of density (or entropy) waves. The next two modes describe variations in velocity field with no

changes in density and pressure. This is consistent with the description of the vorticity of the flow field. All of these quantities are expected to convect with the speed of the background flow which is in agreement with the group velocity found for these modes. The last two modes contain the pressure information and thus describe the potential modes of the system. As expected, the potential variations move in opposite directions for a subsonic flow, and move in the same direction in a supersonic flow.

These eigenvectors, as written, fail the orthogonality test for the eigenvectors with repeated roots. However, it is possible to create a different set of either left or right eigenvectors which are linear combinations of the ones given which will satisfy the orthogonality relations entirely. When this is done the eigenvectors loose their present simple form. This point will be considered later when the well posedness of the non-reflecting boundary conditions is considered.

By looking ahead a few steps in the process of constructing the non-reflecting boundary conditions, a potential problem can be seen with these original left eigenvectors. To do so, first, the eigenvectors are approximated to first order about $\lambda = \mu = 0$. In this approximation, the value of S goes to 1. After this approximation, the statement of non-reflectivity can be written in the following form.

$$(A' - B'\lambda - C'\mu)\,\tilde{u} = \vec{d} \tag{I.27}$$

$$A' = \begin{bmatrix} -1 & 0 & 0 & 0 & 1 \\ 0 & 0 & 1 & 0 & 0 \\ 0 & 0 & 1 & 0 & 0 \\ 0 & 1 & 0 & 0 & 1 \\ 0 & -1 & 0 & 0 & 1 \end{bmatrix} \quad B' = \begin{bmatrix} 0 & 0 & 0 & 0 & 0 \\ 0 & \bar{u} & \bar{v} & \bar{w} & 1 \\ 0 & \bar{u} & \bar{v} & -\bar{w} & 1 \\ 0 & \bar{v} & -\bar{u} & 0 & \bar{v} \\ 0 & -\bar{v} & \bar{u} & 0 & \bar{v} \end{bmatrix}$$

$$C' = \begin{bmatrix} 0 & 0 & 0 & 0 & 0 \\ 0 & 0 & 0 & 0 & 0 \\ 0 & 0 & 2\bar{w} & 0 & 0 \\ 0 & \bar{w} & 0 & -\bar{u} & \bar{w} \\ 0 & -\bar{w} & 0 & \bar{u} & \bar{w} \end{bmatrix}$$

In this equation the matrices A', B', and C' contain the leading order (A') and first-order (B' and C') terms of the left eigenvectors. The vector $\vec{d}$ will contain zeros for all of the modes which need to be set equal to zero in order to enforce non-reflectivity. This Equation I.27 can be inversely transformed from the Fourier-Laplace space to yield.

$$A'\frac{\partial \vec{U}}{\partial t} + B'\frac{\partial \vec{U}}{\partial y} + C'\frac{\partial \vec{U}}{\partial z} = \vec{d} \tag{I.28}$$

This relation is almost in a form to be integrated directly. If the equations can be rewritten in a such a way that the matrix in front of the time derivative (A') is diagonal, then each equation can be integrated in time directly. A simple redefinition of the variables in this equation should produce an equation in this form. By defining

$$\vec{c} = A'\vec{U} \tag{I.29}$$

Equation I.28 can be written in the easier form to solve.

$$\frac{\partial \vec{c}}{\partial t} + B'A'^{-1}\frac{\partial \vec{c}}{\partial y} + C'A'^{-1}\frac{\partial \vec{c}}{\partial z} = \vec{d} \tag{I.30}$$

The problem that evolves is the fact that the matrix A' is singular and therefore has no inverse. By analyzing the first form of this equation (I.28) it can be seen that there is no relationship for the time derivative of w. It can also be seen from this set of equations that there are two equations (second and third) which specify the value of $\frac{\partial v}{\partial t}$. Since in general, it will not be possible to solve both equations simultaneously an additional relation must be satisfied to yield a simultaneous solution to both equations. This relation can be found by subtracting the second and third equations. The simple result is.

$$\frac{\partial w}{\partial y} - \frac{\partial v}{\partial z} = 0 \tag{I.31}$$

Which is identified as the value of the $\hat{x}$ component of vorticity. Specifying a zero magnitude for this component is consistent with the two original equations which set the two vortical modes equal to zero, and the fluid dynamic condition that the vortex field must be divergence free. Although consistent, this relation is not in a form which

is easily solvable in the framework of a numerical flow solver.

This deficiency was overcome by manipulating the second and third equations to yield a relation for $\frac{\partial w}{\partial t}$. The method used was to first take the time derivative of the auxiliary relation I.31 and the z derivative of the second equation of I.28.

$$\frac{\partial^2 w}{\partial y \partial t} - \frac{\partial^2 v}{\partial z \partial t} = 0 \tag{I.32}$$

$$\frac{\partial^2 v}{\partial z \partial t} + \frac{\partial}{\partial z}\left(\bar{u}\frac{\partial u}{\partial y} + \bar{v}\frac{\partial v}{\partial y} + \bar{w}\frac{\partial w}{\partial y} + \frac{\partial p}{\partial y}\right) = 0 \tag{I.33}$$

The $\frac{\partial^2 v}{\partial z \partial t}$ term can be eliminated in I.33 by using I.32. After which, the equation can be integrated in y to give.

$$\frac{\partial w}{\partial t} + \bar{u}\frac{\partial u}{\partial z} + \bar{v}\frac{\partial v}{\partial z} + \bar{w}\frac{\partial w}{\partial z} + \frac{\partial p}{\partial z} = \text{Constant} \tag{I.34}$$

By setting the constant of integration equal to zero and taking the Fourier-Laplace transform of the equation, the following left eigenvector can be obtained.

$$\tilde{v}^L_{2new} = \begin{pmatrix} 0 & -\bar{u}\mu & -\bar{v}\mu & 1-\bar{w}\mu & -\mu \end{pmatrix} \tag{I.35}$$

Which can be shown to be a valid left eigenvector of the system.

The new set of non-reflecting boundary conditions thus becomes.

$$A^*\frac{\partial \vec{U}}{\partial t} + B^*\frac{\partial \vec{U}}{\partial y} + C^*\frac{\partial \vec{U}}{\partial z} = \vec{d} \tag{I.36}$$

$$A^* = \begin{bmatrix} -1 & 0 & 0 & 0 & 1 \\ 0 & 0 & 0 & 1 & 0 \\ 0 & 0 & 1 & 0 & 0 \\ 0 & 1 & 0 & 0 & 1 \\ 0 & -1 & 0 & 0 & 1 \end{bmatrix} \quad B^* = \begin{bmatrix} 0 & 0 & 0 & 0 & 0 \\ 0 & 0 & 0 & 0 & 0 \\ 0 & \bar{u} & \bar{v} & -\bar{w} & 1 \\ 0 & \bar{v} & -\bar{u} & 0 & \bar{v} \\ 0 & -\bar{v} & \bar{u} & 0 & \bar{v} \end{bmatrix}$$

$$C^* = \begin{bmatrix} 0 & 0 & 0 & 0 & 0 \\ 0 & \bar{u} & \bar{v} & \bar{w} & 1 \\ 0 & 0 & 2\bar{w} & 0 & 0 \\ 0 & \bar{w} & 0 & -\bar{u} & \bar{w} \\ 0 & -\bar{w} & 0 & \bar{u} & \bar{w} \end{bmatrix}$$

Since A^* is now invertible, these equations can easily be cast into a form which is suitable for solving in a standard time integration scheme. What remains is to determine whether or not these equations are well posed as stated.

I.2.2 Well Posedness

As shown in the Theory section, it is not entirely sufficient to apply the left eigenvector to the solution in order to set the magnitude of a given mode to zero. To demonstrate this, the non-reflecting boundary conditions at a inlet flow boundary will be considered. At an inlet, the first four modes are all incoming modes for a subsonic flow. Thus the statement of non-reflectivity can be written as.

$$\begin{bmatrix} \tilde{u}_1^L \\ \tilde{u}_{2new}^L \\ \tilde{u}_3^L \\ \tilde{u}_4^L \end{bmatrix} \tilde{u} = \begin{bmatrix} \tilde{u}_1^L \\ \tilde{u}_{2new}^L \\ \tilde{u}_3^L \\ \tilde{u}_4^L \end{bmatrix} \begin{bmatrix} \tilde{u}_1^R & \tilde{u}_2^R & \tilde{u}_3^R & \tilde{u}_4^R \end{bmatrix} \begin{pmatrix} a_1 \\ a_2 \\ a_3 \\ a_4 \end{pmatrix} = \begin{pmatrix} 0 \\ 0 \\ 0 \\ 0 \end{pmatrix} \tag{I.37}$$

This can be rewritten in a more suggestive form as

$$\begin{bmatrix} D_{1,1} & D_{1,2} & D_{1,3} & D_{1,4} \\ D_{2,1} & D_{2,2} & D_{2,3} & D_{2,4} \\ D_{3,1} & D_{3,2} & D_{3,3} & D_{3,4} \\ D_{4,1} & D_{4,2} & D_{4,3} & D_{4,4} \end{bmatrix} \begin{pmatrix} a_1 \\ a_2 \\ a_3 \\ a_4 \end{pmatrix} = \begin{pmatrix} 0 \\ 0 \\ 0 \\ 0 \end{pmatrix} \tag{I.38}$$

where the terms in the matrix are defined as follows.

$$D_{i,j} = \tilde{u}_i^L \tilde{u}_j^R \tag{I.39}$$

In order to have the coefficients (a_i) equal to zero, it is necessary that the matrix D not be singular for values of ω which correspond to modes which are growing in time and decay away from the boundary. For an orthogonal set of eigenvectors, this matrix will only have non-zero entries on the diagonal. But, as long as the eigenvectors form a linearly independent set, this condition need not be met to analyze the well-posedness of the system.

The algebraic steps involved in this process can be reduced substantially if a coordinate system is used which is moving with a velocity $= \bar{v}\hat{y} + \bar{w}\hat{z}$ with no loss in generality. In this system, the values for $\bar{v}$ and $\bar{w}$ will be zero. With this simplification, the matrix becomes.

$$D = \begin{bmatrix} -1 & 0 & 0 & 0 \\ 0 & \bar{u}^2\mu^2 + 1 & -\lambda & 0 \\ 0 & \bar{u}^2\lambda\mu & \mu & 0 \\ 0 & 0 & 0 & D_{4,4} \end{bmatrix} \tag{I.40}$$

$$D_{4,4} = \bar{u} - \sqrt{1 + \left(\bar{u}^2 - 1\right)\left(\lambda^2 + \mu^2\right)} + \left(\lambda^2 + \mu^2\right)\left(\bar{u}^2 - 1\right)\bar{u}$$

Due to the near orthogonality of the eigenvectors, some of the modes are decoupled from the others in this analysis. The first and fourth modes can be evaluated by themselves, while the second and third mode remain coupled. For the first mode, the value in the matrix is -1, which is clearly non-zero always. For the next two modes, it is necessary to take the determinant of the two-by-two system of coefficients in the center of the matrix. This result is.

$$\omega^2 + \bar{u}^2\left(l^2 + m^2\right) = 0 \tag{I.41}$$

For real l and m, the solution for ω is a pair of complex conjugates. Since one of these values has an imaginary part which is greater than zero, this solution represents a mode which is growing exponentially in time. It remains to check the form of this unbounded solution to see if it is a possible solution. For the case where $\bar{v} = \bar{w} = 0$,

the eigenvalue for this mode is.

$$k_{2,3} = \frac{\omega}{\bar{u}} \tag{I.42}$$

Substitution of ω equal to a positive imaginary value into the eigenvalue relation and into the original solution form I.1 gives a mode which is decays away from the inlet boundary. Therefore this is a possible mode of the system which grows in time and therefore violates the well-posedness criteria.

For the fourth mode, the well posedness criteria can be written as.

$$-X + X^2\bar{u} = 0 \tag{I.43}$$

$$X = \sqrt{1 + (\bar{u}^2 - 1)(\lambda^2 + \mu^2)}$$

The solutions to this equation are:

$$X = 0 \tag{I.44}$$

$$X = \frac{1}{\bar{u}} \tag{I.45}$$

These solutions can be reduced to the following expressions.

$$\omega^2 = \left(1 - \bar{u}^2\right)\left(l^2 + m^2\right) \tag{I.46}$$

$$\left(1 - \frac{1}{\bar{u}^2}\right)\omega^2 = \left(1 - \bar{u}^2\right)\left(l^2 + m^2\right) \tag{I.47}$$

For subsonic flow the first set of these solutions will be purely real, and the other will form a pair of complex conjugates. Since once again, a solution has been found with a positive imaginary part, it is necessary to examine the form of this solution. The solution with a positive imaginary part can be written as.

$$\omega = \imath\sqrt{\left|\frac{1 - \bar{u}^2}{1 - 1/\bar{u}^2}\right|(l^2 + m^2)} \tag{I.48}$$

This solution may then be substituted into the eigenvalue evaluated at $\bar{v} = \bar{w} = 0$.

$$k_4 = \frac{\omega\left(S - \bar{u}\right)}{1 - \bar{u}^2} \tag{I.49}$$

$$S = \sqrt{1 - \frac{\left(1 - \bar{u}^2\right)\left(l^2 + m^2\right)}{\omega^2}}$$

For the subsonic case with ω^2 a negative real number, the value for S is always a real number greater than one. Thus, k_4 will be a positive imaginary number. As in the case with the second and third non-reflecting equations, this one is also ill-posed.

For the exit non-reflecting boundary condition, the well posedness criteria is.

$$X + X^2\bar{u} = 0 \tag{I.50}$$

This relation has the same solutions as the one for the fourth inlet mode. Following the same procedures, the eigenvalue is.

$$k_5 = \frac{\omega\left(-S - \bar{u}\right)}{1 - \bar{u}^2} \tag{I.51}$$

Which gives a negative imaginary value for k_5 when ω is a positive imaginary value. Since this condition is imposed at the exit plane, this also gives a possible mode which decays away from the boundary. Therefore, this exit condition is ill-posed as well.

Satisfying the Well-Posedness Condition

Because the equations derived to enforce non-reflectivity cannot be solved in their present ill-posed form, it will be necessary to modify them. Since the vectors used will no longer be true eigenvectors this will result in errors in the imposition of the non-reflective relations. Ideally, the process of modifying these equations should be done in such a manner as to minimize any induced errors. However, a modification to any left eigenvector can change its orthogonality relation with each right eigenvector. This will quickly cause the D matrix in Equation I.40 to loose its present simple form. The resulting well posedness analysis for this modified matrix will become

increasingly more difficult as changes are made to the left eigenvectors.

By inspection of Equations I.41 and I.47, the positive imaginary solution can be avoided if $\overline{u}$ is set to zero in the eigenvectors. While this solution may seem somewhat Draconian, it was found to fix the well-posedness of both the inlet and exit conditions. It is difficult to prove that the system will be strictly well-posed.

I.2.3 Solution Form

By incorporating the modification to fix the ill-posedness of the non-reflecting boundary conditions, the final form of the equations is obtained.

$$A^*_{mod}\frac{\partial \vec{U}}{\partial t} + B^*_{mod}\frac{\partial \vec{U}}{\partial y} + C^*_{mod}\frac{\partial \vec{U}}{\partial z} = \vec{d} \tag{I.52}$$

$$A^*_{mod} = \begin{bmatrix} -1 & 0 & 0 & 0 & 1 \\ 0 & 0 & 0 & 1 & 0 \\ 0 & 0 & 1 & 0 & 0 \\ 0 & 1 & 0 & 0 & 1 \\ 0 & -1 & 0 & 0 & 1 \end{bmatrix} \quad B^*_{mod} = \begin{bmatrix} 0 & 0 & 0 & 0 & 0 \\ 0 & 0 & 0 & 0 & 0 \\ 0 & 0 & \bar{v} & -\bar{w} & 1 \\ 0 & \bar{v} & 0 & 0 & \bar{v} \\ 0 & -\bar{v} & 0 & 0 & \bar{v} \end{bmatrix}$$

$$C^*_{mod} = \begin{bmatrix} 0 & 0 & 0 & 0 & 0 \\ 0 & 0 & \bar{v} & \bar{w} & 1 \\ 0 & 0 & 2\bar{w} & 0 & 0 \\ 0 & \bar{w} & 0 & 0 & \bar{w} \\ 0 & -\bar{w} & 0 & 0 & \bar{w} \end{bmatrix}$$

By defining

$$\vec{c} = A^*_{\text{mod}}\vec{U} \tag{I.53}$$

Equation I.52 can be written in an easier form to solve.

$$\frac{\partial \vec{c}}{\partial t} + E\frac{\partial \vec{c}}{\partial y} + F\frac{\partial \vec{c}}{\partial z} = \vec{d} \tag{I.54}$$

$$E = B^*_{mod} {A^*_{mod}}^{-1} = \begin{bmatrix} 0 & 0 & 0 & 0 & 0 \\ 0 & 0 & 0 & 0 & 0 \\ 0 & -\bar{w} & \bar{v} & \frac{1}{2} & \frac{1}{2} \\ 0 & 0 & 0 & \bar{v} & 0 \\ 0 & 0 & 0 & 0 & \bar{v} \end{bmatrix} \tag{I.55}$$

$$F = C^*_{mod} {A^*_{mod}}^{-1} = \begin{bmatrix} 0 & 0 & 0 & 0 & 0 \\ 0 & \bar{w} & \bar{v} & \frac{1}{2} & \frac{1}{2} \\ 0 & 0 & 2\bar{w} & 0 & 0 \\ 0 & 0 & 0 & \bar{w} & 0 \\ 0 & 0 & 0 & 0 & \bar{w} \end{bmatrix} \tag{I.56}$$

To solve the non-reflecting boundary equations at the inlet, the first four elements of $\vec{d}$ vector are set to zero and the first four equations in this set are solved. The remaining information is obtained by extrapolating from the interior of the flow solution. These steps will be described in greater detail in the following section. To solve for the exit conditions, only the last equation of this set is required. For this case, the last element of the $\vec{d}$ vector must be set to zero. The exit case will require that four pieces of information be extrapolated from the interior.

Dimensional Form of the Solution

Although the derivation of the non-reflecting boundary conditions is greatly simplified by using the non-dimensional form of the equations, the dimensional form is often required for implementation. In the dimensional form, the forward and inverse transformation between the primitive and characteristic variables becomes:

$$\begin{pmatrix} c_1 \\ c_2 \\ c_3 \\ c_4 \\ c_5 \end{pmatrix} = \begin{bmatrix} -\bar{c}^2 & 0 & 0 & 0 & 1 \\ 0 & 0 & 0 & \bar{\rho}\bar{c} & 0 \\ 0 & 0 & \bar{\rho}\bar{c} & 0 & 0 \\ 0 & \bar{\rho}\bar{c} & 0 & 0 & 1 \\ 0 & -\bar{\rho}\bar{c} & 0 & 0 & 1 \end{bmatrix} \begin{pmatrix} \delta\rho \\ \delta u \\ \delta v \\ \delta w \\ \delta p \end{pmatrix} \tag{I.57}$$

$$\begin{pmatrix} \delta\rho \\ \delta u \\ \delta v \\ \delta w \\ \delta p \end{pmatrix} = \begin{bmatrix} -\frac{1}{\bar{c}^2} & 0 & 0 & \frac{1}{2\bar{c}^2} & \frac{1}{2\bar{c}^2} \\ 0 & 0 & 0 & \frac{1}{2\bar{\rho}\bar{c}} & -\frac{1}{2\bar{\rho}\bar{c}} \\ 0 & 0 & \frac{1}{\bar{\rho}\bar{c}} & 0 & 0 \\ 0 & \frac{1}{\bar{\rho}\bar{c}} & 0 & 0 & 1 \\ 0 & 0 & 0 & \frac{1}{2} & \frac{1}{2} \end{bmatrix} \begin{pmatrix} c_1 \\ c_2 \\ c_3 \\ c_4 \\ c_5 \end{pmatrix} \tag{I.58}$$

The matrices used in Equation I.54 become:

$$E = \begin{bmatrix} 0 & 0 & 0 & 0 & 0 \\ 0 & 0 & 0 & 0 & 0 \\ 0 & -\bar{w} & \bar{v} & \frac{\bar{c}}{2} & \frac{\bar{c}}{2} \\ 0 & 0 & 0 & \bar{v} & 0 \\ 0 & 0 & 0 & 0 & \bar{v} \end{bmatrix} \quad F = \begin{bmatrix} 0 & 0 & 0 & 0 & 0 \\ 0 & \bar{w} & \bar{v} & \frac{\bar{c}}{2} & \frac{\bar{c}}{2} \\ 0 & 0 & 2\bar{w} & 0 & 0 \\ 0 & 0 & 0 & \bar{w} & 0 \\ 0 & 0 & 0 & 0 & \bar{w} \end{bmatrix} \tag{I.59}$$

I.2.4 Implementation

The implementation of the non-reflecting boundary conditions depends upon the physical flow situation which is being modeled. For the situation presented in here, the boundary conditions are being used to approximate an infinite flow duct on a truncated domain. With slight modifications the same method can be used to impose non-uniformities at an inlet or exit while preventing the unwanted reflection of outgoing waves as they leave the computational domain. This is described in some detail by Giles [15].

For the case of the approximation of an infinite flow domain, the flow at the boundary can be thought of as composed of two parts. The first part is the mean background flow. This background flow need not be steady. It can be specified explicitly, or solved for in conjunction with the non-reflecting boundary conditions. For this study, the mean background flow was solved for using the one-dimensional characteristic theory as presented in Appendix G. The second part of the flow is the perturbations of the flow quantities about the mean background flow. Some care should be exercised when computing the mean flow quantities for this purpose. In order to be consistent with the Euler equations, the averaging procedure should

conserve mass, momentum and energy. The stream thrust averaging method will satisfy these conditions. For a detailed explanation of this method see Appendix J.

After computing the mean flow quantities, the perturbational quantities can be computed directly by subtracting the mean. From these values the characteristic variables are computed using the transformation given in Equation I.57. Having computed the perturbational and characteristic values, the changes of the flow can be computed for the next time step. This is done separately for the mean background flow and for the perturbational values. The mean background flow changes can be specified in a variety of ways. In general some change is going to be made in the mean flow which will be referred to as: $\Delta\rho_{mean}$, Δu_{mean}, Δv_{mean}, Δw_{mean}, and Δp_{mean}.

The update to the characteristic variables is computed using the non-reflecting boundary condition equations which have been derived previously. However, this will form an incomplete set for both the inlet and exit for subsonic flows. At the inlet, four of the equations will be used, but one more piece of information must be obtained from the interior of the flow solution. At the exit, only one equation will apply. Since it is more instructive to describe the steps required to update the characteristic values in the context of a specific problem, the update of these values at the inlet boundary will be described.

Inlet Boundary

For the inlet the first four non-reflecting boundary equations are required. Since no reflections are desired, the right hand side of these equations are set to zero. Thus, the boundary equations to solve at the inlet are:

$$\frac{1}{\Delta t}\begin{pmatrix}\Delta c_1\\ \Delta c_2\\ \Delta c_3\\ \Delta c_4\end{pmatrix}+\begin{bmatrix}0 & 0 & 0 & 0 & 0\\ 0 & 0 & 0 & 0 & 0\\ 0 & -\bar{w} & \bar{v} & \frac{\bar{c}}{2} & \frac{\bar{c}}{2}\\ 0 & 0 & 0 & \bar{v} & 0\end{bmatrix}\frac{\partial}{\partial y}\begin{pmatrix}c_1\\ c_2\\ c_3\\ c_4\\ c_5\end{pmatrix}+\begin{bmatrix}0 & 0 & 0 & 0 & 0\\ 0 & \bar{w} & \bar{v} & \frac{\bar{c}}{2} & \frac{\bar{c}}{2}\\ 0 & 0 & 2\bar{w} & 0 & 0\\ 0 & 0 & 0 & \bar{w} & 0\end{bmatrix}\frac{\partial}{\partial z}\begin{pmatrix}c_1\\ c_2\\ c_3\\ c_4\\ c_5\end{pmatrix}=\vec{0} \tag{I.60}$$

These equations have been written using a simple first order discrete representation of the time derivative. A higher order approximation of the time derivative could be used as well. The non-reflecting boundary equations can be integrated using the same type of schemes typically used in computational fluid dynamics. Depending on the integration scheme used, it may be necessary to add some numerical dissipation.

It is still necessary to compute a value for Δc_5. Since the fifth eigenvalue of the Euler equations gives an upstream running wave, it is necessary to update the last characteristic value using information from the interior of the computational domain. The simplest method is to extrapolate the changes in the flow variable from the interior, and then compute the change in the fifth characteristic value. When these values are extrapolated, it is important to subtract off the mean change in the flow values since only the perturbational change is desired. A simple first order extrapolation can be used.

$$\Delta\delta\rho_{1,j,k} = \rho^{(n)}_{2,j,k} - \rho^{(n-1)}_{2,j,k} - \left\{\left(\rho^{(n)}_{3,j,k} - \rho^{(n-1)}_{3,j,k}\right) - \left(\rho^{(n)}_{2,j,k} - \rho^{(n-1)}_{2,j,k}\right)\right\} - \Delta\rho_{mean} \qquad \text{(I.61)}$$

In this notation, the superscript denotes the time step and the subscript denotes the spatial indices. The change in the perturbational value of u, v, w, and p can be calculated in the same way. Using the transformation defined in Equation I.57, the change in the fifth characteristic value can be computed at each inlet grid point as follows:

$$\begin{pmatrix} \Delta c_5 \end{pmatrix} = \begin{bmatrix} 0 & -\bar{\rho}\bar{c} & 0 & 0 & 1 \end{bmatrix} \begin{pmatrix} \Delta\delta\rho \\ \Delta\delta u \\ \Delta\delta v \\ \Delta\delta w \\ \Delta\delta p \end{pmatrix} \qquad \text{(I.62)}$$

Now that all of the updates to the characteristic values have been computed, updates to the inlet flow field are rather straight forward. First, the characteristic values are updated. Because these values represent perturbations from the mean flow, the mean change due to these relations should be zero. Therefore, the mean change

has been removed in updating the characteristic values.

$$\begin{pmatrix} c_1^{(n+1)} \\ c_2^{(n+1)} \\ c_3^{(n+1)} \\ c_4^{(n+1)} \\ c_5^{(n+1)} \end{pmatrix} = \begin{pmatrix} c_1^{(n)} - c_{1,mean} \\ c_2^{(n)} - c_{2,mean} \\ c_3^{(n)} - c_{3,mean} \\ c_4^{(n)} - c_{4,mean} \\ c_5^{(n)} - c_{5,mean} \end{pmatrix} + \begin{pmatrix} \Delta c_1 \\ \Delta c_2 \\ \Delta c_3 \\ \Delta c_4 \\ \Delta c_5 \end{pmatrix} \tag{I.63}$$

With the new characteristic values, the new perturbational flow quantities are obtained by using the inverse transform of Equation I.58.

$$\begin{pmatrix} \delta\rho^{(n+1)} \\ \delta u^{(n+1)} \\ \delta v^{(n+1)} \\ \delta w^{(n+1)} \\ \delta p^{(n+1)} \end{pmatrix} = \begin{bmatrix} -\frac{1}{\bar{c}^2} & 0 & 0 & \frac{1}{2\bar{c}^2} & \frac{1}{2\bar{c}^2} \\ 0 & 0 & 0 & \frac{1}{2\bar{\rho}\bar{c}} & -\frac{1}{2\bar{\rho}\bar{c}} \\ 0 & 0 & \frac{1}{\bar{\rho}\bar{c}} & 0 & 0 \\ 0 & \frac{1}{\bar{\rho}\bar{c}} & 0 & 0 & 1 \\ 0 & 0 & 0 & \frac{1}{2} & \frac{1}{2} \end{bmatrix} \begin{pmatrix} c_1^{(n+1)} \\ c_2^{(n+1)} \\ c_3^{(n+1)} \\ c_4^{(n+1)} \\ c_5^{(n+1)} \end{pmatrix} \tag{I.64}$$

The final new flow values are obtained by adding the new perturbational values to the new mean value.

Exit Boundary

The process is essentially identical for the exit. At the exit only the last non-reflecting boundary equation is required.

$$\frac{1}{\Delta t}\begin{pmatrix} \Delta c_5 \end{pmatrix} + \begin{bmatrix} 0 & 0 & 0 & 0 & \bar{v} \end{bmatrix} \frac{\partial}{\partial y} \begin{pmatrix} c_1 \\ c_2 \\ c_3 \\ c_4 \\ c_5 \end{pmatrix} + \begin{bmatrix} 0 & 0 & 0 & 0 & \bar{w} \end{bmatrix} \frac{\partial}{\partial z} \begin{pmatrix} c_1 \\ c_2 \\ c_3 \\ c_4 \\ c_5 \end{pmatrix} = 0 \tag{I.65}$$

The remaining quantities are updated using information extrapolated from the interior. At the exit this becomes.

$$\Delta\delta\rho_{NI,j,k} = \rho^{(n)}_{NI-1,j,k} - \rho^{(n-1)}_{NI-1,j,k}$$
$$- \left\{ \left(\rho^{(n)}_{NI-2,j,k} - \rho^{(n-1)}_{NI-2,j,k} \right) - \left(\rho^{(n)}_{NI-1,j,k} - \rho^{(n-1)}_{NI-1,j,k} \right) \right\} - \Delta\rho_{mean} \tag{I.66}$$

Once again using the transformation defined in Equation I.57, the change in the remaining characteristic values can be computed at each exit grid point as follows:

$$\begin{pmatrix} \Delta c_1 \\ \Delta c_2 \\ \Delta c_3 \\ \Delta c_4 \end{pmatrix} = \begin{bmatrix} -\bar{c}^2 & 0 & 0 & 0 & 1 \\ 0 & 0 & 0 & \bar{\rho}\bar{c} & 0 \\ 0 & 0 & \bar{\rho}\bar{c} & 0 & 0 \\ 0 & \bar{\rho}\bar{c} & 0 & 0 & 1 \end{bmatrix} \begin{pmatrix} \Delta\delta\rho \\ \Delta\delta u \\ \Delta\delta v \\ \Delta\delta w \\ \Delta\delta p \end{pmatrix} \tag{I.67}$$

The remaining steps are identical to the inlet boundary.

Appendix J

Stream Thrust Averaging

In order to derive the overall performance of the compressor it becomes necessary to perform some type of averaging. To be entirely consistent from station to station, stream thrust averaging was chosen as the most appropriate average to use. This method is also the most appropriate form to use for implementing non-reflecting boundary conditions.

In this method, the average quantities are defined as those that would yield the same mass, momentum, and energy fluxes as the flow being averaged. This condition can be stated as follows:

$$\begin{aligned}
\overline{\rho u} = \frac{1}{Area}\int \rho u dA &\equiv A \\
\overline{p} + \overline{\rho u}^2 = \frac{1}{Area}\int \left(p + \rho u^2\right) dA &\equiv B \\
\overline{\rho u v} = \frac{1}{Area}\int \rho u v dA &\equiv C \\
\overline{\rho u w} = \frac{1}{Area}\int \rho u w dA &\equiv D \\
\left(\overline{\rho e} + \overline{p} + \overline{\rho}\frac{\overline{u}^2 + \overline{v}^2 + \overline{w}^2}{2}\right)\overline{u} = & \\
\frac{1}{Area}\int \left[\left(\rho e + p + \rho\frac{u^2 + v^2 + w^2}{2}\right) u\right] dA &\equiv E
\end{aligned} \tag{J.1}$$

Plus the equation of state:

$$\overline{p} = \overline{\rho e}\,(\gamma - 1)$$

Where the over-barred quantities indicate average values. In this particular formulation, the plane of integration is perpendicular to the X axis.

By substituting the remaining equations into the energy equation, a quadratic equation in $\overline{p}$ can be obtained:

$$\left(\frac{-1}{\gamma-1}-\frac{1}{2}\right)\overline{p}^2+B\left(\frac{1}{\gamma-1}\right)\overline{p}+\frac{1}{2}\left(B^2+C^2+D^2\right)-EA=0 \qquad \text{(J.2)}$$

This will yield two roots, but for flows with positive axial fluxes ($B>0, EA>0$), only one of these solutions will yield a positive value. In general the second law of thermodynamics can be used to select the root which corresponds to an increase in entropy. The remaining quantities can then be solved for by back-substituting into the remaining equations.